Dissertation

SUBMITTED TO THE

Combined Faculty of Mathematics, Engineering and Natural Sciences

of Heidelberg University, Germany

FOR THE DEGREE OF

Doctor of Natural Sciences

Put forward by

Miriam Lena Gerharz

Born in: Lahnstein, Germany

Oral examination: 18.12.2025

Nuclear quantum dynamics driven by X-ray free-electron lasers

Referees:

apl. Prof. Dr. Jörg Evers

Prof. Dr. Maurits Haverkort

Zusammenfassung

Mössbauerspektroskopie ist in den Naturwissenschaften fest etabliert. Die außergewöhnlich schmalen Linienbreiten von Mössbauerkernen machen sie zudem zu einer vielversprechenden Plattform für Quantenoptik im Röntgenbereich. Mehrere grundlegende quantenoptische Phänomene, darunter elektromagnetisch induzierte Transparenz und Superradianz, konnten bereits nachgewiesen werden. Über Jahrzehnte hinweg beschränkte jedoch genau diese schmale Linienbreite die Experimente an Synchrotronen auf das Niedriganregungsregime, mit im Mittel weniger als einem resonanten Photon pro Puls. Diese Einschränkung änderte sich mit dem Aufkommen von Röntgen-Freie-Elektronen-Lasern (XFELs), die um Größenordnungen mehr Photonen liefern als Synchrotronen. Dadurch treten Pulse mit mehreren resonanten Photonen regelmäßig auf, was zuvor unmögliche Experimente erlaubt. In dieser Arbeit präsentieren wir mehrere erstmalig durchgeführte XFEL-Experimente innerhalb unserer Kollaborationen. Wir demonstrieren die Röntgenanregung der ^{45}Sc-Kernuhr-Übergangsfrequenz, entwickeln und wenden eine Analyse auf Einzelschussbasis für Mössbauerdaten im Zeitraum an und untersuchen unerwartete Messergebnisse in der resonanten Kernstreuung mit XFELs. Zusätzlich simulieren wir die Abregungsdynamik eines Kernensembles. Neben der Etablierung eines geeigneten Simulationsverfahrens konzentrieren wir uns auf nichtlineare Effekte, die aus Dipol-Dipol-Kopplungen sowie aus nichtlinearen Modifikationen von Propagationseffekten resultieren. Insgesamt zeigen diese Ergebnisse, wie die beispiellose Intensität von XFELs eine neue Ära der Mössbauerforschung eröffnet und sowohl Experimente als auch Theorie entscheidend voranbringt.

Abstract

Mössbauer spectroscopy is well established across the natural sciences. The exceptionally narrow linewidths of Mössbauer nuclei also make them a promising platform for x-ray quantum optics. Several fundamental quantum-optical phenomena, including electromagnetically induced transparency and superradiance, have already been demonstrated. Yet for decades, the same narrow linewidth restricted experiments at synchrotrons to the low-excitation regime, with on average less than one resonant photon per pulse. This limitation changed with the advent of X-ray free-electron lasers (XFELs), which deliver orders of magnitude more photons than synchrotrons. As a result, pulses containing multiple resonant photons occur frequently, enabling experiments previously not possible. In this thesis, we present several first-of-their-kind XFEL-experiments conducted within our collaborations. We demonstrate the x-ray excitation of the ^{45}Sc nuclear clock transition, introduce and apply a single-shot analysis to Mössbauer time-domain data, and investigate unexpected signals observed in nuclear resonant scattering with XFELs. Additionally, we simulate the de-excitation dynamics of a nuclear ensemble. Besides establishing a suitable simulation scheme, we focus on non-linear effects arising from dipole-dipole couplings and non-linear modifications of propagation effects. Together, these results show how the unprecedented intensities of XFELs open a new era for Mössbauer science, advancing both experiment and theory.

Within the framework of this thesis, the following article was published in a refereed journal:

[Shv+23] ***Resonant X-ray excitation of the nuclear clock isomer ^{45}Sc***
Y. Shvyd'ko, R. Röhlsberger, O. Kocharovskaya, J. Evers, G. A. Geloni, P. Liu, D. Shu, A. Miceli, B. Stone, W. Hippler, B. Marx-Glowna, I. Uschmann, R. Loetzsch, O. Leupold, H.-C. Wille, I. Sergeev, M. Gerharz, X. Zhang, C. Grech, M. Guetg, V. Kocharyan, N. Kujala, S. Liu, W. Qin, A. Zozulya, J. Hallmann, U. Boesenberg, W. Jo, J. Möller, A. Rodriguez-Fernandez, M. Youssef, A. Madsen, and T. Kolodziej
Nature **622**, 471–475 (2023)

The thesis author performed the data evaluation leading to the main result. In addition, the thesis author designed the data analysis for the experiment and operated it as part of the experimental team.

The following articles are submitted to refereed journals and are available as preprints:

[Ger+25b] ***Single-shot sorting of Mössbauer time-domain data at X-ray free electron lasers***
M. Gerharz, W. Hippler, B. Marx-Glowna, S. Sadashivaiah, K. S. Schulze, I. Uschmann, R. Lötzsch, K. Schlage, S. Velten, D. Lentrodt, L. Wolff, O. Leupold, I. Sergeev, H.-C. Wille, C. Strohm, M. Guetg, S. Liu, G. A. Geloni, U. Boesenberg, J. Hallmann, A. Zozulya, J.-E. Pudell, A. Rodriguez-Fernandez, M. Youssef, A. Madsen, L. Bocklage, G. G. Paulus, C. H. Keitel, T. Pfeifer, R. Röhlsberger, and J. Evers
arXiv:2509.15833 [quanth-ph]

The thesis author is the sole first author, and in this role developed the single-shot sorting scheme and analyzed the data. In addition, the thesis author designed the data analysis for the experiment and operated it as part of the experimental team.

[Ger+25a] ***Dark-fringe interferometer with dynamic phase control for Mössbauer science***
M. Gerharz, D. Lentrodt, L. Bocklage, K. Schulze, C. Ott, R. Steinbrügge, O. Leupold, I. Sergeev, G. Paulus, C. H. Keitel, R. Röhlsberger, T. Pfeifer, and J. Evers
arXiv:2509.24658 [quanth-ph]

The thesis author is the sole first author, and in this role developed the interferometer scheme and performed the data analysis. In addition, the thesis author was part of the experimental team.

[Liu+25a] ***Probing the Linewidth of the 12.4-keV Solid-State ^{45}Sc Isomeric Resonance***
P. Liu, M. Gerharz, B. Marx-Glowna, W. Hippler, J.-E. Pudell, A. Zozulya, B. Stone, D. Shu, R. Loetzsch, S. Sadashivaiah, L. Bocklage, C. Boemer, S. Liu, V. Kocharyan, D. Krebs, T. Long, W. Qin, M. Scholz, K. Schlage, I. Sergeev, H.-C. Wille, U. Boesenberg, G. A. Geloni, J. Hallmann, W. Jo, N. Kujala, A. Madsen, A. Rodriguez-Fernandez, R. Rysov, K. Tasca, T. Kolodziej, X. Zhang, M. Ilchen, N. Wieland, G. Huber, J. H. Edgar, J. Evers, O. Kocharovskaya, R. Röhlsberger, and Y. Shvyd'ko
arXiv:2508.17538 [quanth-ph]

The thesis designed the data analysis for the experiment and operated it as part of the experimental team. In addition, the thesis author contributed to the data evaluation.

The following article is available as a preprint:

[GE25] ***Cumulant expansion approach to the decay dynamics of interacting Mössbauer nuclei after strong impulsive excitation***
M. Gerharz and J. Evers
arXiv:2510.00970 [quanth-ph]

The thesis author is the sole first author.

Declarations on usage of the material in this document are given at the start of each chapter.

Outside the scope of this thesis, the following article is currently in preparation:

[AGE_p] ***Signatures for non-linear excitation of Mössbauer nuclei in the presence of propagation effects***
D. Adigüzel, M. Gerharz, and J. Evers
in preparation

The thesis author co-supervised the first author, and contributed to shaping the project and interpreting the results.

Contents

Chapter 1

Introduction

"Scientific revolutions are more often driven by new tools than by new concepts."
– Freeman Dyson

1.1 Motivation

The study of quantum dynamics has not only been in the center of scientific interest as we will see in this chapter, but has also brought significant technological progress. The prime example of this is the laser, which is not only one of the most important tools in science, but also has numerous technological applications, e.g., metrology, laser cutting and welding or eye surgery. In the sense of Freeman Dyson's quote, the improvement of laser technology has significantly driven the field of quantum dynamics.

But let us start at the early times of the study of light-matter interactions with relation to quantum dynamics. Already in the early 1800s, William Hyde Wollaston and Joseph von Fraunhofer independently discovered that there are dark lines in the emission spectrum of the sun [Fra17; Wol02]. Only in 1859, Gustav Kirchhoff and Robert Bunsen attributed the dark lines to the presence of certain elements in the outer part of the sun [KB60]. This pioneering work laid the foundation for modern spectroscopy. The new technique lead to the discovery of new elements based on their spectral lines, e.g., rubidium and cesium by Kirchhoff and Bunsen themselves [KB61], red-shifted stars [Hug68], but also to systematic measurements of series in an atomic spectrum, such as the Balmer-series [Bal85] and its generalization by Johannes Rydberg [Ryd90]. In the next decades, the relation of those measured spectral series with theoretically calculated atomic transition lines by Niels Bohr [Boh13] was one of the important steps that laid the foundations of quantum mechanics. Further important steps included the black body-radiation spectrum by Max Planck [Pla01] or the photo-electric effect by Albert Einstein [Ein05]. The new theory of quantum mechanics revolutionized the interpretation of light-matter interactions. Atoms were now described by discrete levels and light was known to consist of photons. A first full quantum framework for light-matter interactions was formulated by Paul Dirac [Dir27]. In the mean-time, the experimental techniques also improved significantly and allowed precise spectroscopic measurements, e.g., Raman scattering of light [LM28; RK28], i.e., the inelastic scattering of photons, or the Lamb shift [LR47] due to virtual photons [Bet47]. On the theoretical side, the Breit-Wigner Theory [BW36] describing resonant scattering and absorption, and the formulation of quantum electrodynamics [Dys49; Fey49; Sch48; Tom46] were important developments.

Building on the improved understanding of light-matter interactions, the next big breakthrough was the development of the maser [GZT55] and the subsequent realization of the laser [Mai60; ST58]. As already mentioned, lasers are nowadays found in nearly every atomic physics laboratory, but also have various industrial applications. Now, a controllable, coherent and monochromatic light source was available. Because of this technological advent, in the following a tremendous amount of important work was performed including the demonstration of second-harmonic generation [Fra+61], optical double-photon absorption [Abe62; Göp31] and early theoretical proposals of laser cooling [HS75]. Further technological improvement of the light sources followed in the next decades in the form of Q-switching [MH62], mode-locking [DiD64; HFP64; Yar65] and chirped pulse amplification [SM85], which allowed to produce stronger and with high-harmonic generation [Bur+77; Lew+94] also shorter pulses up to attosecond pulse durations [Pau+01]. Furthermore, frequency combs [UHH02] improved the spetral precision and quantum states of light, e.g., squeezed-light [Cav81; Slu+85] were produced. Those technological processes led to the ultimate breakthroughs in the field of quantum optics. To only name a few of them, attosecond pulses allow to study the electron dynamics in atoms [Kie+04] or molecules [Cal+14]. Besides, based on the improved laser control and smaller bandwidth, several laser cooling [HS75; PM82; WD75] and trapping schemes [Ash78; Raa+87] have been realized, and subsequently the first Bose-Einstein condensate [Dav+95; Pau+01] and atom interferometry [CM91;

PCC99] were demonstrated. The improved control of the lasers further enabled electromagnetically induced transparency [BIH91; KK86] and related effects [FIM05; LI01], stimulated Raman adiabatic passage [BTS98], and coherent control schemes [SB00]. Nowadays, the laser control and thus the control of the light-matter interactions is so good to fulfill the exceptionally high requirements for analogue quantum simulation [Bar+04; Fey18; Gre+02] or quantum gates [Mon+95]. The utmost frequency precision provided by frequency combs enable the operation of optical clocks [Blo+14] and is the basis for high precision experiments, e.g., gravitational redshift [Bot+22], gravitational wave detection [Abb+16] or variation of fundamental constants [Ros+08].

We have seen that the progress in the field of light-matter interactions is closely related to the progress of available light sources. So far we mainly concentrated on the optical regime, but lasers are nowadays available over a huge range of the electromagnetic spectrum [Trä12]. A similar story has been unfolding in the x-ray regime. After the discovery of x-rays by Wilhelm Röntgen in 1895 [Rön96], x-rays quickly entered the general public mainly with medical applications [TB13], but also with bizarre applications such as fitting of shoes [DH00]. Important steps on the scientific side were x-ray spectroscopy pioneered by Charles Barkla [Bar05; Bar11; BS09], Henry Moseley [Mos13] and Manne Siegbahn [Sie31], diffraction of x-rays by Max von Laue [FKL13] demonstrating that x-rays are indeed electromagnetic waves, x-ray crystallography to reconstruct crystal structures by William Henry Bragg and William Lawrence Bragg [BB13], and the measurement of the Compton effect [Com23] demonstrating that photons have momentum. Especially the structure determination by x-ray diffraction was extremely successful, e.g., providing the structure of DNA [FG53; WC53], penicillin [Cro+49], and insulin [Blu+71].

Despite the already demonstrated success of x-ray science based on x-ray tubes, the particular field of x-ray quantum optics has been limited in its possibilities due to the lack of coherent and bright light sources [Ada+13]. This only changed with the advent of synchrotron radiation sources in the 1960s and 1970s. That electrons in a storage ring loose energy due to synchrotron radiation was predicted in 1944 [IP44] and measured at the General Electric's synchrotron in 1947 [Ble46]. The first storage dedicated to producing synchrotron radiation started operation in the late 1960s [RM73]. With synchrotron radiation sources it was now possible to study quantum optical phenomena also in the x-ray regime [Ada+13]. X-rays can excite electronic transitions, but also nuclear transitions. Thus x-ray quantum optics can be divided into two subfield, x-ray quantum optics with atomic resonances and nuclear quantum optics. While the electronic transitions are typically spectrally broad and short-lived, nuclear transitions can be spectrally narrow and long-lived [RE21]. Among other schemes, with atomic resonances the Hanbury-Brown-Twiss effects [Kun+97], x-ray parametric down conversion [Shw+12], x-ray induced transparency [You+10], four-wave mixing [Glo+12], stimulated emission [Roh+12] and quantum imaging [Sch+17; Tro+23] have been demonstrated.

In the nuclear counter part, especially Mössbauer nuclei have been established as a valuable platform [RE21]. In 1958 Rudolf Mössbauer discovered the recoilless absorption and emission of x-rays by nuclei [Mös58], which is now called the Mössbauer effect and leads to narrow observed linewidths of the transitions in Mössbauer nuclei. For example, the well-established Mössbauer isotope ^{57}Fe has a transition energy of 14.4 keV and a linewidth of 4.7 neV [Röh04], and can be excited by the radioactive decay of ^{57}Co [YL13]. The narrow linewidths allow for high-precision spectroscopy, e.g., measuring material properties such as hyperfine splitting, quadrupole splitting and isomer shift [KS60] and following chemical reactions [Kre+05], but also more bizarre applications like the investigation of the movement of ants [Bon+68] or basiliar membranes [JB67]. The utmost frequency precision enabled the first terrestrial measurement of the gravitational redshift by measuring the frequency shift caused by a height difference in a 22.5 m high tower [PR59; PR60] and the measurement of a second order Doppler effect for accelerated systems as predicted by special relativity [CSW60; Hay+60; Kün63]. Mössbauer spectrometers further play important roles in art [Kei74], archaeology [WK04] and are sent on space missions, e.g., to prove the former existence of water on Mars [Kli+03; Kli+04]. So far all the named applications are based on radioactive sources, where the nuclei are excited via radioactive decay from a parent isotope.

A more efficient and controlled way to excite Mössbauer nuclei is with synchrotron radiation. This can considerably speed up the measurement due to the order of magnitude higher photon flux and brightness as compared to radioactive sources and easily allow for measurements in the time domain [Rub74]. Furthermore, synchrotrons can provide temporal and partial spatial coherence over the nuclear linewidth, such that a first coherent response could be detected in 1985 by Gerdau et al. [Ger+85] leading to the first detection of nuclear forward scattering with synchrotron radiation in 1991 by Hastings et al. [Has+91], which paved the way for many applications nowadays. The high

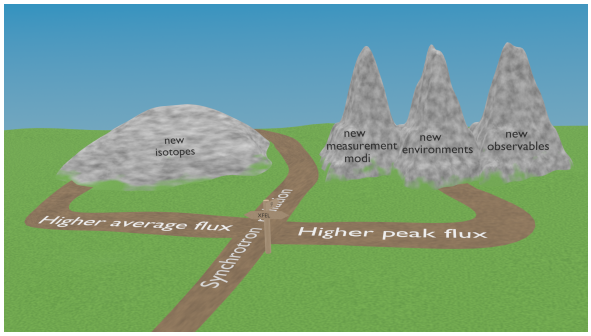

Figure 1.1: Artistic view on new possibilities in Mössbauer science with X-ray free-electron lasers (XFEL). Experiments at XFELs complement the traditional experiments with synchrotron radiation in two different ways – higher peak and higher average photon flux. The higher average flux allows to study isotopes with even smaller bandwidth than at synchrotrons. On the other hand, the higher peak flux implies a higher number of resonant photons and enables new measurement modi, such as in the direction of single shot spectroscopy. In addition, the extremely intense pulses might alter the environment of the nuclei, which could be probed with the nuclei. Third, the higher peak flux allows to study new observables, e.g., photon correlations, because in a large number of pulses more than one resonant photon can be detected.

photon flux allows faster recordings of spectra in the time domain from which material parameters can be extracted similar to in standard Mössbauer spectroscopy with radioactive sources [GBT11; Röh04; Stu04]. Furthermore, nuclear resonant inelastic x-ray scattering, with which for example phonon energy spectra can be measured, has been established with synchrotron radiation [Set+95; Stu04]. With synchrotron radiation also several quantum optical schemes have been successfully demonstrated in the x-ray regime. Among others there is demonstration of storage of excitation [KP16; Shv+96], electromagnetically induced transparency [Röh+12], collective Lamb shift and superradiance [HE13; Röh+10], slow light [Hee+15b], phase control [Hel+91] and related effects [Hee+17], coherent control [Boc+21; Hee+21; Vag+14], timed Dicke states [Hab+17; Scu+06], a quantum memory [LPK12; Vel+24; Zha+19], and phonon-driven control [Naz+25]. Besides a few exceptions, all the named experiments were performed at synchrotrons.

Although the availability of synchrotron radiation sources boosted the field of nuclear quantum optics significantly, for Mössbauer nuclei due to their small linewidth the number of resonant photons per pulse on average is still well below one. However, it was proposed that X-ray free-electron lasers (XFELs) can overcome this difficulty and open a new era for Mössbauer science [RE21; SR08]. With FLASH [Ack+07] the first XFEL started its user operation in 2005, shortly followed by LCLS in 2009, which was the first XFEL providing hard x-rays. Currently, with LCLS [Emm+10], SACLA [Ish+12], PAL-XFEL [Kan+17] and the European XFEL [Dec+20] four XFELs operate at high enough photon energies for typical Mössbauer isotopes. Experiments with those machines now indeed provide pulses with significantly more than one resonant photon per pulse as it was demonstrated in a first experiment by Chumakov et al. in 2018 [Chu+18]. In recent years, self-seeding enabled a further increase in the resonant x-ray flux [Ama+12; Ino+19; Liu+23; Nam+21]. The increase of the resonant photon flux at XFELs as compared to synchrotron radiation sources is not only a quantitative advantage, but especially having more than one resonant photon in a considerable amount of pulses is also an important qualitative improvement. In Fig. 1.1, an artistic view on new experimental possibilities for Mössbauer science with XFELs is given. It is divided into two categories, the higher average flux leading to an increased number of resonant photons per second, and the higher peak flux resulting in an increased number of resonant photons per pulse. Both improvements together bring advancement in several different aspects – the possibility to study new isotopes, new experimental methods such as single-shot measurements, new environments created by the strong XFEL radiation and new observables with more than one photon or higher excitations. In the following paragraphs, we discuss those aspects in detail.

The higher average flux in general increases the amount of signal photons recorded in the de-excitation process and thus allows to study even more narrower transitions, for which only a tiny fraction of the incident light is resonant. Such extremely narrow nuclear transitions do not only provide improved resolution for spectroscopy, but are comparable with optical clock transitions [PO15]. Precisely measurable clock transitions are the basis of the current definition of a second based on an atomic transition in cesium [Bur19] and future improvement thereof based on optical clocks [Dim+24],

fundamental tests such as gravitational red-shift being now measurable on an 1 mm scale [Bot+22], tests on the variation of fundamental constants [Saf+18] as well as every day applications, such as GPS [Ash03]. So far all those applications rely on atomic clock transitions. In [PO15] it has been pointed out that nuclear clock transitions are promising because of the smaller systematic frequency shifts due to shielding by the electronic shell, possible operation in solid state and thus large ensembles of emitters and because of the higher transition frequencies. Furthermore, nuclear transitions are more sensitive for certain tests, e.g., coupling to ultralight dark matter [Fuc+25] or temporal fluctuations from gravitational waves [BC25]. There are two main candidates for a nuclear clock, a thorium isotope (^{229}Th) and a scandium isotope (^{45}Sc). The first one has an extraordinary low lying excited state of only 8.4 eV [Zha+24] making it accessible with XUV frequency combs. A low-lying state was already predicted in 1976 [KR76], but it took several iterations of the transition energy [Bec+07; HR94; Sik+20] and 40 years until the transition energy could be directly measured after excitation via a radioactive parent isotope [Wen+16]. Only last year, the first direct laser-excitation was reported [Elw+24; Tie+24]. Nonetheless, already shortly after the first laser excitation, the nuclear transition was compared to the well-established ^{87}Sr optical clock transition [Zha+24], thus providing the resonance transitions on a 10^{-13} level. Furthermore, the frequency comparison with a different clock formed an important step on the way to a nuclear clock. The transition energy of the other mentioned isotope, ^{45}Sc, was indirectly measured to be 14.4 keV [HLN64], which is in the hard x-ray regime. As there exists no radioactive parent isotope, which by decay would populate the excited state, and synchrotrons also did not provide sufficient photon flux to successfully search for the exact transition energy, it was an open challenge to directly excite ^{45}Sc for more than 30 years [SS90]. However, XFELs provide several orders of magnitude more photon flux and can overcome this challenge.

On the higher peak flux side, which leads to more resonant photons per pulse, the first discussed advancement is that of new measurement modi. For many systems, the higher peak photon flux at XFELs allows single-shot measurements, i.e., obtaining enough information in the signal following a single x-ray pulse. Those measurements are now routinely possible and the diffraction before destruction paradigm [CCT14] has pushed the limits of imaging and structure determination [Aqu+15]. Examples for single-shot analysis include imaging [Cha+06; Sei+11], structure determination [Red+13], crystallography [Bar+22; Cha+11] and absorption spectroscopy [Har+23], but also pulse characterization [Boe+24; Har+13], which can be used in the subsequent analysis. Single-shot measurements are also extremely beneficial for Mössbauer science because they can solve the typical problem of extensive averaging and are predicted to be possible with XFELs [SR08]. As in other disciplines, this simplifies the study of non-repetitive or less likely processes. A first proof-of-principle demonstration that information can be extracted from a single-shot recording has been done by Chumakov et al. [Chu+18]. However, this uses only one single shot with a very high photon number to extract a single fit parameter and the demonstration of broader usage remains open.

A second new possibility due to the higher peak flux is that it not only provides more resonant photons, but also more non-resonant photons per pulse, which enables the study of new environments. In standard Mössbauer spectroscopy, the nuclei are used to probe the properties of their solid state environment, e.g., isomer shift, quadrupole splitting or hyperfine splitting [Hen12]. Under the intense XFEL irradiation, especially including the off-resonant part, the solid state environment could potentially change. Demonstrated changes of matter properties after irradiation with an XFEL include saturated absorption [Nag+09; Rac+15; Yon+14], reverse saturated absorption [Cho+17], the transition between both effects in warm dense matter [Mer+24] as well as a modified electronic structure response [Alo+20]. In all these examples, the studied effect is based on electronic resonances and is oftentimes probed with the electronic resonances, e.g., the resulting spectrum. Therefore, the understanding of the underlying mechanisms is difficult, especially for unexpected effects, because the probe might also be affected by the non-linear effect. For Mössbauer nuclei even at XFELs the response of the nuclei themselves is expected to be in the well-understood low-excitation regime like for synchrotrons [LKE25b]. Therefore, the nuclei could serve as excellent observers to study the XFEL induced dynamics in their surroundings.

Third, the higher peak flux implies a qualitative improvement of having a significant number of pulses with more than one resonant photon [Chu+18; RE21]. This allows to study relations between photons from the same x-ray pulse as demonstrated in [Chu+18]. The progress at XFELs and especially the proposal to build an X-ray free-electron laser oscillator (XFELO) [KSR08] and first demonstrations of the concept [Mar+23; Rau+25], which could increase the resonant photon flux by another four orders of magnitude, have sparked the interest into theoretical examination of the dynamics beyond the linear regime [Ada+19]. It is projected that with an XFELO, full inversion of

a nuclear ensemble is possible [LKE25b]. Several approaches have been suggested for theoretically modeling the subsequent decay dynamics. Progress was made by restriction to the single most superradiant symmetric collective eigenstate [HKE16], with a perturbative approach [WE23] and the use of matrix-product states [Kon+25]. However, all those approaches describe a specialized part of the problem and open questions remain.

To summarize, at the example of lasers we have seen that new technology has always resulted in a boost of new experiments. With the availability of XFELs a boost in the x-ray regime is already visible in some fields and we expect XFELs to significantly advance the field of Mössbauer science in a similar manner.

1.2 Goals of this thesis

In the previous section, we have motivated why experiments with Mössbauer nuclei at XFELs are expected to bring significant improvement in the field of Mössbauer science. However, to our knowledge until the beginning of this thesis only one experiment was performed at an XFEL [Chu+18] and theoretical support beyond the low-excitation regime was limited [HKE16]. Therefore, the goal of this thesis was to experimentally and theoretically explore the so far rather empty landscape of new regimes, which are now accessible with Mössbauer nuclei at XFELs or which will become possible with further improvement, e.g., at an XFELO.

On the experimental side, first experiments with Mössbauer nuclei at a self-seeded XFEL were performed by our collaborations. Because of the novelty of experiments with Mössbauer nuclei at XFELs, different challenges had to be faced. This includes rather technological questions. How can we perform a motor scan to align components in the experiment? How do we analyze the scattering data containing significantly more than one photon? But also the answer to more conceptual questions was unclear. Can we measure nuclear coherent scattering in the forward direction, a standard measurement to extract material parameters at synchrotrons [GBT11; Röh04], or of a thin-film cavity, which is a standard platform for nuclear quantum optics [RE21], at all? If so, do the results match the expectations from synchrotron experiments? Can we even perform single-shot measurements with the higher amount of resonant photons? Does the higher spectral flux allow us to measure extremely narrow resonances? In this thesis, we will answer these questions while focusing mainly on the data analysis during and after the experiments.

Because there is no standard method to study the nuclear dynamics after impulsive excitation beyond the low-excitation regime, for the theoretical investigations, the first challenge is to find a suitable framework. Can we gain insights analytically even beyond the low-excitation regime or do we need to numerically simulate the dynamics? What is a suitable method for the simulations? After answering these questions, we will study the effect of the nuclear dipole-dipole coupling as well as coupling mediated by a propagating light field especially beyond the low-excitation regime, which could be realized by an XFELO [LKE25b].

In summary, in this thesis we investigate and demonstrate new possibilities with Mössbauer nuclei due to the recent and the expected advancement of available light sources.

1.3 Thesis outline

In Chapter 2 an introduction into the topic of nuclear quantum dynamics is given. At first, we introduce the platform of Mössbauer nuclei, which is followed by a discussion of accelerator-based light sources. In the third section, we describe the system on a quantum optical level.

In the main part of the thesis, we demonstrate several of the advances in nuclear quantum dynamics possible with XFELs following the lines of the different advances schematically displayed in Fig. 1.1.

The first part of the thesis is about our experiments performed at the European XFEL. It starts with an overview over the developed data analysis for the experiments performed at European XFEL in Chapter 3. This includes data analysis for live view and simple evaluation tasks during the experiments as well as more complicated but standardized calibration and processing of data after the experiment.

Following this, the excitation of the ^{45}Sc nuclear clock transition is the focus of Chapter 4. Here, we mainly focus on the data evaluation that finally lead to the resonance curve in [Shv+23] and analyze different stochastic methods (cumulative distribution, kernel density estimate and histogram)

to retrieve the final resonance energy. Besides this the signal to noise ratio and count rates are estimated.

A new measurement mode, namely single-shot sorting of Mössbauer time-domain data can be found in Chapter 5, which is based on [Ger+25b]. We demonstrate an algorithm to sort single-shot data into two different classes. The algorithm is based on finding representatives of each class by a clustering algorithm and subsequently sort all data by comparison to those representatives. Furthermore, photon number estimates are derived and the stability of the single-short sorting is tested.

The last of the experiment related chapters focuses on the nuclei as spectators of effects happening after irradiation of the host material with XFEL pulses, which possibly modifies the environment. Here we study anomalies arising in nuclear resonant scattering. The extraction of parameters of the environment surrounding the nuclei, revealed unexpected values. The results are analyzed in detail by splitting the datasets by different parameters, e.g., the photon number per pulse.

In the second part, we focus on the theoretical study of new observables motivated by XFELs and XFELOs and simulate the de-excitation dynamics of a nuclear ensemble after impulsive excitation in the low-excitation regime and beyond. Because we want to study large ensembles beyond the low-excitation regime, numerical methods are required. The well-established techniques used here are presented in Chapter 7. We will mainly work with a set of equations for the simulation derived from a cumulant expansion [Kub62], but use the python package QuTiP [JNN12; JNN13] for benchmarking and a Monte-Carlo simulation based on the continuous-discrete truncated Wigner approximation [MF23] for cross-checks.

For the truncated Wigner approximation approach, the preparation of the initial state is not straight forward for our studies. Therefore, in Chapter 8 different sampling schemes are discussed.

Finally, with the numerical methods we can investigate the de-excitation dynamics of the nuclear ensemble after impulsive excitation. First, in Chapter 9, the nuclear dynamic in the low-excitation regime and beyond is studied in the presence of dipole-dipole couplings [GE25]. This analysis is mainly performed with a translational invariant model, but finite size effects are discussed in addition.

Second, non-linear excitations with light propagation similar to the work in [AGE_p; Kon+25] are studied in Chapter 10. We will discuss clear signatures of excitations beyond the low-excitation regime in the propagation effects.

Chapter 11 is a stand-alone chapter describing an inline interferometer based on different polarization states. Here, we focus on the theoretical description of the setup.

The thesis concludes with a summary of the most important results and an outlook to future perspectives.

Chapter 2

Background – Quantum optics with Mössbauer nuclei

In this chapter, we introduce the topic of quantum optics with Mössbauer nuclei. At first, the Mössbauer nuclei are introduced, which is followed by a discussion of x-ray light sources and experimental aspects. In the second part, we turn to the quantum optical description of the system.

2.1 Mössbauer nuclei

A particular class of nuclear transitions are those in Mössbauer nuclei, which feature especially narrow linewidths because of the Mössbauer effect (for details see Section 2.1.1). A large amount of Mössbauer transitions has been found so far [Röh04], and an overview over their linewidth and transition energy is given in Fig. 2.1 in form of the blue circles. Three specific transitions are highlighted by larger circles. First, there is the ^{229}Th transition (light blue), which has an exceptionally low transitions energy of $E \approx 8\,\mathrm{eV}$ [Zha+24] and can therefore be excited by XUV frequency combs. The other two highlighted transitions are those in ^{57}Fe (magenta) and ^{45}Sc, (purple), which are both accessible by XFELs and are the two transitions investigated in this thesis. More details on these two are given in Section 2.1.2. Furthermore, ^{57}Fe is the most used Mössbauer isotope [Röh04]. For comparison also some important optical clock transitions are displayed with the green crosses. While most Mössbauer isotopes have lower quality factors $Q = E/\Gamma$, for some exceptions, such as ^{229}Th and ^{45}Sc, the quality factors are on a comparable level as those of optical clock transitions. The red horizontal lines indicate the different photon energy regimes of visible, ultraviolet (UV) or x-ray energies. Here we mainly focus on possible excitation with XFELs, which is indicated by the orange window. Note that at synchrotron radiation sources also higher transition energies are available, e.g., up to 100 keV at PETRA III [Wil+10].

2.1.1 Mössbauer effect and zero-phonon transitions

For the resonant scattering of x-rays with nuclear transitions, the largest challenge is the photon recoil. The recoil energy is given by [YL13]

$$E_R = \frac{E^2}{2Mc^2}\,, \tag{2.1}$$

with transition energy E, mass of the nucleus M and the speed of light c. For a single nucleus of ^{57}Fe the recoil energy is $E_R = 1.9\,\mathrm{meV}$, which is three orders of magnitude larger than the natural linewidth $\Gamma_0 = 4.7\,\mathrm{neV}$. Note that for transitions with lower transition energies the recoil is less relevant, e.g., for the sodium D-line at 2.1 eV the recoil energy is $E_R \approx 2.5 \times 10^{-3}\,\Gamma_0$ [Ste25]. Due to the recoil, the absorption and emission lines are shifted so far from each other that they do not overlap anymore and no coherent resonant scattering is possible [YL13]. If the nucleus is embedded in a solid state environment, the recoil momentum can be spread out over the solid and recoilless absorption and emission are possible [YL13]. This was first found by Rudolf Mössbauer [Mös58], which is why it is called the *Mössbauer effect*.

The absorption of the recoil energy by the solid can lead to the creation of phonons, i.e., a collective excitation of the lattice. Only for a zero-phonon transition, the emission and absorption take place at the same energy. The probability f_{LM} of a zero-phonon transition, which is also called the *Lamb-Mössbauer factor* [Röh04], can be calculated with the matrix element [GG71]

$$f_{\mathrm{LM}} = \text{const.} \times |\langle L_0 | e^{i\vec{k}\vec{x}} | L_0 \rangle|^2 = e^{-\vec{k}^2\vec{x}^2}\,, \tag{2.2}$$

with the vibrational zero-phonon state $|L_0\rangle$, the wavevector of the emitted photon $\vec{k}$ and the center of mass of the nucleus $\vec{x}$. In the last step, we used that $|L_0\rangle$ is normalized. We can replace $\vec{x}^2$ by $\langle x^2 \rangle$

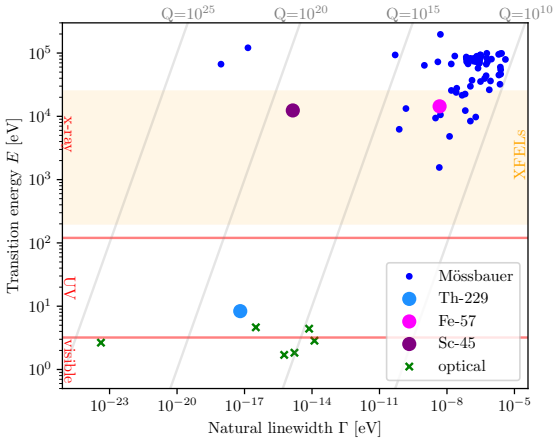

Figure 2.1: Overview of transition energy E and natural linewidth Γ of the most important Mössbauer isotopes (circles). Highlighted are ^{229}Th (light blue) [Zha+24], ^{57}Fe (magenta) [Röh04] and (purple) ^{45}Sc [Shv+23]. For comparison some optical clock transitions are shown by the green crosses: Ca^+, Sr^+, Hg^+, Yb^+ and Al^+[Lud+15]. The gray lines indicate lines of constant quality factor $Q = E/\Gamma$. The red horizontal lines indicate the different energy regimes and the energy window currently accessible by XFELs [Eurb; LCL] is marked by the orange shaded area. The figure was inspired by similar plots in [Len21; RE21; Wen+16].

because the vibrations are random and find [GG71]

$$f_{\mathrm{LM}} = \exp\left(\frac{-E_0^2\langle x^2\rangle}{\hbar^2 c^2}\right), \tag{2.3}$$

with transition energy E_0, mean-square displacement $\langle x^2\rangle$, reduced Planck constant $\hbar$ and speed of light c. The dependence on the transition energy E_0 sets a natural upper limit for the transition energy E_0 at which the Mössbauer effect is still measurable. The highest recorded energy for which the Mössbauer effect was measured so far is the 166 keV transition in ^{139}La [WTA73].

To further evaluate this expression, we need to assume a model for the lattice vibrations and thus $\langle x^2\rangle$. On can show that using the Debye model, the expression in Eq. (2.3) evaluates to [GG71]

$$f_{\mathrm{LM}} = \exp\left\{-\frac{6E_R}{k\theta_D}\left[\frac{1}{4} + \left(\frac{T}{\theta_D}\right)^2 \int_0^{\theta_D} \mathrm{d}x \frac{x}{e^{-x}-1}\right]\right\}, \tag{2.4}$$

with the Debye temperature θ_D and the recoil energy E_R as in Eq. (2.2). For the typical workhorse ^{57}Fe, the Debye temperature is $\theta_D = 430\,\mathrm{K}$, and thus at room temperature ($T = 300\,\mathrm{K}$) the Lamb-Mössbauer factor is $f_{\mathrm{LM}} \approx 0.8$ [She+04]. From Eq. (2.4) we can read off that the Lamb-Mössbauer factor f_{LM}, i.e., the probability of recoilless resonant scattering, increases for lower temperatures. However, due to the already high value at room temperature $f_{\mathrm{LM}} \approx 0.8$, experiments are often performed at room temperature, which is also the case for all experiments discussed in this thesis.

2.1.2 Specific Mössbauer isotopes

For this thesis, we will focus on two Mössbauer isotopes, ^{57}Fe and ^{45}Sc.

Iron isotope ^{57}Fe

The isotope ^{57}Fe is the most used Mössbauer isotope due to its natural abundance, relevance in biology, geology, and chemistry and the availability of a suitable parent isotope for measurements with radioactive sources [GBT11; Smi12]. The level scheme of ^{57}Fe is displayed in Fig. 2.2(a). ^{57}Fe has a magnetic dipole (M1) transition with a transition energy of $E = 14.4\,\mathrm{keV}$ and a natural linewidth of $\Gamma = 4.7\,\mathrm{neV}$ corresponding to a lifetime of $\tau = 141\,\mathrm{ns}$. The excited state can decay directly to the ground state by sending out a photon with 14.4 keV or via internal conversion. In the case of internal conversion, the energy of the excited state is transferred to the electronic shell and ejects an inner-shell electron, which is followed by fluorescence. The dominant fluorescence lines are K_α at

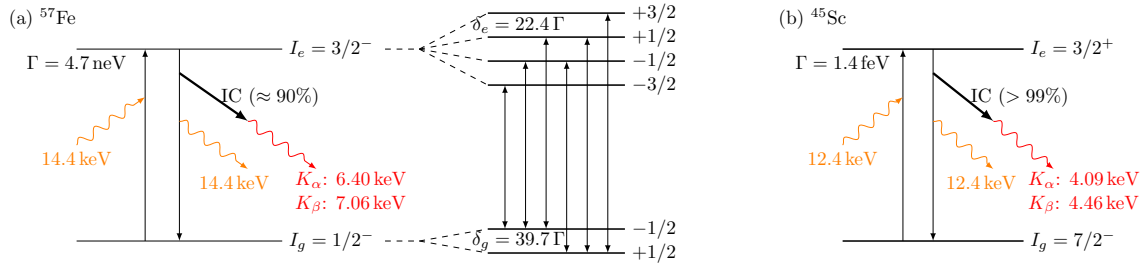

Figure 2.2: Nuclear level schemes of (a) ^{57}Fe and (b) ^{45}Sc. The excited state with natural linewidth $\Gamma = 4.7\,\mathrm{neV}$ ($\Gamma = 1.4\,\mathrm{feV}$) of the nuclei can be excited with photons matching the transition energy of $E = 14.4\,\mathrm{keV}$ (12.4 keV) for ^{57}Fe (^{45}Sc). The decay can either happen directly via sending out a photon with the same energy or via internal conversion (IC), where the energy is transferred to the electronic shell and subsequent fluorescence is observed. For both isotopes, the internal conversion is the dominant decay channel. Furthermore, the spin and parity of the ground I_g and excited state I_e are displayed. For ^{57}Fe, also the level structure including hyperfine splitting as it occurs in the presence of a magnetic field is displayed (not to scale) for an internal magnetic field of approximately $B = 33\,\mathrm{T}$. The two (four) sublevels of the ground (excited) state and their respective magnetic quantum numbers m are shown in the right part of panel (a). In this case six transitions can be driven. For ^{45}Sc, the hyperfine splitted level structure is not observed yet. Data for ^{57}Fe is taken from [BB86; Röh04; Tho+09], data for ^{45}Sc from [Shv+23].

6.40 keV and K_β at 7.06 keV. The ratio of direct decay to internal conversion is $1 : \alpha$, where α is the element specific internal conversion coefficient. Because of $\alpha_{\mathrm{Fe}} \approx 8.5$ [Röh04], the internal conversion is the dominant decay channel. The internal conversion also leads to the total linewidth $\Gamma = 4.7\,\mathrm{neV}$ being enhanced as compared to the pure radiative linewidth $\Gamma^{\mathrm{rad}} = 0.49\,\mathrm{neV}$ [Röh04].

In the presence of a magnetic field, the ground and excited state split into two and four levels, respectively. At room temperature a bulk sample of α-iron has an internal magnetic field of $B \approx 33\,\mathrm{T}$, which leads to energy differences of $\delta_g = 39.7\,\Gamma$ and $\delta_e = 22.4\,\Gamma$ for the ground and excited state [Hee14; Röh04], respectively. According to the selection rules $\Delta m = 0, \pm 1$, where Δm is the difference of the magnetic quantum numbers, six transitions can be driven. For $\Delta m = 0$, the transitions are linearly polarized parallel to the magnetic field, for $\Delta m = \pm 1$ they are circularly polarized in the plane perpendicular to the magnetic field.

In natural iron the dominant iron isotope is ^{56}Fe with a contribution of about 2% of ^{57}Fe. For this reason in experiments oftentimes enriched iron is used, which consists of nearly 95% ^{57}Fe [Röh04]. If not stated otherwise, we consider enriched α-iron throughout the thesis.

Scandium isotope ^{45}Sc

In ^{45}Sc, there is a magnetic quadrupole (M2) transition [Shv+23], whose level scheme is displayed in Fig. 2.2(b). While the transition energy $E = 12.4\,\mathrm{keV}$ is similar to those of ^{57}Fe, the linewidth $\Gamma = 1.4\,\mathrm{neV}$ is six orders of magnitude smaller featuring a very long lifetime of $\tau \approx 500\,\mathrm{ms}$ [Shv+23]. For ^{45}Sc with $\alpha = 424$ the internal conversion is the dominant decay channel mainly resulting in K-fluorescence at 4.09 keV (K_α) and 4.46 keV (K_β).

So far, the hyperfine splitting structure is not measured because this measurement needs coherent scattering, which up to this date has not been observed yet [Liu+25a].

The natural abundance of ^{45}Sc is 100%, i.e., natural scandium only consists of ^{45}Sc.

2.1.3 General experimental aspects

A typical setup of an Mössbauer experiment is schematically displayed in Fig. 2.3(a). It consists of a sample, which in our case is either an α-iron foil of several μm thickness enriched with ^{57}Fe (see Fig. 2.3(b)) or a thin-film cavity with a thin layer (few nm) of ^{57}Fe inside (see Fig. 2.3(c)). The foil is probed in the forward direction while the cavity is probed in reflection. The scattering of a foil probed in forward direction will discussed in Section 2.1.4. The description of the scattering by a cavity is more complicated, but not of relevance for this thesis. A detailed description can be found in [Hua+20; Len21; Röh04]. A stainless steel foil is placed on a Mössbauer drive, which moves it with velocities v typically up to 10 mm/s, which according to the Doppler shift detunes the electric field scattered of the stainless steel foil by up to approximately $100\,\Gamma$ from the field scattered by the

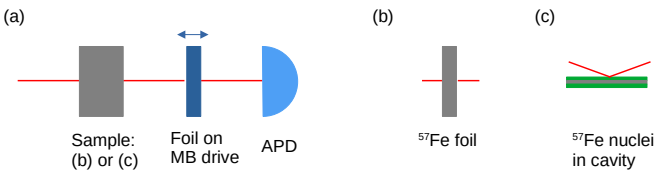

Figure 2.3: (a) Schematic of the typical experimental setup. The x-ray beam (red) impinges on a sample (gray). The outgoing beam passes a stainless steel foil on a Mössbauer drive (dark blue) before being detected by Avalanche Photo Diodes (APDs) (light blue). (b) The sample can be a ^{57}Fe-foil, which is probed in forward direction. (c) Alternatively, the sample can be a thin layer of resonant nuclei (gray) embedded in a thin-film cavity (green) and probed in grazing incidence.

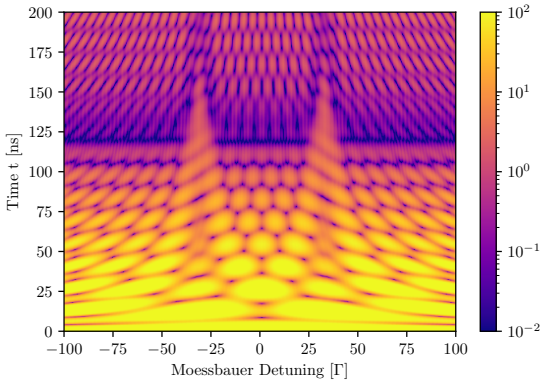

Figure 2.4: Example of an energy-time-spectrum, i.e., the intensity as a function of detuning and time. The energy-time spectrum is calculated with `pynuss` [Hee19] for a 2 μm thick ^{57}Fe-sample with only the two linear transitions being driven. The stainless steel foil is 2 μm thick.

sample. This provides spectral information. Finally, the arrival time of the x-ray photons is measured with Avalanche Photo Diodes (APDs) and provides information in the time domain [Röh04].

Measuring the arrival time and Mössbauer drive velocity or each photon allows to create two-dimensional energy-time spectra. The outgoing intensity as a function of time t and detuning Δ is given by [Cal+05]

$$\begin{aligned} I(\Delta, t) =& |E_{\text{sample}}(t) + e^{i\Delta\cdot t} E_{\text{ref}}(t)|^2 \\ =& |E_{\text{sample}}(t)|^2 + |E_{\text{ref}}(t)|^2 + 2\cdot|E_{\text{sample}}(t)|\cdot|E_{\text{ref}}(t)|\cdot\cos\left(\Delta\cdot t + \Delta\phi\right) , \end{aligned} \tag{2.5}$$

with the electric fields of sample $E_{\text{sample}}(t)$ and reference stainless steel foil $E_{\text{ref}}(t)$ and their relative phase difference $\Delta\phi$. An example of an energy-time-spectrum is displayed in Fig. 2.4. The oscillations described by $2\cos\left(\Delta\cdot t + \Delta\phi\right)$ are clearly visible. Furthermore, at time $t \approx 125\,\text{ns}$ there is a clear minimum in the intensity corresponding to the first dynamical beat (see Section 2.1.4) of a 2 μm thick ^{57}Fe-foil. Finally, in the frequency domain, especially for late times, there are dominant structures around $\pm 31\,\Gamma$, at which the two linearly-polarized lines are expected (see Fig. 2.5(a)). Integrating over late times indeed approximately reveals the frequency spectrum of the sample [Röh+10].

2.1.4 Coherent nuclear forward scattering

One of the main kind of measurements is the coherently scattered signal in forward direction in the frequency as well as in the time domain. Here we concentrate on the signal following a short impulsive, but small excitation pulse as it is the case for synchrotron radiation and XFELs. In this case the ingoing electric field is given by $E_{\text{in}}(t) \propto \delta(t)$ and $\tilde{E}_{\text{in}}(\omega) \propto 1$ in time and frequency space, respectively. To calculate the scattered electric field as it is done in detail in Section 2.3.3, we consider the low-excitation approximation, which is a valid approximation for current synchrotron and XFEL experiments [LKE25b; Röh04].

In the low-excitation limit, we can describe the interaction of the incoming light with the sample by the response function formalism. If $\tilde{E}_{\text{in}}(\omega)$ and $E_{\text{in}}(t)$ are the incoming electric field in frequency

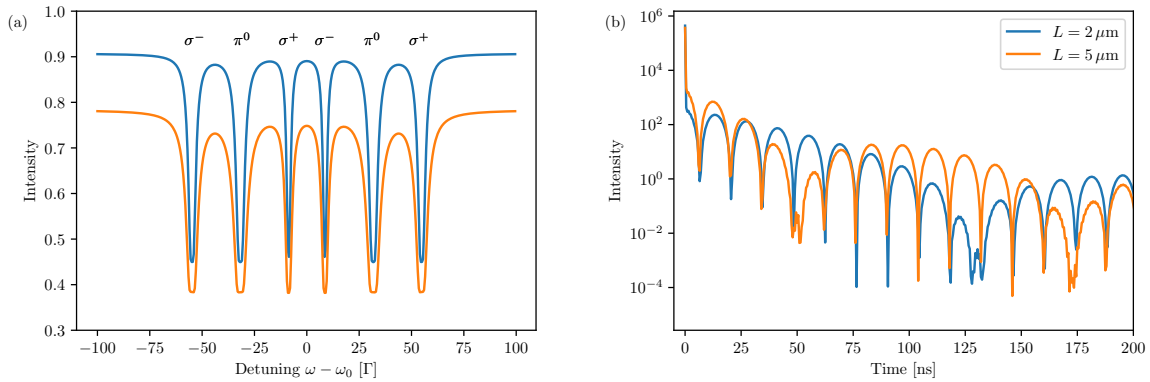

Figure 2.5: (a) Forward scattered intensity as a function of the detuning $\Delta = \omega - \omega_0$ for a $2\,\mu$m (blue) and a $2\,\mu$m (orange) thick enriched ^{57}Fe-foil with all six lines being driven. The symbols above the absorption dips indicate, whether the line is circularly ($\sigma^{\pm}$) or linearly (π^0) polarized. (b) Forward scattered intensity as a function of time t for a $2\,\mu$m (blue) and a $2\,\mu$m (orange) enriched ^{57}Fe-foil with only the two linearly polarized lines (second and fifth line in (a)) being driven. In both panels, the incident light field is assumed to be linearly polarized. The simulations are performed with the python library `pynuss` [Hee19].

and time space, respectively, the corresponding outgoing fields are given by [KAK79]

$$\tilde{E}_{\text{out}}(\omega) = \tilde{R}(\omega) \cdot \tilde{E}_{\text{in}}(\omega)\,, \tag{2.6a}$$

$$E_{\text{out}}(t) = R(t) * E_{\text{in}}(t)\,, \tag{2.6b}$$

with the response function of the sample $\tilde{R}(\omega)$ ($R(t)$) in frequency (time) space.

Frequency domain

The response function of the sample in frequency space is given by [KAK79; Röh04]

$$\tilde{R}(\omega) = \exp\left[\frac{-ib}{\omega - \omega_0 + i\frac{\Gamma}{2}}\right]\,, \tag{2.7}$$

with the transition frequency $\omega_0 = E/\hbar$, linewidth Γ and the thickness parameter

$$b = \sigma_0 f_{\text{LM}} n L \Gamma\,. \tag{2.8}$$

Here σ_0 is the resonant cross-section, f_{LM} the Lamb-Mössbauer factor, n the number density, and the physical thickness L. Plugging in the parameters for enriched α-iron at room temperature, which is our default sample type, the thickness parameter b is related to the physical thickness L by $b = \Gamma \cdot L[\mu\text{m}]/0.249$ [Adi24]. For a detailed derivation of Eq. (2.7) see Section 2.3.3. Including the hyperfine splitting of the transitions leads to [Shv+98; Smi99]

$$\tilde{R}^{\text{hyp}}(\omega) = \exp\left[\sum_{l=1}^{6} c_l \frac{-ib}{\omega - \omega_l + i\frac{\Gamma}{2}}\right]\,, \tag{2.9}$$

where ω_l now denotes the transition frequency of transition l and c_l is the Clebsch-Gordon coefficient of transition l. With this, the outgoing electric field after an impulsive excitation $\tilde{E}_{\text{in}}(\omega) = \tilde{E}^0_{\text{in}}$ is given by [Shv+98; Smi99]

$$\tilde{E}_{\text{out}}(\omega) = \tilde{R}^{\text{hyp}}(\omega) \cdot \tilde{E}_{\text{in}}(\omega) = \exp\left[\sum_{l=1}^{6} c_l \frac{-ib}{\omega - \omega_l + i\frac{\Gamma}{2}}\right] \tilde{E}^0_{\text{in}}\,. \tag{2.10}$$

Aligning the internal magnetic field with an external magnetic field relative to the incident light polarization in the experiment allows to choose which set of transitions is driven [Röh04; SBH99].

A simulated typical frequency spectrum, in which all six lines are driven, is shown in Fig. 2.5(a). The six lines corresponding to the six Lorentzians in Eq. (2.10) are visible. The difference in the

depths of the dips for the 2 μm thick (blue) and the 5 μm thick foil (orange) is due to the different electronic absorption for different thicknesses. From the frequency spectrum, much information about the environment of the nuclei can be read off. For example, as the energy shifts due to hyperfine splitting δ_e and δ_g are directly related to the strength of the magnetic field B, from the position of the lines, one can infer the strength of the magnetic field. For more information, see [GBT11; YL13]. We can also see that assuming that the lines are well-separated from each other is a valid approximation. This is even more the case in a setting where not all six lines are driven.

Time domain

The sample response in time domain can be calculated via a Fourier transform of $\tilde{R}^{\mathrm{hyp}}(\omega)$. To be able to analytically perform the Fourier transformation, we assume that the lines are well-separated from each other and that we can approximate

$$\tilde{R}^{\mathrm{hyp}}(\omega) \approx \sum_{l=1}^{6} \exp\left[c_l \frac{-ib}{\omega - \omega_l + i\frac{\Gamma}{2}}\right] . \tag{2.11}$$

We can then Fourier transform every summand separately and find [Shv+98; Smi99]

$$R^{\mathrm{hyp}}(t) \approx \delta(t) - e^{-\Gamma t/2}\theta(t) \sum_{l=1}^{l} c_l e^{-i\omega_l t} \sqrt{\frac{bc_l}{t}} J_1\left(2\sqrt{bc_l t}\right) . \tag{2.12}$$

More details on the derivation can be found in Section 2.3.3 and in [Rei14]. For impulsive excitation ($E_{\mathrm{in}}(t) = E^0_{\mathrm{in}}\delta(t)$) the outgoing electric field is given by [KAK79; Röh04]

$$E(t) = R^{\mathrm{hyp}}(t) * E_{\mathrm{in}}(t) \approx \left[\delta(t) - \theta(t)e^{-\Gamma t/2} \sum_{l=1}^{l} c_l \sqrt{\frac{bc_l}{t}} J_1\left(2\sqrt{bc_l t}\right) e^{-i\omega_l t}\right] E^0_{\mathrm{in}} . \tag{2.13}$$

This equation consists of several parts with different physical interpretation and an example realization with only two driven lines is displayed in Fig. 2.5(b). At first, we have the $\delta(t)$ peak that represents the strong unscattered signal. As it arrives immediately at $t = 0$, it is typically called the *prompt pulse*. In contrast, the resonantly scattered second part is referred to as the *delayed signal*. The $\theta(t)$ function as the prefactor of the second summand ensures that the scattered contribution only gives a signal after the excitation at $t = 0$. Next, we have the exponential decay in $e^{-\Gamma t/2}$. The envelope of the signal is not only formed by the exponential decay, but an additional contribution $\sqrt{\frac{bc_l}{t}} J_1\left(2\sqrt{bc_l t}\right)$ with the Bessel function of first kind J_1 from multi-scattering effects in thicker samples. The minima of the envelope correspond to the roots of the Bessel function J_1 and thus depend on the thickness of the sample as we can see by comparing the blue and the orange curve. They are referred to as the *dynamical beats* and can be used to determine the thickness of the sample. Such dynamical beats are visible in Fig. 2.5(b) at around 130 ns for the 2 μm thick foil (blue) and at around 50 ns and 175 ns for the 5 μm thick foil (orange). The last term $e^{-i\omega_l t}$ resembles the slightly different transition frequencies of the different lines and leads to beatings between the different transition frequencies. In the example case only the two linearly polarized lines are driven. Since their transition energies $\omega_l = \omega_0 \pm \Delta_{\mathrm{lin}}$ are symmetric around ω_0, this leads to a periodic simulation proportional to $\sin(\Delta_{\mathrm{lin}} t)$ with Δ_{lin} being the absolute value of the frequency shift with respect to the unsplitted transition frequency ω_0 of those lines. If more lines are driven, there are several beating frequencies and the structure is more complicated. From the positions of the dynamical beats information about the orientation of the magnetic field relative to the incident light polarization as well as the strength of the internal magnetic field can be inferred. In analogy to the frequency spectrum, the intensity as a function of time is called *time spectrum*. For more information about material properties encoded in the time spectrum refer to [GBT11].

2.2 Accelerator-based light sources

After discussing how the signal from a Mössbauer sample excited by a short light pulse looks like, we now want to have a closer look at accelerator-based light sources, which provide those pulses.

The common feature of all accelerator-based light sources is that bunches of electrons are accelerated up to highly relativistic energies (Lorenz factor $\gamma \gg 1$). They then pass a magnetic field and due

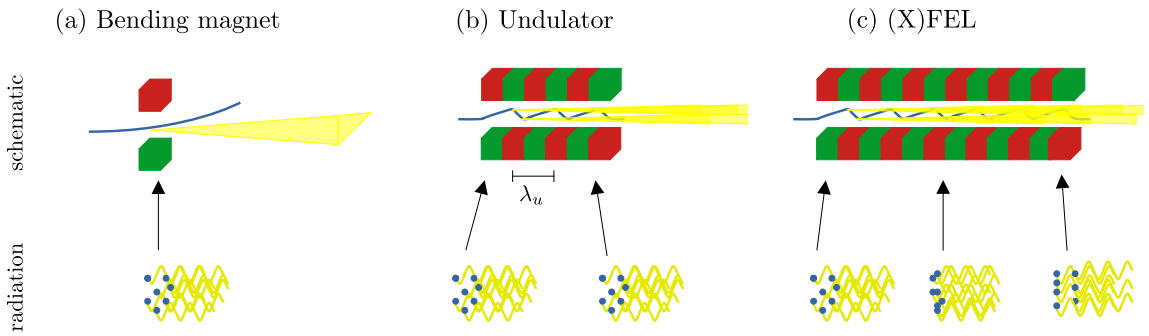

Figure 2.6: Different tools to produce x-rays with accelerator based light sources. The top row shows a schematic of the production, the lower row a schematic of the electron bunch and the radiation at different parts of the production. (a) The simplest scheme is the bending magnet. Here, an electron beam (blue) enters a magnet (red/green blocks indicating north and south pole) in which it is deflected. Due to the deflection the electrons tangentially radiate synchrotron radiation. All electrons irradiate independently of each other as can be seen in the schematic of the radiation. (b) In an undulator, the electron beam (blue) passes through a sequence of alternating magnets with period λ_u. In each of them, the electron beam is deflected and sends out synchrotron radiation. The radiation from the different magnetic sections adds up coherently. Although the electron beam travels parallel to the x-ray beam, the undulators are typically too short to have a notable effect on the electrons. (c) At (X)FELs very long undulators are used. The long interaction of the electron beam with the photon beam leads to aligning of the electrons at the nodes of their own radiation field, which is called *micro-bunching*. While the radiation at the beginning of the undulator is not phase matched, at the end of the undulator due to the bunching the electrons irradiate in phase.

to the accelerated motion send out synchrotron radiation. The specific setup of the magnetic field defines the properties of the different light sources. An overview is given in Fig. 2.6, and the different types are discussed in the following.

The description of the three different types is based on [KHL17; MR11]. While [MR11] gives a simple overview, in [KHL17] a more detailed theoretical description can be found.

2.2.1 Synchrotron radiation sources

Bending magnet

The simplest setup is that of a bending magnet as displayed in Fig. 2.6(a). If the electron bunch passes through a magnetic field perpendicular to its direction of motion, it is deflected due to the Lorentz force. This force is also used to keep the electrons on the circular motion in a storage ring. As this deflection is an accelerated motion, the electrons start sending out dipole radiation. Because of the relativistic speed of the electrons, the symmetric dipole radiation pattern in the rest frame of the electrons is highly focused in the forward direction in the laboratory frame with an opening angle of approximately $1/\gamma$, where γ is the Lorentz factor. In addition, the Lorentz boost shrinks the radiated wavelength in the rest frame λ_{rest} to $\lambda_{\text{lab}} = \lambda_{\text{rest}}/\gamma$ resulting in x-ray wavelengths. The resulting spectrum of a bending magnet is a broad band spectrum, and due to the electrons following a circular trajectory with many emission points, the light cone opening is wide.

Undulator

Nowadays third and fourth generation synchrotrons do not use bending magnets anymore, but undulators. An undulator as shown in Fig. 2.6(b) consists of several magnets with alternating polarities, thus creating an alternating magnetic field with N_u oscillations of period λ_u. The defining parameter of an undulator is the undulator parameter [KHL17]

$$K = \frac{eB_0\lambda_u}{mc2\pi} = 0.934\lambda_u[\text{cm}]B_0[\text{T}]\,, \tag{2.14}$$

with the undulator period λ_u, the magnetic field of the undulator B_0, the natural constants mass m and charge e of an electron and the speed of light c. For an undulator, it is $K \leq 1$. If K is larger, we are in the wiggler regime, which is not discussed here. With this, the fundamental wavelength is

given by [KHL17]

$$\lambda_1 \approx \lambda_u \frac{1}{2\gamma^2}\left(1 + \frac{K^2}{2} + \gamma^2\phi^2\right), \tag{2.15}$$

with the angle of emission ϕ. Thus, in forward direction $\phi = 0$ the wavelength λ_u is reduced by a factor of $1/\gamma^2$. This can also be understood qualitatively because the electrons in their rest frame see a reduced undulator period $\lambda_u' = \lambda_u/\gamma$ and irradiate with that wavelength. The Lorentz boost back to the laboratory frame gives another factor of γ. With the K parameter, especially the gap between the magnets, which determines the magnetic field strength B_0, the radiation wavelength can be fine tuned.

Each electron makes N_u oscillations in the undulator, and the amplitude of the oscillatory electron trajectory is small, which is why the radiation from the N_u oscillations overlaps. This effectively corresponds to a train with with N_u cycles and leads to an intrinsic bandwidth of [KHL17]

$$\frac{\Delta\lambda}{\lambda_1} \sim \frac{1}{N_u} \tag{2.16}$$

peaked around λ_1 and higher harmonics.

As an example, the 10 m undulator used at the nuclear resonance scattering beamline P01 at PETRA III [DES25b; Wil+10] has a period length $\lambda_u = 36\,\mathrm{mm}$, $N_u = 2 \times 137$ periods, a peak magnetic field $B_0 = 0.72\,\mathrm{T}$ resulting in a maximum undulator parameter $K = 2.4$ and radiates at a first harmonic of $\lambda_1 = 0.5\,\mathrm{nm}$ ($E = 2.5\,\mathrm{keV}$) [DES25a].

Considering the whole electron bunch of N_e electrons, the radiation from each electron has a random relative phase. Therefore, in a simple model where all electrons irradiate the same field E the outgoing x-ray intensity

$$I \approx |\sum_l^{N_e} e^{i\phi_l} E_\mathrm{rad}|^2 = \sum_l^{N_e} |E_\mathrm{rad}|^2 \propto N_e \tag{2.17}$$

is proportional to the number of electrons N_e. In the second step we have used the averaging over the random phases ϕ_l.

2.2.2 X-ray free-electron laser

X-ray free-electron lasers (XFELs) are also based on the undulator principle. However, instead of using undulators on the order of 10 m length, XFELs use undulators with more than 100 m length [Dec+20; Emm+10]. Therefore, the time which the electrons spend in the undulator is significantly longer leading to important modifications of the radiation.

Self-amplified spontaneous emission

So far we have only considered the transverse motion of the electron, which is determined by the magnetic field and results in a transverse velocity of [KHL17]

$$v_x = \frac{Kc}{\gamma}\cos(k_u z), \tag{2.18}$$

with $k_u = 2\pi/\lambda_u$. However, because the electrons are traveling close to the speed of light, they also experience the electric field of their own radiation

$$\vec{E}(z,t) = \hat{e}_z E_0 \sin(kz - \omega t + \phi), \tag{2.19}$$

where $\hat{e}_z$ is the unit vector in z-direction and $\omega = 2\pi c/\lambda$ and ϕ the frequency and phase of the irradiated electric field respectively. Therefore, the work performed on the electron is [KHL17]

$$W = \vec{F}\cdot\vec{v} = -e\vec{E}\cdot\vec{v} = \frac{-eE_0K}{\gamma}\cos(k_u z)\sin(kz - \omega t + \phi). \tag{2.20}$$

If the work is positive, the electron is accelerated in the longitudinal direction, if the work is negative the electron is decelerated. Note that in general the electromagnetic wave propagates ahead of the electrons, such that no interaction is possible. However, due to the periodicity of the electric field

the interaction indeed takes place. Because W depends on the position of the electron relative to the electric field, the interaction with the electric field leads to the electrons accumulating at the nodes of the electric field. This results in the electron bunch being divided into subslices with spacing λ in the longitudinal direction, which is called *micro-bunching* and is indicated in the lower part of Fig. 2.6(c). Note that this process in principal occurs in any undulator, but the undulators used at synchrotrons are to short to result in a notable effect on the radiation.

Because of the micro-bunching, at the end of an undulator all electrons radiate in phase. Therefore, here in the simple model where all electrons irradiate the same field E the outgoing x-ray intensity

$$I \approx |\sum_{l}^{N_e} e^{i\phi_l} E_{\mathrm{rad}}|^2 = |\sum_{l}^{N_e} E_{\mathrm{rad}}|^2 \propto N_e^2 \tag{2.21}$$

is proportional to the squared number of electrons N_e. In the second step we have used that all electrons radiate in phase. The increase from a linear to a quadratic scaling with the number of electrons N_e is what brings the orders of higher intensities at XFELs as compared to synchrotrons.

The process of amplification due to micro-bunching is called *self-amplified spontaneous emission (SASE).*

Hard x-ray self-seeding

The process of SASE starts from noise and thus the pulses have very poor longitudinal coherence, which is why the output consists of several independent wavepackets also called spikes both in the temporal as well as in the frequency domain [Fel+97]. This problem can be overcome by a two stage SASE FEL [Fel+97] consisting of two undulators with a monochromator in between. The first undulator produces x-ray light with the SASE process. In a simplified picture, the monochromator cuts out a certain window in the frequency domain thereby reducing the spectral bandwidth of the SASE beam. Therefore, the electric field entering the second undulator is monochromatized. In addition, it dominates over the electric field generated by the SASE process at the beginning of the second undulator. Those two effects together result in a micro-bunching in the second undulator with less energy spread as in the SASE case. Because the second undulator is seeded with the XFEL radiation from the first one, this scheme it called *hard x-ray self-seeding.* It results in a narrower spectral bandwidth of the output and improved longitudinal coherence as compared to a SASE beam [Fel+97]. A detailed review of the process, especially focusing on the experimental realization, is given in [Gel20].

For example, with hard x-ray self-seeding at European XFEL [Liu+23], it is possible to reduce the 10-20 eV wide SASE to a spectral band width of less than 1 eV and therefore increase the peak spectral density by a factor of ten approximately.

Note that even the approximately 1 eV wide seeded beam is still very broad on the scale of Mössbauer transitions. Therefore, experiments with Mössbauer nuclei directly benefit from the increased peak spectral flux.

2.2.3 Comparison between synchrotrons and X-ray free-electron lasers

Synchrotron and seeded XFEL radiation both provide intense x-ray beams, but with different properties. While full transversal coherence is provided by XFELS naturally, it is only reached with synchrotrons of the fourth generation, which also only became available in the last decade [Cha23]. Furthermore, XFEL pulses are on the femtosecond scale and thus much shorter than the pulses at synchrotrons, which are a few picoseconds [Wil21]. The largest difference however is the peak photon flux. For XFELs, this can be 2×10^{25} photons per pulse, while even the most powerful synchrotrons do not exceed the 10^{16} level so far [Wil21]. Therefore, XFELs provide orders of magnitude more resonant photons [RE21] and can overcome the important threshold of one resonant photon per pulse in a considerable amount of pulses.

For experiments with Mössbauer nuclei, the shorter pulse length probably does not make a difference as even the picosecond level is short compared to the typical decay time scales, which are hundreds of nanoseconds. Therefore, the most crucial differences are the several orders of magnitude higher photon flux and a better transverse coherence. Note that the spatial coherence is only improved compared to third generation synchrotrons, but the new synchrotrons of fourth generation also have full transverse coherence.

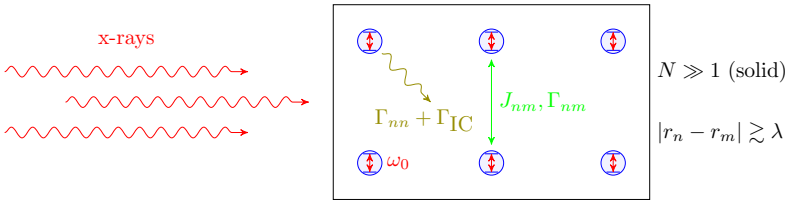

Figure 2.7: Schematic overview of the system. Hard x-rays centered around the nuclear transition frequency ω_0 (red) enter the solid state crystalline sample (black rectangle) with $N \gg 1$ nuclei (blue circles). Neglecting the hyperfine splitting, each nucleus can be represented by a two-level system with transition frequency ω_0. The nuclei can couple coherently J_{mn} and incoherently Γ_{mn} to each other (green) and can decay via spontaneous decay Γ_{nn} and internal conversion Γ_{IC} (olive). Because of the short wavelengths λ, the distance between two nuclei $|r_n - r_m|$ is typically on the order of the wavelength or larger $|r_n - r_m| \gtrsim \lambda$, such that free-space couplings are usually weak.

2.3 Quantum optical description

After describing the platform of Mössbauer nuclei and how we can excite them in experiments, we now want to describe the system in a quantum optical picture. For simplicity, we do not consider hyperfine splitting here. However, as typically the hyperfine splitted lines are well-separated from each other (see Figs. 2.2 and 2.5), hyperfine splitting can often simply be taken into account by summing over the different hyperfine splitted transition frequencies.

2.3.1 Lindblad master equation

In Fig. 2.7, the system to be studied is shown. A solid state sample with $N \gg 1$ nuclei is excited with a resonant hard x-ray pulse. No matter whether this pulse comes from a synchrotron radiation source (ps duration [Wil21]) or XFEL (fs duration [Wil21]) the pulse is orders of magnitude shorter than the typical lifetime and the timescale given by the couplings. Thus, the pulse can be considered instantaneous and the excitation and de-excitation process can be decoupled. While the excitation dynamics is studied elsewhere [LKE25a; LKE25b], here we focus on the de-excitation dynamics. The de-excitation dynamics is governed by the couplings between the nuclei indicated in green and olive arrows, which will be part of the discussion in this chapter.

State description

Before we start with the time evolution, we first introduce the description of the quantum state of the system. A general state of a two-level system, e.g., of nucleus j, can be written as

$$|\Psi\rangle_j = \cos\frac{\theta}{2}|g\rangle_j + e^{i\phi}\sin\frac{\theta}{2}|e\rangle_j\,, \tag{2.22}$$

with $|g\rangle_j$ and $|e\rangle_j$ being the ground and excited state of the nucleus j, respectively. As displayed in Fig. 2.8 the single two-level state in Eq. (2.22) can be represented on the Bloch sphere [NC10] by interpreting the angles θ and ϕ in Eq. (2.22) as the polar and azimuthal angle on a unit sphere, respectively. In this interpretation, the polar angle θ represents the angle of excitation. According to the area theorem [AE87; MH67] an incident short pulse prepares the nucleus in an initial state with

$$\theta_0 = \mathcal{A} = \int_0^T \Omega(t')\mathrm{d}t'\,, \tag{2.23}$$

where $\mathcal{A}$ is the area of the time-dependent Rabi frequency $\Omega(t, z_j) = \vec{d}\cdot\vec{E}(t)/\hbar$ with dipole moment $\vec{d}$ and electric field $\vec{E}(t, \vec{r}_j)$ at position of the nucleus $\vec{r}_j$ integrated over the interaction time T, in which the pulse is applied. For simplicity, we assume that the phase of the electric field is constant in time and depends only on the position of the nucleus z_j. In this case the phase of the initial state is determined by the phase of the electric field at position of the nucleus z_j

$$\phi_0 = \arg\left(\frac{\vec{d}\cdot\vec{E}(z_j)}{\hbar}\right) = \vec{k}\cdot\vec{r_j}\,, \tag{2.24}$$

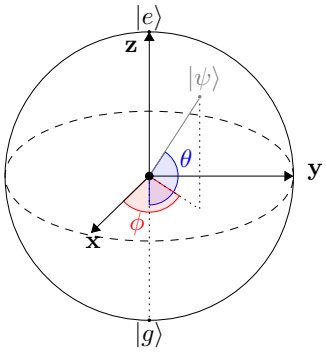

Figure 2.8: State representation on the Bloch sphere. A state $|\psi\rangle$ can be represented by two angles θ an ϕ as in Eq. (2.22). They can be represented as spherical coordinates on the unit sphere with the polar angle θ (blue) describing the degree of excitation and the azimuthal angle ϕ (red) the phase.

with incident light vector $\vec{k}$ and position of the nucleus $\vec{r}_j$. Therefore, the initial state of nucleus j after the impulsive excitation is given by

$$|\Psi_0\rangle_j = \cos\frac{\mathcal{A}}{2}|g\rangle_j + e^{i\vec{k}\vec{r}_j}\sin\left(\frac{\mathcal{A}}{2}\right)|e\rangle_j\,. \tag{2.25}$$

The initial state of the total system $|\Psi\rangle$ after the excitation is the tensor product of the single-nucleus states of all nuclei and given by

$$|\Psi\rangle = \bigotimes_{j=1}^{N}|\Psi\rangle_j\,. \tag{2.26}$$

In the low excitation regime $\mathcal{A} \ll \pi$, the state of the total system can be approximated by a superposition of the ground state and a non-localized single excitation

$$|\Psi_0\rangle \approx |g_1,\ldots,g_N\rangle + \frac{\sin\left(\frac{\mathcal{A}}{2}\right)}{\sqrt{N}}\sum_{j=1}^{N}e^{i\vec{k}\vec{r}_j}|g_1 g_2\ldots e_j\ldots g_N\rangle\,. \tag{2.27}$$

This state is similar to the non-classical nuclear exciton [HT99] or timed Dicke state [Scu09]. By analyzing only those events which led to a detection of a scattered photon, this latter part can effectively be post-selected from an experiment with a classical light source. Note, however, that the two states are very different: The classical one in Eq. (2.27) has a non-vanishing expectation value of the dipole moment operator, whereas the quantum exciton state does not.

As the system is an open quantum system, it is best described by a density matrix

$$\rho = |\Psi\rangle\langle\Psi|\,, \tag{2.28}$$

which also captures the loss of coherence due to interaction with the environment. For clarity, we omit the operator hats throughout this thesis. In the case of a two-level system in the state in Eq. (2.22), the density matrix ρ is given by

$$\rho = \underbrace{\cos^2\frac{\theta}{2}|e\rangle\langle e|}_{\rho_{ee}} + \underbrace{\cos\frac{\theta}{2}\sin\frac{\theta}{2}e^{i\phi}|e\rangle\langle g|}_{\rho_{eg}} + \underbrace{\cos\frac{\theta}{2}\sin\frac{\theta}{2}e^{-i\phi}|g\rangle\langle e|}_{\rho_{ge}} + \underbrace{\sin^2\frac{\theta}{2}|g\rangle\langle g|}_{\rho_{gg}}\,, \tag{2.29}$$

where we have omitted the index j for simplicity. We further identified the four matrix elements $\rho_{ab} = \langle a|\rho|b\rangle$. The matrix elements ρ_{gg} and ρ_{ee} describe the population of the ground and exciting state, respectively, and it is $\rho_{gg}+\rho_{ee} = 1$. The two other terms ρ_{eg} and ρ_{ge} are the complex conjugate of each other $\rho_{eg} = \rho_{eg}^*$ and describe the quantum superposition of the states. Thus, the closer these two matrix elements are to zero, the more classical the system behaves.

Time evolution

Time evolution of a density matrix is determined by the Lindblad master equation [BP07]

$$\frac{\mathrm{d}}{\mathrm{d}t}\rho = \frac{1}{i\hbar}[H,\rho] + \mathcal{L}[\rho]\,. \tag{2.30}$$

In principal, the Hamiltonian consists of a nuclear part, a photonic part and the interaction between both. However, as we are mainly interested in the nuclear de-excitation dynamics, one can trace out the photonic part of the system and describe the system by an effective Hamiltonian [HE13; Len+20]. This procedure as well as the resulting effective Hamiltonian [Ase+17b]

$$H = \hbar\omega_0 \sum_{n=1}^{N} \sigma_n^+ \sigma_n^- - \hbar \sum_{n,m} J_{mn} \sigma_n^+ \sigma_m^- \tag{2.31}$$

and Lindbladian [Ase+17b]

$$\mathcal{L}[\rho] = \sum_{n,m} \frac{\Gamma_{mn}}{2} \left(2\sigma_m^- \rho \sigma_n^+ - \sigma_n^+ \sigma_m^- \rho - \rho \sigma_n^+ \sigma_m^-\right) \tag{2.32}$$

are well-established to describe an ensemble of atoms with photon-mediated couplings [Ase+17a; Ase+17b; Cha+18; DKW02; FT02]. Here, the coherent couplings J_{mn} and the incoherent couplings Γ_{mn} between two nuclei n and m enter the equations. In addition, the diagonal part of of the Lindbladian Γ_{nn} describes single particle decay.

The free-space couplings are given by [AP01; KEK07]

$$J_{mn} + i\frac{\Gamma_{mn}^{\mathrm{rad}}}{2} = \frac{1}{\hbar} \vec{d}^* \cdot \chi(\vec{r}_n, \vec{r}_m) \cdot \vec{d}, \tag{2.33}$$

with dipole moment $\vec{d}$ and a tensor [AP01; KEK07]

$$\chi_{pq}(\vec{r}_m, \vec{r}_n) = \frac{k_0^3}{4\pi\epsilon_0} \left[\delta_{pq} \left(\frac{1}{\eta_{mn}} + \frac{i}{\eta_{mn}^2} - \frac{1}{\eta_{mn}^3} \right) - \frac{R_{mn}^p R_{mn}^q}{|\vec{R}_{mn}|^2} \left(\frac{1}{\eta_{mn}} + \frac{3i}{\eta_{mn}^2} - \frac{3}{\eta_{mn}^3} \right) \right] e^{\eta_{mn}}, \tag{2.34}$$

determined from the Green's function with the resonant wavevector k_0, the vacuum permittivity ϵ_0, the vector between nucleus n and m $\vec{R}_{mn} = \vec{r}_n - \vec{r}_m$ and the normalized distance $\eta_{mn} = k_0|\vec{R}_{mn}|$. For a thin-film cavity environment, the calculation of the couplings can be found in [Len+20; Tom95] and references therein. Here $\Gamma_{mn}^{\mathrm{rad}}$ describes the radiative part of the decay. The full decay rate Γ_{mn} is speed up by the internal conversion, which adds an additional decay rate to the diagonal terms $\Gamma_{mn}^{\mathrm{IC}} = \Gamma^{\mathrm{IC}} \delta_{mn}$, such that the full decay rate is given by $\Gamma_{mn} = \Gamma_{mn}^{\mathrm{rad}} + \Gamma^{\mathrm{IC}} \delta_{mn}$.

Note that for simplicity, the hyperfine splitting is neglected here. It can simply be introduced by an additional sum running over the different resonance frequencies ω_0^j of the hyperfine splitted transitions j.

2.3.2 Propagation effects

So far we have only considered a short excitation pulse and no further driving of the nuclei. However, in an extended system, e.g., in nuclear forward scattering through a thin foil, the nuclei in the back of the sample, i.e., further downstream, also see the electric field emitted by the nuclei in the front of the sample. Here, we want to discuss two methods to include this effect either by including the electric field in a semi-classical description or by including propagation effects via an effective coupling.

Maxwell-Bloch equations

In the Maxwell-Bloch equations [SZ97], the nuclei are treated quantum mechanically and the electric field is treated classically. The derivation presented here closely follows [Len21; Lia14; Rei14]. The starting point is again the Lindblad master equation in Eq. (2.30), but we now consider each nuclei separately. The interaction with an electric field propagating in the z-direction can be introduced by a driving term in the Hamiltonian with the Rabi frequency

$$\Omega(t, \vec{r}_{\mathrm{nuc}}) = \frac{\vec{d} \cdot \vec{E}(t, \vec{r}_{\mathrm{nuc}})}{\hbar}, \tag{2.35}$$

with the dipole moment of the transition $\vec{d}$ and the electric field $\vec{E}$ at the position of nucleus $\vec{r}_{\mathrm{nuc}}$

$$E(t, z) = \frac{E_0(t)}{2} e^{-i\nu t + ik_0 z} + c.c., \tag{2.36}$$

where $\nu = \omega_0 + \Delta$ is the carrier frequency of the electric field detuned from the resonance frequency ω_0 by Δ and $E_0(t)$ its time-dependent envelope. For simplicity, we assume that the electric field does not have an additional phase modulation. The result with phase modulation can be found in [NA85]. Applying the rotating-wave approximation, the Hamiltonian is given by [SZ97]

$$H(t) = \hbar\omega_0\sigma^+\sigma^- - \frac{\hbar}{2}\Omega(t)e^{-i(\omega_0+\Delta)t}\sigma^+ - \frac{\hbar}{2}\Omega(t)e^{i(\omega_0+\Delta)t}\sigma^- \,. \tag{2.37}$$

With Eq. (2.30), we derive the time evolution of the density matrix elements $\rho_{ab} = \langle a|\rho|b\rangle$ [Rei14]:

$$\frac{\mathrm{d}}{\mathrm{d}t}\rho_{gg} = +\Gamma\rho_{ee} - i\frac{\Omega(t)}{2}e^{-i\nu t}\rho_{ge} + i\frac{\Omega^*(t)}{2}e^{+i\nu t}\rho_{eg} \,, \tag{2.38a}$$

$$\frac{\mathrm{d}}{\mathrm{d}t}\rho_{ee} = -\Gamma\rho_{ee} + i\frac{\Omega(t)}{2}e^{-i\nu t}\rho_{ge} - i\frac{\Omega^*(t)}{2}e^{+i\nu t}\rho_{eg} \,, \tag{2.38b}$$

$$\frac{\mathrm{d}}{\mathrm{d}t}\rho_{eg} = -\frac{\Gamma}{2}\rho_{eg} - i\omega_0\rho_{eg} + i\frac{\Omega(t)}{2}e^{-i\nu t}\rho_{gg} - i\frac{\Omega^*(t)}{2}e^{+i\nu t}\rho_{ee} \,. \tag{2.38c}$$

$$\rho_{ge} = \rho_{eg}^* \,. \tag{2.38d}$$

Switching into the interaction picture by absorbing the oscillations into $\bar{\rho}_{ge} = \rho_{ge}e^{-(\omega_0+\Delta)t+i\phi(t)}$, the equations simplify to the *Optical Bloch equations* [Rei14; SZ97]

$$\frac{\mathrm{d}}{\mathrm{d}t}\bar{\rho}_{gg}(t) = -i\Omega(t)\bar{\rho}_{eg}(t) + i\Omega^*(t)\bar{\rho}_{ge}(t) + \Gamma\bar{\rho}_{ee}(t) \,, \tag{2.39a}$$

$$\frac{\mathrm{d}}{\mathrm{d}t}\bar{\rho}_{ee}(t) = +i\Omega(t)\bar{\rho}_{eg}(t) - i\Omega^*(t)\bar{\rho}_{ge}(t) - \Gamma\bar{\rho}_{ee}(t) \,, \tag{2.39b}$$

$$\frac{\mathrm{d}}{\mathrm{d}t}\bar{\rho}_{eg}(t) = -i\Omega^*(t)\left(\bar{\rho}_{gg}(t) - \bar{\rho}_{ee}(t)\right) - \left(\frac{\gamma}{2} + i\Delta\right)\bar{\rho}_{eg}(t) \,, \tag{2.39c}$$

$$\bar{\rho}_{ge} = \bar{\rho}_{eg}^* \,. \tag{2.39d}$$

To also derive the differential equation describing the time evolution of the electric field, we first restrict the propagation to one dimension z. Furthermore, we want to apply the slowly-varying envelope approximation. This approximation assumes that the envelope of the electric field evolves slowly enough compared to its carrier frequency to neglect second order derivatives of the electric field in time and space. Because of the high transition frequencies in the x-ray regime ($\approx 10^{19}$ Hz) compared to the nuclear decay time scale (typically $\approx 10^{-7}$ s) on which the envelope evolves, the requirement is fulfilled. In addition, the slowly-varying envelope approximation neglects the backward wave, which could only occur if there was a seed in the backward direction. With the slowly-varying envelope equation we derive the differential equation for the electric field [Lia14]

$$\left(\frac{1}{c}\frac{\partial}{\partial t} + \frac{\partial}{\partial z}\right)\bar{\vec{E}}(z,t) = i\frac{2\pi}{\epsilon_0\lambda}nd\vec{\bar{\rho}}_{eg}(z,t) \,, \tag{2.40}$$

with the vacuum permittivity ϵ_0, the resonant wavelength λ, the dipole moment $\vec{d}$, and the particle number density n. Inserting Eq. (2.35), we obtain the differential equation for the Rabi frequency [Hee+21; Lia14]

$$\left(\frac{1}{c}\frac{\partial}{\partial t} + \frac{\partial}{\partial z}\right)\Omega(z,t) = i\eta\bar{\rho}_{eg}(z,t) \,, \tag{2.41}$$

where $\eta = b/(2L) = \sigma_0 f_{\mathrm{LM}} n\Gamma/2$ with the resonant cross-section σ_0, the Lamb-Mössbauer factor f_{LM}, and the number density n. Eqs. (2.39) and (2.41) form the so-called *Maxwell-Bloch equations*. Together they form a closed set of differential equations, which can be studied numerically for a general solution. In special situations, e.g., in the low-excitation regime (cf. Section 2.3.3), the differential equations can be solved analytically.

Burnham-Chiao ringing

To derive a simple model for the dynamics of pulse propagation through a resonant medium we use a slightly different parametrization for the semi-classical formulation of the light-matter interaction [AC70; BC69; GH82; HL83; MH67], which was first extensively studied by Burnham and Chiao [BC69] and is thus called *Burnham-Chiao ringing*. Instead of describing the system by the

density matrix elements ρ_{ee} and ρ_{eg} as in the optical Bloch equations, the excitation angle θ is used. To proceed, five key assumptions need to be fulfilled: 1. The calculation only considers times, which are short compared to the characteristic time scale given by Γ. This allows us to neglect $\tau = 1/\Gamma$ in Eq. (2.38). In Mössbauer science, the experiments typically take place only on a few τ, which is why especially for short time after excitation this approximation is fulfilled. 2. We assume small attenuation, which is why we can assume that all atoms see the same pulse. That this is a valid assumption is discussed in [LKE25a]. 3. The system must be described by Maxwell's equations. For coherent nuclear forward scattering, this is fulfilled because relativistic, QED, non-linear effects or similar do not play a role. This assumption is needed to describe the evolution of the electric field correctly. 4. In the calculations, the backward wave is neglected, which is necessary for assuming that there is no radiation from the nuclei at any position of the sample while the pulse is passing through. This directly leads us to the last assumption. 5. The last assumption is the validity of the slowly varying envelope approximation. The two assumptions 4. and 5. have already been used in Section 2.3.2. If all assumptions are fulfilled, a simple set of differential equations describes the system [AB65; BC69; GH82]:

$$\frac{\partial^2}{\partial z \partial \tau}\theta(\tau, z) = -Q \sin\left(\theta(\tau, z)\right) , \tag{2.42a}$$

$$\frac{\partial}{\partial \tau}\theta(\tau, z) = \frac{2d}{\hbar} E(\tau, z) , \tag{2.42b}$$

with retarded time $\tau = t - L/c$, $Q = b/L$ with thickness of the sample L, thickness parameter b as defined in Eq. (2.8) and dipole moment d. The boundary conditions are $\theta(\tau = 0) = \mathcal{A}$ with $\mathcal{A}$ being the degree of initial excitation and $E(\tau = 0, z = 0) = 0$. The characteristic time scale of the system $1/\Gamma$ is usually orders of magnitude larger then the propagation time of the electric field L/c. Therefore, time retardation can be neglected, and using the variable transform $q = 2\sqrt{Qtz}$, Eq. (2.42) can be mapped onto [BC69]

$$\frac{\mathrm{d}^2}{\mathrm{d}q^2}\theta(q) + \frac{1}{q}\frac{\mathrm{d}}{\mathrm{d}q}\theta(q) + \sin\left(\theta(q)\right) = 0 , \tag{2.43}$$

with boundary conditions $\theta(0) = \theta_0$ and $\frac{\mathrm{d}}{\mathrm{d}q}\theta(q)|_{q=0} = 0$. With Eq. (2.42b) the electric field is then given by

$$E(t, z) \propto \frac{\mathrm{d}}{\mathrm{d}t}\theta(t, z) = \frac{1}{\sqrt{2}}\sqrt{\frac{b}{t}}\frac{\mathrm{d}}{\mathrm{d}q}\theta(q) . \tag{2.44}$$

For arbitrary initial excitation angles, the differential equation in Eq. (2.43) cannot be solved analytically. However, in the case of small excitation $\theta \ll 1$, we can approximate $\sin\left(\theta(q)\right) \approx \theta(q)$, and Eq. (2.43) becomes the Bessel differential equation of 0-th order. The differential equation Eq. (2.43) is then solved by

$$\theta(q) = \theta_0 J_0(q) , \tag{2.45}$$

where J_0 is a Bessel function of first kind. Using the relation $\frac{\mathrm{d}}{\mathrm{d}q}J_0(q) = -J_1(q)$ with $q = 2\sqrt{bt}$, the electric field is given by

$$E(t) \propto \sqrt{\frac{b}{t}} J_1\left(2\sqrt{bt}\right) . \tag{2.46}$$

The Bessel function leads to a beating-like structure in the intensity $I(t) = |E(t)|^2$, which is called the *Burnham-Chiao ringing* and has been observed not only in nuclear [Bür99], but also in many other systems [Frö+91; Gru+08; Hed+25; Nie+05; Oka+19; Skr+73; ZHO23]. For higher excitation, the minima shift as theoretically described in [BC69] and measured e.g., in [Nie+05].

With the crucial approximation of neglecting the single-particle decay ($\Gamma = 0$), the Burnham-Chiao model provides a simple model to analyze propagation effects even beyond the low-excitation approximation. In the low-excitation approximation, we recover the result discussed in Section 2.1.4 without the single-particle decay.

Effective coupling

Another possibility to include propagation effects is to apply an effective coupling between the nuclei, which is mediated by the propagating electric field. In [Can+15; MCD17] a formalism mapping a cloud of atoms with a propagating electric field onto a 1D waveguide coupled to the atoms is

presented, which will be shortly summarized in the following. The starting point are the Maxwell-Bloch equations. The wave equation for the forward $E_+(z,t)$ and backward $E_-(z,t)$ propagating component of the electric field $E(z,t) = E_+(z,t) + E_-(z,t)$ is [MCD17]

$$\left(\frac{1}{c}\frac{\partial}{\partial t} \pm \frac{\partial}{\partial z}\right) E_\pm(z,t) = i\sqrt{\frac{\Gamma_{1\mathrm{D}}}{2}}\rho_{eg}(z,t)\,, \tag{2.47}$$

where we have introduced the coupling rate of an individual emitter to the one-dimensional input mode $\Gamma_{1\mathrm{D}}$. The strength of the coupling can be determined by [MCD17]

$$\Gamma_{1\mathrm{D}} = \frac{\mathrm{OD}}{2N}\Gamma\,, \tag{2.48}$$

with the optical depth of a target with thickness L [RL24]

$$\mathrm{OD} = \int_0^L \mathrm{d}s\, n(s)\sigma = \sigma_0 n L\,, \tag{2.49}$$

with number density n and resonant cross section σ_0. In the last step, we have evaluated the integral along path s for a uniform target. For enriched α-iron it is $\mathrm{OD} = 16.0752 \cdot L\,[\mu\mathrm{m}]$. Note that Eq. (2.48) allows us to simulate the system with a smaller number of emitters than physically required to match the thickness L. For simplicity, we assume that the electric field is on resonance $\Delta = 0$ and thus the relevant Bloch equation for ρ_{eg} is

$$\frac{\mathrm{d}}{\mathrm{d}t}\bar{\rho}_{eg}(z,t) = i\sqrt{\frac{\Gamma_{1\mathrm{D}}}{2}}\left[\bar{\rho}_{gg}(z,t) - \bar{\rho}_{ee}(z,t)\right] E(z,t)\,. \tag{2.50}$$

We can map the one-dimensional Maxwell-Bloch equations onto a an ensemble of nuclei coupled to a waveguide [MCD17]. Again, time retardation can be neglected, which simplifies the problem drastically [AC70]. The coupling via the waveguide can then be included by additional terms in the Hamiltonian and Lindbladian [MCD17]

$$H_{\mathrm{prop}} = \frac{\Gamma_{1\mathrm{D}}}{2}\sum_{n,m}^{N} \sin\left(k_0|z_n - z_m|\right)\sigma_n^+\sigma_m^-\,, \tag{2.51a}$$

$$\mathcal{L}_{\mathrm{prop}}\left[\rho\right] = \frac{\Gamma_{1\mathrm{D}}}{2}\sum_{n,m}^{N} \cos\left(k_0|z_n - z_m|\right)\left(2\sigma_m^-\rho\sigma_n^+ - \sigma_n^+\sigma_m^-\rho - \rho\sigma_n^+\sigma_m^-\right)\,. \tag{2.51b}$$

Note that the structure of the terms is the same as in Eqs. (2.31) and (2.32), such that only a modification of the coupling takes place and we have modified couplings

$$\tilde{J}_{mn} = J_{mn} - \frac{\Gamma_{1\mathrm{D}}}{2}\sin\left(k_0|z_n - z_m|\right)\,, \tag{2.52a}$$

$$\tilde{\Gamma}_{mn} = \Gamma_{mn} - \Gamma_{1\mathrm{D}}\cos\left(k_0|z_n - z_m|\right)\,. \tag{2.52b}$$

Those couplings are essentially a projection of the free-space dipole-dipole couplings onto the forward propagation mode. The coupling between the nuclei and the incident electric field can be included in the Hamiltonian by [MCD17]

$$H_{\mathrm{drive}} = -\sqrt{\frac{\Gamma_{1\mathrm{D}}}{2}}\sum_{j=1}^{N}\left(\Omega(t,z_j)\sigma_j^+ + h.c.\right)\,, \tag{2.53}$$

where $\Omega(t,z_j)$ is the time-dependent Rabi frequency.

Because the coupling terms are added to the Hamiltonian and Lindbladian, respectively, the presented formalism in principle allows to study the propagation effects with additional couplings, which is not possible with the Maxwell-Bloch equations.

2.3.3 Low-excitation regime

So far in the quantum optical description we have considered arbitrary degrees of excitation $\mathcal{A}$. However, although the pulses of synchrotron radiation and also of XFELs are strong, there is only a

very small amount of resonant photons because the spectral width of these pulses is typically orders of magnitude larger than the natural linewidth [Hee+17]. Therefore, the population of the excited state is tiny [LE20; LKE25b; Shv99], and it is a valid approximation that there is no population in the excited state

$$\rho_{ee} = \langle \sigma^{ee} \rangle \approx 0\,. \tag{2.54}$$

Applying this approximation, we can derive the analytical expressions in Eqs. (2.10) and (2.12), which we have only stated in their discussion in Section 2.1.4 so far.

The linear approximation simplifies the equations describing propagation effects Eq. (2.39) significantly because it decouples the optical Bloch equations and the only two remaining relevant equations are

$$\frac{\mathrm{d}}{\mathrm{d}t}\bar{\rho}_{eg}(z,t) = -i\Omega^*(t) - \left(\frac{\gamma}{2} + i\Delta\right)\bar{\rho}_{eg}(z,t)\,, \tag{2.55a}$$

$$\left(\frac{1}{c}\frac{\partial}{\partial t} + \frac{\partial}{\partial z}\right)\Omega(z,t) = i\eta\bar{\rho}_{eg}(z,t)\,. \tag{2.55b}$$

Setting the field at position $z = 0$ to $\Omega(t,0)$, this coupled differential equation can be solved analytically in frequency space [SO08]. With $\Omega(t,z) = \frac{1}{2\pi}\int \tilde{\Omega}(\omega,z)e^{-i\omega t}$ the solution in frequency space is given by [Rei14]

$$\tilde{\Omega}(\omega,z) = \exp\left[\frac{-i\eta/2}{\omega + \Delta + i\frac{\Gamma}{2}}\right]\Omega_0(\omega,0)\,. \tag{2.56}$$

The solution in time space can be calculated from this via the inverse Fourier transformation [Rei14]

$$\Omega(t,z) = \frac{1}{2\pi}\int \mathrm{d}\omega\Omega_0(\omega,0)\exp\left(\frac{-ib(z)}{\omega - \omega_0 + i\gamma} - i\omega t\right)\,, \tag{2.57}$$

where we have introduced $b(z) = \eta z/2$, $\gamma = \Gamma/2$ and neglected the retardation such that the retarded time $\tau = t - \frac{z}{c} \approx t$ [AC70]. Given that the lifetime is on nanosecond time scale and for a typical μm-thick sample z/c is on the order of tens of femtoseconds, this is a valid approximation.

The electric field can be calculated with Eq. (2.35). In frequency space, it is simply given by an exponential of a Lorentzian profile, the representation in time space needs a few more considerations. Let us start with

$$E(t,z) = \left[\frac{1}{2\pi}\int \mathrm{d}\omega \exp\left(\frac{-ib(z)}{\omega - \omega_0 + i\gamma} - i\omega t\right)\right]E_{\mathrm{in}}^0\,. \tag{2.58}$$

By using the Taylor expansion of the exponential, we can rewrite this as

$$E(t,z) = \left[\frac{1}{2\pi}\int \mathrm{d}\omega e^{-i\omega t} + \frac{1}{2\pi}\int \mathrm{d}\omega \sum_{n=1}^{\infty} e^{-i\omega t}\frac{1}{n!}\left(\frac{-ib(z)}{\omega - \omega_0 + i\gamma} - i\omega t\right)^n\right]E_{\mathrm{in}}^0\,. \tag{2.59}$$

The first term is the Fourier transform of $\delta(t)$ resembles the unscattered part of the outgoing electric field. The second term describes the interaction with the sample. It can be evaluated by an integration in the complex plane resulting in [KAK79; Rei14; Röh04]

$$E(t) = \left[\delta(t) - \sqrt{\frac{b}{t}}J_1\left(2\sqrt{bt}\right)e^{-i\omega_0 t}e^{-\gamma t}\theta(t)\right]E_{\mathrm{in}}^0\,, \tag{2.60}$$

with the Bessel function of first kind $J_1(x)$. An alternative derivation of Eq. (2.60) based on the refractive index is given in [Bür99]. For a detailed interpretation of the different terms see the discussion following Eq. (2.13).

2.4 Conclusion

To summarize, in this chapter we have presented an introduction into quantum optics with Mössbauer nuclei.

First, we introduced the field of Mössbauer science, where after an introduction into the Mössbauer effect and the two isotopes used in this thesis, we have seen different experimental aspect and especially discussed coherent nuclear forward scattering. In the second section, we have seen different x-ray light

sources with the special focus on the functionality of synchrotrons and XFELs, and their differences. Those first two sections give the background for the experiments performed at an X-ray free electron laser in the first part of this thesis and the stand-alone Chapter 11.

The foundations for the second part of this thesis were laid in Section 2.3, which describes the de-excitation dynamics of a nuclear ensemble from a quantum optics perspective. The photon-mediated dipole-dipole couplings of the nuclei where introduced as well as the resulting propagational effects. In general, the principle description is valid for arbitrary excitations, however only in the low-excitation regime analytical expressions can be obtained.

Part I

Experiments performed at an X-ray free electron laser

Chapter 3

Data analysis at European XFEL

The standardized data analysis presented in this chapter was developed for the experiments leading to the following publications:

Resonant X-ray excitation of the nuclear clock isomer ^{45}Sc
Y. Shvyd'ko, R. Röhlsberger, O. Kocharovskaya, J. Evers, G. A. Geloni, P. Liu, D. Shu, A. Miceli, B. Stone, W. Hippler, B. Marx-Glowna, I. Uschmann, R. Loetzsch, O. Leupold, H.-C. Wille, I. Sergeev, M. Gerharz, X. Zhang, C. Grech, M. Guetg, V. Kocharyan, N. Kujala, S. Liu, W. Qin, A. Zozulya, J. Hallmann, U. Boesenberg, W. Jo, J. Möller, A. Rodriguez-Fernandez, M. Youssef, A. Madsen, and T. Kolodziej
Nature **622**, 471–475 (2023)

Single-shot sorting of Mössbauer time-domain data at X-ray free electron lasers
M. Gerharz, W. Hippler, B. Marx-Glowna, S. Sadashivaiah, K. S. Schulze, I. Uschmann, R. Lötzsch, K. Schlage, S. Velten, D. Lentrodt, L. Wolff, O. Leupold, I. Sergeev, H.-C. Wille, C. Strohm, M. Guetg, S. Liu, G. A. Geloni, U. Boesenberg, J. Hallmann, A. Zozulya, J.-E. Pudell, A. Rodriguez-Fernandez, M. Youssef, A. Madsen, L. Bocklage, G. G. Paulus, C. H. Keitel, T. Pfeifer, R. Röhlsberger, and J. Evers
arXiv:2509.15833 [quanth-ph]

Probing the Linewidth of the 12.4-keV Solid-State ^{45}Sc Isomeric Resonance
P. Liu, M. Gerharz, B. Marx-Glowna, W. Hippler, J.-E. Pudell, A. Zozulya, B. Stone, D. Shu, R. Loetzsch, S. Sadashivaiah, L. Bocklage, C. Boemer, S. Liu, V. Kocharyan, D. Krebs, T. Long, W. Qin, M. Scholz, K. Schlage, I. Sergeev, H.-C. Wille, U. Boesenberg, G. A. Geloni, J. Hallmann, W. Jo, N. Kujala, A. Madsen, A. Rodriguez-Fernandez, R. Rysov, K. Tasca, T. Kolodziej, X. Zhang, M. Ilchen, N. Wieland, G. Huber, J. H. Edgar, J. Evers, O. Kocharovskaya, R. Röhlsberger, and Y. Shvyd'ko
arXiv:2508.17538 [quanth-ph]

3.1 Motivation

As discussed in Chapter 1, the advancement of light sources and possibility to perform experiments at XFELs provides new opportunities for Mössbauer science. However, experiments at this new light sources are by far not as standardized as at synchrotron radiation sources, especially those with Mössbauer nuclei. Before the experiments of our collaborations at the European XFEL [45S22; 45S24; 57F22; 57F23; 57F25], only one other experiment was performed at the SACLA XFEL [Chu+18] and the experiments by our collaboration were the first experiments of their kind at the European XFEL at all. Therefore, many new analysis scripts and tools had to be developed together with the data analysis group, which were crucial for the successful experiments reported in [Ger+25b; Liu+25a; Shv+23]. An overview of the standardized parts of the newly developed analysis software is given in this chapter. Further detailed and beamtime specific data analysis is discussed in the respective chapters.

As already said, Mössbauer experiments are currently not standard experiments at XFELs in contrast to Mössbauer experiments at synchrotron radiation sources. To stress the importance of developing a data analysis chain for Mössbauer experiments at European XFEL we start with an overview over the typical data analysis for a synchrotron experiment with ^{57}Fe and compare it to the availability at the European XFEL.

The first step in any Mössbauer experiment at an accelerator-based light source is to set the incident photon energy to the Mössbauer transition energy. This has to be done on a level comparable to the spectral width of the incident x-rays. At synchrotrons, for standard Mössbauer isotopes such as

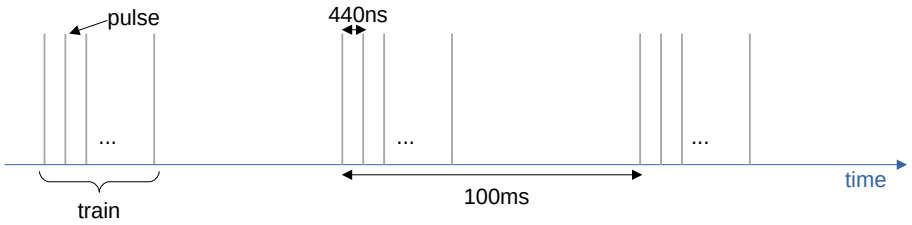

Figure 3.1: Pulse structure at European XFEL. At European XFEL the pulses come in trains of up to hundreds of pulses every 100ms. Within the train, the pulses have a fixed temporal distance, which was 440 ns in the setting used in our experiments.

^{57}Fe, the machine settings to produce the respective photon energy are well-known. At European XFEL, the absolute photon energy is not measured with build-in devices and can therefore only be adjusted approximately with the standard equipment, which currently is not accurate enough for Mössbauer experiments. However, it can be measured with the *Bond method* [Bon60; Shv+23], which was provided by our collaborators from Jena and essentially determines the photon energy from the Bragg angle.

The Bragg angle can be measured by a motor scan, which measures the intensity of a diode at a constant position as a function of a certain rotation angle of the crystal. A motor scan is a standard measurement procedure at synchrotrons. At the European XFEL however, such a motor scan could be run, but only approximately analyzed in real time because the data-matching from different pulses is only approximately until now [Eurc]. Before the development of our custom motor scan analysis tool, for precise motor scans, after the measurement the data had to be saved and migrated to a different storage from which it could be analyzed precisely, which took several minutes.

Once the photon energy is set, the sample is adjusted. After a rough alignment by hand, the fine alignment is typically done by scanning the number of resonant photons against a motor position. Again, this is a standard procedure at synchrotrons, but was not available at the European XFEL. Here, the difficulty is not only to perform a motor scan at all, but in addition the signal has to be processed before to measure only the resonantly scattered photons. Without the possibility to perform a precise motor scan with the resonant photons as the signal it would not have been possible to adjust the setup.

At synchrotron experiments, the number of resonant photons also provides an important observable to monitor the experiment, e.g., whether the count rate is decreasing. At XFELs due to the higher peak photon flux, the number of resonant photons per pulse is not easily resolvable for arbitrary settings. As a flexible measure taking over the role of the number of resonant photons the integrated APD signal of the delayed photons is implemented.

Finally, measuring time spectra or energy-time spectra is typically readily implemented at synchrotrons. For technical details see e.g. [Vel+24]. For the experiments at the European XFEL, code to process the raw data into those standard measurements had to be developed.

Similarly to the ^{57}Fe-experiments, also for the ^{45}Sc-experiments, new data analysis routines had to be implemented. Here, parts of the ^{57}Fe analysis could be reused, e.g., motor scans, but the processing of the raw detector data was implemented new.

Lastly, another big difference between synchrotron and XFEL experiments is the size of data collected during an experiment. While at synchrotrons, the data recorded during one beamtime typically easily fits on a standard hard disc, our experiments at the European XFEL had up to 100 TB of data.

3.2 Data structure at European XFEL

Before we go into details of the data analysis, the special data structure at the European XFEL is introduced.

At the European XFEL, the x-ray pulses arrive in a train-like structure with 10 Hz. That means, that every 100 ms a specified number of pulses n_{pulses} arrives with typically 440 ns temporal separation. A schematic of the pulse structure is shown in Fig. 3.1. All data, e.g., machine parameters, motors or detectors, are tagged with a train number and can be processed based on this [Fan+18]. Some instruments are able to measure data even on a pulse-resolved basis. However, they still send the data

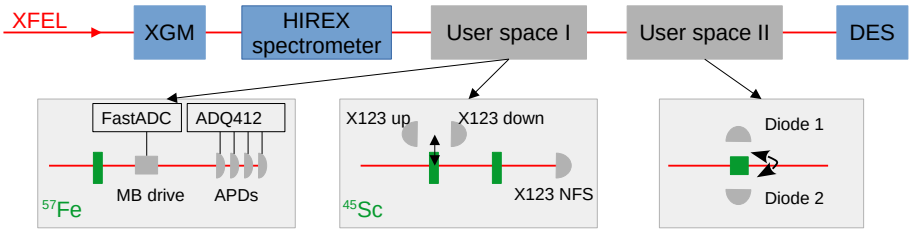

Figure 3.2: Simplified setup only containing the most relevant measurement devices for data evaluation. The blue boxes of x-ray gas monitor (XGM), HIREX spectrometer and diagnostic end station (DES), which among other diagnostic tools contains a spectrometer, represent beamline instruments. The user devices are indicated by the gray boxes. In the ^{57}Fe experiments [57F22; 57F23; 57F25], a sample (green rectangle) was placed in the beam and Avalanche Photo Diodes (APDs) measure the time information of the resonant photons. Their analog voltage signal is digitalized using an ADQ412. Optionally, a Mössbauer drive (MB drive) can be placed in the setup for energy information. Because less time resolution is needed, the analog signal of the Mössbauer drive can be processed with the fastADC. In the ^{45}Sc experiments [45S24; 57F23], Amptek-X123 detectors are used at three different positions of the experiment. Their digital output is send to the data acqusition system directly. In both types of experiment the second user part is the same and measures the absolute photon energy with the Bond method [Bon60; Shv+23]. Here, a rotating crystal (green) is used with two diodes measuring the intensity for absolute measurements of the photon energy. The black arrows indicate moving devices. For more details on the experimental setup see the respective chapters. The devices are explained in detail in the main text.

to the data system combined within one train. Instruments which record data in a pulse-resolved way are called *fast devices*, those recording only train-resolved *slow devices*.

In all experiments, European XFEL's software framework *karabo* [Hau+19] is used for control and data acquisition. Each device has a unique name and typically many properties, e.g., the actual position of a motor. These properties can be set, e.g., to move a motor, or read, e.g., the position of the motor. Here, the focus is on the read out.

There are two fundamentally different access points to the data. One is the *online cluster* to which data is sent in real time and where it can be analyzed in real time, but the data is typically not stored permanently. The other one is the *offline cluster*, where data is stored for later analysis. To store data on the offline cluster, a *run* has to be taken, which can be e.g., a motor scan which should be saved or just acquiring for a specified time. The data on the offline cluster is stored on a per run basis and is available for a long time according to the data policy of European XFEL [Eur17; Eur23].

3.3 Important devices from a data analysis perspective

A simplified setup showing only the most important devices for data evaluation can be found in Fig. 3.2. This is a non-complete list of devices used in the experiment, but rather focuses on the different types from a data-analysis perspective. The different components are explained in the following.

3.3.1 Beamline instruments

Several devices, which are routinely used at the beamline and also in our experiments, are discussed in the following.

X-ray gas monitor. The x-ray gas monitor (XGM) [Mal+19] sits upstream in the tunnel and measures the spectrally and temporally integrated absolute pulse energy in μJ. It has two different measurement modi running in parallel to measure the average pulse energy over a train or to measure the pulse energy pulse-resolved. For the train averaged data a single float is given per train, for the pulse-resolved an array of length n_{pulses}.

HIREX/DES spectrometer. The HIgh REsolution Hard X-ray single-shot (HIREX) [Kuj+20] and diagnostic end station (DES) [Boe+17; Boe+24] spectrometers to measure the incident photon energy are equipped with the same detector, such that for the data analysis they can be treated similar. The HIREX spectrometer is upstream of the experiment and can in principle be used all the time during the experiment. The DES spectrometer is located downstream of the experiment and

usually blocked by the APDs. However, it is often used in an early phase of the experiment, when no blocking elements are in the beam, and could also be used in the first ^{45}Sc-experiment [45S22].

Both spectrometers consist of a bend crystal reflecting the light depending on the photon energy. The reflected light is detected with a Gotthard-I detector [Moz+12], and recently upgraded with a Gotthard-II detector [Zha+18], respectively. For each train, a 2D matrix is returned with the relative photon energy on one and the different pulses on the other axis. Because not only the photon energy, but also alignment of the crystal influences the conversion from detector channel to photon energy, the two spectrometers are mainly used for relative energy measurements.

Motors. All motors belong to the slow devices. Among several settings, most importantly the actual position, the target position and a possible encoder position are saved. In addition, it is possible to save details on motor scans.

3.3.2 User instruments

Because the performed experiments are non-standard experiments, e.g., the detectors and further experimental equipment were brought by the users and were included into the European XFEL data system.

Avalanche photo diodes. For the experiments with ^{57}Fe, Avalanche photo diodes (APDs) measure the prompt and delayed photons as a function of time after the excitation. At the time, where a photon arrives at an APD, the applied constant voltage has a dip. For details on the APDs see [Röh04] and references therein. For few photons arriving at the same time, the depth of the dip is approximately proportional to the number of photons. This analog voltage signal of each APD is digitalized on a per-train level using an ADQ-412 with 0.25 ns time resolution. Those digital traces can later in the analysis be split up into n_{pulses} subtraces, one for each pulse in the train. This detector is used in the experiments with ^{57}Fe.

Mössbauer drive. The Mössbauer drive is used for gaining energy information (see Section 2.1.3). The information on the velocity and thus the energy information, is encoded in a voltage signal by a coil that measures the movement [Vel+24]. This voltage is then digitalized on a per-train level using an Analogue to Digital Converter (ADC). The data acquisition is controlled with European XFELs fastADC application [Eura]. Similar to the APD signal, in the later analysis, the digital voltage signal is analyzed on a per-pulse basis resulting in one detuning per pulse. Note that the detuning change of the Mössbauer drive is slow compared to the pulse spacing, such that we can assume that it is constant over one pulse.

X123 detectors. In the ^{45}Sc-experiments, Amptek-X123 detectors are used to measure x-ray photons in an energy- and time-resolved way with an extremely low background of 2×10^{-4} ph/s [Shv+23]. The detectors can be used in different measurement modi. The simpler one is to acquire data for a specified time and return the spectrum of all photons during that time. In this measurement mode, one spectrum per run is returned and real-time analysis of the spectrum is not possible until the specified acquisition time is over. The second measurement mode records time and energy of all photons per train. In this mode, the data can be analyzed in real time.

Diodes. The diodes are slow devices recording a single number signal for each train. Typically, two diodes are connected measuring the scattered x-ray light with a high dynamical range. This is mainly used for absolute photon energy measurements and during alignment.

3.4 Online analysis

The online analysis serves for real time analysis during the experiment. It is mainly used for alignment of components and monitoring of beam parameters and measurement results. Thereby, it is crucial to determine if a test or measurement was successful and to decide how to continue. To have full flexibility regarding the analysis procedures, European XFELs processing framework `EXtra-metro` [EuXd] is used, which provides simple access to the data and flexible processing as we will see in the following. To display the real time analysis, the gui of `extra-foam`'s [EuXc] MID special suite `Correlator` is chosen.

3.4.1 Principal functionality

The principle concept is that data is quickly analyzed within a train and plotted afterwards. To this end a so-called *context*-file is written, which uses the programming language python with custom

extensions by the European XFEL team. Within this file, small code snippets define the viewgraphs, which will be updated with the live data. Extra-metro provides a graphical user interface to show the viewgraphs.

As a simple example, the pulse energy measured with the XGM is monitored. First, the neccessary modules are loaded

```
from metropc.analysis.functions import gaussian
from extra_foam.utils import rich_output, Series as S, LinearROI
```

Afterwards, the XGM data is loaded and returned as a function of the train ID

```
@View.Compute(name="XGM/pulse_energy_vs_train_ID")
def xgm_slow_vs_trainId(tid: "internal#train_id",
             xgm_slow_data: "karabo#SA2_XTD1_XGM/XGM/DOOCS.controlData.slowTrain.value",
             ):
    """
    Parameters
    ----------
    tid: int
        Train ID.
    xgm_slow_data: float
        Mean value of XGM over train.

    Returns
    -------
    rich_output: rich_output
        Output to be displayed by the GUI.
    """

   ydata = {"y1": S(xgm_slow_data, "XGM (slow)")}

   return rich_output( tid,  **ydata,
                       title="XGM slow",
                       xlabel="train id",
                       ylabel="XGM slow  [uJ]",
                       max_points=2000)
```

The first line defines the kind and the name of the view. The next lines define the input into the function. The train ID is loaded from the meta data and the XGM data from karabo. Afterwards a rich_output is generated, which allows to define axis labels, title, curve labels and the number of shown points.

Oftentimes for monitoring data like the pulse energy, the output is not needed for every train, but it is rather desired to have the data over a longer time. Therefore, an average over several trains is useful, which can be implemented with a local average.

```
@View.Compute_LocalAverage(N=10, name="XGM/averaged_pulse_energy_vs_train_ID")
def xgm_slow_vs_trainId_avg(xgm: "view#XGM/pulse_energy_vs_train_ID"):
    """
    Parameters
    ----------
    xgm: view
        Output of view. View.values has shape (train ID, XGM value).

    Returns
    -------
    rich_output: rich_output
        Output to be displayed by the GUI.
    """
    return rich_output (  x=xgm.values[0],
                          y1=S(xgm.values[1],"XGM slow (averaged)"),
                          title =  "XGM slow  [uJ] (averaged)",
                          xlabel= "train id",
                          ylabel="XGM slow  [uJ]")
```

The first line now has the additional decorator "LocalAverage", where N defines over how many trains the average is computed. Here, N=10 means that the average is computed over 10 trains and thus output is generated every second. In the next line, as input now the output of the view defined above, which returns the XGM value as a function of train ID, is loaded. Finally, the rich_output is generated. An example of the averaged XGM value is shown in Fig. 3.3.

Similarly a global average can be calculated, which averages over all trains since the last reset of the respective plot.

3.4.2 APD signal

As already discussed in Section 3.3.2 the data for each APD separately is recorded per train and needs to be processed, e.g., to be split up into pulses. First, some parameters obtained from calibration

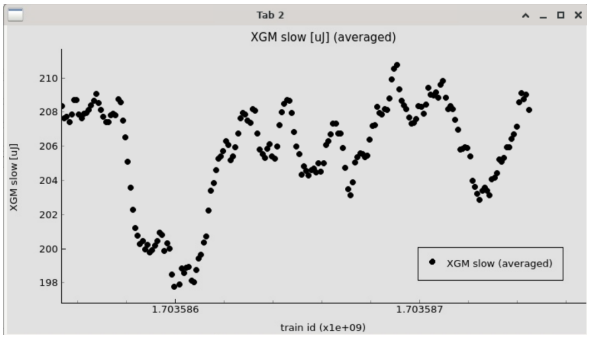

Figure 3.3: Screenshot of the online view showing the averaged XGM value vs train ID.

measurements (see Section 3.6.2) are set

```
parameters(data_per_ns_apd = 4,          #   data points per ns
           pulse_separation_ns = 440,   # separation of x-ray pulses in ns
            apd_xray_arrival_1A = -50 + 72978 + 23, # index at which the xray pulse arrives
            apd_xray_arrival_1C = -50 + 72978 + 26, # index at which the xray pulse arrives
            apd_xray_arrival_2A = -50 + 72978 + 0, # index at which the xray pulse arrives
            apd_xray_arrival_3A = -50 + 72978 + 9, # index at which the xray pulse arrives
            apd_xray_arrival_3C = -50 + 72978 + 14, # index at which the xray pulse arrives
            threshold_apd = 200, # values below threshold is considered noise and set to 0
            )
```

Those parameters define the number of datasamples per ns (data is recorded with 0.25 ns resolution), pulse separation between two pulses within one train, and the arrival times of the first pulse in a train in the respective APD. Those parameters are used to split the APD signal into individual pulses. In addition, the threshold under which data is considered noise is set. The index, at which the first x-ray pulse arrives is artificially shifted by 50 datasamples, which is equivalent to 12.5 ns, such that the x-ray pulses do not arrive at t=0 but t=12.5 ns when being viewed. This is useful for integration over the prompt pulse.

Afterwards, a function is defined, which is evaluated for every train and processes the APD data. The function is explained step by step in the following. First, the analog voltage output of each APD, which was digitalized using an ADQ412, is loaded from karabo. Here, each channel corresponds to one APD. In addition, the number of pulses in the train is loaded from another view.

```
def split_pulses(   ch1A_raw2: "karabo#MID_EXP_ADQ/ADC/ADQ412:network[digitizers.
    channel_1_A.raw.samples]",
                    ch1C_raw2: "karabo#MID_EXP_ADQ/ADC/ADQ412:network[digitizers.
                        channel_1_C.raw.samples]",
                    ch2A_raw2: "karabo#MID_EXP_ADQ/ADC/ADQ412:network[digitizers.
                        channel_2_A.raw.samples]",
                    ch3A_raw2: "karabo#MID_EXP_ADQ/ADC/ADQ412:network[digitizers.
                        channel_3_A.raw.samples]",
                    ch3C_raw2: "karabo#MID_EXP_ADQ/ADC/ADQ412:network[digitizers.
                        channel_3_C.raw.samples]",
                    nPulses : "view#PULSES/npulses_vs_trainID"):
    """
    Parameters
    ----------
    ch*_raw: list
        List containing voltage trace of respective APD.
    nPulses: int
        Number of pulses in train.

    Returns
    -------
    data_list: array
        APD data in shape (APD ID, pulse ID, time).
    """
     lastPulse = nPulses.values[1] # number of last pulse in train

     # data structure changed for proposal p8006 and traces have now shape (datasamples, 1)
         . To reuse subsequent code, reshape data to former format (datasamples)
     ch1A_raw = np.copy(ch1A_raw2[:,0])
     ch1C_raw = np.copy(ch1C_raw2[:,0])
     ch2A_raw = np.copy(ch2A_raw2[:,0])
     ch3A_raw = np.copy(ch3A_raw2[:,0])
     ch3C_raw = np.copy(ch3C_raw2[:,0])
```

Next, the data is cut shortly before the first x-ray pulse of the train arrives. Afterwards, for all APDs the first x-ray pulse of a train arrives at the same time. For better handling of the cut traces, they

are all cut to the same length. The cutting in addition significantly reduces the data because only those parts of the APD trace where an x-ray pulse arrived are considered.

```
# get the maximum XFEL pulse arrival time from the four channels
maximum = max(apd_xray_arrival_1A, apd_xray_arrival_1C, apd_xray_arrival_2A,
    apd_xray_arrival_3A ,apd_xray_arrival_3C)

# cut all channel data such that the x-ray pulse arrives at array element 0 and that
    all arrays have the same length
ch1A = ch1A_raw[apd_xray_arrival_1A:-(maximum-apd_xray_arrival_1A+1)]
ch1C = ch1C_raw[apd_xray_arrival_1C:-(maximum-apd_xray_arrival_1C+1)]
ch2A = ch2A_raw[apd_xray_arrival_2A:-(maximum-apd_xray_arrival_2A+1)]
ch3A = ch3A_raw[apd_xray_arrival_3A:-(maximum-apd_xray_arrival_3A+1)]
ch3C = ch3C_raw[apd_xray_arrival_3C:-(maximum-apd_xray_arrival_3C+1)]
```

Naturally, the APD has some defined positive voltage as the null line. Every arriving photon reduces this baseline by a fixed amount, which represents the recorded signal. For better handling of the data afterwards, the null line is shifted onto zero by subtracting the mean value before the first x-ray pulse arrival. Furthermore, the signal is inverted subsequently. As a result, every arriving photon now leaves a roughly Gaussian peak on a roughly zero baseline.

```
# get an offset value for the channel as mean over many array elements before the
    arrival time
avg_start = -1000
avg_stop = -500

offset_1A = int(np.mean(ch1A_raw[apd_xray_arrival_1A+avg_start:apd_xray_arrival_1A+
    avg_stop]))
offset_1C = int(np.mean(ch1C_raw[apd_xray_arrival_1C+avg_start:apd_xray_arrival_1C+
    avg_stop]))
offset_2A = int(np.mean(ch2A_raw[apd_xray_arrival_2A+avg_start:apd_xray_arrival_2A+
    avg_stop]))
offset_3A = int(np.mean(ch3A_raw[apd_xray_arrival_3A+avg_start:apd_xray_arrival_3A+
    avg_stop]))
offset_3C = int(np.mean(ch3C_raw[apd_xray_arrival_3C+avg_start:apd_xray_arrival_3C+
    avg_stop]))

# correct the channels for the offsets
ch1A -= offset_1A
ch1C -= offset_1C
ch2A -= offset_2A
ch3A -= offset_3A
ch3C -= offset_3C

# combine into one list and invert signal
apds = [-ch1A, -ch1C, -ch2A, -ch3A, -ch3C]
```

Finally, the long train-spanning voltage trace is cut into separate parts for every pulse in the train.

```
data_list = []
for i in range(5):
    apd = apds[i]
    # determine how many pulses are available in the data
    num_pulse = int (np.shape(apd)[0] // (pulse_separation_ns * data_per_ns_apd))
    # do not use more pulses than in the data OR than deliverd by XFEL
    num_pulse = min(num_pulse, lastPulse+1) ## +1 due to pulses counting from 0

    # split the APD trace into individual pulses
    # if less pulses are desired, then manually change here
    pulses = []
    for pulse_idx in range(num_pulse):
        start_idx = int (pulse_idx * pulse_separation_ns * data_per_ns_apd)
        stop_idx = start_idx + int(pulse_separation_ns) * data_per_ns_apd
        data = apd[start_idx:stop_idx]
        # bin to 1ns
        data = data.reshape(-1,data_per_ns_apd).mean(axis=1)
        # save data
        pulses.append(data)

    data_list.append(pulses)
# return the data array, shape is (APD ID, pulse ID, time)
return np.array(data_list)
```

The list with shape (APD ID, pulse ID, time) is returned. In this shape, the APD data can now be live analyzed. One possibility is to sum over all pulses and APDs and have a GlobalAverage to display the live time spectrum. Another possibility is to integrate over specific regions of interest in the time domain to discriminate the unscattered prompt pulse, which is artificially shifted to be at around 12.5 ns, and the resonant delayed signal after the prompt pulse. Both signals can be monitored as a function of time or can be used as signal for motor scans to align components (see Section 3.4.3). In the online analysis it is not possible to extract arrival times from the voltage traces because the

analysis is too complicated (see Section 3.6.4). Instead the voltage traces themself are analyzed, which is a good representation of the actually detected photons and sufficient for live online analysis.

3.4.3 Motor scans

The MID beamline is equipped with a scantool called *karabacon* [Eurc] to perform motor scans, which can display a signal of interest against the motor position and do limited arithmetics. However, at the beginning of our experiments, the scantool was not capable of matching the data according to their train ID and could not bin together the signals at equal motor positions. The latter has only become available recently. Thus, the scantool is useful for rough alignment scans, but not for fine alignment, where properly matching data and binning is needed. Furthermore, some motor scans are performed with the resonant photons recorded with the APDs. As discussed in Section 3.4.2, this data needs extensive processing, which until now is not possible in the scantool. Therefore, motor scans could only be analyzed once they are finished and the data is migrated to the offline cluster, which leads to a waiting time of a few minutes. Because this severely restricts the experimental progress, together with the data analysis team of the European XFEL a motor scan view in the online analysis was developed.

The heart of the motor scans is a routine, which automatically detects, which motors are currently scanned. First, the motor position is loaded from karabo for all motors. This can be the actual, target or encoder position of the motor. For simplicity, in the example code only two motors are loaded. In addition, the karabacon configuration, i.e., scan tool configuration, is loaded from karabo.

```
 @View.Compute(hidden=True)
def motor(tid: "internal#train_id",
    ## motors
    exp_r1 : "karabo#MID_EXP_UPP/MOTOR/R1.actualPosition.value"=None,
    exp_r2 : "karabo#MID_EXP_UPP/MOTOR/R2.actualPosition.value"=None,
    ## karabacon
    config: "karabo#MID_RR_SYS/MDL/KARABACON.actualConfiguration.value"=None,
    ):
    """
    Parameters
    ----------
    exp_r1/2: float
        Motor position of respective motor
    config: string
        The scan configuration.

    Returns
    -------
    result: list
        List of scanned motors with tuples of shape (motor name, motor position)
    """
```

Next, from the karabacon configuration the scanned motors are read. Again, for simplicity only two motors are included.

```
    # only proceed if valid karabacon config is found
    if config!=None:
        # get moving motor list from karabacon status
        motors = [m.split(":")[0] for m in eval(config.split("---")[1].strip("Motors: "))]
        # assign motors names according to this list
        dict = {
            'MID_EXP_UPP/MOTOR/R1' : exp_r1,
            'MID_EXP_UPP/MOTOR/R2' : exp_r2,
            }

        number_of_configured_motors = len(motors)
```

Finally, for each configured motor, the motor data defined in the beginning is read and appended to the result, which is returned. For consistency in the code, the number or returned motors is always equal to a predefined `max_number_of_motors`. If less motors are scanned, the first motor is appended at the end to fill up to the desired number.

```
        result = [(motors[i], dict[motors[i]]) for i in range(number_of_configured_motors)]
        for i in range(max_number_of_motors - number_of_configured_motors):
            result.append((motors[0], dict[motors[0]]))

        return result
```

For every train, the above described function returns a list of tuples (name, motor position) with length `max_number_of_motors`, which can be used by other views.

For example, for all motors in the list, we can display the motor position as a function of the train ID, i.e., as a function of time.

```
for i in range(max_number_of_motors): # loop over list of motors
    @View.Compute(name=f"XX_scan/motor_{i+1}_vs_trainId")
    def motor_position(tid: "internal#train_id", motorArray: "view#motor", i=i):
        """
        Parameters
        ----------
        tid: int
            train ID
        motorArray: list
            List of scanned motors tuples (name, value).
        i: int
            Index of scanned motor

        Returns
        -------
        rich_output
            Output to be displayed by the GUI.
        """
        data = motorArray[i]
        return rich_output(x=tid, y1=data[1],
                           title=f"position of motor {i+1}: {data[0]}",
                           xlabel="Train ID", ylabel="position",
                           max_points=600)
```

This view loads the train ID and the data from the function `motor` and views the motor position as a function of the train ID. In addition, the name of the i-th motor is displayed.

As an example for a motor scan the data of one of the two diodes is shown against the motor position.

```
    @View.Compute(name=f"XX_scan/diode1_vs_motor{i+1}")
    def diode1_vs_motor(motorArray: "view#motor", photon_counts: "view#DIODES/
        diode1_vs_trainId", i=i):
        """
        Parameters
        ----------
        motorArray: list
            List of scanned motors tuples (name, value).
        photon_counts: view
            Output of view showing diode 1. view.data has shape (train ID, value of diode
                1).
        i: int
            Index of scanned motor
        """

        data = motorArray[i]
        return rich_output(x=data[1], y1=photon_counts.data[1],
                           title=f"Diode 1 intensity vs motor position {i+1}: {data[0]}",
                           xlabel="Motor position", ylabel="Intensity")
```

Again the motor data is loaded from the function `motor`. The data of diode 1 is loaded from a preloading view, which shows the value of diode 1 as a function of the train ID. To bin y-data according to values of x-data, the data analysis group implemented an additional analysis method in extra-foam's MID special suite Correlator. Instead of the data of diode 1, any other processed detector data returning one value per train can be used.

With this implementation, proper motor scans with correct train matching and binning are now possible. In addition, processed data like the APD data with prompt or delayed integration ROI can be used in the real-time display of motor scans.

3.4.4 Online analysis of ^{57}Fe-experiments

The complete online analysis implemented for the ^{57}Fe experiments is represented by the flowchart in Fig. 3.4. The blue boxes represent the input coming from the data acquisition system karabo.

Some of this data is processed in the gray boxes. The splitting into pulses for the APD signal as well as the moving motor detection routine were already discussed above. By integrating the APD signal over different regions of interest in time, a measure for the prompt, the delayed and the total counts can be received. To receive one value per train from the Mössbauer drive, a linear slope is fitted to the voltage trace of a train. From this fit the Mössbauer detuning for each pulse in the train is read off.

There are different kind of views. The most standard one is to monitor the respective signal as a function of train ID, which effectively provides the signal as a function of real time. Oftentimes, this signal is not required to update with 10 Hz, such that a local average over typically 10 trains is

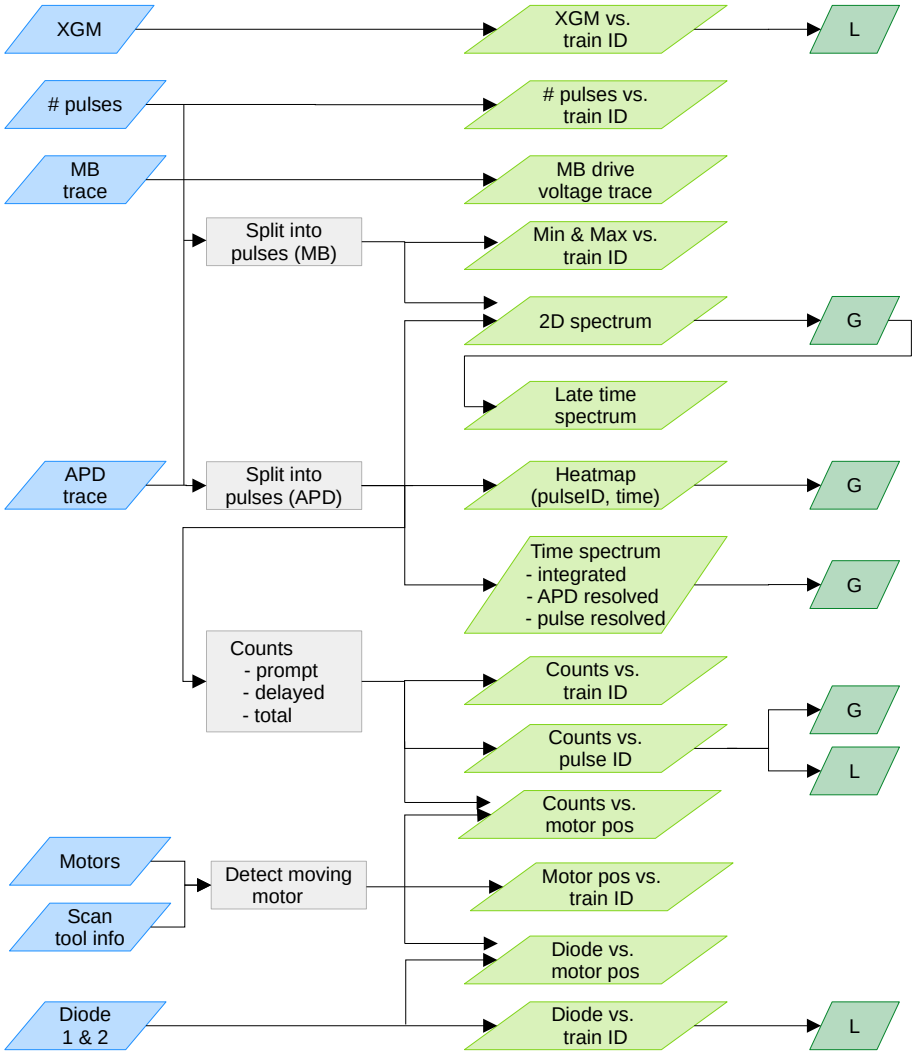

Figure 3.4: Flowchart of the online analysis for ^{57}Fe experiments. The blue rhomboids indicate input coming from karabo for every train. The gray rectangles represent processing of data and the green rhomboids the available views. Light green rhomboids indicate principle views, the dark green local (L) or global (G) averages of these. Details are in the main text.

applied. The other standard view is some detector signal as a function of motor position. Besides this, there are some special views involving the APD signal. First and foremost, the time spectrum can be calculated per APD as well as per pulse ID, or fully integrated. In addition, ROIs can be dynamically defined to integrate the APD signal in the prompt pulse and delayed signal regions. This forms a measure for the number of photons in the respective regions, which is primarily used for motor scans with the APDs. Additionally, it is used to monitor the count rate over real time and as a function of pulse ID. Furthermore, a heatmap showing the APD trace as a function of pulse ID and time after excitation is generated. For the Mössbauer drive, the voltage trace per train can be shown and the mininmum and maximum per train. Combining the information from the APDs and the Mössbauer drive, a time-energy spectrum can be generated, from which, by integration over late times, a late time spectrum (see Section 2.1.3) can be generated.

3.4.5 Online analysis of ^{45}Sc-experiments

Similarly, the online analysis for the ^{45}Sc experiments is illustrated in Fig. 3.5. Again, blue rhomboids represent input from karabo while light green rhomboids show the possible views with potential averaging indicated in dark green. Gray boxes indicate data processing for the more complex data.

As in the experiment for ^{57}Fe, most views are monitoring data as a function of real time. In addition to the discussed views in Section 3.4.4, here also the machine energy, which can provide

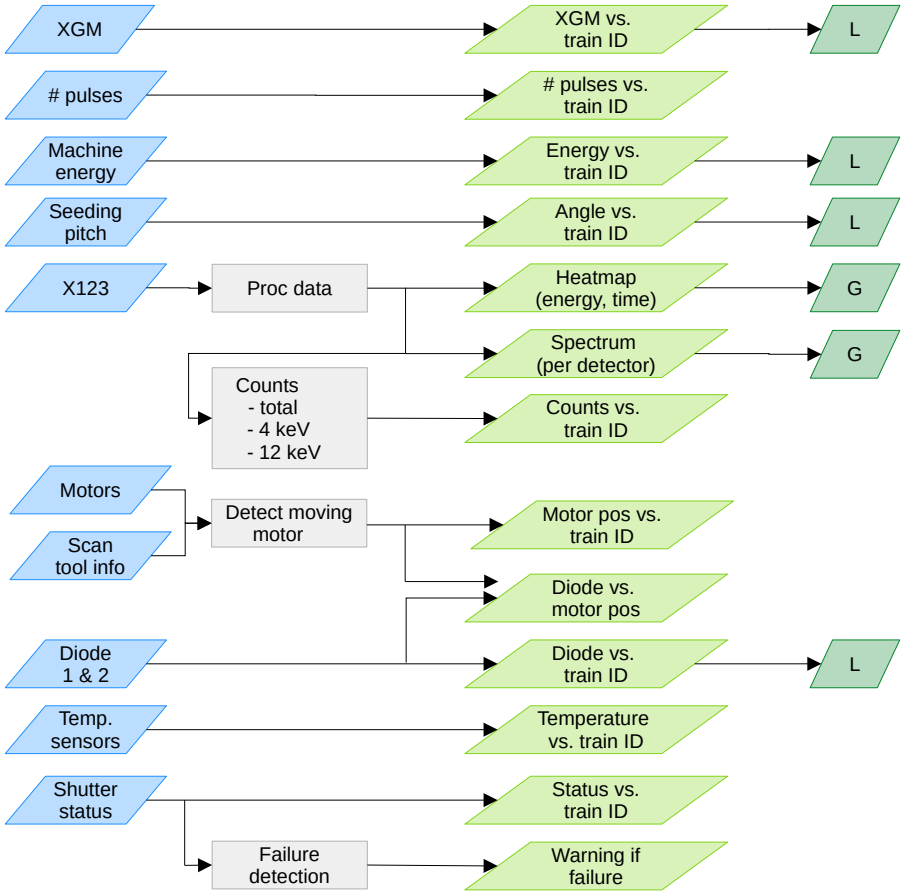

Figure 3.5: Flowchart of the online analysis for ^{45}Sc experiments. The blue rhomboids indicate input coming from karabo for every train. The gray rectangles processing of data and the green rhomboids the available views. Light green rhomboids indicate principle views, the dark green local (L) or global (G) averages of these. Details are in the main text.

the users control over the photon energy, the seeding pitch angle, and two temperature sensors are monitored. The data of the X123 detectors is first processed to provide the energy channel and time after excitation of each detected photon. This can be viewed as a histogram. Furthermore, from the processed data, the number of counts in the fluorescence region around 4 keV and the nuclear signal around 12.4 keV can be determined and monitored. The data processing of this detector is explained in more detail in Section 3.5.3. Finally, the experimental setup contains several shutters running with 10 Hz, whose functionality is very crucial especially to protect the NFS detector directly in the beam. Therefore, for each shutter the status value is returned and can be monitored. Furthermore, failures are detected by comparing the shutter status value to a threshold, thus creating boolean information on the state. Unfortunately, in extra-foam, currently no feature to trigger an alarm based on a boolean is implemented. However, returning the maximum over all trains of a view since the last reset of this observable (similar to the global average), it can be captured whether a failure occurred since the last reset. If a detector failure is detected, this triggers a visual alarm in form of an orange-yellow blinking window.

3.5 Data And Metadata iNspection Interactive Thing (DAMNIT)

The *Data And Metadata iNspection Interactive Thing* in short *DAMNIT* [EuXa] is a tool developed by European XFEL's data analysis group. It automatically calculates predefined *Variables*, whenever the data of a new run arrives at the offline cluster, and stores the computed data in a table with one row per run. These variables can be anything, e.g., the XGM mean pulse energy, the center of the

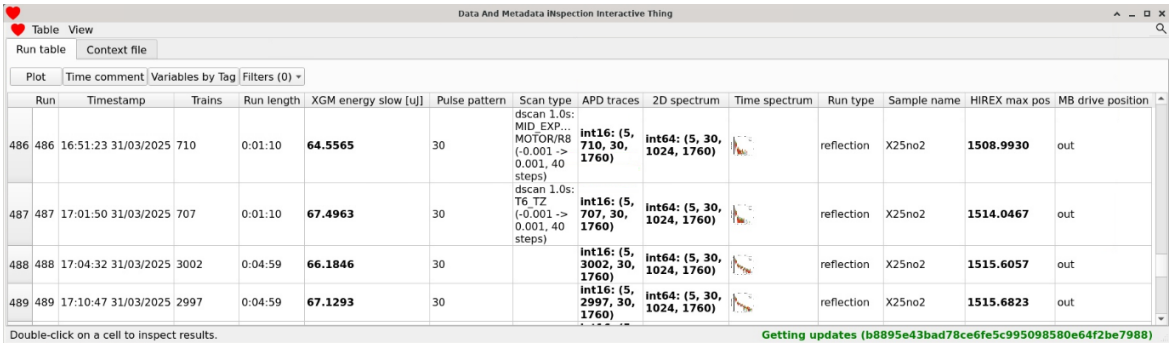

Figure 3.6: Screenshot of part of the table generated with DAMNIT for the latest ^{57}Fe-experiment p8006 [57F25]. Displayed are the run number, the time stamp of the run, the number of trains, the run length, the xgm pulse energy averaged over each train, the number of pulses, the scan type if a scan was performed, the data of the APD signal, the data of the Energy-Time spectrum, a figure containing the time spectrum, the run type and sample type read from the metadata, the seeding peak position and whether the Mössbauer drive is in or out. Values printed in bold font are summary values of the respective data indicating that the underlying data is more complex than a single float or string. For more details on the respective variables see Section 3.5.4.

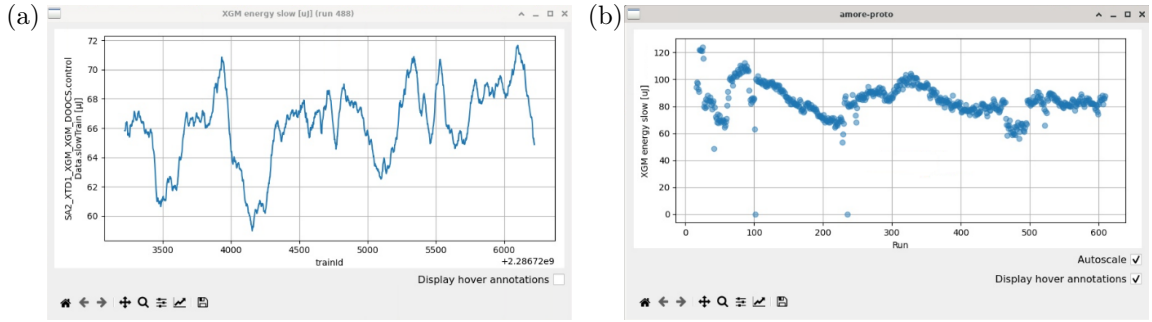

Figure 3.7: Screenshots of XGM data in DAMNIT for the latest ^{57}Fe-experiment p8006 [57F25]. (a) XGM averaged over train vs train ID for a single run. (b) XGM averaged over run vs run number.

seeding peak, certain motor positions or more complex processed data. An example used in the latest ^{57}Fe-experiment p8006 [57F25] is shown in Fig. 3.6.

3.5.1 Principal functionality

To illustrate the principal functionality, like in the online analysis, the data of the XGM is used. A variable can simply be defined by a python function.

```
@Variable(title="XGM energy slow [uJ]", summary="mean", tags = ["Beam"])
def xgm_energy_slow(run):
    """
    Parameters
    ----------
    run: run object
        Run for which the varibale should be computed.

    returns
    -------
    xgm_values : xarray
        Xarray of shape (train ID, xgm average over train).
    """
    xgm_values = run["SA2_XTD1_XGM/XGM/DOOCS", "controlData.slowTrain"].xarray()
    return xgm_valus
```

The function returns the slow XGM value per train and is decorated by a decorator `@Variable`, which specifies the name of the variable as is appears in the table. Oftentimes, the resulting value is not a single number per run. In this case it is useful to specify a summary, which is displayed in the table. Here, the summary is set as mean value over all trains. Such values, which are represend by a summary value in the table are printed in bold font. In addition, tags can be set to a function and in the GUI the tags to be shown can be selected.

In Fig. 3.7(a), the resulting XGM value averaged over one train is displayed against the train number exemplarily for one run. These figures can be simply generated by double-clicking on the respective cell of the table. Furthermore, the GUI allows to view the cell values - may they be single floats or summary values - as a function of the run number. As an example, in Fig. 3.7(b) the mean XGM value of a run is shown for all runs in the proposal.

3.5.2 APD signal

As discussed in Section 3.4.2, the APD data has to be processed to have pulse-resolved information, which typically takes a few minutes for a run acquired over ten minutes. Using DAMNIT this processing can be done automatically for every new run, thus making the processed data readily available for data analysis as fast as possible and reducing waiting time until decisions based on the data can be made. The processing is performed analogously to the one in the online analysis and is explained in the following.

First, the run is loaded. Sometimes it happens, that some source misses data for a specific train. In order to align the data per train properly, the function `run.select()` provides the functionality to only load trains in which all instruments of a specified list have data. Here, `full_selection` contains all relevant measurement devices for the experiment.

```
@Variable(title="APD traces", cluster=True, tags = ["Delayed photons"])
def APD_traces(run, run_idx:"meta#run_number", num_pulses:"var#n_pulses"):
    """
    Function to load all APD data of one train already splitted into one trace per x-ray
        pulse.

    Parameters
    ----------
    run: XFEL run data
        The loaded run.
    run_idx: int
        Number of run, from which the APD trace is taken.
    num_pulses: int
        The number of x-ray pulses in each train loaded from function n_pulses.

    Returns
    -------
    data_list_all_chunks: list
        List containing the APD data information. Format is (APD ID, train ID, pulse ID,
            time).
    """
    run = run.select(full_selection, require_all=True)
    data_list_all_chunks = []

    pulses_per_train = num_pulses
```

Note, that in the decorator the `cluster` variable is set to `True`, which results in this computation being performed on the offline cluster, reducing the analysis time significantly. No summary is specified, such that the default one, which is the shape, is returned. Next, the APD data is analyzed. To not load too much data at the same time, the data is loaded in chunks of at most 1000 trains. Here, the baseline correction (`baselineCorrection`) and splitting into pulses (`split_pulses`) are separated into two functions, but together they are equivalent to the function discussed in Section 3.4.2. Finally, the data is reordered into the desired shape and returned

```
    # do analysis for chunks of at most 1000 trains
    sel_split = run.split_trains(trains_per_part=1000)
    for sel_part in sel_split:
        data_list = []
        for k in range(5): # loop over all apds
            # apd has dimensions [train id, time]
            apd = sel_part[detectorPathAPDs, detectorsAPDs[k]].ndarray()

            # apply baseline correction
            apd = baselineCorrection(apd)

            # split the apd traces
            pulses = split_pulses(apd, apdID= k, pulses_per_train = pulses_per_train,
                run_idx = run_idx)
            data_list.append(np.array(pulses))

        # reordering of indices
        data_list = np.einsum('aijk->jaik', np.array(data_list))

        if len(data_list_all_chunks) == 0:
            data_list_all_chunks = data_list
        else:
```

```
            data_list_all_chunks = np.concatenate( (data_list_all_chunks, data_list ) )

    # reordering of indices
    data_list_all_chunks = np.einsum('jaik->ajik', np.array(data_list_all_chunks))
    return data_list_all_chunks
```

This processed and saved data now allows quick access to the APD signal on a per pulse basis.

3.5.3 X123 signal counts

For the X123 detectors a very useful variable to have in the table is the number of signal photons, i.e., photons within a specific energy region of interest. This number is computed automatically, such that the number of signal photons is easily accessible for monitoring, e.g., whether the XFEL beam is still on resonance.

Three equivalent detectors were used in the experiment placed upstream and downstream of the moving ^{45}Sc-foil to measure the fluorescence and downstream of a static ^{45}Sc-foil to measure nuclear forward scattering (c.f. Fig. 3.2). The data analysis will be explained exemplarily for the upstream detector. In addition, as already mentioned in Section 3.3.2, the X123 detectors can be run in two different modi. One just returns the spectrum after a certain measurement time, the other one returns time and energy information for each photon for every train. The latter mode was used in the last ^{45}Sc-experiment p6536 [45S24] and the respective analysis in DAMNIT to get the number of signal photons is presented in the following.

First, the raw data of the detector is loaded. The time information is stored by a least significant bit b_{ls} continuously running from 0 to `least_bits`$=2^{16}$ and a most significant bit b_{ms} counting up by one every time the most significant bit has reached 2^{16}. Both values are given in μs and set to zero by the train trigger. Thus the time after train-arrival is given by

$$t = \left(b_{\mathrm{ms}} \cdot 2^{16} + b_{\mathrm{ls}}\right) \mu\mathrm{s}\,. \tag{3.1}$$

After loading the data, the time is converted from least and most significant bit into time in μs and stored in a list together with the amplitude information.

```
@Variable(title="D_up total data", summary="mean")
def D_up_raw_data(run):
    """
    Parameters
    ----------
    run: XFEL run data
        The loaded run.

    Returns
    -------
    merged: list
        List of tuples (time, amplitude) containing all recorded photons within run.
    """
    time_least = run["MID_EXP_UPP/DET/SDD_DETECTOR-1:daqListOutput", 'data.timeTag'].
        ndarray().astype(int)
    time_most = run["MID_EXP_UPP/DET/SDD_DETECTOR-1:daqListOutput", 'data.timeTagMsb'].
        ndarray().astype(int)
    amplitude = run["MID_EXP_UPP/DET/SDD_DETECTOR-1:daqListOutput", 'data.amplitude'].
        ndarray().astype(int)

    merged_list = []
    for i in range(len(amplitude)):
        time = np.array(time_most[i])*least_bits + np.array(time_least[i])
        amplitudes_train = np.asarray(amplitude[i])
        for j in range(len(time)):
            merged_list.append((time[j], amplitudes_train[j]))

    merged = np.array(merged_list)
    return merged
```

Next, the raw data is cut to the data within the region of interest (ROI) around 4 keV, in which the fluorescence photons of scandium are expected (see Section 2.1.2). The lower (upper) limit is set in `D1_4keV[0]` (`D1_4keV[1]`). Only tuples for which the amplitude, i.e., photon energy, is within these bounds and the time is larger than a threshold of 15 ms for background suppression, are returned.

```
@Variable(title="D_up 4keV data", summary="mean")
def D_up_4keV_data(run, merged_list: "var#D_up_raw_data"):
    """
    Parameters
    ----------
    run: XFEL run data
```

```
        The loaded run.
    merged_list : list
        List containing photon events in shape (time, amplitude).

    Returns
    -------
    list_roi: list
        List of tuples (time, amplitude) containing only photons wihtin energy ROI.
    """
    list_roi = []

    t_thresh = 15000
    list_roi = []
    for i in range(len(merged_list)):
        t, A = merged_list[i]
        if (A>=D1_4keV[0]) and (A<=D1_4keV[1]) and (t>t_thresh):
            list_roi.append((t, A))

    return list_roi
```

Finally, the number of signal photons in the fluorescence ROI around 4 keV, measured with the upstream detector, is simply given by the length of the data array within the ROI.

```
@Variable(title="D_up 4keV counts")
def D_up_4keV_counts(run, merged: "var#D_up_4keV_data"):
    """
    Parameters
    ----------
    run: XFEL run data
        The loaded run.
    merged : list
        List containing photon events in the 4keV ROI. Shape is (time, amplitude).

    Returns
    -------
    counts: int
        Number of counts within 4keV ROI.
    """
    counts = np.shape(merged)[0]
    return counts
```

Similarly, the number of signal photons in the 12.4 keV region and for the downstream detector can be calculated.

3.5.4 DAMNIT variables for ^{57}Fe-experiments

The above discussed examples are only a small part of all variables implemented in DAMNIT for the experiments with ^{57}Fe. A comprehensive list of variables implemented for those experiments as used in beamtime p8006 is given in Table 3.1. The different categories are shortly discussed in the following.

General. The general variables contain information about the measurement, such as number of trains and pulses as well as the duration of the run and the size of the total collected data of the run. In addition, if a motor scan was performed, the most important scan information, i.e., name of scanned motor, scan range and number of steps, are given. Furthermore, the run and sample type are read from the meta data of the run.

Beam. The beam variables contain information about the XFEL beam. The HIREX spectrum and maximum position give information about the spectral properties, the XGM energies about the integrated pulse energy. The two variables pulses and pulse pattern tell which pulses in the train are sent to the experiment. The transmission, according to optional attenuators through different parts of the beamline upstream of the experiment between the undulator and the experimental hutch [Mad+21], is given in the transmission variables.

Delayed photons. The delayed photons variables are all based on the processing of the APD traces, which is the key part of this category. In addition, the data of the Mössbauer drive is processed. On one hand, whether the Mössbauer drive is in the beam or not, and on the other hand, the Mössbauer detuning for each pulse. Using the Mössbauer and APD data, an energy-time-spectrum can be generated. Another important information is an estimate for the number of resonant photons. This is calculated by the area under the APD traces summer over all trains and pulses. It can be approximately normalized after determining the single-photon area as in Section 3.6.4. This number can then be compared with a predefined number of wanted counts. Finally, DAMNIT can also provide figures. For the ^{57}Fe experiments, the two most important ones are a time spectrum, i.e.,

	name	summary	description
General	Trains	–	Number of trains in run
	Run length	–	Duration of run
	Data size [TB]	–	Data size (raw and proc combined) of run
	Scan type	–	If motor scan was performed, information about which motor, scan range and number of steps.
	Run type	–	Run type as specified in DAQ
	Sample name	–	Sample name as specified in DAQ
Beam	HIREX spectrum	mean	Spectrum of HIREX averaged over whole run
	HIREX max pos	mean	Pixel, where maximum of mean HIREX spectrum is
	XGM energy [μJ]	mean	Pulse energy measured with XGM, pulse resolved
	XGM energy slow [μJ]	mean	Pulse energy measured with XGM, averaged over train
	Pulses	–	Number of pulses per train
	Pulse pattern	sum	Pattern of which pulses within train are filled
	XTD1 transmission	mean	Transmission set by attenuators in beamline module XTD1
	XTD6 transmission	mean	Transmission set by attenuators in beamline module XTD6
	OPT transmission	mean	transmission set by attenuators in optics hutch
	total transmission	mean	Combined transmission through above elements
Delayed photons	APD traces	shape	Processed APD data in shape (APD ID, train ID, pulse ID, time)
	MB drive position	–	"In" or "out" depending on motor position
	MB detuning	shape	MB detuning per pulse in shape (pulse ID, train ID).
	2D spectrum	shape	Energy-Time spectrum integrated over all trains in shape (APD ID, pulse ID, detuning, time)
	Time spectrum	–	Plot of intensity vs time integrated over all pulses
	Fig 2D spectrum	–	Energy-Time spectrum integrated over all pulses and APDs

Table 3.1: Variables implemented in DAMNIT for the experiments with ^{57}Fe as used in the latest beamtime p8006. If no summary is stated, the variable returns a single value or a figure. Details on the variables are given in the main text.

intensity as a function of time after excitation, and the energy-time spectrum, i.e., a two-dimensional histogram with time and Mössbauer detuning on the x- and y-axis.

3.5.5 DAMNIT variables for ^{45}Sc-experiments

Also for the experiments with ^{45}Sc, the above discussed examples are only a small part of all variables implemented in DAMNIT and a comprehensive list of variables implemented for those experiments as used in the latest beamtime p6536 [45S24] is given in Table 3.2. The different categories are shortly discussed in the following.

General. The general variables contain information such as number of trains, duration of run and the size of the measured data. In addition, it is detected whether, and if so which, motors are moved. Furthermore, from the motor position, the NFS sample in the beam is read out.

Beam. The beam variables contain information about the XFEL beam as before, i.e., spectral information, pulse energy and number of pulses. In addition, the machine energy, which is the XFEL energy tuning knob partially available to the users, and the seeding angle, which mainly defines the energy of the seeding peak, are given.

X123. In the experiment three different X123 detectors (D_up, D_down and D_NFS) were used. They were all used in the same measurement mode such that the data processing is the same. For each of them the total data and number of counts, as well as the data and counts in two regions of interest, one around 4 keV and one around 12 keV, are determined. The exact procedure is described in Section 3.5.3.

	name	summary	description
General	Trains	–	Number of trains in run
	Run length	–	Duration of run
	Data size [TB]	–	Data size (raw data) of run
	Moving motors	–	Motor names of moving motors
	NFS sample	–	Name of NFS sample read from motor position
Beam	HIREX spectrum	mean	spectrum of HIREX averaged over whole run
	HIREX max pos	mean	Pixel, where maximum of mean HIREX spectrum is
	energy	mean	Machine energy
	seeding angle	mean	Pitch angle of seeding crystal
	XGM energy slow [μJ]	mean	Pulse energy measured with XGM, averaged over train
	Pulses	–	Number of pulses per train
X123	D_up total data	–	List of (time, amplitude) for recorded photons
	D_up total counts	–	Number of total recorded photons
	D_up 4keV data	–	List of (time, amplitude) for recorded photons around 4 keV
	D_up 4keV counts	–	Number of photons recorded around 4 keV
	D_up 12keV data	–	List of (time, amplitude) for recorded photons around 12 keV
	D_up 12keV counts	–	Number of photons recorded around 12 keV
	D_down total data	–	List of (time, amplitude) for recorded photons
	D_down total counts	–	Number of total recorded photons
	D_down 4keV data	–	List of (time, amplitude) for recorded photons around 4 keV
	D_down 4keV counts	–	Number of photons recorded around 4 keV
	D_down 12keV data	–	List of (time, amplitude) for recorded photons around 12 keV
	D_down 12keV counts	–	Number of photons recorded around 12 keV
	D_NFS total data	–	List of (time, amplitude) for recorded photons
	D_NFS total counts	–	Number of total recorded photons
	D_NFS 4keV data	–	List of (time, amplitude) for recorded photons around 4 keV
	D_NFS 4keV counts	–	Number of photons recorded around 4 keV
	D_NFS 12keV data	–	List of (time, amplitude) for recorded photons around 12 keV
	D_NFS 12keV counts	–	Number of photons recorded around 12 keV

Table 3.2: Variables implemented in DAMNIT for the experiments with ^{45}Sc as used in the latest beamtime p6536. If no summary is stated, the variable returns a single value or a figure. An exception of this is the X123 data. For the X123 data, none of the implemented summaries is meaningful, which is why they are also stated without summary. Details on the variables are given in the main text.

3.6 Near-online and offline analysis

The near-online and the offline analysis are essentially the same and both are based on standard jupyter notebooks. The only difference is that near-online refers to analysis of finished runs during the experiment, while offline refers to the potentially more complex analysis after the experiment. This section provides a few simple and generally necessary examples, which are a by far not complete list of analyses performed. All data-analyses in Chapters 4 to 6 are performed with those jupyter notebooks and provides further insights on what is possible.

3.6.1 Loading data

There are two options to read data. One option is to load the run data directly from the raw or processed data using the European XFEL library `EXtra-data` [EuXb], the other is reading from the data created by DAMNIT [EuXa]. In the data analysis both methods are used. If data exists in DAMNIT, the default is to read from this data. However, for some devices no DAMNIT data is created and the raw data is read.

One of the goals when developing the analysis pipeline presented in this chapter was to make it easily accessible for everyone without much preknowledge. In addition, the pipeline should be easy to update for new experiments, e.g., if data format or name of devices change. Note that name changes can in principle also be adapted for by defining aliases for the device names. To simplify the read-in of the data, in an additional python-file a customized class `RunData` is defined and all notebooks read-in data by using this class.

An instance `data` of this class is initialized and loads the most basic data by `RunData(run_number)` which is defined by the following code snippet.

```
from extra_data import open_run # load from raw data
from damnit import Damnit # load from damnit data
from dataclasses import dataclass # for class

@dataclass
class RunData:
    run_number: int
    n_trains: int
    n_pulses: int

    def __init__(o, run_number, fromDamnit=False):
        '''
        Initialize a RunData instance and load the basic run data.

        Parameters
        ----------
        run_number: int
            Number of the run.
        fromDamnit : boolean
            Load data from DAMNIT or raw data.

        Returns
        -------
        o: RunData
            Instance of the class RunData containing basic information (run number, number
                of trains, number of pulses) about the run.

        '''
        o.run_number = run_number
        db = Damnit(proposal_nr) # Load database
        df = db.table(with_titles=True) # convert into pandas dataframe

        if fromDamnit:
            o.n_trains = int(get_ds(run_number, "n_trains")) # number of trains
            o.n_pulses = get_ds(run_number, "n_pulses") # number of pulses
            o.energy =  get_ds(run_number, "energy") # photon energy
            o.xgm_slow = get_ds(run_number, "xgm_slow") # XGM averaged over train
        else:
            run = open_run(prop_num, run_number) # load run data
            run = run.select(full_selection, require_all=True) # only use trains, where all
                important devices have data
            o.n_trains = len(run.train_ids) # number of trains
            o.n_pulses = int(run["SA2_XTD1_XGM/XGM/DOOCS", pulseEnergy.
                numberOfBunchesActual'][0].ndarray()[0]) # number of pulses
```

Depending on `fromDamnit`, data can be either loaded from the DAMNIT database or the raw data by using the respective data specific reading functions. The `full_selection` again takes care of the train matching as in DAMNIT.

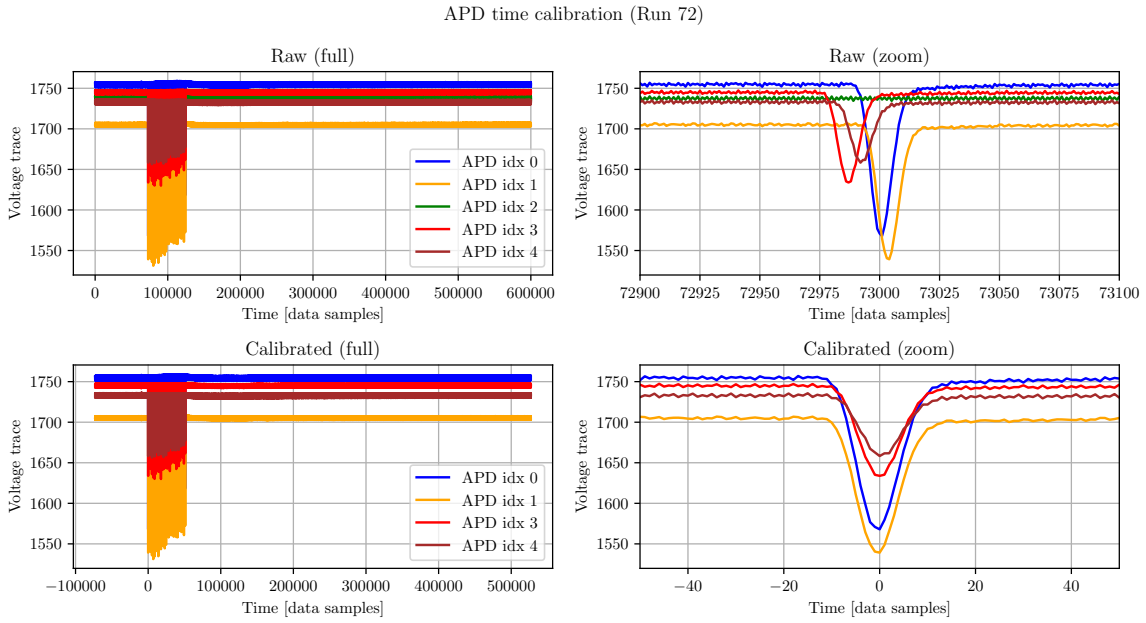

Figure 3.8: Time calibration of APD data during beamtime p8006. The raw data (top) and time calibrated APD trace (bottom) is shown for all used APDs in run 72. The left panels show the full trace, while the right ones are zoomed into the region of the first pulse in the train. The time axis is in datasamples with 4 samples per ns. The APD indices correspond to ADQ412 channels 1A, 1C, 2A, 3A, 3C. Note that the APD with idx 2 (green) was not in operation.

Usually not all data of a run has to be read in a specfic analysis. Therefore, reading the data is split into several topics, e.g., `read_run_data_APD` reading the processed APD data from DAMNIT into `data.apd`. That way a user using the jupyter notebooks in the analysis pipeline does not need to handle the reading of the data and can concentrate on their analysis.

3.6.2 Calibration of APD signal

Time calibration. To calibrate the time zero, at which the first pulse of the train arrives, for each APD the raw data trace averaged over all trains is loaded from the raw data for a run without sample in the beam. An example is shown in the top row of Fig. 3.8. On the left side, the full raw voltage trace for each APD is displayed. We can see the dips in the voltage traces, which correspond to the prompt pulse for each x-ray pulse in the train. The right panel is a zoom in to the first pulse in the train clearly showing the different time offsets for the different APDs. They are caused by slight differences in the cabling.

The local minima are searched for with `scipy.signal.find_peaks` in the inverted trace. Afterwards the positions of the minima are evaluated. From the mean distance, the pulse separation is determined, from the index of the first minimum the offset of each channel:

```
Calculated pulse separation: 1760.0 data samples
Calculated offset 1A: (72987 + 14) data samples
Calculated offset 1C: (72987 + 17) data samples
Calculated offset 2A: (72987 + None) data samples
Calculated offset 3A: (72987 + 0) data samples
Calculated offset 3C: (72987 + 5) data samples
```

Those calibrated pulse separation and offsets are used to split the APD traces over a whole train into the different pulses as explained in Section 3.4.2. The pulse separation corresponds to the set value of 440 ns. In the lower row in Fig. 3.8 the traces are shifted according to the respective offsets. As a result, the prompt pulse arrives at time channel 0 for all APDs. In order to have the prompt pulse fully in the APD trace for one shot, we artificially set the arrival of the prompt pulse to 12.5 ns. In further analysis, this is compensated for in the time spectra, but allows to also study the prompt pulse behavior easily.

Note, that for channel 2A, which in the experiment was used to detect incoherent scattering, no offset could be determined as this channels did not see photons in the analyzed run. It is set to the

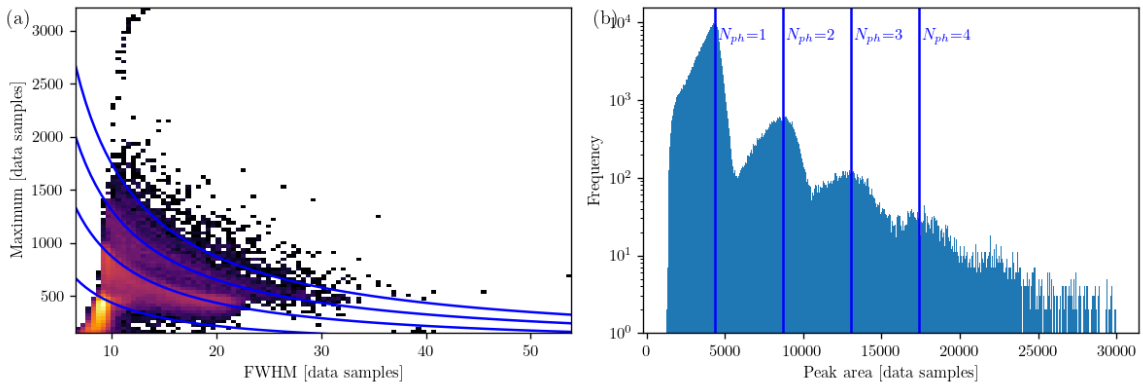

Figure 3.9: Analysis of single photon area in experiment p3334. (a) A two-dimensional histogram showing the peak heights and widths. (b) Histogram of the area under the traces within analysis ROI. For the analysis all data measured in the nuclear forwards scattering setting were used. The blue lines in both panels indicate n-times the single-photon area.

same as 3A, but was not used in the experiment afterwards.

Single photon area and peak analysis. The other important calibration is to find the characteristics of a single-photon peak, which is its width, height, and area. Because the APDs are all driven with slightly different high voltage and are not identical, this analysis is performed for each APD separately.

To gain high enough statistics, the APD data for several runs is loaded. Ideally, those runs should contain moderate photon numbers. If there are too many photons, the chances that more than ten photons arrive close to each other resulting in a pileup and a potential non-linear response of the APDs. If there are too few photons, the chances for seeing a few photon response and also the overall statistics are worse.

The peak analysis is performed for every pulse in the DAMNIT APD data (see Section 3.5.2). First, the background of the respective APD trace is corrected with a better baseline correction than the rough one in DAMNIT. If the count rate is small, it can be expected that photons at late times, i.e., after 400 ns, are extremely rare. Thus the average after 400 ns is subtracted as the baseline. Afterwards, the peaks in the trace are searched for in an iterative way, which is illustrated in the following pseudo-code.

```
trace = data.apd[apd ID, train ID, pulse ID, :]
maximum = maximum(trace)
max_pos = maximum_index(trace)
while maximum > threshold:
    trace_in_roi = roi(trace, max_pos, width)
    area = sum(trace_in_roi)
    peak_heights, peak_widths = find_peak_properties(trace_in_roi)
    trace[roi] = 0
    maximum = maximum(trace)
    max_pos = maximum_index(trace)
```

The maximum within the time range from 20 ns to 400 ns is searched for. Note, that in the processing of the APD traces in Section 3.5.2, the arrival time of the prompt pulse is set to 12.5 ns on purpose. If the maximum is higher than a previously defined threshold (typically 150 data samples) the peak analysis is started. If the maximum is lower than the threshold, the analysis for the respective trace is terminated and the next trace is analyzed. The analysis continues with finding the ROI around the maximum position, in which the signal is above a second threshold (typically 50 data samples) and maximally ±10 ns wide. Within this ROI, the area under the curve is determined by the sum over the trace in the ROI, and using `scipy.signal.find_peaks` and `scipy.signal.peak_widths` the peak is analyzed. Afterwards, the trace in the ROI is set to zeros and the analysis is continued with finding the maximum of the modified trace.

In Fig. 3.9, the results of the analysis are exemplarily shown for one APD. In panel (a) a two-dimensional histogram of the peak heights and widths is shown. The bright spot of single-photon peaks is clearly visible and corresponds to a height of 580 data samples and a full-width half-maximum (FWHM) of 9.4 data samples, which corresponds to 2.35 ns. For the two-photon events, a banana-like shape is visible as indicated by the second lowest of the blue lines, which represent points with

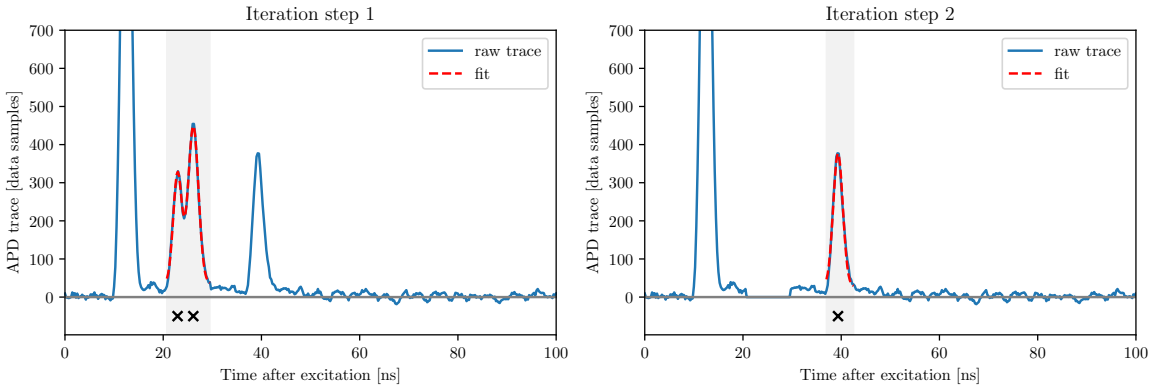

Figure 3.10: Example of photon arrival time reconstruction. In blue the raw trace is shown. The gray rectangle indicates the ROI around the maximum position. In this ROI the sum of several Gaussians is fitted, which is shown by the red dashed line, with the resulting arrival times marked by the black crosses. After the first iteration step, the respective ROI is set to zero and the analysis is continued with the modified trace. The shown trace is of APD 1 in run 444, train 20, pulse 11 in experiment p3334.

same area. It ranges from peaks with same FWHM, but double height, i.e., two photons at the same time, towards peaks with smaller heights close to the single-photon peak and about twice the FWHM, which represent double peaks of two photons arriving close to each other. Furthermore, the second "banana" of three-photon events is clearly visible. Panel (b) shows a histogram of the areas of the analyzed peaks. These areas are defined as the sum over the trace in the peak ROI. Clearly the single-, double- and triple-photon peaks are visible. The single-photon area is defined as the maximum position of the first peak. The blue lines indicate multiples of this, which clearly fits also the two-photon and three-photon peaks . These multiples of single-photon areas are also represented in panel (a) by the blue lines.

The same analysis is run for all APDs to characterize the respective single-photon peak.

3.6.3 Pseudo time spectra

One of the main tasks in the near-online analysis in the experiments with ^{57}Fe is to view and analyze time spectra, i.e., intensity as a function of time after excitation. In the near-online analysis during the experiment, those time spectra are generated by summing up the APD traces instead of creating an actual histogram of the photon arrival times for which a long preanalysis is needed (see Section 3.6.4). To distinguish the two kinds of time spectra, the former ones, where the APD traces are integrated, are referred to as *pseudo time spectrum*. For sufficient statistics, they represent the actual underlying time spectrum convoluted with the single-photon peak. They closely resemble the actual time spectra and provide a good fast alternative for near-online analysis.

To create such a pseudo time spectrum, the APD data is summed over all trains. Typically, the pulse ID and APD ID are kept as a dimension because of potential differences for different pulses in the train and APDs. The summed up time spectra in the shape of (APD ID, pulse ID, time [ns]) are saved for fast viewing and comparing of different runs. The summation can also be performed over several runs.

Afterwards, the precalculated time spectra can be further analyzed with prepared notebooks, e.g., for differences between different pulses. Besides, two time spectra can be compared to each other or can be fitted.

It is possible to normalize the pseudo time spectra by the single-photon area, such that the area under the trace gives an estimate for the number of photons. That way a rough uncertainty estimate can be made by taking the square root of the normalized intensity at every time $I(t) \pm \sqrt{I(t)}$. Note that this only works if the estimated photon number is high enough to have reasonable statistics in the spectrum.

3.6.4 Estimating photon arrival times

Extracting the photon arrival times from the APD trace is a difficult task especially for higher count rates. In [Chu+18] Chumakov et al. reconstruct the photon arrival times by fitting a sum of single-

photons responses to the detector traces. Here, a similar technique is applied.

Like for the peak analysis performed in Section 3.6.2, an analysis ROI is found. With the knowledge of the size of a single-photon area, the number of photons in the ROI can be estimated. For reliable results the fit function should not be ambiguous. Especially, if two Gaussians on top of each other are assumed, the fitting routine runs into problems. Therefore, before fitting the peak properties are analyzed with `scipy.signal.find_peaks`. If the photon number estimate indicates, that there are two photons in the ROI, at first the voltage trace is tried to be modelled with a double-Gaussian. If the peak property analysis results in two peaks, those properties are used as the initial fit conditions. If the peak property analysis found only one peak, the two peaks might be close to each other and as initial fit parameters the peak properties with slightly shifted times (± 2 ns) are used. It can happen, that the two photons arrive close to each other such that they do not produce a double-Gaussian profile. In this case the double-Gaussian fit fails and triggers the fitting of a single Gaussian. For more than two estimated photons in the ROI, in a similar way, the number of summed Gaussians is reduced stepwise if the fit fails. The automatic fitting is currently implemented for up to four photons within one ROI. Note that there can be several ROIs in one trace. For higher photon numbers, the photon number estimate is not precise enough and the fitting becomes to hard. Still, manual fitting might work in some cases. After one ROI is analyzed, the trace in this ROI is set to zero and the next peaks are searched for.

An example reconstruction is shown in Fig. 3.10. In the left panel, the raw trace is displayed in blue. As described before, a ROI around the maximum position is defined, which is marked by the gray rectangle. Depending on the photon number estimate in this ROI, the sum of several Gaussians is fitted giving the arrival times marked by the black crosses. Afterwards, the trace in the ROI is set to zero and the analysis is repeated as shown in the right panel.

The photon arrival time analysis is very robust for moderate count rates. For too high count rates, the dynamical range of the APDs is not large enough to have a linear response over the whole time range. In this case, especially at early times saturation effects might disturb the signal. More details on this are discussed for reflectivity measurements in Chapter 5, where for a few traces with many photons this is an issue. If saturation effects occur, the height of the voltage signal does not correspond linearly to the number of photons and the presented photon number estimate, which is required for the photon arrival estimate, does not work reliable anymore. In addition the fitting function becomes ambiguous. For most data, especially all nuclear forward scattering data from foils presented in this thesis, saturation problems do not play an important role and the photon arrival time estimate works fine.

Note that the photon arrival time estimate is a too complex analysis for the near-online analysis during the short time of the experiment, but a very crucial one for the more detailed analysis after the experiment. With this data, further analyses, like analyzing photon number distributions and creating actual time spectra, can be performed.

3.6.5 Near-online analysis for ^{45}Sc-experiments

Automatic update of resonance curve. For the resonance search in the first ^{45}Sc experiment [45S22] for every run, which had a duration of a few minutes, the incident photon energy was slightly changed. During the experiment the measurement mode, which provides only one spectrum at the end of each run, was used, which made an implementation into the online analysis with extra-foam as presented in Section 3.4 very tricky. In order to still see how the resonance curve slowly builds up over many hours, an automatically updating viewgraph was designed showing the most relevant data, i.e., the pulse energy, the signal photons and the signal photons normalized by the pulse energy as a function of run number and incident photon energy. The relevant jupyter notebook monitors the DAMNIT data folder and updates the graph automatically as soon as data from a new run is available.

This provides a "second online analysis" on slower time scales of hours instead of minutes and with the recorded run data. In addition, the decoupling from the online analysis ensures, that the view graphs are not cleared by accident while working with the online analysis.

A detailed review of the offline analysis of the first experiment is provided in Chapter 4.

Energy-Time information. In the second ^{45}Sc experiment [45S24], the X123 detectors provided not only energy, but also time information of the signal photons. Therefore, an important quality check of the data was made by plotting the energy-time information of each recorded photon. Signal photons should accumulate around 4 keV and 12 keV for the fluorescence and NFS signal, respectively,

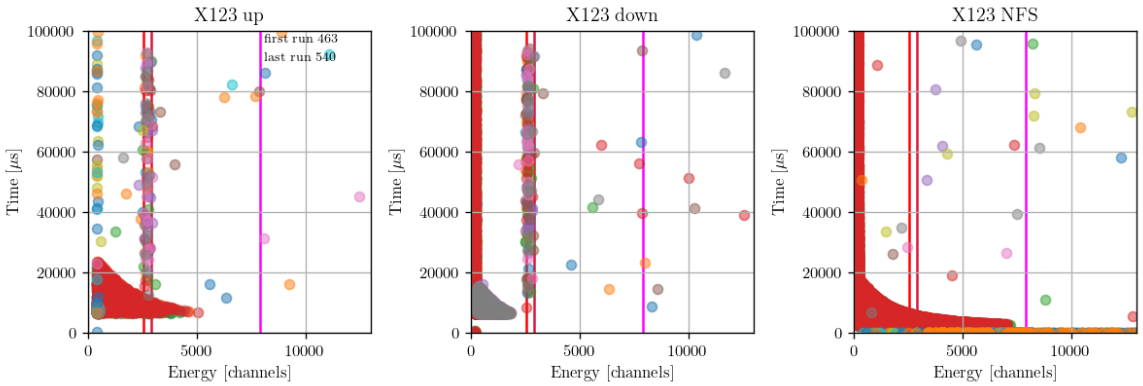

Figure 3.11: Example of Energy-Time information from the three X123 detectors in experiment p6536. The different colors indicate different runs. The energy channel where the K_α and K_β fluorescence lines are expected are indicated by the red vertical lines, the 12 keV NFS signal by the magenta line.

and should exceed the background. An example of such a plot is shown in Fig. 3.11. The triangle in the lower left corner is attributed to noise from the non-resonant light. The fluorescence signal can be clearly seen, the NFS signal is on the level of the background. In addition, the data can be integrated along the energy axis within a ROI for a rough estimate of the lifetime, and can be integrated along the time axis for spectral information. Such a signal count analysis is crucial for the decisions on which samples to measure.

3.7 Summary and outlook

Both experiment types using the Mössbauer isotopes ^{57}Fe and ^{45}Sc are non-standard experiments at the European XFEL and XFELs in general. Therefore, unlike at synchrotron radiation sources, no Mössbauer specific analysis was available. Together with the help of the data analysis group from the European XFEL we developed the data analysis for Mössbauer experiments at the European XFEL with ^{57}Fe and ^{45}Sc, which was essential for the success of the experiments.

At the European XFEL the data analysis is divided into three different categories. First, the online analysis is used for real-time analysis throughout the experiment. This includes motor scans, especially with processed data, which are crucial for alignment of the setup. Furthermore, the data quality, e.g., in form of a time spectrum or the number of resonant signal photons, can be investigated in real-time. A big difference as compared to synchrotrons experiments is the processing of the APD data due to the unique pulse structure at the European XFEL and the amount of photons in each shot. Second, there is the near-online analysis during the experiment, which is mainly used for inspection of recorded data and subsequent decision on how to proceed in the experiment. For example, this can be analyzing recorded time spectra in the ^{57}Fe-experiments or the number of signal photons in the ^{45}Sc-experiments. Lastly, there is the offline analysis, which is the detailed analysis after an experiment has been finished. Unless for synchrotron experiments, in which the determination of photon arrival times is simple due to observing none or one photon in most pulses, the photon arrival times at an XFEL have to be determined by fitting the voltage traces. A similar approach was also used in [Chu+18]. However, with the current setup, this approach only works if the photon numbers are not too high. For each of the three categories, examples for the developed standard analysis in the respective kind of experiment are given.

The developed data analysis focuses on the standard techniques used for the respective isotopes. Especially for ^{57}Fe time-spectra, energy spectra and energy-time-spectra are default measurements, that are well-established at synchrotron facilities. Therefore, analysis of these kinds of data is the key for many applications of Mössbauer science at synchrotrons, but in the future possibly also at XFELs. Furthermore, the modular structure of the workflow enables straightforward access to individual components and allows step-wise improvement, for instance by a more sophisticated photon arrival time reconstruction.

Chapter 4

Excitation of the ^{45}Sc nuclear clock transition

This chapter is contains the data evaluation for the main result in the following publication:

Resonant X-ray excitation of the nuclear clock isomer ^{45}Sc
Y. Shvyd'ko, R. Röhlsberger, O. Kocharovskaya, J. Evers, G. A. Geloni, P. Liu, D. Shu, A. Miceli, B. Stone, W. Hippler, B. Marx-Glowna, I. Uschmann, R. Loetzsch, O. Leupold, H.-C. Wille, I. Sergeev, M. Gerharz, X. Zhang, C. Grech, M. Guetg, V. Kocharyan, N. Kujala, S. Liu, W. Qin, A. Zozulya, J. Hallmann, U. Boesenberg, W. Jo, J. Möller, A. Rodriguez-Fernandez, M. Youssef, A. Madsen, and T. Kolodziej
Nature **622**, 471–475 (2023)

4.1 Motivation

The utmost precision of optical clocks [Blo+14] forms the basis of applications, such as measurements of the gravitational redshift [Bot+22] or variation of fundamental constants [Ros+08].

Nuclear clock transitions have several potential benefits over optical clock transitions [PO15]. Smaller systematic frequency shifts are expected due to shielding by the electronic shell. Possible operation in solid state and thus large ensembles of emitters as well as the higher frequency are expected to increase the statistical uncertainty of the frequency measurements. One candidate for a nuclear clock is Th^{229} [PO15] and tremendous steps towards a nuclear clock including the coupling to the well-established ^{87}Sr optical clock transition were already made [Zha+24]. Nonetheless, there is a second candidate for a nuclear clock, which is ^{45}Sc [Shv+23; SS90]. This naturally provides a suitable solid state environment and a high transition frequency. However, compared to ^{229}Th, the higher transition energy of ^{45}Sc makes a suitable light source more challenging. A proposal on how to measure long-lived Mössbauer transitions [SS90] has been unsuccessful because synchrotrons do not provide enough resonant photons to search for such a narrow transition. However, this situation changed with the advent of XFELs and in [Shv+23] our collaboration reports the successful direct x-ray excitation of ^{45}Sc. In this chapter, we discuss the underlying data analysis.

4.2 Experimental setup

The goal of the experiment, which was performed at the "Material Imaging and Dynamics" beamline (MID) [Mad+21] at the European XFEL [Dec+20], was to directly excite the ^{45}Sc nuclear clock transition for the first time. A schematic of the setup, which was mainly developed by the groups in Argonne, Hamburg, and Jena, is shown in Fig. 4.1. The self-seeded XFEL pulses with a central photon energy of about 12.4 keV and spectral full-width half-maxmimum of about 1.3 eV arrive in trains of 400 pulses every 100 ms. The total length of such a train is 176 μs, such that the temporal pulse-structure within a train is negligible on the time scales relevant for the ^{45}Sc nuclear clock transition, which has a lifetime of about 500 ms [HLN64]. Thus, one train is referred to as a *macro-pulse*.

After the incident beam hits the sample in the resonance detection unit, the sample is moved between the beam and the two silicon solid-state drift detectors (Amptek X123) synchronized with the XFEL pulses. When the x-ray pulse arrives, the sample is in the beam, and afterwards moved to the detection unit. This procedure reduces the background because efficient shielding can be placed between the x-ray beam and the detectors. Because of the motion, data acquisition of the two detectors only took place between 20 ms and 80 ms after excitation.

The incident photon energy is measured with a single shot spectrometer in the Diagnostic End Station (DES) of MID [Boe+17; Kuj+20]. Unfortunately, those are only relative measurements as the absolute photon energy depends on the exact alignment of the spectrometer. However, several

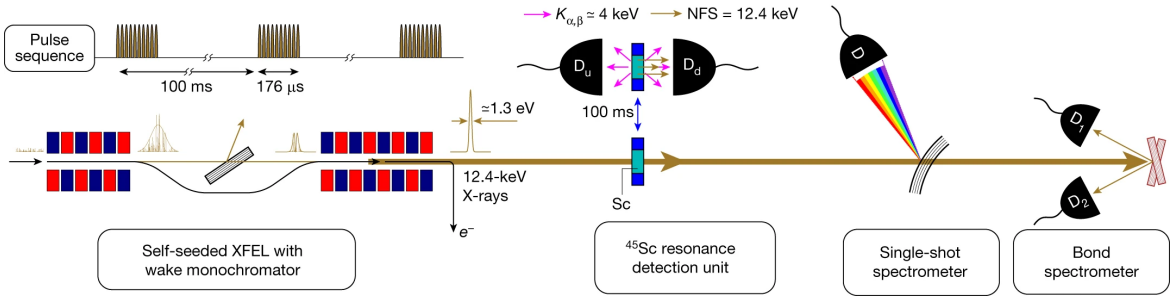

Figure 4.1: Upstream and downstream x-ray counters D_u and D_d detect time-delayed nuclear decay products—both inelastic K_α, K_β fluorescence and coherent elastic NFS. To minimize the detection background, the decay product detectors are offset from the beam path and the sample is moved to the detectors after irradiation with each pulse train. The resonance energy is measured with x-ray single-shot and Bond spectrometers. Material (text and figure) from [Shv+23].

measurements at different incident photon energies with a Bond spectrometer [Bon60] allow for an absolute energy calibration [Shv+23]. For the experiment the incident photon energy was systematically scanned over 100 eV with a scan tool newly developed at the European XFEL for this occasion.

For more details on the experimental setup, see the original publication [Shv+23].

4.3 Data processing

During the experiment, several scans with increasing or decreasing incident photon energy were recorded. Each scan consists of several runs, which are taken for a fixed respective incident photon energy. In Fig. 4.2, an overview over the data taken for each run is shown. We see the photon flux integrated over the whole run, the incidence photon energy and the number of signal photons. These three observables are discussed in the following.

4.3.1 Integrated flux

Due to the stochastic nature of the SASE process, the spectrally integrated pulse energy varies throughout the experiment and needs to be corrected for in the data analysis. It can be measured with the XGM on a train-resolved basis. On average, the flux per macro-pulse during the experiment was approximately 35 mJ.

In Fig. 4.2(a), the flux integrated over the run is shown as a function of the run number. The different colors indicate different scans. Two regimes are visible, until run 405 scans with 200 s acquisition time were performed, afterwards the run length was increased to 500 s to perform high statistic scans around the resonance region. In addition, especially in the second half of the experiment, the fluctuations in the integrated pulse energy from run to run are clearly visible.

Note that for the experiment in principle the pulse energy integrated only over the resonant part of the spectrum should be analyzed, which is not possible due to the extremely narrow resonance. Nonetheless, because the frequency spectrum of the pulse is stable, when averaging over one run, we expect the ratio of the resonant photon flux and the integrated photon flux to be constant. Therefore, we can use the integrated photon flux as measured by the XGM for normalization to the resonant photon flux.

4.3.2 Different measures for incident photon energy

The experiment crucially relies on an absolute and precise measurement of the incident photon energy, which is shown in Fig. 4.2(b). In the experiment, different measures were used and are discussed in the following.

DES spectrometer

The spectrometer in the DES was used to measure the spectrum of each macro-pulse. It consists of a bent crystal, which diffracts the beam onto a pixel screen. The resolution depends on the used crystal reflection and was 0.223 eV/channel in the experiment. The absolute photon energy depends on the

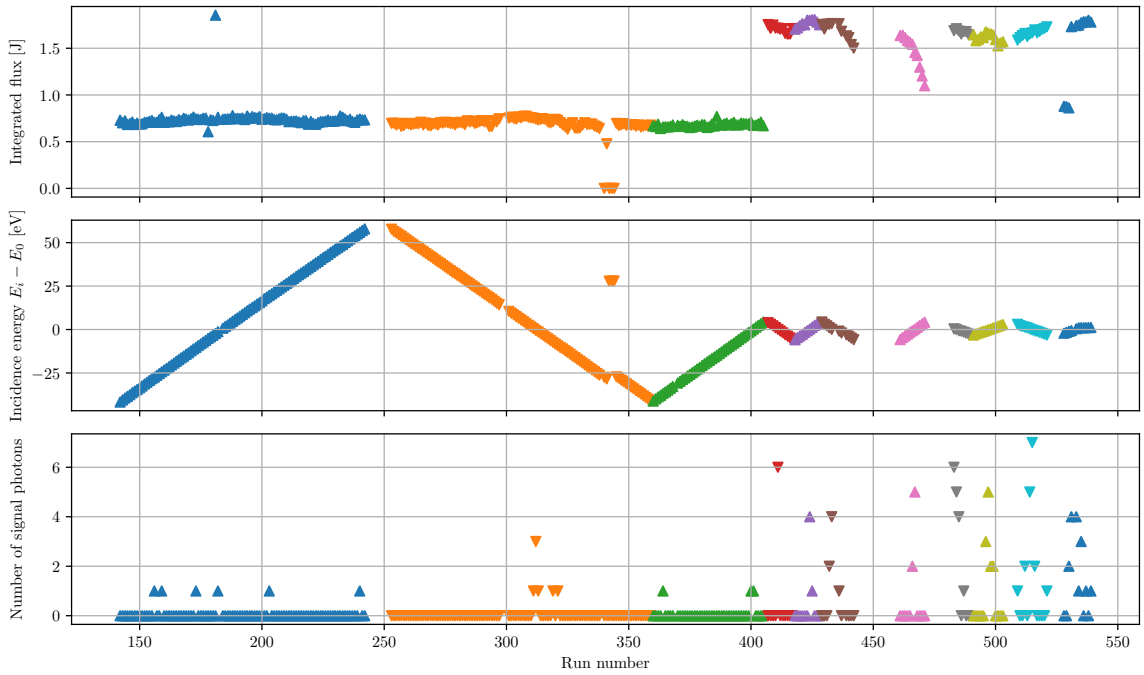

Figure 4.2: Overview over the experimental data used in the analysis. For each run, the integrated flux (top), incidence photon energy (center), and number of signal photons (bottom) are shown. The different colors indicate the different scans. The markers indicate whether the scan is performed with increasing (upwards triangle △) or decreasing (downwards triangle ▽) incident photon energy. Details on the three observables are given in the main text.

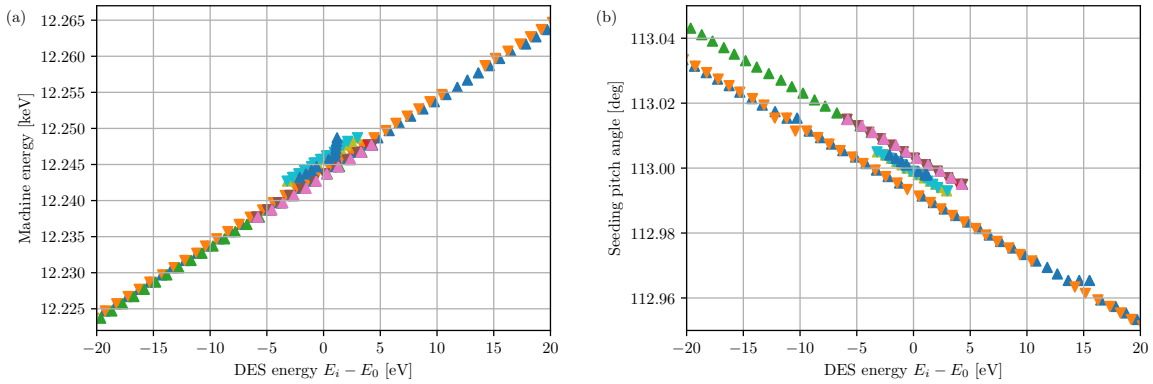

Figure 4.3: Comparison of the different energy measures. (a) The machine energy as a function of the DES energy. (b) The pitch angle of the seeding crystal as a function of the DES energy. The colors correspond to the different scans in Fig. 4.2. The markers indicate whether the scan is performed with increasing (upwards triangle △) or decreasing (downwards triangle ▽) incident photon energy. Details on the different energy measures are given in the main text.

exact alignment of the spectrometer. Nonetheless, as long as the alignment of the spectrometer is not changed, it can be calibrated with absolute photon energy measurements at different energies.

We can fit the mean spectrum of each run with a Gaussian fit function to find the incident photon energy. This energy is referred to as the *DES energy* and will be used as the primary relative energy measure. The mean width of the fitted spectra is $\sigma_{\text{mean}} = (0.63 \pm 0.11)\,\text{eV}$, which dominates the jitter over a train of the center value E_i. Note that the real spectral width is smaller because the spectra from the DES spectrometer are convoluted with the instrument function.

Although the actual data analysis is performed on the raw data in channels of the DES spectrometer detector to not increase the uncertainty of the incident photon energy, for better readability in the text and figures we converted all raw values to eV as described in the next paragraph.

Bond method

The bond method was operated by our collaborators from Jena to measure the absolute photon energy, and thus to calibrate the raw channels of the DES spectrometer to an absolute energy value. A conversion of the DES energy in raw channels to eV can be made with

$$E_i = E_i\,[\text{channel}] \cdot \frac{0.215\,\text{eV}}{\text{channel}} + 12341.8\,\text{eV}\,. \tag{4.1}$$

Here, the analysis is performed on the raw data in channel to not introduce additional uncertainties from the conversion into the analysis, but for illustration, the results and figures are given in eV using the above conversion. More details on the method and corresponding uncertainties can be found in [Shv+23].

Machine energy

The machine energy is one of the control parameters of the photon energy at the European XFEL. It is related to the undulator gap. For this experiment, a new tool was implemented at the European XFEL, which allows to scan the incident photon energy from the experiment hutch. If a change in the machine energy is detected by this new tool, it triggers the adjustment of the seeding crystal and also the undulator parameters if necessary. Thus, the machine energy is the scan control parameter for the incident photon energy scans.

In Fig. 4.3(a) the machine energy is plotted against the DES energy of the respective run. There is an approximately linear relationship. However, a closer look reveals that the machine energy is shifted in the upstream and downstream scans. This demonstrates that the control of the incident photon energy via the machine energy works within a scan. From scan to scan, however, the same set machine energy does not lead to the same DES energy. As the spectrometer is expected to work reliably, we conclude that from scan to scan the optimization of the seeding crystal and undulator parameters after a change of the machine energy results in slightly different incident photon energies. In addition, at some point in the experiment, the macro to scan the machine energy had to be readjusted, which resulted in a significant change of the incident photon energy for a set machine energy as can be seen by the offset short diagonal. Summarizingly, we conclude that there is a linear relationship between the DES energy and the machine energy, but different offsets due to different origins occur.

Seeding pitch angle

As hard-x-ray self-seeding was used in the experiment, the incident photon energy is defined not only by the undulator settings, but also by the orientation of the seeding crystal. The incident photon energy is well-defined by the seeding crystal pitch angle, however, only as long as there is no change in the roll angle of the crystal. Unfortunately, during the experiment changes in the roll angle occurred, therefore resulting in a complicated relationship between the seeding crystal pitch angle and the incident photon energy and not for all settings absolute calibration measurements were performed with the Bond method. Nonetheless, if the roll-angle is constant, a simple linear relation between the seeding pitch angle and the DES energy can be used to interpolate the incident photon energy for runs in which the DES spectrometer failed to save data.

The seeding pitch angle as a function of the DES energy is shown in Fig. 4.3(b). We see three parallel lines, which are stable within the respective line. The stability shows, that in general there is a linear relationship within a scan and the seeding pitch angle can be used to interpolate the incident photon energy for runs in which no spectrum from the DES spectrometer was measured. The two

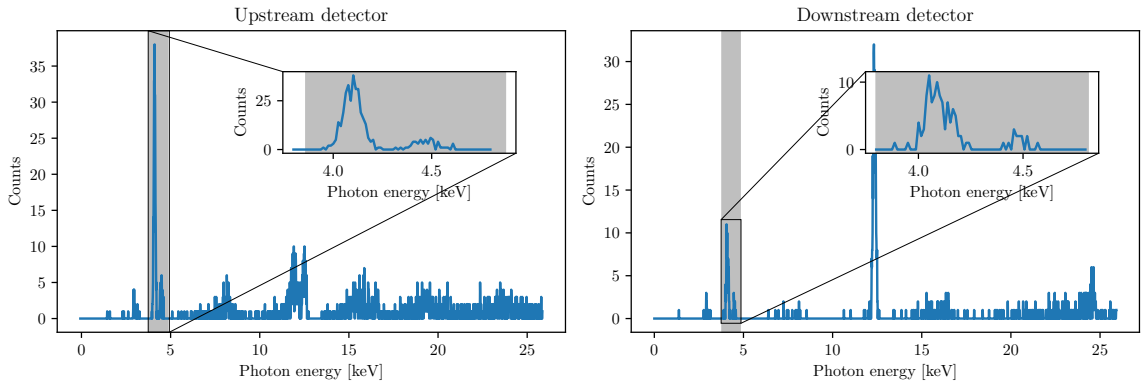

Figure 4.4: Measurement of the direct K_α- and K_β-fluorescence at around 4 keV via electronic scattering immediately after the x-ray pulse arrival. The two panels show the results for the upstream and downstream detectors, respectively. A zoom to the region around 4 keV is given in the insets. The ROI, in which signal photons are counted is displayed in gray.

shifts of the diagonal lines are from a shift in the seeding roll angle as well as the restart of the energy scan macro.

Incident photon energy measure

Ideally, we would use the machine energy for the incident photon energy determination because it is the scan parameter. Unfortunately, we have seen that there is no fixed linear relationship to the DES energy over all scans. Similarly, the seeding pitch angle does not allow us to determine the incident photon energy easily over all scans. The absolute value of the photon energy can be measured with the Bond. However, this method is time consuming and was thus performed only at selected settings.

Therefore, to determine the incident photon energy, a combination of the different methods is used. As the primary measure for the *incident photon energy* E_i, we use the DES energy, which is calibrated to absolute values with Bond measurements at selected energies. For runs, in which the DES energy is not available, it can be interpolated from the neighboring runs based on the seeding pitch angle.

4.3.3 Determination of signal photons

The energy scale of each of the SDD detectors was roughly calibrated by a measurement with a radioactive source. For an improved calibration, in the experiment we recorded the direct electronic scattering and thus the K_α and K_β lines, which have photon energies of 4.09 keV and 4.46 keV, respectively. The results are shown in Fig. 4.4. We can clearly see the fluorescence at around 4 keV. Furthermore, we see multi-photon pile-ups in the detector at multiples of the 4 keV region. Around the fluorescence lines, we define an approximately 1 keV wide region of interest (ROI), in which the photons are considered signal counts. To reduce the background noise during the excitation, the signal photons are only recorded between 20–80 ms after every macro-pulse.

4.3.4 Raw data - incident vs outgoing photon energy

After the energy measures of incident and outgoing photon energy are discussed, the energy of the recorded photons are shown as a function of the incident photon energy for all runs in the analysis in Fig. 4.5. The two colors of the dots indicate the two detectors in the resonance detection unit. The background noise is uniformly distributed and only higher in between the two orange vertical lines due to more measurement time inside this region close to the resonance. A clear accumulation of the energy of the outgoing photons in between the horizontal pink lines around $E_f \approx 4.5$ keV, where the K_α and K_β lines are expected, is visible already in the overview panel (a), but even better in the zoom-in in panel (b). Furthermore, no significant signal above the background noise is visible inbetween the horizontal dark yellow lines around $E_f = 12.4$ keV, where the coherent nuclear forward scattering signal is expected.

In the next step, the signal in panel (b), i.e., the signal in the ROI of E_f and E_i, will be used to extract the resonance curve and the resulting resonance energy. In this region around the incident

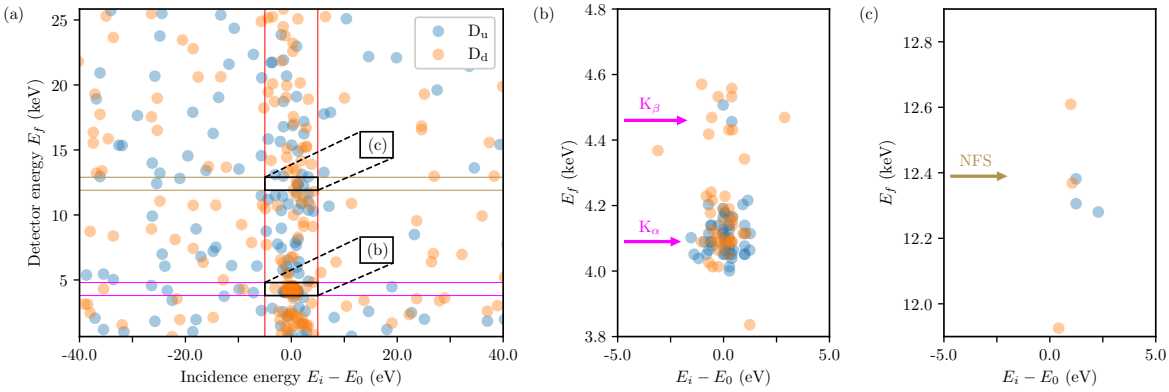

Figure 4.5: The photons were recorded in a time window of about 20–80 ms after every pulse-train excitation. Each photon is shown by a blue circle for D_u and a yellow circle for D_d. (a), All detector counts with $E_f \leq$ 26keV for incident energies in a range of -40 eV$\leq E_i - E_0 \leq$40 eV around the ^{45}Sc resonance energy E_0. Vertical red lines indicate a 10-eV ROI around $E_i = E_0$. Horizontal dark yellow lines indicate a 1-keV ROI around E_f=12.4 keV, whereas the horizontal magenta lines indicate a 1-keV ROI around E_f=4.3 keV, the approximate energy of the fluorescence photons. (b), Close-up of the 4.3-keV ROI, showing two clusters of counts centred at the energies of Sc K_α and K_β fluorescence. (c), Close-up of the 12.4-keV ROI. Material from [Shv+23] (text verbatim, figure adapted).

resonance energy and the outgoing fluorescence energy, a total of 93 photons were detected. The very small number of signal photons demonstrates how demanding the experiment was. Furthermore, the low statistics made the data evaluation challenging.

4.4 Determination of resonance energy

The measured resonance curve is a convolution of the actual resonance with the incident pulse shape. Because the actual resonance is orders of magnitude smaller than the incidence pulse shape, the measured curve is dominated by the latter one. Thus, the measured curve should be well represented by a Gaussian centered around the resonance energy with a width of the incident pulse width.

In the experiment the machine energy was scanned, but there is not a fixed linear relation to the DES energy over all scans as we have seen in Fig. 4.3. Therefore, the DES energy, i.e., the actual incident photon energy, does not follow the steps of the scan. As a consequence, all runs have a slightly different incidence energy and the signal photons cannot simply be summed up at different energy steps. Due to the small statistics, the resulting resonance energy can depend strongly on the analysis method as well as the analysis parameters and the best method is not known a priori. Therefore, for the data analysis three different methods are used with different parameters: the cumulative probability function, a kernel density estimate and the classic histogram. They are discussed in the following sections.

4.4.1 Cumulative distribution function

The first evaluation method uses the combined information of all measurements around the resonance energy. For each run the tuple consisting of incident photon energy, the number of signal photons and the integrated pulse energy is stored. Depending on whether the normally ordered cumulative distribution function (CDF) $\Phi^{\text{normal}}(X) = P(x \leq X)$ with $P(x)$ being the underlying probability density function or the reversely order CDF $\Phi^{\text{reversed}}(X) = P(x \geq X)$ is evaluated, the run data is sorted with ascending or descending incident photon energy. Afterwards, for each incident photon energy step $\tilde{E}_i$ the number of signal photons in runs with $E_i \leq \tilde{E}_i$ ($E_i \geq \tilde{E}_i$) are summed up and are divided by the total integrated pulse energy over those runs for normalization to the integrated photon flux. Afterwards, the distribution is normalized to form the normally (reversely) ordered CDF in Fig. 4.6. The errorbars indicate the uncertainty of signal photons summed up until this step according to a Poissonian counting statistic. The uncertainty of the incident photon energy is within the size of the points.

We can now extract the resonance energy from a fit to the CDFs. For a Gaussian probability

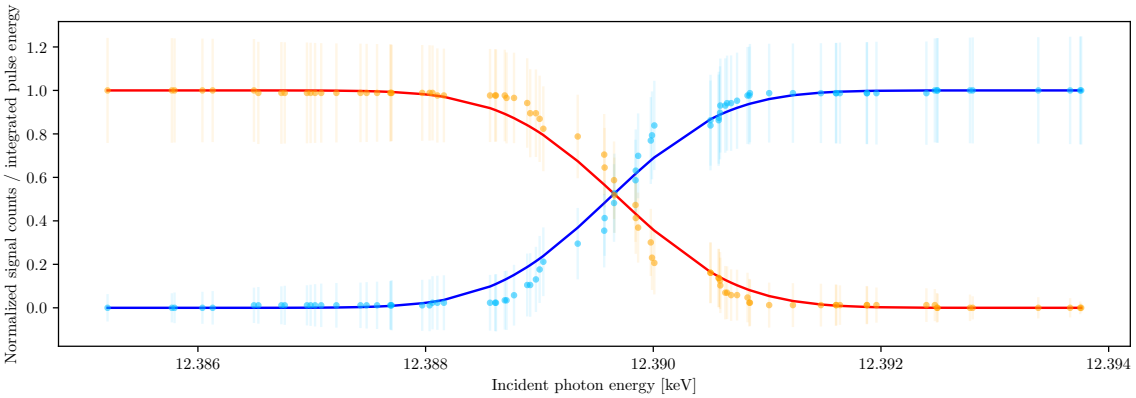

Figure 4.6: Normally ordered (light blue) and reversely ordered (orange) CDF with respective fits in blue and red. The errorbars indicate the uncertainty of the number of signal photons summed up towards this point. The uncertainty in the incident photon energy is within the size of the data points.

distribution, the normally ordered and reversely ordered CDF is given by

$$\Phi^{\text{normal}}(x) = \frac{1}{2}\left[1 + \text{erf}\left(\frac{x-\mu}{\sqrt{2}\sigma}\right)\right], \tag{4.2a}$$

$$\Phi^{\text{reversed}}(x) = 1 - \frac{1}{2}\left[1 + \text{erf}\left(\frac{x-\mu}{\sqrt{2}\sigma}\right)\right], \tag{4.2b}$$

respectively, with mean μ and standard deviation σ and can be fitted to the respective curves. To estimate the uncertainty of the fit results, the usual way via the covariance matrix is not possible as this assumes independent data points and uncorrelated residuals, which is not the case for a CDF. Thus, instead of using a standard fitting routine like least-squares and including the errorbars as used in Fig. 4.6, i.e., the uncertainty of the number of signal photons, bootstrapping is performed for an uncertainty estimate of the fit parameters taking into account the uncertainty of the input data. To this end, for each repetition, the energy of each run is drawn from a normal distribution centered around the incident photon energy with the uncertainty of the DES energy fit as the width, and the number of signal photons is drawn from a Poissonian distribution with the actual number of signal photons as the mean. For each modified set, the CDF is calculated as explained above within the 10 eV region of interest, which is shown in Fig. 4.5, and fitted with the respective function in Eq. (4.2). After 1000 repetitions, the fit result and its uncertainty of each parameter are calculated as the mean and standard deviation over the fit results in each repetition. For the normally and reversely ordered CDF, the resulting mean and width are given by

$$E_0^{\text{normal}} = (12389.61 \pm 0.22)\,\text{eV}, \qquad \sigma^{\text{normal}} = (0.80 \pm 0.15)\,\text{eV}, \tag{4.3a}$$

$$E_0^{\text{reversed}} = (12389.71 \pm 0.22)\,\text{eV}, \qquad \sigma^{\text{reversed}} = (0.82 \pm 0.15)\,\text{eV}, \tag{4.3b}$$

respectively. The fit results of the two different orderings agree well with each other. The final result of the CDF analysis for the resonance energy is given by the mean of both directions

$$E_0^{\text{CDF}} = (12389.7 \pm 0.3)\,\text{eV}, \tag{4.4}$$

$$\sigma^{\text{CDF}} = (0.81 \pm 0.21)\,\text{eV}, \tag{4.5}$$

The standard deviation of $\sigma = (0.81 \pm 0.21)$ eV is in good agreement with the mean spectral width $\sigma_{\text{mean}} = (0.63 \pm 0.11)$ eV. Note, that this so far only contains the uncertainty from the analysis. For the final result, the uncertainty of the Bond measurement has to be included.

4.4.2 Kernel density estimate

A qualitatively different method to extract the resonance energy from the data is that of a kernel density estimate (KDE). This tackles the problem, that the runs are all performed at slightly different incident photon energies, but each run does not have enough statistics to analyze it on its own. Again, for each run j the tuple consisting of incident photon energy E_i^j, the number of signal photons N_s^j

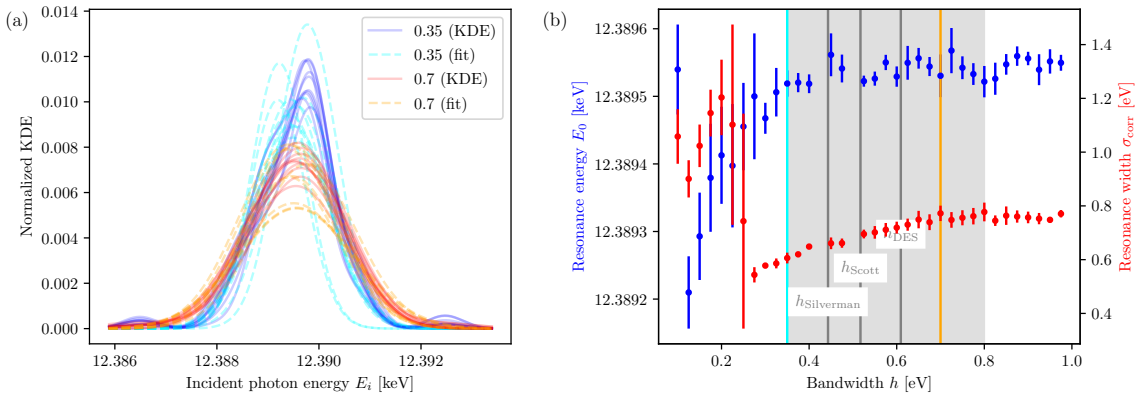

Figure 4.7: Results of the KDE analysis. (a) The KDE of the resonance curve for two different kernel bandwidths with ten repetitions each (dark colors, solid) and corresponding Gaussian fits (light colors, dashed). (b) Fitted resonance energy E_0 and width σ_{corr} as a function of the kernel bandwidth h with the uncertainties given by the standard deviation. The colored vertical lines represent the bandwidths in (a). The gray vertical lines correspond to $h_{\text{Silverman}}$, h_{Scott} and h_{DES}, while the gray shaded area indicates the region over which the mean is evaluated.

and the integrated pulse energy E^j_{pulse} is used. The number of signal photons is normalized by the integrated pulse energy and the kernel density estimate is then formed as [Dek+05; Sil86]

$$\text{KDE}(E_i) = \sum_j \frac{N^j_s}{E^j_{\text{pulse}}} K(E_i - E^j_i), \tag{4.6}$$

with here the kernel of choice

$$K(E_i - E^j_i) = \frac{1}{\sqrt{2\pi}h} \exp\left(-\frac{(E_i - E^j_i)^2}{2h^2}\right), \tag{4.7}$$

being a Gaussian centered around E^j_i with bandwidth h. For the choice of the bandwidth there are several options. One is to use the spectral width of the beam $\sigma_{\text{beam}} = 0.63\,\text{eV}$ and thus $h_{\text{DES}} = \sigma_{\text{beam}} = 0.63\,\text{eV}$. Furthermore, there are several different estimates for an optimal bandwidth. Among others, there is Scott's rule [Sco15]

$$h_{\text{Scott}} = \sigma n^{-1/5}, \tag{4.8}$$

and Silverman's rule [Sil86]

$$h_{\text{Silverman}} = 0.9 \cdot \min\left(\sigma, \frac{IQR}{1.34}\right) n^{-1/5}, \tag{4.9}$$

where σ is the standard deviation, $\text{IQR} = q_n(0.75) - q_n(0.25)$ the interquartile range, i.e., the difference of the upper quartile $q_n(0.75)$ and the lower quartile $q_n(0.25)$[Dek+05], and n the size of the dataset $\{E^j_i\}$. Restricting the dataset to the 10-eV ROI around the resonance as shown in Fig. 4.5(b), it is $h_{\text{Scott}} = 0.54\,\text{eV}$ and $h_{\text{Silverman}} = 0.50\,\text{eV}$. However, for insight into the analysis the bandwidth h is varied between 0.1 eV and 1 eV.

To account for the uncertainty in the number of signal photons, for each bandwidth 100 repetitions of bootstrapping are performed, in which for each run, a random number is drawn from the Poissonian distribution with the number of signal photons as mean. To the resulting KDEs for each repetition a Gaussian is fitted to find the center and width of the KDE. A few examples are displayed in Fig. 4.7(a). To retrieve the actual width of the resonance curve, it has to be taken into account, that the resulting KDE is a discrete convolution of the actual underlying distribution with the kernel. As here both are of Gaussian form, the KDE is also Gaussian and the actual width σ_{corr} can easily be corrected for this

$$\sigma_{\text{corr}} = \sqrt{\sigma^2_{\text{fit}} - h^2}. \tag{4.10}$$

In Fig. 4.7(b) for each bandwidth h, the mean resonance energy E_0 and mean the corrected width σ_{actual} are shown with the uncertainty given by the respective standard deviations from the bootstrapping. The fit values are stable over a broad range of bandwidths h. Because there is no unambiguous

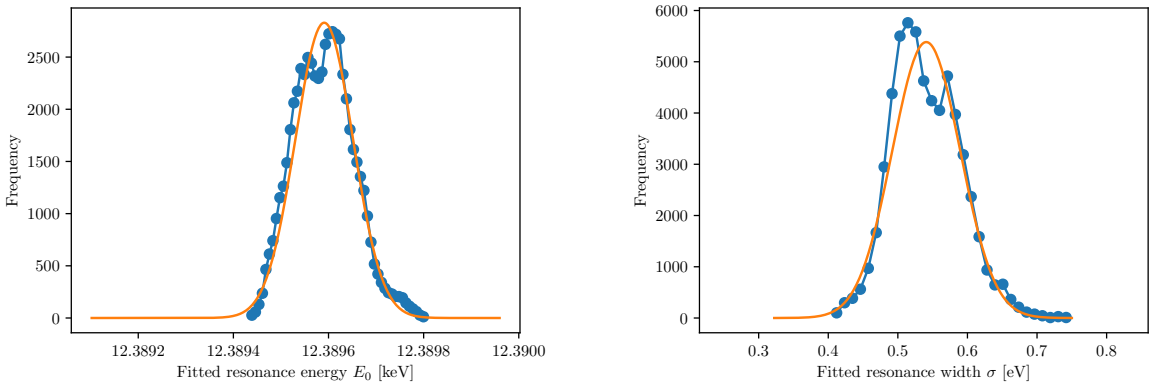

Figure 4.8: Histograms of the resonance center and standard deviation width obtained by sampling over bin sizes and centers. The solid orange lines show the respective the Gaussian fits.

choice of the bandwidth h, the fit results are averaged over the stable region from $h = 0.35\,\text{eV}$ to $h = 0.8\,\text{eV}$ and give the final resonance energy and width

$$E_0^{\text{KDE}} = (12389.54 \pm 0.09)\,\text{eV}\,, \tag{4.11a}$$

$$\sigma^{\text{KDE}} = (0.71 \pm 0.11)\,\text{eV}\,. \tag{4.11b}$$

Again, the width agrees with the mean spectral width of the incident pulse.

4.4.3 Histogram

The third analysis approach, which is used, is a histogram. As there is no natural choice of the bin size and the bin center along the incident photon energy axis, the fit results are sampled over a broad range of bin sizes and bin shifts (shift of the bins along the energy axis). To this end, the following analysis is performed: First, a bin size and bin shift are chosen and the resonance region is split into the bins. The energy of each bin is defined by its center value. For each bin, the total number of signal photon counts, as well as the corresponding integrated pulse intensity are calculated. Afterwards, the detector counts are normalized by the integrated pulse energy on a per-bin basis and a Gaussian with amplitude A, center E_0 and width σ is fitted to the binned data. Because of the finite bin size h, the resonance widths have to be corrected according to Sheppard's correction [KK54; She97]

$$\sigma_{\text{corr}} = \sqrt{\sigma^2 - h^2/12}\,. \tag{4.12}$$

For each choice of bin size and shift, E_0 and σ_{corr} are stored. Repeating this analysis for many bin sizes and shifts, histograms are obtained for E_0 and σ_{corr}. For this sampling, bin sizes in the range of $[0.460, 1.148]\,\text{eV}$ with step size $0.002\,\text{eV}$ are considered. These bin sizes were then sampled for bin shifts in the range $[-(\text{bin size})/2, +(\text{bin size})/2[$ around the resonance in 200 steps. The corresponding histograms are shown in Fig. 4.8. As expected from such a sampling, the results are approximately normally distributed. The kink in both distributions might be caused by small sidebands, which are also visible in Fig. 4.7 and are caused by artifacts due to noise counts and the binning procedure. In Fig. 4.8, the solid orange lines show Gaussian fits to the histograms. The center and width of these Gaussian fits then determine value and uncertainty of the respective observable

$$E_0^{\text{histo}} = (12389.59 \pm 0.06)\,\text{eV}\,, \tag{4.13}$$

$$\sigma_{\text{histo}} = (0.54 \pm 0.05)\,\text{eV}\,, \tag{4.14}$$

which again agrees with the width of the incident pulse.

4.4.4 Comparison

The results of the three different methods are summarized in Table 4.1 and agree within the uncertainties, which is remarkable because the idea behind the analysis methods is very different. The cumulative density function combines the data for more statistics in a very natural way, namely by

	E_0 [eV]	σ [eV]
CDF	12389.7 ± 0.3	0.81 ± 0.21
KDE	12389.54 ± 0.09	0.71 ± 0.11
Histogram	12389.59 ± 0.06	0.54 ± 0.05

Table 4.1: Analysis result of resonance energy E_0 and width σ for the three different methods: cumulative density function (CDF), kernel density estimate (KDE), and histogram.

using the cumulative information. This has the advantage that we do not need to choose a kernel or band width. Unfortunately, the small statistics in the tail lead to larger uncertainties on the side with smaller (higher) incident photon energy for the normally ordered (reverse) CDF., which can lead to large uncertainties in the fitting. The kernel density estimate deals with the problem of low statistics by smoothing out the information of a single count to have more overlap, while the histogram sums up the counts in certain regions to increase the statistics within these regions. Both the kernel density estimate as well as the histogram suffer from the need of choosing a kernel widths or bin width, respectively, which in our case cannot be done unambiguously due to the not equally distributed measurement points and the low statistics.

We find that the cumulative distribution has the largest uncertainty, while the histogram has the smallest. Note that the given uncertainties are only the uncertainties from the data evaluation methods as discussed. The results are given in eV with a rough energy calibration, but the evaluation is based on the raw data, which is why the uncertainties from the calibration are neglected so far. They are considered in the final result in Eq. (4.26) and are on a similar level as the uncertainties in Table 4.1.

All methods agree well with each other and have their advantages and disadvantages. Because the histogram is the simplest method, we choose it as the main analysis method for the final resonance curve in Section 4.7.

4.5 Signal-to-noise ratio

For the signal-to-noise ratio, the count rate in the background region is compared to the count rate on resonance.

To calculate the background count rate, the background region is defined as the energy region outside a 5σ, i.e., 5 standard deviations, region around the resonance. In this region there are $N_{\mathrm{bg}} = 10^{+4}_{-3}$ counts in an acquisition time of $t_{\mathrm{bg}} = 59163\mathrm{s}$, which results in a background count rate of

$$R_{\mathrm{bg}} = \frac{N_{\mathrm{bg}}}{t_{\mathrm{bg}}} = \left(1.7^{+0.7}_{-0.5}\right) \times 10^{-4}\,\mathrm{ph/s}\,. \tag{4.15}$$

The uncertainty (one standard deviation) is dominated by the Poissonian uncertainty of the counts. The acquisition time given above is calculated by taking the mean acquisition time of the two detectors and summing over all runs with incident photon energy in the background region.

In the signal region, defined as 5σ around the resonance, there are $N_{\mathrm{sig}} = 93 \pm 9$ counts in an acquisition time of $t_{\mathrm{sig}} = 34009\mathrm{s}$, which gives an average count rate of

$$R^{\mathrm{avg}}_{\mathrm{sig}} = (2.73 \pm 0.16) \times 10^{-3}\,\mathrm{ph/s} \tag{4.16}$$

in the signal region. However, to determine the count rate on resonance, the shape of the resonance curve in the signal region, i.e., a Gaussian with the mean value and width obtained in our resonance analysis in Section 4.4.3, needs to be taken into account. The amplitude is fixed by demanding that the integral over the signal region remains the same as in the homogeneous case,

$$\int_{x_0-5\sigma}^{x_0+5\sigma} R^{\mathrm{max}}_{\mathrm{sig}} \exp\left[\frac{(x'-x_0)^2}{2\sigma^2}\right] dx' = \int_{x_0-5\sigma}^{x_0+5\sigma} R^{\mathrm{avg}}_{\mathrm{sig}} dx'\,. \tag{4.17}$$

From the scaled Gaussian, the count rate on resonance evaluates to

$$R^{\mathrm{max}}_{\mathrm{sig}} = (1.09 \pm 0.11) \times 10^{-2}\,\mathrm{ph/s}\,. \tag{4.18}$$

The signal-to-noise ratio (SNR) is then given as

$$\mathrm{SNR} = \frac{R_{\mathrm{sig}}^{\mathrm{max}}}{R_{\mathrm{bg}}} = 65^{+28}_{-21}\,. \tag{4.19}$$

The uncertainty is dominated by the Poisson uncertainty of the low number of counts in the background region.

4.6 Experimental count rate analysis

For each run j with integrated pulse energy $E_{\mathrm{pulse}}^{(j)}$ the pulse energy delivered onto resonance is estimated as

$$E_{\mathrm{res}}^{(j)} = E_{\mathrm{pulse}}^{(j)} \sqrt{\frac{1}{2\pi}} \frac{\gamma}{\sigma}\, e^{-\frac{\left(\omega_0 - \omega^{(j)}\right)^2}{2\sigma^2}}\,, \tag{4.20}$$

where γ is the ^{45}Sc line width, $\omega^{(j)}$ and σ the resonance energy and spectral width of the incident pulse in run j, and ω_0 the ^{45}Sc resonance energy. From this, the total pulse energy delivered into the Scandium resonance is obtained as the sum over all runs in the energy scans,

$$E_{\mathrm{res}}^{\mathrm{total}} = \sum_j E_{\mathrm{res}}^{(j)} = 1.14 \times 10^{-5}\ \mu\mathrm{J}\,, \tag{4.21}$$

independent of whether they had a signal count or not. From this, via the energy per resonant photon, we can calculate the total number of photons delivered into the Sc resonance

$$N_{\mathrm{res}}^{\mathrm{total}} = \frac{E_{\mathrm{res}}^{\mathrm{total}}}{12.4\,\mathrm{keV}} = 5725\,. \tag{4.22}$$

Within a spectral region of 5 standard deviations around the resonance, in total $N_{\mathrm{sig}} = 93$ signal photons were recorded. This results in an experimental count rate of

$$\sigma_K = \frac{N_{\mathrm{sig}}}{N_{\mathrm{res}}^{\mathrm{total}}} = 0.0162 \pm 0.0017\ \mathrm{ph}_K/\mathrm{ph}_{\Gamma_0}\,. \tag{4.23}$$

Correcting this value for the x-ray beam attenuation A=0.44(9) on the path from the XGM to the sample and for limited detection efficiency D_{eff}=0.084(7), which is dominated by the coverage of the solid angle, a count rate of

$$\sigma_K^{\mathrm{exp}} = 0.44 \pm 0.13\ \mathrm{ph}_K/\mathrm{ph}_{\Gamma_0} \tag{4.24}$$

is obtained. In this analysis, the relative uncertainties of the correction factors are added to the total relative uncertainty, and all absolute uncertainties are given in standard deviations.

Including further the Poisson uncertainty $\sqrt{N_{\mathrm{sig}}}$ into the uncertainty analysis, the corresponding value becomes

$$\sigma_K^{\mathrm{exp}\prime} = 0.44 \pm 0.17\ \mathrm{ph}_K/\mathrm{ph}_{\Gamma_0}\,. \tag{4.25}$$

Note that even for different incident pulse line widths (σ in Eq. (4.20),) the results remain very well within the above-mentioned uncertainty budget.

4.7 Final resonance curve result

For the final resonance curve shown in Fig. 4.9, the analysis with a histogram is chosen. The different colors indicate four example choices of bin size and shift, the black line a Gaussian centered around the resonance energy $E_0 = (12389.59 \pm 0.06)\,\mathrm{eV}$ with width σ. The normalization for the left y-axis is chosen in such a way that the integration over the curve yields the total recorded number of photons in a range of 5 standard deviations around the resonance of $N_{\mathrm{sig}} = 93$.

The yield shown by the axis on the right hand side follows from a simple axis scale conversion, in such a way that the maximum of the resonance corresponds to 0.44 $\mathrm{ph}_K/\mathrm{ph}_{\Gamma_0}$ as calculated in

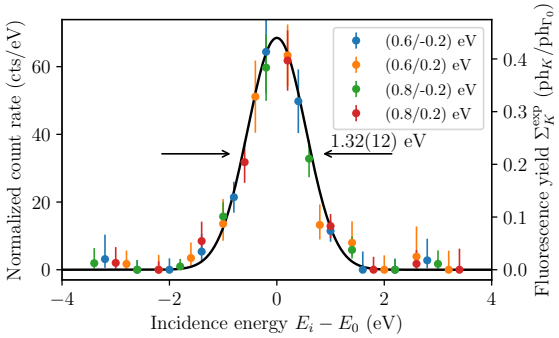

Figure 4.9: Final resonance curve given by the normalized count rate or fluorescence yield as a function of the incident photon energy E_i. The different colors exemplarily show four different choices of bin size and and shift. The black curve shows the Gaussian centered around the resonance energy E_0 with width σ. The full-width half-maximum $FWHM = 2.35\sigma$ is also indicated and corresponds to the incident photon beam spectral width. Figure adapted from [Shv+23].

Eq. (4.25). The width indicated in the figure is the FWHM width in eV, with the standard deviation error in brackets. The error bars in y-direction are obtained as Poisson count uncertainty for the unnormalized number of signal counts in the bin. This uncertainty is then scaled by the integrated flux and normalized in the same way as the count rate itself. Due to the small count rates, the uncertainties are asymmetric because they are obtained from the Poissonian distribution [Geh86].

Including the uncertainty of the absolute energy calibration, the resonance energy is determined to be [Shv+23]

$$12,389.59^{\pm 0.15(\mathrm{stat})}_{+0.12(\mathrm{syst})}\,\mathrm{eV}\,. \tag{4.26}$$

Note that the uncertainties are asymmetric due to asymmetric uncertainties in the absolute energy calibration (see [Shv+23]).

4.8 Summary and Outlook

In summary, after shortly presenting the experimental setup we discussed the data analysis leading to the final resonance curve in [Shv+23] and the demonstration of the direct x-ray excitation of ^{45}Sc.

First, the raw data was processed. This included the integrated incident photon flux determination as well as choosing a meaningful measure for the incident photon energy and a region of interest for the fluorescence signal. We further saw that the incident photon energy scan unfortunately did not have clear equal distant steps because one machine energy setting resulted in different actual incident photon energies in the different scans. Furthermore, only 93 signal photons were recorded. Therefore, no unambiguous choice of bins to bin the data was possible. Because of the low count rate different settings for the binning have a significant impact on the determined resonance energy. For this reason, in the following we determined the resonance energy with three different methods – the cumulative distribution, a kernel density estimate and a histogram. The best method was not clear a priori, but all methods result in values for the resonance energy and width, that agree with each other. Because of its simplicity, for the final resonance curve we decided for the histogram as the analysis method. In addition to the resonance energy determination, the signal-to-noise ratio was estimated and the experimental count rate analyzed. Finally, the resonance energy was measured more than 300 times more precisely than previously known.

The next step on the road towards a nuclear clock is the better understanding of the transition properties. This includes an even more precise measurement of the transition energy with a monochromator and a lifetime measurement after direct excitation. Furthermore, measuring the time-dependence of coherent nuclear coherent scattering would provide the transition width, which is usable for coherent scattering experiments. The coherent nuclear scattering is also the basis for further applications like Mössbauer spectroscopy with feV resolution and measurements of the gravitational red-shift in the sub-millimeter regime. A first step in this direction was made in [Liu+25a].

Chapter 5

Single-shot sorting of Mössbauer time-domain data at X-ray free electron lasers

This chapter is based on the following preprint:

Single-shot sorting of Mössbauer time-domain data at X-ray free electron lasers
M. Gerharz, W. Hippler, B. Marx-Glowna, S. Sadashivaiah, K. S. Schulze, I. Uschmann, R. Lötzsch, K. Schlage, S. Velten, D. Lentrodt, L. Wolff, O. Leupold, I. Sergeev, H.-C. Wille, C. Strohm, M. Guetg, S. Liu, G. A. Geloni, U. Boesenberg, J. Hallmann, A. Zozulya, J.-E. Pudell, A. Rodriguez-Fernandez, M. Youssef, A. Madsen, L. Bocklage, G. G. Paulus, C. H. Keitel, T. Pfeifer, R. Röhlsberger, and J. Evers
arXiv:2509.15833 [quanth-ph]

Content has been reproduced verbatim, but the article was restructured to suit the format of this thesis. In particular, main text and supplementary material were merged and additional motivation is provided in the context of this thesis.

5.1 Motivation

Mössbauer nuclei provide extremely high energy resolution [Smi12], but the narrow spectral width implies the need for averaging over many x-ray shots. The reason is that the signal rate per shot is low since the spectral width of the x-ray light is orders of magnitude broader than the nuclear resonance, such that the vast majority of the intense initial x-ray light is off-resonant and hence not contributing to the excitation.

This averaging requirement poses a severe challenge for studying statistical or non-repetitive dynamics, out-of-equilibrium dynamics or related phenomena with Mössbauer spectroscopy [SR08]. If the sample dynamics is not always the same after each x-ray shot, then the averaging inevitably ranges over different evolution pathways from the out-of-equilibrium state back into equilibrium, thereby impeding their disentangling and understanding.

For instance, statistical nuclear dynamics are expected in the random sequence of coherent and incoherent emissions from a higher-excited nuclear ensemble, potentially involving the transient formation of entanglement [Cab+99; Moe+07; Thi+07]. More generally, Mössbauer nuclei are widely used to probe the dynamics of their surrounding host material [GBT11; GW99; She12], with even non-repetitive host dynamics being mapped onto the nuclear dynamics. Particularly following external stimuli [Boc+21; Hee+21; KKR99; Sak+17; Shv+96; VSK13], the nuclear dynamics can change drastically. In the simplest case, the stimulus induces dynamics only with a certain success probability. More interestingly, the host dynamics can involve quantum mechanical superpositions, probabilistically leading to different measurement outcomes. Examples include the laser pumping of the electronic sub-system of the host [KKR99], which can also be prepared in a superposition state. Laser-pumping can also control the vibrational state of the host [VSK13], or the switching of spin-crossover complexes [Sad+21; Sak+17]. Analogously, magnons have been studied via their transient impact on the nuclear dynamics [Boc+21]. In chemistry [GBT11], Mössbauer spectroscopy is pivotal, e.g., for studying biochemical reactions involving iron [SW00], but the study of short-lived transient intermediate states is difficult using Mössbauer spectroscopy [Kre+05].

5.1.1 Progress of light sources

Here, we demonstrate the disentangling of different Mössbauer dynamics by analyzing time-domain data on the single-shot level. For this, we tackle the averaging challenge from two sides. First, we demonstrate coherent nuclear forward scattering of self-seeded radiation delivered by the European

XFEL [Dec+20; Liu+23], which allowed us to record Mössbauer datasets with up to 900 signal photons per x-ray shot using the isotope ^{57}Fe. These shots with highest photon number directly reveal the nuclear dynamics up to about 50 ns after excitation. Second, we develop an approach which generalizes the analysis to shots with lower signal photon rate, and to longer times after excitation. It relies on the presence of distinct evolution pathways from out-of-equilibrium back into equilibrium, which we denote as dynamics classes. We determine the classes from the data, and assign each shot to a class. Analyzing the shots of each class separately then avoids an averaging over different dynamics. The purely data-driven approach does not involve theoretical modeling, such that it applies to a priori unknown effects.

Increasing the signal photon rate until sufficient time-domain data can be recorded using single x-ray shots [SR08] is a seemingly simple solution to the averaging challenge. XFELs [Bar+10; Dec+20; Emm+10; Ish+12] are routinely used for single-shot measurements involving electronic resonances [Bos+16; RSW19; URM12] and have recently moved this approach also within reach for Mössbauer resonances. As a first proof-of-principle experiment, Chumakov and co-workers extracted the nuclear hyperfine splitting in ^{57}Fe from single-shot data with about 60 signal photons [Chu+18]. Meanwhile, self-seeding enabled a further increase in the resonant x-ray flux [Ama+12; Ino+19; Liu+23; Nam+21]. This way, recently the ultra-narrow Mössbauer transition in ^{45}Sc could resonantly be excited [Shv+23] (c.f. Chapter 4). However, the corresponding observation of coherent nuclear forward scattering, which is the key requirement for most applications of Mössbauer nuclei, has not been reported before.

5.1.2 Proof-of-principle demonstration of Mössbauer single-shot analysis

Despite this progress, recording Mössbauer single-shot datasets beyond the proof-of-principle stage remains a challenge, since, due to the XFEL photon-number distribution [Gor+18], the shots with highest signal-photon number only form a negligible fraction of all shots [Chu+18]. The vast majority of shots typically does not have sufficient signal for a single-shot analysis. Increasing the x-ray intensity further is subject to sample damage, since the "probe-before-destroy" paradigm [Neu+00] established for electronic scattering cannot straightforwardly be generalized to Mössbauer nuclei due to the long lifetimes of the nuclear excited states. This is particularly important if focusing to smaller excitation volumes is desired in order to avoid extensive spatial averaging. Recording Mössbauer single-shot data is further limited by the dynamical range of the commonly-used APDs, since the overall exponential decay of the scattered photon intensity typically spans over several orders of magnitude, thereby exceeding the linear detection range. As an example, in the present experiment, we observe APD saturation effects at early times in the shots with highest signal-photon number, even though they resolve the nuclear dynamics only for about 50 ns after excitation. Another challenge is the desired scope of single-shot measurements, which is to probe non-repetitive phenomena. In [Chu+18], a known theory was fitted to the data in order to extract a single parameter, namely the frequency of an oscillation throughout the entire time-domain. By contrast, lifting the requirement to average over many shots is particularly important if the phenomenon under study has a comparably subtle effect on the time-domain data. Further, the requirement of fitting theory models restricts the analysis to known effects.

We overcome these challenges in directly recording and evaluating Mössbauer single-shot datasets using a sorting approach on the single-shot level.

5.1.3 Single-shot sorting in other areas

Note that sorting approaches are well-established, e.g., in the context of coherent diffractive imaging [Dol+25; Sch15; SWC12; Zim+23], where the scattering data is used to determine the sample orientation on a per-shot basis. However, this classification is concerned with geometric properties, and not with dynamics. Another example is coherent correlation imaging [Klo+23], which classifies recorded camera images in Fourier space. Measure-and-sort approaches are also used involving auxiliary diagnostics measurements, e.g., to determine the unknown delay between optical pump and XFEL probe pulses [Har+13], or to characterize XFEL pulses temporally [Fun+24; Har+18] and spectrally [Str+22]. However, analogous approaches have not been explored with nuclear resonances before, and standard XFEL diagnostics do not straightforwardly apply to nuclear resonances because of their ultra-narrow spectral width, which typically cannot be resolved.

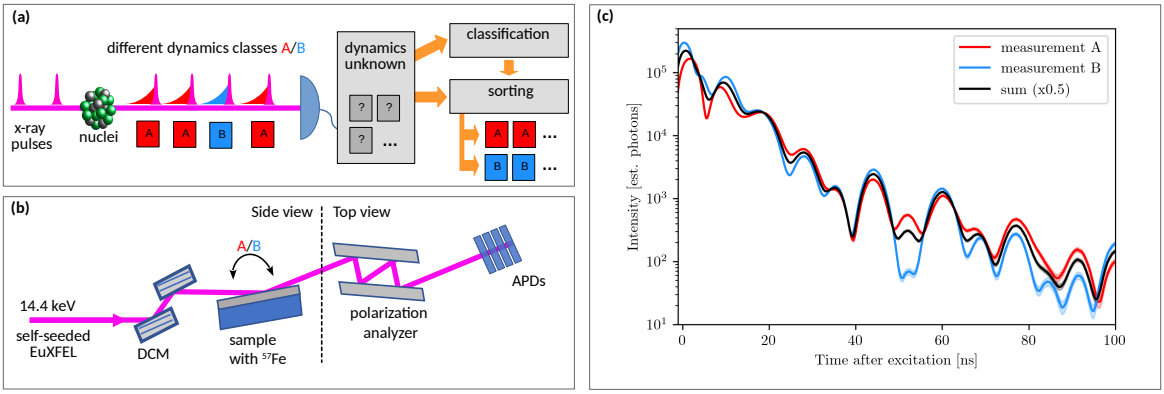

Figure 5.1: (a) Single-shot sorting. We consider a generic experiment in which Mössbauer nuclei may undergo different dynamics following an x-ray excitation. Two dynamics classes "A" and "B" are indicated in red and blue as examples. The information on the dynamics is typically lost for most shots during the measurement (gray squares). Our data-driven approach identifies different dynamics classes, and subsequently sorts all shots according to the identified classes. This way, the classes can be analyzed separately, avoiding an averaging over different dynamics. (b) Schematic experimental setup at European XFEL. The self-seeded x-rays pass through a double-crystal monochromator (DCM), which removes the SASE background, and are then reflected from a thin-film waveguide containing ^{57}Fe nuclei. The nuclear-resonant signal and the off-resonant background are separated using a polarization analyzer. The time-dependent intensity of the x-rays scattered by the nuclei is then recorded using APDs. The two dynamics classes are deterministically implemented using slightly different scattering geometries, as explained in the main text. (c) Average intensities as a function of time after x-ray excitation for dynamics classes A (red) and B (blue) separately, as well as their average (black). Only the latter signal is accessible without per-shot information on the dynamics. The shaded areas around the lines indicate the 1σ uncertainty band (see Section 5.2.2).

5.2 Experimental details

5.2.1 Experimental setup

The schematic setup of our approach was mainly developed by the groups in Hamburg and Jena and is illustrated in Fig. 5.1(a). We consider a generic Mössbauer experiment at an XFEL source (Fig. 5.1(a)) comprising a large number of shots, each initiated by the arrival of an x-ray pulse. After each x-ray excitation, detectors record the time-dependent scattered light intensity as a signature of the nuclear dynamics. As an example, one of two dynamics classes (A or B) is randomly realized in each shot. For most shots, the information on the dynamics class is not accessible by standard measurement approaches due to insufficient signal photon statistics, as indicated by the gray squares. Our goal therefore is to sort the data on a single-shot level such that the dynamics classes can be distinguished and analyzed separately.

In order to demonstrate our approach, we performed an experiment at the Materials Imaging and Diagnostics (MID) instrument of the European XFEL [Mad+21]. The schematic setup is shown in Fig. 5.1(b). The XFEL was operated in self-seeding mode [Liu+23] with an average pulse energy of 170 μJ and bandwidth of 1.2 eV. The accelerator was operated in the 2.2 MHz mode, with 30 pulses per train and 440 ns separation between two subsequent pulses, which matches the nuclear life time very well. The photon energy was set to the nuclear resonance energy of 14.4 keV employing absolute energy measurements via the Bond method [Bon60]. The incoming self-seeded x-rays pass MID's Si(111) double-crystal monochromator (DCM) with about 1 eV transmission bandwith, in order to remove the off-resonant SASE background. The x-rays are naturally polarized in the horizontal plane, and a channel-cut Si(840) polarization analyzer in crossed setting is used to block this polarization channel, thereby protecting the APDs from the incident beam. The ^{57}Fe Mössbauer nuclei are embedded in a thin-film waveguide sample (structure fitted to be Si/Pt(14.8 nm)/^{57}Fe(15.3 nm)/Pt(2.1 nm)[Ger+25b]) aligned to reflect the beam in grazing incidence geometry. A weak external magnetic field is applied to align the nuclear magnetization along the beam propagation direction, so that the circular polarizations are eigen-polarizations and the incident horizontal linear σ-polarization experiences strong scattering into the perpedicular π-polarization. This polarization component will pass the analyzer and its time-dependent intensity is recorded with

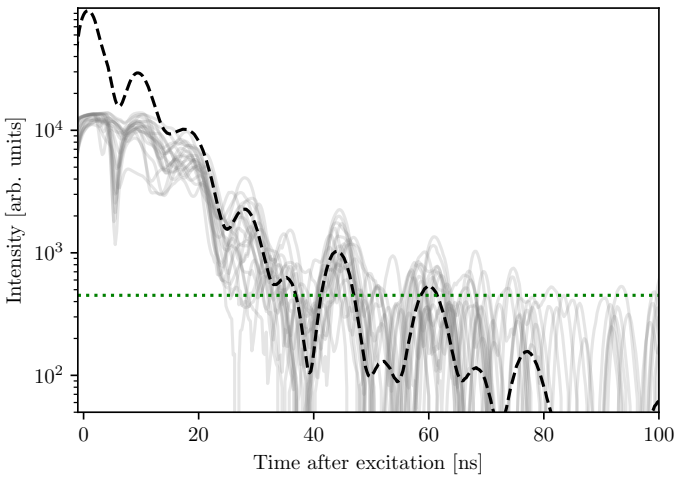

Figure 5.2: Example high-signal shots. Out of the full dataset, the 20 shots with highest signal content are shown in gray. The lines are plotted semi-transparent. This way, for example, the individual single-photon detection events at late times can be distinguished from the overlapping data at early times via the plot density. The black dashed line displays the time-domain data averaged over the full dataset. The green dotted line indicates the average height of the APD signal for individual recorded photons.

APDs. An averaged detection signal is shown in Fig. 5.1. Examples for single shot raw data with high, medium and low signal content are shown in Fig. 5.5 and are discussed in Section 5.2.2.

To allow for a quantitative assessment of our approach, we designed the experiment such that it features two different dynamics classes, and that it is known which shot belongs to which class. To this end, two separate measurements are performed using a single target, but for two slightly different incident angles of the x-rays onto the waveguide (4.15 mrad and 4.03 mrad obtained by fitting [Ger+25b]), which represent the two dynamics classes (indicated as A/B in Fig. 5.1(b)) . This way, the time-domain data of each of the two classes can be obtained separately by averaging over the data of each measurement for later reference. This information is blinded in the actual analysis. The two measured reference datasets averaged over all shots of each subset are shown in Fig. 5.1(c). They can be well-described by standard low-excitation theory [Ger+25b], and exhibit characteristic differences at around 5 ns after excitation, around 50 ns, and after 70 ns. Note that the measured data are not histograms of signal photon arrival times, as they are established, e.g., for nuclear resonant scattering experiments at synchrotrons. Rather, they are sums of the full APD detector signals, since a disentangling of shots with tens or even hundreds of signal photons into individual arrival times is challenging (see Fig. 5.2).

5.2.2 Detected signal

Detection

Since the individual shots contain up to several hundred signal photons, the majority of which arrives in a comparably short time interval after the x-ray excitation, the employed APDs cannot distinguish the individual arriving photons. Therefore, rather than counting arrival times, we record the entire time-dependent voltage traces of the APDs using fast digitizers. As a result, the recorded time-domain data is convoluted by the detector response. For isolated signal photons, the detector response can be modeled using a Gaussian envelope of about 2.5 ns temporal full-width at half maximum. In order to estimate the uncertainty of the measurements, the recorded voltage traces are scaled with the area of the single-photon detector response, such that the area under the curve is equal to the estimated integrated number of photons. Subsequently, a Poissonian uncertainty can be applied.

Raw data

In Fig. 5.2, the 20 shots with highest signal content are displayed. For comparison, the reference time-domain data obtained by averaging over all shots is displayed as the black dashed line. There are three important observations. First, up to 20 ns there is a strong deviation in the recorded

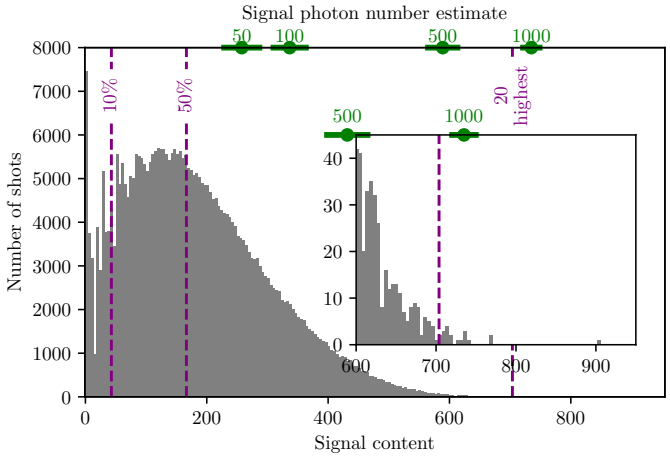

Figure 5.3: A histogram of the signal content in the single shots. Estimates on the corresponding photon numbers and their uncertainties are indicated by the green bars on the top axis. For details on the photon number estimate see the "Signal content" in Section 5.2.2. In addition, the purple dashed lines indicate low (10% of the traces), medium (50% of the traces) and high (20 highest traces) signal content as used in Fig. 5.5. The inset shows a zoom into the highest signal region.

intensity of the single shots as compared to the averaged time-domain data. This can be attributed to saturation effects in the detector, due to the limited dynamical range of the APDs employed in the experiment. This saturation is most pronounced at early times due to the overall approximately exponential decay of the scattered intensity with time. Furthermore, the saturation is strongest for the shots with highest signal content shown in the figure. By contrast, the majority of shots has a lower signal content, and therefore is less affected by the detector saturation. As a result, the averaged data deviates from the shots with highest signal content, and better represents the true amount of light scattered by the nuclei. Second, we can analyze whether the individual shots with highest signal content contain sufficient count statistics to allow for an analysis of the time-domain data on a single-shot basis. We find that this is indeed the case at short times, although bounded by the saturation effects discussed above. However, at times later than approximately 50 ns after the excitation, the recorded single-shot intensities approach the level of individual recorded photons, such that the dynamics can no longer be reconstructed reliably. Finally, we find that at times around 5 ns, the data of the subset of shots with highest signal content clearly divides into two different subsets. One exhibits a pronounced dip in the intensity, while the other subset remains approximately constant. This feature is reflected by the region of interest from 3 ns to 7 ns identified by the clustering approach in Section 5.3.2. Other features distinguishing the two dynamics classes A and B in our measurement are visible at later times in the averaged time-domain data (see Fig. 5.1(c)), but they cannot be resolved on the single-shot level due to the low statistics. Around $t = 0$ ns, the averaged time-domain data comprise prompt scattering contributions, which can be attributed to the finite polarization extinction of the analyzer, the convolution of the signal with the single-photon detector response, and to background photons. Instead, the distinct feature at around 5 ns also appears in the corresponding idealized theory calculation, and can be attributed to the first quantum beat due to the interference of different scattering channels between the involved hyperfine states.

Signal content and photon number estimate

Because the signal content should not be dominated by the high statistics at early times, but should account for a signal spread out over the entire analysis region, the signal content is defined by the area under the logarithm of the APD trace. The logarithm suppresses early-time contributions and enhances the relative importance of later times. A histogram of the distribution of signal content is displayed in Fig. 5.3. In addition, in Fig. 5.3 an estimate on the photon number corresponding to a certain range of signal content is given. To this end, 1000 single-shot traces with a specific photon number N are simulated by drawing N random numbers from the averaged time-domain data and summing up the single-photon detector response of those. For those artificial traces the signal content is calculated. To avoid influence of the saturation effects, the signal content is evaluated only after

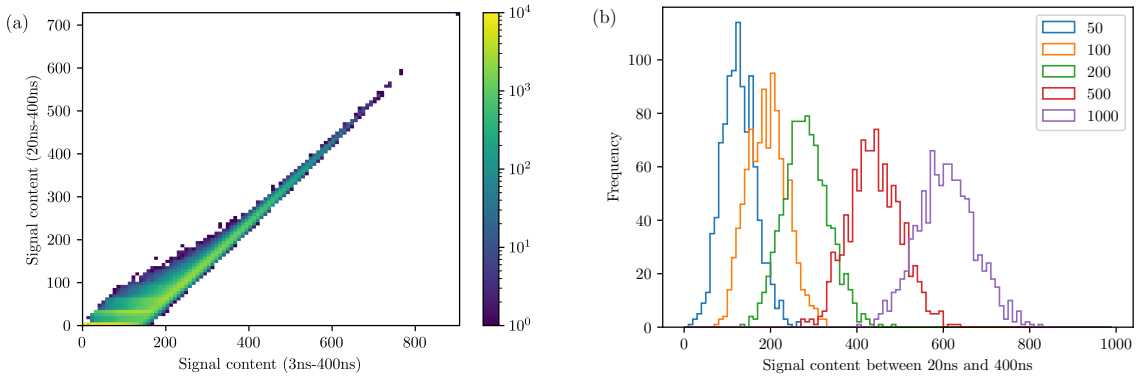

Figure 5.4: Analysis for photon number estimate. (a) Histogram correlating the signal content between 3 ns to 400 ns as used in the main analysis to the signal content between 20 ns to 400 ns. The colors indicate the number of traces. (b) Histogram of the signal content between 20 ns and 400 ns of the simulated traces. For each photon number N, which is represented by the different colors, N arrival times are drawn randomly from the mean time spectrum and convoluted with the single pulse response to receive a simulated trace and calculate the corresponding signal content. Repeating this process 1000 times results in the displayed histograms.

20 ns. This is a valid approach due to the good correlation between the signal content evaluated from 3 ns onwards and the signal content evaluated from 20 ns onwards, which is displayed in Fig. 5.4(a). Histograms with the signal content evaluated from 20 ns onwards of the 1000 simulated single-shot traces are displayed in Fig. 5.4(b) for different numbers of photons N used in the simulation. For each N this results in an approximately Gaussian distribution. Finally, for all shots in our measured dataset, whose signal content from 20ns onwards lies within the 1σ interval around the mean of the Gaussian distribution, the mean and standard deviation of the signal content over the whole time range is calculated. This is the estimated signal content and its uncertainty for a given photon number N, which is indicated by the green dots and errobars in the figure. It is important to note that the shots with highest signal content are statistical outliers, and the 20 spectra shown above only constitute a tiny fraction of the 362.610 shots measured during the experiment (181.350 shots for A, and 181.260 for B). To illustrate this further, example shots with high, medium and low signal content are shown in Fig. 5.5. For the high signal content shots, the ten shots with highest signal content are used, for medium signal content the ten with highest signal content out of the lower half and for low signal content the ten highest out of the lowest 10%. The respective cutoffs are shown in Fig. 5.3 as the dashed purple lines. In the high-signal single-shot data, the difference at around 5 ns is clearly visible while later features already lack statistics. In the shots with medium signal content, the differences at around 5 ns are still partially visible, while the low signal shots contain only a small number of photons.

5.3 Single shot sorting of Mössbauer time domain data

5.3.1 Overview

For the analysis, we do not use any of the prior knowledge about the sample or measurement geometry throughout the analysis. Instead, the information on the dynamics class is eliminated by combining the different shots of the two measurements into a single dataset, with its average shown as the black line in Fig. 5.1(c). The analysis sequence is illustrated in Fig. 5.6. The first step is to identify dynamics classes (model 1 and 2) in the "blinded" data (indicated by the gray rectangles), which can then be used to sort all shots accordingly. For this clustering step, only a selection of the shots with the highest signal content is used, which circumvents the statistical uncertainty in the data associated with low-count shots. This way time-domain data representing the specific features of each class can be extracted more reliably from the measured data. In the following we denote this step as model-building. Generally, Mössbauer time-domain data features an approximately exponentially decaying scattered light intensity, due to the spontaneous emission of the nuclei. Shots suitable for the model-building should ideally contain information, i.e., recorded signal photons, across a broad time range

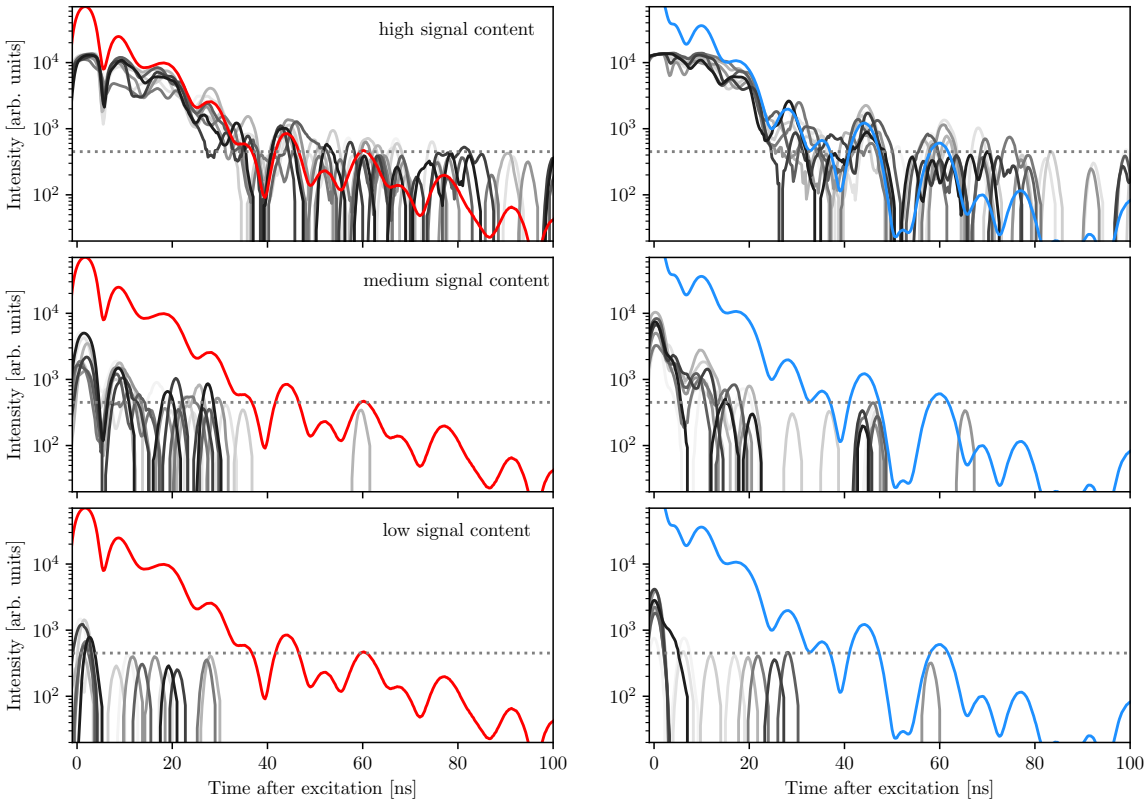

Figure 5.5: Example single-shot time-domain data. For measurement A (left column) and B (right), ten single-shot examples with high (top row), medium (center) and low (bottom) signal content, respectively, are shown in different shades of gray. The selected traces are the ones with highest signal content overall (high), of the lower half of the shots according to the signal content (medium) and of the lowest 10% of the shots according to the signal content (low) In red (blue) the averaged data belonging to measurement A (B) are displayed. The gray dashed line indicates the average height of the APD signal for individual recorded photons.

after excitation, which is why the logarithm of the APD trace is applied to linearize this scaling. The signal content is then defined as sum over the logarithm of the APD trace (see Section 5.2.2). To avoid prompt artifacts from the intense incident x-ray pulse, the first 3 ns are excluded from the analysis (see Section 5.2.2).

5.3.2 Clustering of highest signal content traces

In order to search for the presence of different dynamics classes, we employ an agglomerative clustering algorithm [Jr63] on the set of the N_{hs} shots with highest signal content. The clustering is based on calculating the pairwise distances between the N_{hs} shots. As a distance measure $d(a,b)$ between two shots a and b, we use the negative Poissonian log-likelihood $P(a,b) = -\sum_i a_i \cdot \ln b_i - b_i - \ln\Gamma(a_i+1)$, symmetrized by using the maximum of both directions $d(a,b) = \max\left[P(a,b), P(b,a)\right]$ and evaluated within an analysis region of interest (ROI) on the time axis. As illustrated in the "clustering" box in Fig. 5.6, the two closest shots are joined into a single cluster. This clustering step is then repeated until only two clusters remain (For the result when enforcing three clusters see Fig. 5.10 and Section 5.3.4). We employ the complete-linkage measure [Joh67] to quantify the distance between two clusters, which is defined by the maximum of the pairwise distances between individual elements of the two clusters.

Next, we assess if the data indeed comprises different dynamics classes, by evaluating the quality and consistency of the clustering. For this, we use the silhouette score [Rou87], which quantifies how similar a shot is to the other elements of its own cluster, on a scale given by its distance to the other clusters. The measure compares the distance $\bar{d}_i$ of shot i to the averaged time-domain data of its own cluster normalized by its standard deviation, with the respective distance $\bar{d'}_i$ to the second cluster. The silhouette score of a cluster then is evaluated as $s_i = (\bar{d}_i - \bar{d'}_i)/\max\{\bar{d}_i, \bar{d'}_i\}$, and thus ranges from -1 to $+1$. A high score requires that the distance of shot i to its own cluster is much smaller

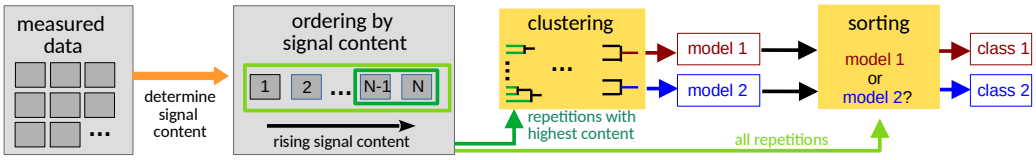

Figure 5.6: Overview of the clustering and sorting. A subset of shots with highest signal content is used to identify different dynamics classes using a clustering algorithm. The resulting two models are then used as a reference in order to sort all shots of the experiment into corresponding sets which can then be analyzed separately.

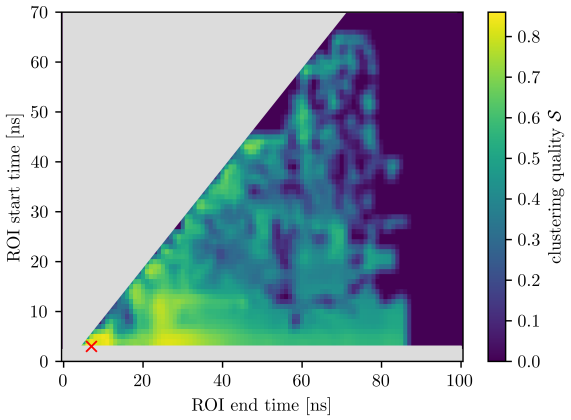

Figure 5.7: Overall clustering quality $\mathcal{S}$ as a function of the analysis region of interest start and end times. Results are shown for the subset of $N_{\mathrm{hs}} = 20$ shots with highest signal content. A moving Gaussian average filter of width $\sigma = 1\,\mathrm{ns}$ was applied to the data to reduce the influence of outliers and to favor stable analysis parameter regions. The lighter the color, the better the clustering quality $\mathcal{S}$, with the optimum found for the analysis ROI of (3 ns, 7 ns) and marked by the red cross. In gray invalid regions are marked.

than the distances to the shots of the other clusters, $\bar{d}_i \gg \bar{d'}_i$. Therefore, a high mean silhouette score $\bar{s}_j$ averaged over all elements in cluster j indicates that indeed a separate dynamics class was successfully identified in the data. As a measure for the overall clustering quality $\mathcal{S}$ of both clusters, we use the minimum of the average scores of the two clusters $\mathcal{S} = \min_{j\in\mathrm{clusters}}\{\bar{s}_j\}$ to ensure that both dynamics classes are well-represented. This clustering quality measure can be simply extended to more clusters and can be used to identify the optimal number of clusters, which in our case results in two clusters as expected.

In order to determine the optimum analysis parameters, i.e., the number of highest-signal shots N_{hs} and the analysis ROI, we maximize the clustering quality $\mathcal{S}$. For this, the above analysis is systematically repeated for different numbers of shots N_{hs} and analysis ROIs. This way, the analysis parameters for the model building are fixed based on the experimental data without the need for prior knowledge about the system, nor theory modeling of it. As an example, we show the overall clustering quality $\mathcal{S}$ as a function of start- and end time of the analysis ROI for $N_{\mathrm{hs}} = 20$ shots in Fig. 5.7. In order to reduce the influence of outliers and to favor stable analysis parameter regions, a narrow moving Gaussian average filter of width $\sigma = 1\,\mathrm{ns}$ is applied to the clustering quality $\mathcal{S}$ in this figure. We find that best clustering qualities are grouped in certain ROI ranges, and we select the optimum ROI via the maximum of the clustering quality, indicated by the red cross in Fig. 5.7. Early times for the ROI are likely favored since the signal rate rapidly drops with time after excitation due to the exponential decay. We found that the clustering quality $\mathcal{S}$ is maximized by including the $N_{\mathrm{hs}} = 20$ shots with highest signal content out of all 362,610 shots into the model building, and by using an analysis ROI between 3 ns and 7 ns. Note that the clustering quality and the optimum ROIs are similar over a broader range of N_{hs}, which indicates that the analysis is stable against variations in the analysis parameters.

The assessment of the clustering algorithm is based on the overall clustering quality $\mathcal{S}$. As a more detailed consistency check for the clustering, the individual silhouette scores of the shots used for the model building are shown in Fig. 5.8 for the optimum analysis parameters $N_{\mathrm{hs}} = 20$ and analysis ROI between 3 ns and 7 ns. Each horizontal bar represents the silhouette score of a single shot with the

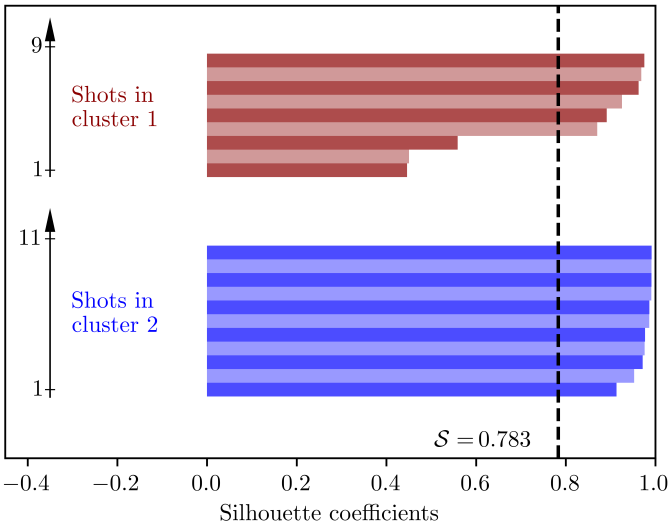

Figure 5.8: Individual silhouette coefficients for the shots used in the model building. The figure shows the individual silhouette scores of the $N_{\mathrm{hs}} = 20$ shots of the experiment used for the model-building. The ROI for comparing different shots ranges from 3 ns to 7 ns. Each bar represents one shot with the colors indicating to which cluster the respective shot belongs. There are 9 shots in cluster 1, and 11 in cluster 2. The mean clustering quality $\mathcal{S} = 0.783$ is represented by the dashed black line.

colors indicating the cluster, to which the shot belongs. For better visibility, the clusters are spatially separated. A large fraction of the shots has a silhouette score larger than 0.5, many even larger than 0.8, indicating good clustering [KR05]. However, a few shots have a small silhouette score indicating that they do not so clearly belong to either cluster. Nonetheless, those outliers are only few and together with the fact that a stable ROI is found, which is similar for different number of high-signal content shots N_{hs}, the model generation is reliable.

After having identified the optimum analysis parameters based on the clustering quality $\mathcal{S}$, a further consistency check is possible by analyzing the individual silhouette scores s_i of the different shots in all clusters. Indeed, we find that our approach identified two clusters comparable in size, and that the majority of shots in both clusters has a high individual silhouette score.

5.3.3 Sorting of all traces

Once the dynamics classes are identified and corresponding models are generated, we proceed with the entire set of measured shots, independent of their signal content, and assign each shot to one of the models (see "sorting" in Fig. 5.6). Note that this comparison of individual shots with the generated models has a crucial advantage over the direct comparison of individual shots. A direct comparison of two shots with low signal content is subject to comparably high statistical uncertainties. In contrast, the statistical fluctuations are greatly reduced in the models comprising a number of shots, such that a comparison of a low-signal shot with one of the models is more reliable. For this comparison, we employ the negative Poissonian log-likelihood $P(a, b)$, regarding the individual shots as the data to be tested against the models. This sorting step results in one set of shots for each of the dynamics classes determined throughout the sorting.

The two sets of sorted data can now be analyzed individually. Summing over each set separately results in two time-dependent intensities, which reflect the nuclear dynamics in the two respective dynamics classes, and form the main results of the data-driven analysis. They are shown as solid lines in Fig. 5.9. The two time-dependent intensities clearly differ at certain times, e.g., around 5 ns and 50 ns as well as from 70 ns to 90 ns, indicating that the clustering algorithm indeed identified different types of dynamics. In order to verify the data-driven analysis approach, we finally unblind the information on the experimental settings for each of the shots, which we have due to the specific design of the underlying experiment, but which was not used during the data-driven analysis. The resulting "true" reference time-domain data for the two different dynamics classes are shown as dashed lines in Fig. 5.9. We find that the results of the data-driven analysis indeed follow the reference measurements closely. In particular, the regions with characteristic higher deviations between the

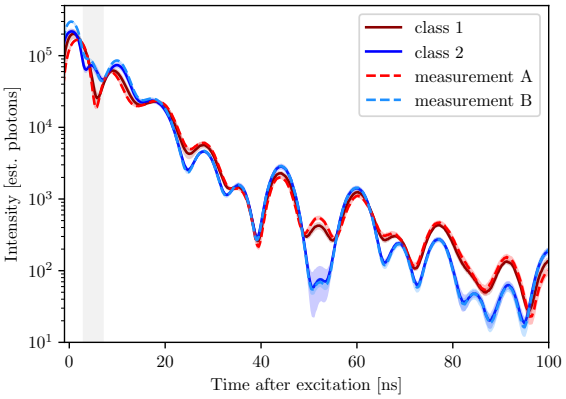

Figure 5.9: Measured time-domain data in experimental settings A (red dashed) and B (blue dashed), which serve as a reference to benchmark the analysis. The 1σ uncertainty band of the measurements is indicated by the shaded area around the respective lines (see Section 5.2.2). The corresponding results of the data-driven single-shot analysis (class 1 and 2) are shown as solid lines. Here an estimate of the uncertainty based on the data variability is given by the standard deviation of the subset analysis in see Section 5.3.4, which is drawn as the shaded band around the lines. The two time-domain datasets are scaled for better comparability by fitting an overall scaling factor from 0 ns to 100 ns. The ROI (3-7 ns) used for the analysis is indicated in gray.

two dynamics classes are well-reproduced in both cases. Interestingly, the regions around 50 ns, or after 70 ns, are well-recovered even though they are far outside the analysis ROI from 3 ns to 7 ns used to generated the original models. Note that deviations at initial times up to 4 ns are likely due to saturation effects (see Section 5.2.2).

5.3.4 Stability of analysis

The stability, reproducibility and consistency of the analysis can be tested in various ways. First, we artificially create repetitions of the experiment with different statistical realizations of the photon detection by dividing the full dataset randomly into 5 subsets. Note that this division at the same time corresponds to a reduction of the effective measurement time realized in the experiment by a factor of 5, thereby rendering the analysis more challenging. Subsequently, the complete sorting algorithm described in the main part is applied to each of the subsets. To improve the statistics of this analysis, we repeat this procedure ten times with new randomly chosen subsets. Afterwards, the 50 reconstructed time-domain datasets can be compared to each other and their standard deviation at any instance in time provides an estimate of the uncertainty of the analysis due to data variability. For the sorting analysis discussed in the main part, the uncertainties are indicated as the shaded areas around the respective lines in Fig. 5.9. It can be seen that the uncertainties are small compared to the difference between the averaged time-domain data of the two measurement sets, such that they can reliably be distinguished.

Next, we can use a stability analysis in order to verify the identification of dynamics classes, as shown in Fig. 5.10. As a first test, we perform the analysis only on the shots belonging to one of the measurements, A or B, while still enforcing the determination of two clusters in the clustering analysis. The results are shown in the left panel (a) of Fig. 5.10. The red and blue solid lines display the recovered averaged time-domain data of the two classes. The dashed lines show the recovered time-domain data of Fig. 5.9, corresponding to class 1 (red dashed) and class 2 (blue dashed) as a reference. For better clarity, the two cases with data of measurement A and measurement B are shifted with respect to each other along the y-axis. We find that the two recovered datasets (test class 1 and test class 2) agree within their uncertainty, such that we conclude that the algorithm did not identify different dynamics classes. Furthermore, the recovered averaged time-domain datsets agree with the reference data for measurement A in case that the shots of A were used for the analysis, and analogously for B. Thus, the analysis works as expected.

In a third test, we repeat the main analysis with data of both measurements A and B, but allow for three clusters in the clustering analysis. The corresponding results are shown in the right panel (b) of Fig. 5.10. As a first observation, we find that the overall uncertainties are considerably larger

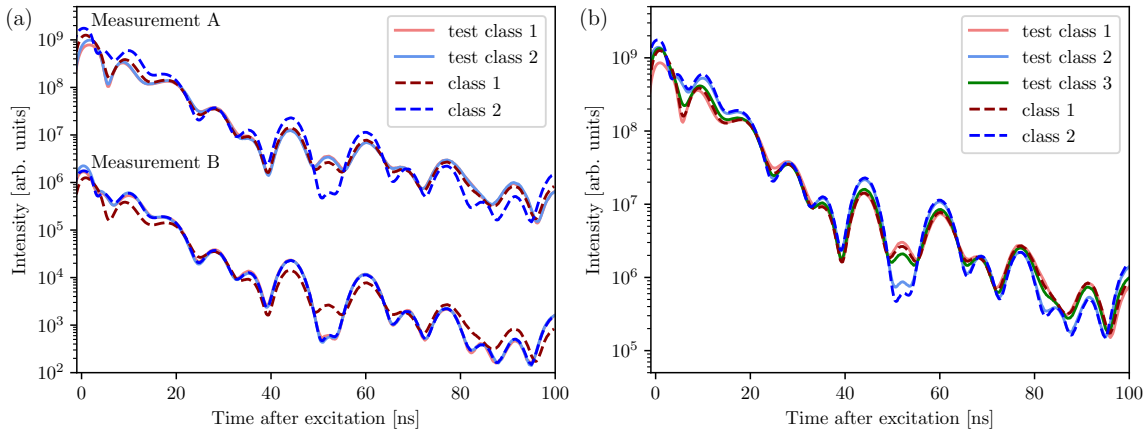

Figure 5.10: Stability of analysis. (a) In the top part of the panel, the analysis is only performed on the shots from measurement A. The lines "test class 1/2" show the time-domain data of the two classes reconstructed from the subsets. For comparison, the dashed lines ("class 1" and "class 2") represent the analysis results of the full dataset in Fig. 5.9. It can be seen that for the dataset restricted to measurement A, the two recovered classes agree with each other within their uncertainty, as expected. Furthermore, they agree well with "class 1", which corresponds to measurement A. For completeness, the same analysis is performed with the data only from measurement B and shown in the lower part of the panel. For better visibility, the results for data for the two measurement settings are shifted along the y-axis such that they can be better distinguished from each other. (b) Results of the sorting analysis applied to the full dataset comprising measurement settings A and B, but with clustering into three classes. The results of these three test classes are shown as solid lines. The time-domain data is scaled for better comparability by fitting an overall scaling factor in the time range from 0 ns to 100 ns. The uncertainty bands of the different sets are calculated by a statistical analysis as explained in Section 5.3.4. As a reference, also the results of the sorting analysis in Fig. 5.9 are displayed in addition (dashed lines "class 1" and "class 2").

than in the case with two clusters (see Fig. 5.9), indicating a less reliable analysis. Second, we find that two of the recovered time-domain data (test class 1 and test class 3) agree well with each other, within their respective uncertainties. They also agree well with the reference data "class 1" obtained with the analysis involving only two clusters in Fig. 5.9. Correspondingly, the third of the recovered time-domain data (test class 2) agrees well with with the second reference data "class 2". Thus, the analysis is consistent with only two dynamics classes in the data, as expected.

Overall, we therefore conclude that the sorting algorithm works as expected, in particular with regards to the correct number of dynamics classes extracted from the data.

5.4 Summary and Outlook

We have demonstrated the possibility to perform coherent nuclear forward scattering experiments using self-seeded XFEL radiation. The exceptionally high resonant flux per shot unlocks fundamentally new applications for Mössbauer nuclei. In particular, our results demonstrate the possibility to disentangle different evolution pathways from the out-of-equilibrium state back into equilibrium by analyzing time-domain datasets on the level of single shots. For this, we identify different dynamics classes and sort the data accordingly. Since the clustering analysis is data-driven and does not require a theoretical modeling of the data, also previously unknown phenomena can be searched for. The analysis can readily be applied to standard experimental approaches, without the need for dedicated measurements or instrumentation.

Importantly, we found that our sorting analysis is capable of clearly revealing the differences in the two dynamics classes also for times larger than approximately 50 ns after excitation. By contrast, even the rare shots with highest signal-photon number do not contain sufficient counts to resolve these differences in the dynamics directly, due to the overall approximately exponential decay of the scattered light intensity with time (see Section 5.2.2). This highlights the advantage of the sorting approach over the direct single-shot analysis.

By repeating the clustering analysis for different final numbers of clusters, the most probable number of dynamics classes can be identified. In the present experiment, we find that an analysis

with two clusters yields the highest clustering quality and stability, consistent with the original experimental design (see Section 5.2.1). In practice, already a stable and reproducible identification of qualitatively different time-domain data is a clear indication that the experiment comprises different classes of dynamics (see Section 5.3.4).

We envision that the single-shot sorting approach applied to coherent forward scattering data recorded with self-seeded x-ray pulses will open up new applications for Mössbauer science. Broadly speaking, different dynamics classes can originate from the nuclei themselves, or from the surrounding host environment. Under XFEL excitation conditions, even the unperturbed nuclear relaxation dynamics of a multiply-excited nuclear ensemble back to the ground state comprises different sequences of coherent and incoherent emission events. The time-resolved observation of the emitted photons can project the nuclear ensemble onto entangled states [Thi+07], or correlate independent excitation volumes in the sample [Cab+99; Moe+07]. An analysis on the single-shot level provides a route towards the observation of the nuclear ensemble in a quantum state. Furthermore, a major contribution to the incoherent decay is formed by internal conversion [LMS17], such that our method provides an opportunity to study the interaction between the nuclei and the electronic environment in a controlled way. On the other hand, the majority of current-day applications of Mössbauer nuclei are related to studying the structure and dynamics of the surrounding host material. The host evolution may also impose different dynamics onto the nuclei, e.g., if it involves quantum-mechanical superposition states with probabilistic measurement outcomes. Our sorting approach opens an avenue to developing the nuclei as non-invasive high-resolution probes for the electronic, phononic and structural dynamics of the environment geared towards the unique excitation conditions at XFELs. At these machines, mostly interactions of the x-rays with electronic degrees of freedom are used to probe targets, while these electronic properties oftentimes are subject to the investigation themselves, such that the probe and the probed system are intrinsically intertwined. By contrast, nuclei form an independent subsystem, and thereby offer valuable complementary information. Key examples involve the dynamics after impulsive pumping of the electronic [KKR99], vibrational [VSK13], spin [Sad+21; Sak+17] or magnetic [Boc+21] state of the host material. We further envision the extension of the sorting approach to nuclear inelastic scattering [CR98; VSK13], which next to the study of phonons could also allow one to generalize XFEL Mössbauer studies to liquids, gases, plasmas, higher-energy nuclear transitions, "detect-before-destruct" approaches, or other samples with low probability for recoilless x-ray-nucleus interactions [Bar+96; Ser+06]. Furthermore, coherent control mechanisms with Mössbauer nuclei [Boc+21; Hee+21] could be transferred towards the single-shot domain.

Chapter 6

XFEL anomalies in nuclear resonant scattering

6.1 Motivation

Seeded XFELs provide orders of magnitude higher intensities than synchrotrons, typically within a bandwidth of about 1 eV. However, due to the narrow nuclear resonance, e.g., $\Gamma = 4.7\,\text{neV}$ for ^{57}Fe, only a tiny fraction of the total beam intensity is resonant. Therefore, at XFELs the response of the nuclei is expected to still be in the low-excitation regime [LKE25b]. A first experiment at SACLA confirmed this expectation by demonstrating that the time spectrum of an iron-borate sample in reflection geometry behind a high-resolution monochromator measured at an XFEL is the same as measured at a synchrotron [Chu+18].

However, during calibration measurements in our first experiment with ^{57}Fe at the European XFEL [57F22], we found totally unexpected behavior of scattering in the nuclear forward direction off an 8 μm thick enriched α-iron foil. While the time spectrum could be fitted with the standard theory presented in Section 2.1.4, the fitted thickness was to small. We call this unexpected behavior the *thickness anomaly* and continued to study it also in the next experiment [57F23]. In the new experiment, we could not only confirm the thickness anomaly, but in addition also found unexpected behavior when introducing attenuators in the experiment. The count rates and time spectra depend strongly on the amount of attenuating material upstream the sample although the total amount of attenuating material in the beam is kept constant. In the low-excitation regime, this is also unexpected and therefore called the *attenuator anomaly*. Understanding the origin of those two anomalies is crucial for further experiments, such as the original goal of measuring the collective Lamb-shift under XFEL conditions [57F22; 57F23], and to establish Mössbauer spectroscopy at XFELs.

Here, we present the data evaluation studying both anomalies in detail with the data from the second experiment [57F23]. Although the underlying physical mechanism is yet to be found, we discuss potential explanations. Finally, we shortly discuss a third experiment dedicated to analyze the anomalies in detail [57F25].

6.2 Thickness anomaly

6.2.1 Experimental setup

The experiment p3334 [57F23] was performed at the MID instrument [Mad+21] of the European XFEL [Dec+20]. The setup is shown in Fig. 6.1. Trains containing 30 pulses of hard x-ray self-seeded XFEL light with a total pulse energy, i.e., including the SASE pedestal, of approximately 200 μJ were

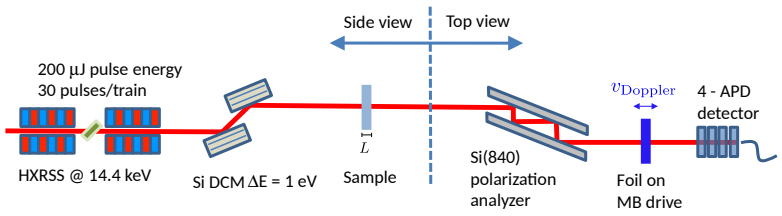

Figure 6.1: Experimental setup for thickness anomaly measurements. The self-seeded XFEL beam at 14.4 keV photon energy reaches the experiments in trains of 30 pulses with approximately 200 μJ pulse energy each. Afterwards, an optional monochromator can reduce the bandwidth to 1 eV. The sample is a stack of enriched ^{57}Fe-foils. A polarization analyzer removes the unscattered background. Optionally, a stainless steel foil mounted on a Mössbauer drive can be inserted to measure energy-time spectra. Finally a stack of four APDs records the arrival times of the x-ray photons.

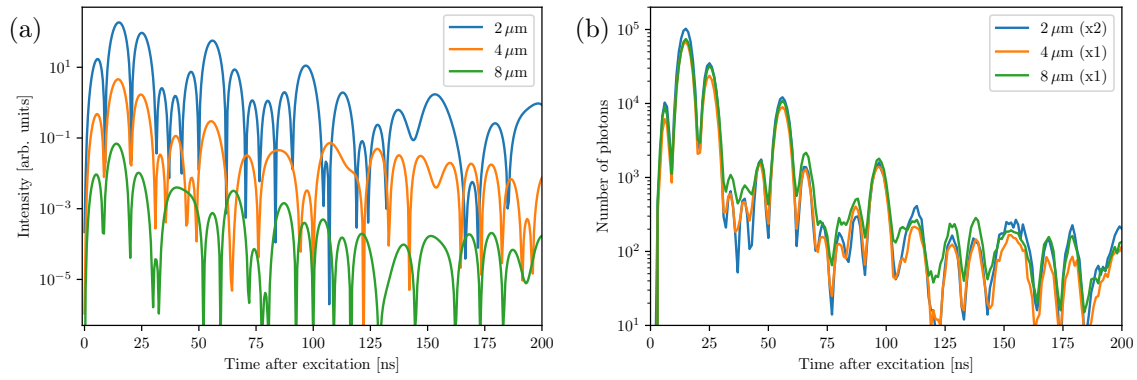

Figure 6.2: (a) Expected time spectra for the different foil thicknesses. For better visibility, the spectra are shifted vertically. (b) The measured time spectra for the foils of different thickness with monochromator. The spectrum of the 2 μm-foil is scaled for better comparability.

used. The XFEL light is intrinsically horizontally polarized. Optionally, MID's Si(111) double-crystal monochromator (DCM) was placed in the beam to reduce the bandwidth of the incoming light to 1 eV, thus effectively removing the SASE pedestal. The samples consist of stacks of one, two or four slices of an approximately 2 μm thick α-iron foil enriched with ^{57}Fe. Therefore, the samples are referred to as the 2 μm-, the 4 μm-, and the 8 μm-foil. The samples are placed in a magnetic field, which is perpendicular to the beam and rotated by 45° with respect to the beam polarization. Therefore, all six hyperfine transitions are driven and scattering into the other polarization component occurs. A Si-840 polarization analyzer [Mar+21] filters out the horizontal polarization component and thus the unscattered light. Otherwise, due to the high intensities at XFELs, the APDs would be too much saturated by the prompt pulse and blind for the delayed resonant photons. The scattered light can be rotated into the perpendicular polarization component and can thus pass the analyzer. It is detected with a stack of four APDs. To reduce saturation effects, in the case without DCM an approximately 1 mm-thick aluminum plate was placed before the APDs, in the measurements with DCM an approximately 0.5 mm-thick stack of aluminum foils.

6.2.2 Comparison of time spectra

In Fig. 6.2(a) the expected time spectra for the different foils are shown. The time spectra for different thicknesses vary because of the envelope Bessel function in Eq. (2.12), which depends on the thickness. The measured time spectra with monochromator are displayed in Fig. 6.2(b). It can be easily seen that the measured time spectra approximately agree with each other and all show a time spectrum roughly equivalent to that expected for a 2 μm-foil, but not corresponding to their actual physical thickness. This observation was unexpected and is therefore now called the *thickness anomaly*. Note that in the linear regime, the fact, that the foils in the experiment are no monolithic foils, but stacked foils should not make a difference. The first idea was that maybe, because the different slices are only loosely mounted between two Kapton foils, they are moving relative to each other, such that the 2 μm-parts do not add up coherently as expected, but incoherently. If the motion is slightly different for each pulse and at least on the order of a wavelength, which is 86 pm, this could lead to a thinner effective thickness. The effect of coherent versus incoherent interaction is discussed in more detail in Section 6.2.7.

The possibility to measure with and without DCM, which effectively is with and without SASE pedestal, allows to investigate the effect of the non-resonant SASE pedestal. Note that at synchrotrons the experiments are typically performed with high-resolution monochromators well below 1 eV[Röh04]. For the interpretation of the results, it should also be kept in mind that the DCM does not only reduce the bandwidth, but in addition has transmittance losses, and therefore leads to a reduced pulse energy on the sample. Assuming the standard theory, which is well-established at synchrotrons, there should be no difference for a monochromator with a bandwidth of approximately 1 eV as at MID because it is still many orders of magnitude wider than the resonance. In Fig. 6.3 for the 8 μm-foil the time spectra measured with (blue solid line) and without (red solid line) monochromator are compared. It can be immediately seen that they do not agree. For a quantitative analysis, the data can be well

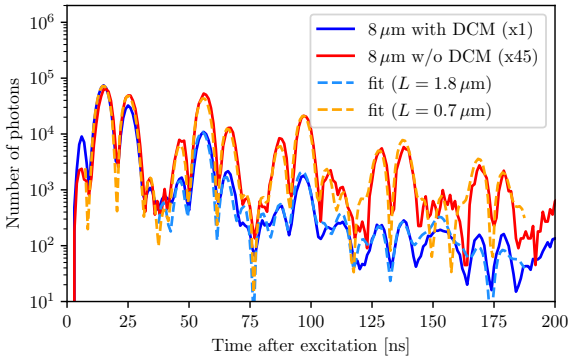

Figure 6.3: Comparison of time spectra measured with (blue solid line) and without (red solid line) monochromator for the 8 μm-foil. For better comparability, the time spectrum without monochromator is scaled. The dashed lines indicate respective fits with standard theory.

fitted with the standard theory in Eq. (2.12) (dashed lines), but the resulting thicknesses are

$$L_{\mathrm{w}} = 1.8\,\mu\mathrm{m} \quad \text{and} \quad L_{\mathrm{w/o}} = 0.7\,\mu\mathrm{m}\,, \tag{6.1}$$

for the measurements with and without monochromator, respectively. This is in strong contradiction to the standard theory, which does not predict any difference, and the physical thickness of $L_{\mathrm{actual}} = 8\,\mu$m. For the other foils the results are qualitatively similar.

The measurements without monochromator also rule out the potential explanation that the stacked foils do not add up coherently and thus the fit result is close to the thickness of the single foils in the stack. Furthermore, in the latest experiment p8006 [57F25] the samples were monolithic and the thickness anomaly still exists.

The fact, that the fitted thickness does not match the physical thickness under intense XFEL irradiation was very surprising. A more detailed analysis will be done in the following section. So far, this effect is not explained, but some ideas will be discussed in Section 6.2.7.

6.2.3 Pulse-resolved analysis

The train structure allows to disentangle effects on different times scales. While pulses within a train come every 440 ns, the time difference between the last pulse of the previous train and the new train is nearly 100 ms. Thus a pulse-resolved analysis can help to disentangle effects on short time scales within a train and long-term effects.

Count rates

At first, the count rates of the prompt pulse are analyzed in Fig. 6.4(a,b) for the different foils and the measurements with and without monochromator. It can be seen that they are clearly not constant over one train. This can be related to heating of the crystal optics, i.e., the monochromator and the polarization analyzer. During a pulse train the crystals heat up, which slightly changes the lattice plane distance and thus distorts the alignment. Until the next pulse train arrives, the optics have cooled down again. This is also the reason why only 30 pulses per train were used in the experiment as more pulses could not be well transported through the crystal optics. Furthermore, the count rates are highest for the thinnest foil and thus the lowest absorption in the beam as expected. The count rates with monochromator are higher because for the measurements without monochromator, a 1 mm thick aluminum foil ($\approx 10\%$ transmission) was placed in front of the APDs to avoid APD saturation and especially subsequent electronic ringing, while for the measurements with monochromator only a 0.5 mm thick stack of aluminum ($\approx 30\%$ transmission) is used. The transmission ratio approximately matches the count rate ratios for the different foils. Nonetheless, after correcting the count rates for the different amount of attenuating aluminum, the count rate in the measurements with monochromator are slightly lower, which is probably due to transmission losses of the monochromator.

For the delayed count rates, we notice that the thicker the foil, the higher the count rate, and the count rates have approximately similar ratios as the ratios of the thicknesses, which is the expected behavior. This seems obvious, but is a very important observation as it indicates, that even though

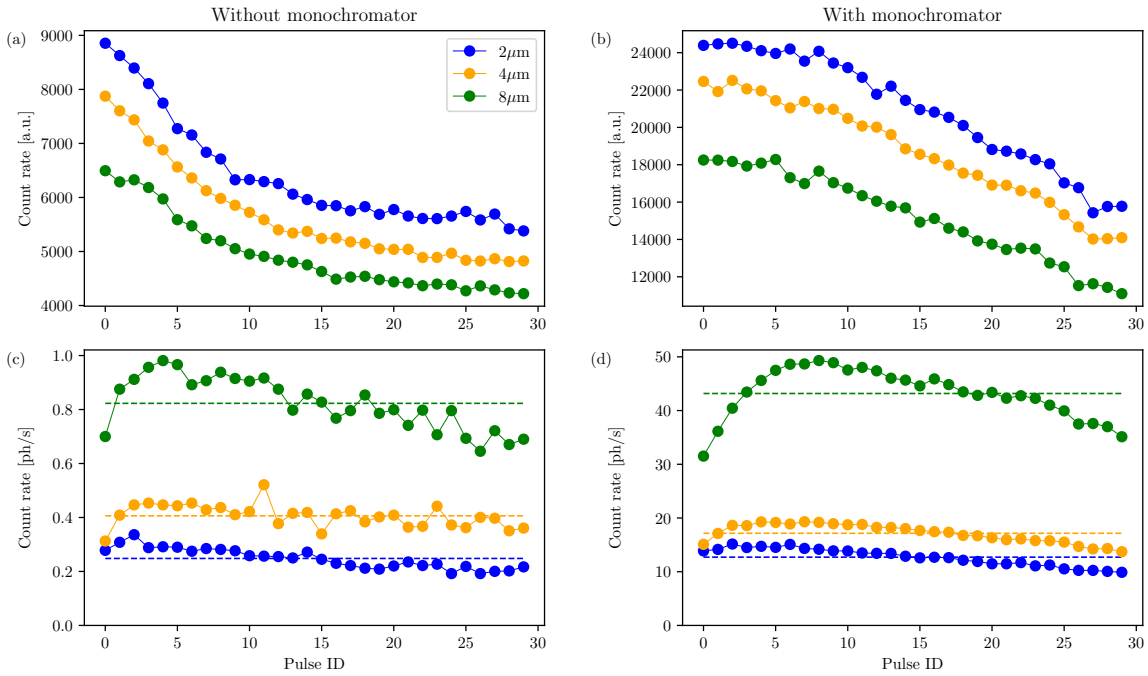

Figure 6.4: Count rates of prompt (a, b) and delayed photons (c,d) as a function of pulse ID in a train for the measurements without (a,c) and with (b,d) monochromator. For the prompt pulse, the APD traces are summed up over the whole run and integrated over the time window from -2.5 ns to 2.5 ns, because no photon arrival time extraction is possible. For the delayed counts, the number of photons between 5 ns and 400 ns after excitation is used. The different colors correspond to the different samples. The mean delayed count rates are indicated by the dashed lines of same color in (c,d). For the measurements without monochromator the mean count rates are (0.25±0.04) ph/2 (2 μm sample), 0.41±0.04 ph/s (4 μm sample) and 0.82±0.10 ph/s, (8 μm sample) for the measurements with monochromator 12.7±1.6 ph/2 (2 μm sample), 17.2±1.7 ph/s (4 μm sample) and 43 ± 5 ph/s, (8 μm sample).

the time spectra do not look as expected, the whole sample takes part in the scattering and not only the first 1 μm or 2 μm of the sample. Furthermore, the count rates with monochromator are approximately 50 times higher than those without monochromator with the same sample. This is unexpected, because the ratio is significantly higher than for the prompt pulse. Lastly, also the delayed count rates are not constant throughout the train but show a general trend of rising first and lowering at later times. Interestingly, the curve shapes are different as compared to the prompt count rates, which indicates that also the sample changes its behavior over a train.

Fitting of time spectra

For each foil and each pulse in the train a separate time spectrum can be generated and fitted with the standard theory presented in Section 2.1.4. Because of the small count rates for the measurements without monochromator, 5 pulses are combined to increase the statistics.

To find the global optimum of the fit parameters, a combination of evolutionary algorithms [Coe05; Rec78] and the standard Nelder-Mead [GH12] with the python library `scipy` [Vir+20] is used. To quantify the deviation of the theoretical model from the experimental data, a Poissonian likelihood distribution is used. This accounts for Poissonian shot noise, which is our main source of uncertainty in the time spectra. The Poissonian likelihood measures the probability [HJ01]

$$P(n_{\mathrm{exp,i}}|P_{\mathrm{theo,i}}) \propto (n_{\mathrm{theo,i}})^{n_{\mathrm{exp,i}}} \frac{e^{-n_{\mathrm{theo,i}}}}{n_{\mathrm{exp,i}}!}\,, \tag{6.2}$$

how likely it is to find $n_{\mathrm{exp,i}}$ counts in the experiment assuming a prediction of $n_{\mathrm{theo,\,i}}$ counts under the assumption of Poissonian shot noise. Using Bayes theorem [Dek+05], the reversed probability, which is needed for the fitting process, can be derived as [Len21]

$$P(n_{\mathrm{theo,i}}|P_{\mathrm{exp,i}}) \propto P(n_{\mathrm{exp,i}}|P_{\mathrm{theo,i}})\,. \tag{6.3}$$

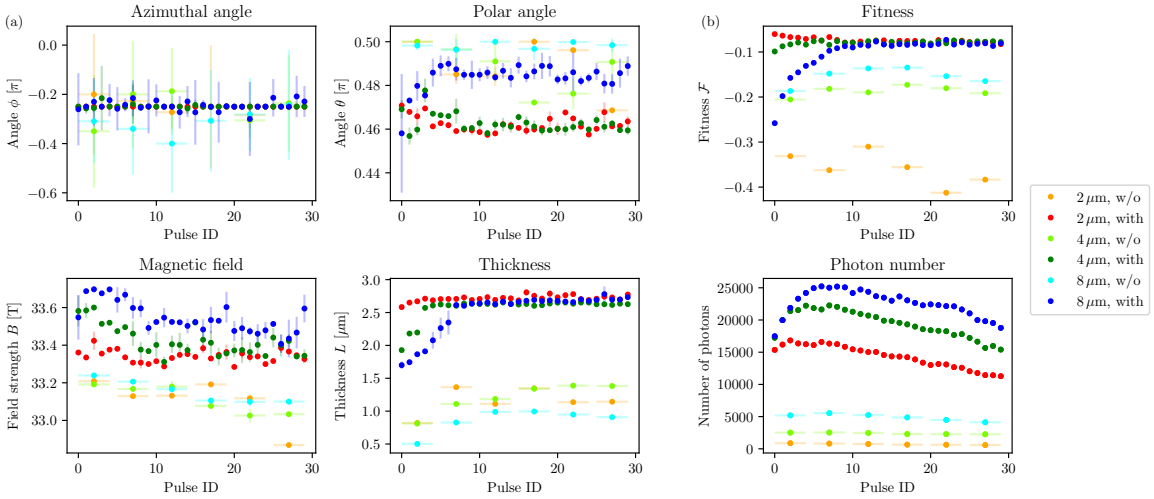

Figure 6.5: (a) Pulse-resolved fit results for different parameters and the normalized fitness of the fit. We fit the orientation of the magnetic field relative to the incident light polarization, which is characterized by the azimuthal ϕ and polar angle θ, the magnetic field strenght B and the thickness of the sample L. (b) The fitness $\mathcal{F}$ representing the goodness of the fit and the photon number as a function of the pulse ID. The different colors indicate the different datasets. The horizontal errorbars show combined pulses, the vertical the statistical uncertainties.

This is discussed in more detail in [Len21]. For numerical reasons typically, instead of the likelihood itself, its logarithm is used. Thus, the fitting fitness $\mathcal{F}$ is defined by a Poissonian log-likelihood [HJ01; Len21]

$$\mathcal{F} = \sum_i \log n_{\text{theo,i}} \cdot n_{\text{exp,i}} - n_{\text{theo,i}} - \Gamma\left(n_{\text{exp}} + 1\right) \,, \tag{6.4}$$

with the Gamma function $\Gamma(z)$. The larger this number, the higher the probability to measure the experimental data with the fitted parameters and thus the higher the fit quality. The evolutionary algorithms introduce some randomness to find the global minimum and are therefore not deterministic. To take this into account, each time spectrum is fitted ten times and the reported fit results are the mean values with the uncertainty given by the statistical standard deviation. The theoretical models for a given set of parameters are calculated with the python library `pynuss` [Hee19]. More details on the fitting procedure is given in Appendix A.1.

In Fig. 6.5(a) the fit results for the different foils are displayed and will be discussed in the following. The respective fits can be found in Figs. A.1 to A.6. To better interpret the results, in Fig. 6.5(b) the fitness $\mathcal{F}$ and the integrated photon number are shown. It can be clearly seen that the time spectra with monochromator have higher fitnesses than those without. This should be kept in mind when analyzing the fit parameters. In general, we see modifications of the fit parameters with the pulse ID, which are correlated with the photon number. The photon number modifications over the train are due to varying transmission through the x-ray crystal optics caused by heating.

The first two parameters define the direction of the magnetic field via azimuthal and polar angle with respect to the beam axis. In principle, in the given setting with the analyzer perpendicular to the incident polarizations, it can be demonstrated that the azimuthal angle ϕ is indefinite (see Appendix A.1.1). Nonetheless, in the experiment the polarization blocking of the polarization analyzer is not perfect (purity estimated to be on the order of 10^{-5} [HL25]), which results in a favored value of the azimuthal angle. However, this is widespread and uncertain. Nonetheless, the results for the different settings agree with each other. For the polar angle θ, from the experimental setting an angle of approximately $\theta = \pi/2$ is expected. Considering alignment uncertainties, the fit values are reasonable.

The next fit parameter is the strength of the internal magnetic field at the positions of the nuclei. This is expected to be around $B = 33$ T, which is the case for all settings. Interestingly, the magnetic field seems to slightly decrease over the train.

Most interesting are the fitted thicknesses because already in the comparison of the time spectra in Section 6.2.2 the time spectra seemed to be from samples, which are not matching the actual physical thickness. Here, this finding is confirmed. The time spectra measured without the monochromator

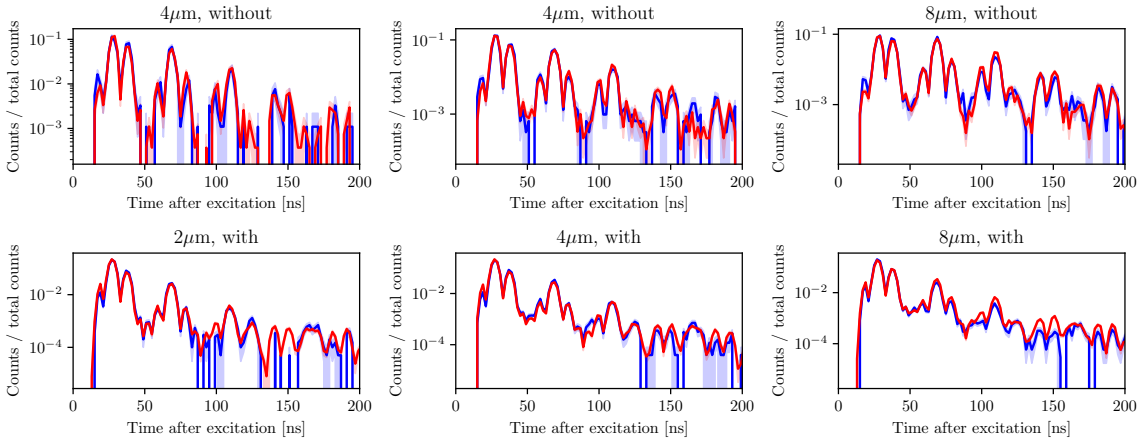

Figure 6.6: Time spectra for small (blue) and large (red) pulse energies for the measurements with different foils and with as well as without monochromator as indicated in the respective subtitles. For the measurements without monochromator, the small (large) intensity time spectra are defined by summing over the 40% of the pulses with smallest (highest) pulse energy, for the measurements with monochromator by the 15% outliers. For better comparability, the time spectra are normalized by the number of total counts in the spectrum.

have a fitted thickness of about 1 μm, the measurements with monochromator around 2.5 μm independently of the actual thickness. With monochromator, the intensity on the sample and the bandwidth is reduced and thus closer to the case with synchrotron radiation. Therefore, the effect is probably reduced and a fitted thickness closer to the actual thickness is expected. In the pulse-resolved analysis it is visible that, especially for the thicker foils, the fitted thickness rises within the first few pulses. Note that those differences have a similar shape as the count rates in Fig. 6.4. When interpreting the fitted thickness results it should be noted that the actual defining parameter is not the physical thickness L, but the thickness parameter b, which is related to L by (see Eq. (2.8))

$$b = \sigma_0 f_{\mathrm{LM}} n \Gamma \cdot L \,, \tag{6.5}$$

with resonant cross section σ_0, Lamb-Mössbauer factor f_{LM}, nuclear number density n, and linewidth Γ. Thus any change of the parameters involved could result in a different fitted thickness.

The fact, that we can fit the time spectra, although with a modified thickness, is quite remarkable because it tells us that even though the thickness does not match the expected value, the system can be described with the standard theory in Section 2.1.4. Therefore, although we do not know the physical origin of the thickness anomaly yet, we expect that the effect is caused by modifications of time scales different from the nuclear nanosecond scales.

6.2.4 Pulse-energy resolved analysis

The XGM measures the total, i.e., resonant and non-resonant combined, pulse energy on a shot-to-shot level. Because of the narrow linewidth of ^{57}Fe (4.7 neV) compared to the incident x-ray pulse width (0.1 − 1 eV) this property is dominated by the non-resonant pulse energy. For all measurements, the pulse energy measured with the XGM is approximately Gaussian distributed with mean values between 186 μJ and 200 μJ and standard deviations of roughly 40 μJ.

To investigate the effect of the pulse energy, in Fig. 6.6, the time spectra only integrated over the pulses with smallest (blue) and highest (red) pulse energy. For the measurements with (without) monochromator, for the integration the 15% (40%) of all pulses with smallest or highest pulse energy, respectively, are used. In general, for all measurements the two spectra are very similar to each other. Nonetheless, in the time region between 135 ns and 200 ns, for the measurements with monochromator, differences are visible and a similar trend is visible for all three foils. However, this deviations are significantly smaller than the differences between expected and measured time spectra resulting from the thickness anomaly as discussed before.

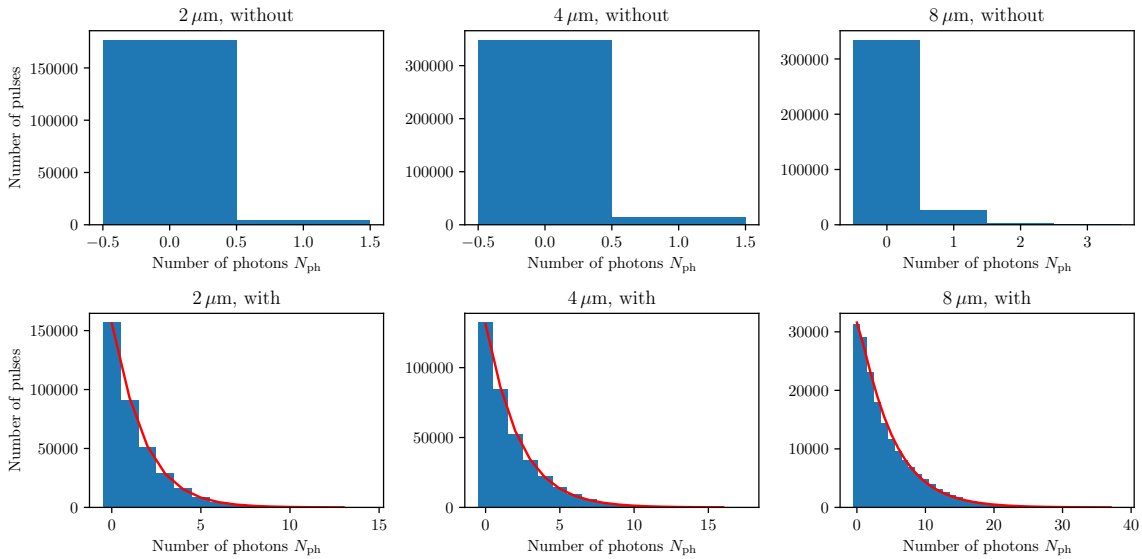

Figure 6.7: Photon number distribution for the different measurements with and without monochromator and different foil thickness. For the measurements with monochromator also the fit of a negative binomial distribution is shown (red line). The corresponding fit parameters are given in Table 6.1.

6.2.5 Photon-number resolved analysis

While in the previous section, the effect of the total pulse energy, which is dominated by the non-resonant pulse energy, was discussed, also the resonant pulse energy can be investigated. To this end, a photon-number resolved analysis is performed.

Photon number distribution

The photon number distribution of an FEL or XFEL, even if operated in seeded mode, is not simply a Poissonian distribution because of the randomness in the SASE process. It can rather be modeled by a Gamma-distribution, which models a chaotic source obeying Gaussian statistics, [Zha+20]

$$P_{\text{Gamma}}\left(N_{\text{ph}}; M, \langle N_{\text{ph}}\rangle\right) = \frac{M^M}{\Gamma(M)} \left(\frac{N_{\text{ph}}}{\langle N_{\text{ph}}\rangle}\right)^{M-1} \exp\left(-M\frac{N_{\text{ph}}}{\langle N_{\text{ph}}\rangle}\right), \tag{6.6}$$

with mean photon number $\langle N_{\text{ph}}\rangle$ and number of degrees of freedom M. The Poissonian statistics of the detection is taken into account by fitting with a Poissonian log-likelihood. The sample response will be dominated by a Poissonian distribution, such that the combined photon distribution is given by the convolution of a Gamma-distribution with a Poissonian-distribution resulting in a negative Binomial distribution [Chu+18; Goo15]. The negative binomial distribution in terms of mean photon number $\langle N_{\text{ph}}\rangle$ and number of degrees of freedom M is given by [Hil11]

$$P_{\text{neg}}(N_{\text{ph}}; M, \langle N_{\text{ph}}\rangle) = \frac{\Gamma(N_{\text{ph}}+M)}{\Gamma(M)\,\Gamma(N_{\text{ph}}+1)} \left(\frac{\langle N_{\text{ph}}\rangle}{\langle N_{\text{ph}}\rangle + M}\right)^{N_{\text{ph}}} \left(\frac{M}{\langle N_{\text{ph}}\rangle + M}\right)^{M}. \tag{6.7}$$

Note, that this is the observed mean photon number while the actual photon number is given by $\langle \bar{N}_{\text{ph}}\rangle = \eta\langle N_{\text{ph}}\rangle$ with the detection efficiency η.

In Fig. 6.7 the photon number distributions for the different foils and measurements with and without monochromator are displayed. For the thicker foils the probability to find a larger number of photons after excitation is higher. This is in agreement with the higher count rates for thicker foils, which was found in Fig. 6.4 due to more resonant material in the beam. Similarly, the shift towards higher photon numbers in the measurements with monochromator agrees with the higher count rates in this setting.

Furthermore, the measurements with monochromator provide enough statistics to fit the negative binomial distribution in Eq. (6.7) by using a Poissonian log-likelihood. The fit results are displayed in Table 6.1 and are indicated in Fig. 6.7 by the red line. For all three measurements, the mode

	number of modes M	mean photon number $\langle N_{\mathrm{ph}} \rangle$
2 μm	1.14± 0.04	1.247 ± 0.018
4 μm	1.06 ± 0.03	1.701 ± 0.024
8 μm	1.09 ± 0.03	4.32 ± 0.07

Table 6.1: Fit results of fitting a negative binomial distribution to the photon number distribution for the measurements with different foils and with monochromator.. The corresponding data is shown in the lower row of Fig. 6.7.

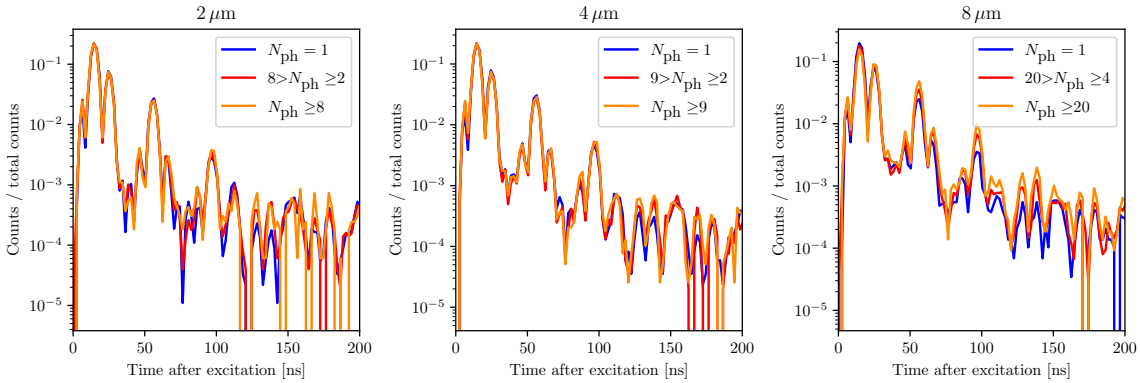

Figure 6.8: Photon-resolved time spectra for the measurements with monochromator. For each dataset, the time spectrum from pulses containing only one photon (blue) is compared to the time spectrum from pulses containing a medium number of photons (red) and a high number of photons (orange). For better comparability, the time spectra are normalized by their respective number of total counts.

numbers M agree within their uncertainties and indicate a single-mode source. The mean photon number $\langle N_{\mathrm{ph}} \rangle$ rises with rising foil thickness. This is the expected behavior, as a thicker foil should have a stronger scattering signal and agrees with the observations in Section 6.2.3. This sounds trivial, but in the context of the unexpected behavior of the time spectra, it is a very crucial observation. It makes an explanation of the unexpected time spectra behavior by the XFEL pulse only exciting the first 2 μm unlikely. In addition, the ratios of the mean photon numbers agree with the ratios of the respective mean count rates, which are given in Fig. 6.4.

Time spectra

For the measurements with monochromator the statistics of the photon number distribution is high enough to evaluate the time spectrum in a photon-number resolved way. To this end, we define a low, medium and high photon number regime for each foil separately depending on the highest occurring photon number in the respective measurement. For the low photon number regime, we use only pulses with a single photon, which is the typical regime at synchrotrons. The medium regime has a lower bound at 10% of the maximal occurring photon number, but at least 2 photons, and an upper bound at half of the maximum photon number. For the high photon number regime, we consider pulses with at least half of the maximal occurring photon number. Integration over pulses in the respective regime gives the time spectrum of this photon number regime. For the measurements with monochromator and the three different foils, those time spectra are shown in Fig. 6.8. In general, the time spectra in the low (blue), medium (red) and high (orange) high photon number regime agree with each other. For the 8 μm foil there are some minor deviations in the spectrum especially at around 70 ns and 110 ns after excitation. The differences are similar to the differences discussed in Section 6.2.4 and might originate from intensity effects similar to the differences in the measurements with and without monochromator, which are correlated with the photon number. Note, that the recorded photon number does not equal the incident photon number due to internal conversion and finite detection probability, however they are correlated. Unfortunately, the statistics are not sufficient enough to evaluate the time spectra in more detailed steps of the photon number. Nonetheless, we can conclude that the different photon numbers cannot explain the thickness anomaly by a non-linear excitation of the nuclei. Not only is the number of resonant photon compared to the number of nuclei

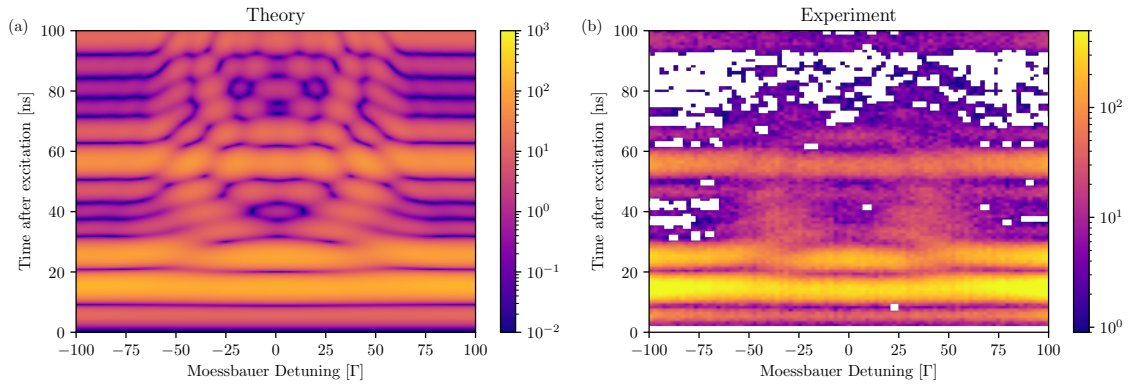

Figure 6.9: Comparison of the energy-time-spectrum as predicted from theoretical calculations (a) and measured in the experiment (b). Clearly a reduced prominence of the interference fringes in the experimental data is visible. The measurement is performed for the 8 μm foil with the monochromator. The colorbar represents the number of counts in the respective bin. The measurements are performed with 1 mm of aluminum in front of the sample to reduce the intensity on the sample. In the white regions no data was recorded.

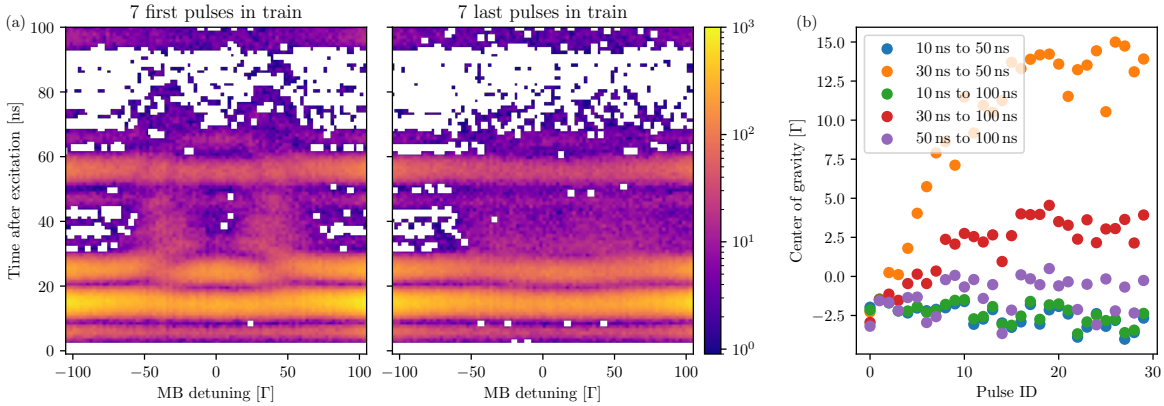

Figure 6.10: (a) Energy-time-spectrum integrated over only the first seven and last seven pulses in the train. The colorbar represents the number of counts in the respective bins. (b) The shift towards higher Mössbauer detuning in (a) can be quantitatively analyzed by displaying the center of gravity for each pulse ID. The different colors represent different integration time regions for the calculation of the center of gravity. The measurements are performed with 1 mm of aluminum in front of the sample to reduce the intensity on the sample.

in the solid state target negligible, such that non-linear effects are extremely unlikely. But in addition the differences in the photon-resolved spectra are significantly smaller than the effect of the thickness anomaly.

6.2.6 Loss of interference

During the experiment, also an energy-time-spectrum was measured by inserting the Mössbauer drive with a stainless steel foil (see Fig. 6.1) for the 8 μm foil with the monochromator. As we have seen in Section 2.1.3, the interference fringes in the energy-time spectra are due to interference of the sample and an analyzer foil on the Mössbauer drive. While the nuclear forward scattering is based on the coherent response of a single target, the energy-time spectra are based on the interference between two targets. To reduce the beam intensity on the sample 1 mm of aluminum was placed in front of the sample. Without the attenuation no interference pattern was visible. Assuming approximately the fit parameters from Section 6.2.3, the sample can be theoretically modeled. Here, the analyzer foil on the Mössbauer drive was an approximately 2 μm thick stainless steel foil. Unfortunately, no separate time spectrum of the stainless steel foil alone exists, such that a sample parameter characterization from the experimental data was not possible. However, this foil was used several times in other

experiments, such that the sample parameters from other experiments can be used for a qualitative comparison. In addition, the sample was placed behind the polarization analyzer, which is why it was only hit by weak x-ray light and thus a behavior as at a synchrotron is expected. From the sample and analyzer foil properties, a theoretical prediction of the energy-time-spectrum can be calculated and is displayed in Fig. 6.9(a). Along the y-axis, the temporal beating structures as in the discussed time spectra are visible. In addition, along the x-axis, interference fringes are evident, which arise from the interference of the sample and analyzer foil response.

The experimental result is displayed in Fig. 6.9(b). While the temporal structure is similar to the theoretical prediction, the interference fringes are significantly less prominent. This can be best seen in the time region between 30 ns and 50 ns. A first measurement without the aluminum attenuator in front of the sample showed even less pronounced interference fringes. Furthermore, in a new experiment [57F25] it was possible to regain the interference by reducing the incident x-ray beam intensity on the sample even further. Therefore, it was clearly demonstrated, that for the measurements in nuclear forward scattering, the prominence of the interference correlates with the incident x-ray intensity on the sample.

The energy-time-spectrum, like the time spectrum, can be analyzed in a pulse-resolved way. However, due to the limited statistics integration over several pulses is necessary. The energy-time-spectra integrated over only the first seven and the last seven pulses within a train are compared in Fig. 6.10(a). The interference is reduced over the train and interestingly, the spectrum seems to shift towards positive detunings, which is again most prominently visible in the region between 30 ns and 50 ns. This effect can be studied in more detail by integrating the energy-time-spectrum in a certain region of interest in the time domain. This increases the statistics, such that the analysis is possible on a single-pulse basis. For the resulting counts as a function of Mössbauer detuning, the center of gravity, i.e., the average Mössbauer detuning when weighted by the number of counts per bin, can be calculated. For different integration regions in the time domain, which are indicated by different colors, the center of gravity is displayed as a function of pulse ID in Fig. 6.10(b). For integration regions starting at 10 ns (blue and green dots), in which the shift is dominated by the earliest horizontal lines without interference, and integration regions starting from 50 ns (violett dots), which are dominated by the third horizontal band at around 50 ns, no significant dependency on the pulse ID exists. However, for the integration regions starting at 30 ns (orange and red dots), the shift slowly rises until approximately pulse 10 at which it has reached a plateau. The shift is most prominent in the time region between 30 ns and 50 ns (orange dots) because it has enough statistics and does not contain one of the peaks in the time domain, i.e., the horizontal bars, at which the interference is small. Focusing on this region, the shift reaches up to $\Delta = 15\,\Gamma$ equivalent to speed of $v = c\Delta/E = 1.5\,\mathrm{mm/s}$, at which the analyzer foil on the Mössbauer drive moves. Here the formula for the Doppler shift with speed of light c and photon energy $E = 14.4\,\mathrm{keV}$ was used. If the frequency shift is actually due ot a mechanical movement, using the pulse separation of 440 ns and integrating the displacement over all pulses, it can be concluded that the over a train the sample would have moved by 12.5 nm.

6.2.7 A possible explanation with a modified theory

One possible explanation for the thickness anomaly, which is inspired by the loss of interference and the fact that the count rates still scale depending on the actual physical sample thickness, is presented in this section. As discussed in Section 2.1.4, the dynamical beats in the time spectrum are due to coherent interference of the different layers. However, a yet to be discussed physical mechanism could lead to an incoherent summation of the electric field from different layers. If, for example, the sample would consist of two parts, whose responses are incoherently summed up, the sample would appear to have half the thickness, but still the expected count rate. This would directly lead to a reduced thickness while the time spectra can still be fitted well with standard theory.

An effectively incoherent summation could also arise from another mechanism. By an also yet unknown mechanism the sample could be split into several subslices. In addition, due to the intense and fluctuating XFEL pulses, each subslice could have a random phase, which fluctuates from shot to shot. For a single subslice with response in frequency space $R(\omega)$, the response can be divided into a non-scattering ("1") and a scattering part ("$T(\omega)$")

$$R(\omega) = 1 + T(\omega)\,, \tag{6.8}$$

where electronic scattering was neglected for simplicity. The electric field behind a sample excited by

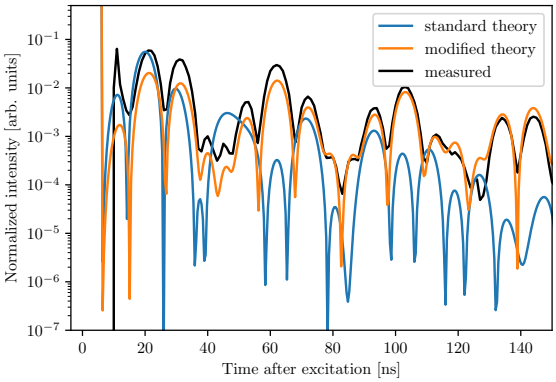

Figure 6.11: Comparison of standard theory (blue) and calculation with $N = 15$ subslices in the modified theory in Eq. (6.12) (orange) to experimental data with 8 μm foil and monochromator (black). For comparison all time spectra are normalized by their respective sum under the curve.

a short pulse such as a synchrotron or XFEL pulse, i.e., $E_{\text{in}}(t) = \delta(t)$, equivalent to $E_{\text{in}}(\omega) = 1$, is given by

$$E_{\text{out}}(\omega) = R(\omega) \cdot E_{\text{in}}(\omega) = R(\omega)\,. \tag{6.9}$$

An instantaneous phase jump from 0 to ϕ immediately after the excitation acts only on the scattering part of the response. The relevant time scale for the phase jump is the nuclear lifetime τ, e.g., $\tau = 141\,\text{ns}$ for ^{57}Fe. Following the formalism in [Hee+17; Hel+91; Rei14], it can be demonstrated that the electric field behind N identical targets with responses $R(\omega)$, but individual phases ϕ_j is given by

$$E_{\text{out}}^{(N)}(\omega) = 1 + T(\omega) \sum_{j=1}^{N} e^{i\phi_j} R(\omega)^{N-j}\,. \tag{6.10}$$

A detailed derivation of this formula is given in Appendix A.2. The first "1" represents the unscattered contribution. If scattering takes place, indicated by "$T(\omega)$", this can happen in any of the N subslices, which is represented by the sum over j. For each term of scattering in different subslices, the relevant phase is that of the subslice in which the first scattering takes place due to the incident x-ray light at the time of excitation. Finally, the $R(\omega)^{N-j}$ describes the interaction with the downstream subslices. In the experiment, the electric field is not measured directly, but the intensity

$$\begin{aligned} I(\omega) =& |E_{\text{out}}(\omega)|^2 \\ =& 1 + 2\text{Re}\left[T(\omega) \sum_{j=1}^{N} e^{i\phi_j} R(\omega)^{N-j}\right] + |T(\omega)|^2 \sum_{j=1}^{N}\sum_{k=1}^{N} e^{i(\phi_j - \phi_k)} R(\omega)^{N-j} \left(R(\omega)^{N-k}\right)^*\,. \end{aligned} \tag{6.11}$$

Although a physical mechanism, which could induce such phases, is yet to be discussed, due to the stochastic properties of XFEL pulses, it can be assumed that the phases are randomly fluctuating from shot to shot. In addition, the measured time spectra are averaged over very many pulses such that the phases average out. For the intensity, this means that all terms containing phase differences vanish and the final result for the averaged intensity is

$$I_{\text{avg}}(\omega) = 1 + |T(\omega)|^2 \sum_{j=0}^{N-1} |R(\omega)^j|^2\,, \tag{6.12}$$

where the order of the sum was reversed to simplify the expression. The first "1" again corresponds to the non-scattered light, while the $T(\omega)$ describes the scattering process. If scattering takes place, there are many options, where scattering can take place. These options are described by the sum, which is an incoherent sum over the combined scattering response of j subslices. Because of the transmission of two samples with thicknesses L_1 and L_2 being multiplicative, i.e., $R(L_1) \cdot R(L_2) = R(L_1 + L_2)$, the sum effectively sums over the response of a stack with thicknesses j-times the single-subslice thickness. The expression in Eq. (6.12) strongly depends on the number of subslices N.

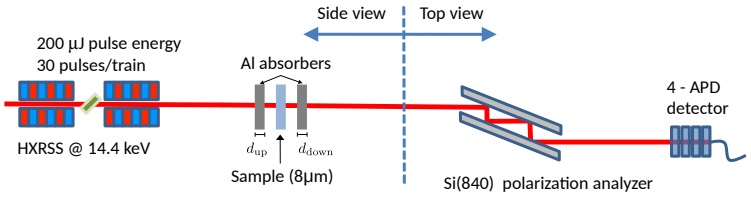

Figure 6.12: Setup for the attenuator anomaly. Trains with 30 pulses of the hard x-ray self-seeded beam at 14.4 keV and approximately 200 μJ pulse energy each enter the setup. Upstream and downstream of the 8 μm sample aluminum attenuators with thicknesses d_{up} and d_{down}, respectively, and $d_{\mathrm{up}} + d_{\mathrm{down}} = 1$ mm are placed. The polarization analyzer is used to suppress non-resonantly scattered light. For the detection of the scattered photons a stack of four APDs is used.

In Fig. 6.11 the measured time spectrum for the 8 μm foil with monochromator (black line) is compared to the expected time spectrum (blue) line. As discussed in Section 6.2.2, there is a strong deviation. In addition, the result of the proposed theory in Eq. (6.12) is displayed for $N = 15$ subslices (orange line), which clearly matches the measured spectrum better than the expected spectrum. However, as already said the result strongly depends on the number of subslices N and $N = 15$ fits the data reasonably well. In addition, the overall decay of the measured spectrum is slower than in the expected spectrum and also slightly slower than in the spectrum with the modified theory.

6.2.8 Summary of the thickness anomaly

To summarize, we found two unexpected results in the context of the thickness anomaly. First, independent of the physical thickness, the time spectra look similar and the fitted thickness is too thin compared to the physical thickness. Second, for the same foil, the time spectrum and the fitted thickness differ for the measurements with and without monochromator. While both effects are unexpected, it is remarkable that the time spectra can be fitted with standard theory, assuming a modified thickness. This indicates that still coherent nuclear forward scattering takes place, but a yet to be determined mechanism modifies the effective thickness. Additional analysis revealed that there are small differences as a function of the pulse ID, which we attribute to different transmittance through the x-ray optics because of heating of the crystals. As a function of the total pulse energy measured by the XGM and as a function of the photon number, no significant differences in the time spectra are visible. While, within a single sample, the coherence is not lost, the energy-time spectra reveal a loss of interference between the sample and a second foil mounted on a Mössbauer drive. This effect is especially strong for later pulses in a train, where the interference fringes are completely washed out and the center of gravity shifts. In the last part, we presented a simple model, which could explain a thinner thickness. If the sample is split into N slices and the response of each slice is multiplied with a random phase, averaging over many shots leads to a modified response. By tuning the number of slices to $N = 15$, the time spectrum of a thinner foil can be approximately reproduced.

6.3 Attenuator anomaly

6.3.1 Experimental setup

The experimental setup to investigate the attenuator anomaly is displayed in Fig. 6.12. The self-seeded XFEL pulses impinge on the sample, which is placed between two aluminum attenuators. During the experiment the thickness of the upstream attenuator d_{up} is varied, but the thickness of the downstream attenuator d_{down} is modified accordingly such that the total amount of attenuating material $d_{\mathrm{up}} + d_{\mathrm{down}} = 1$ mm is constant. The total absorption of both attenuators together thus is always around 90%, while the pulse energy on the sample is varied. The photons are detected by a stack of four APDs, which are placed behind a polarization analyzer to suppress non-resonant photons. In all measurements the 8 μm foil is used as the nuclear resonant sample.

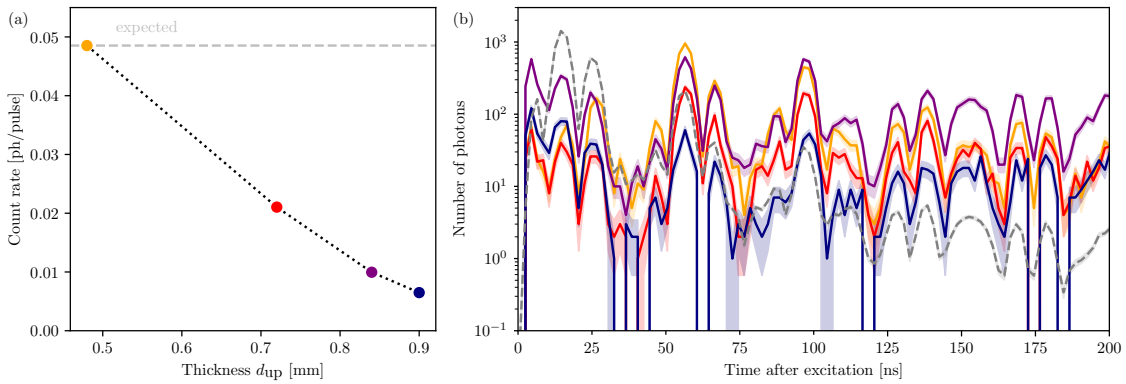

Figure 6.13: (a) The count rates for the measurements with different thickness of the aluminum attenuator upstream the sample. (b) The time spectra for the measurements with different attenuation. The colors correspond to the thicknesses of the upstream attenuator d_{up} in panel (a). For reference the measurement without aluminum attenuators is shown by the gray dashed line. As a sample the 8 μm foil without DCM was used.

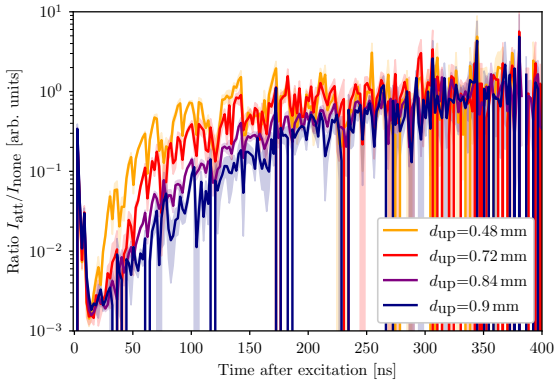

Figure 6.14: Ratio I_{att}/I_{none} of the time spectra with (I_{att}) and without (I_{none}) attenuators for different amount of attenuating material upstream d_{up}. Note that the scaling is only defined up to a shift on the y-axis. Here, the ratios are scaled such that the mean ratio between 300 ns and 400 ns is equal to 1. All measurements are performed without DCM.

6.3.2 Experimental results

Because the nuclei even at an XFEL are driven only very weakly, the nuclei are expected to remain in the low-excitation regime with linear behavior. Therefore, the results are expected to not depend on the distribution of attenuating material d_{up} and d_{down}, as long as the total amount of attenuating material $d_{up} + d_{down}$ is constant. This is because for a linear process it does not matter, whether less photons are impinging on the sample or whether a certain proportion of the signal photons is absorbed before the detector. In Fig. 6.13 the experimental findings for the measurements with varying thickness of the upstream attenuator d_{up} are summarized and are discussed in the following.

As discussed in the introduction of this section, a count rate independent of the thickness of the upstream attenuator d_{up} is expected in the experiment. Instead, the count rate drops significantly with rising thickness of the upstream attenuator d_{up}, as can be seen from Fig. 6.13(a). This is the first observation in the *attenuator anomaly*.

Even more surprisingly, the measured time spectra in Fig. 6.13(b) show a strong dependence on the thickness of the upstream attenuator d_{up}, which is the second observation of the *attenuator anomaly*. This dependence is mainly a strong deviation in the envelope from the reference measurement without the attenuators, while the quantum beat structure remains the same.

The differences can be further investigated by calculating the ratio of the measurement with attenuators I_{att} and the reference measurement without attenuators I_{none} for all times. The results for the different amounts of attenuating material upstream the sample is displayed in Fig. 6.14. Due

to the different count rates, there is an intrinsic scaling factor between the measurement with and without attenuators. It is not known so far where the attenuator anomaly comes from and whether the different shape is due to redistribution or an overall scaling. Thus the scaling factor is in principle undefined. For better comparability, the ratios are scaled such that the mean ratio between 300 ns and 400 ns is equal to 1 in all settings. The general shape of the ratio $I_{\mathrm{att}}/I_{\mathrm{none}}$ is independent of the upstream attenuator thickness d_{up}. At very early times, the variation from the reference time spectrum without attenuators is small. Afterwards, all measurements feature a dip at around 20 ns before rising again with decreasing speed. The less attenuating material is in front of the sample, the steeper is the rise.

The investigation of the ratio of the measurement with attenuators I_{att} and the reference measurement without attenuators I_{none} indicates, that something is happening on nanosecond time scales. However, the physical origin is not known so far.

6.3.3 Discussion of possible effects

For synchrotron experiments, it does not matter whether attenuators are placed in front or behind the sample as long as the total amount of attenuating material in the beam is constant. At the XFEL experiment we have seen unexpected and strong dependence of the count rates and the time spectra on the positioning of the attenuating material, which we call the attenuator anomaly. So far, the origin of the attenuator anomaly is not known. Nonetheless, we can speculate on possible effects.

First, aluminum is a crystalline material and as such problematic if combined with a polarimeter. Our setup is designed in such a way that resonant scattering in the sample rotates the incident horizontal polarization into the vertical polarization component. The polarization analyzer is aligned to ideally only let the vertical component pass, thereby blocking the unscattered light. The crystalline aluminum attenuators in front and after the sample could potentially spoil this alignment and lead to modified count rates.

The second effect is that as ^{57}Fe has an abundance of approximately 2% and if the used aluminum is not highly-purified aluminum, it might still contain small amounts of ^{57}Fe in the attenuators, which is resonantly excited. However, from the synchrotron experience, this would be unexpected to explain the observed effects.

6.3.4 Summary of the attenuator anomaly

To study the attenuator anomaly, we keep the amount of attenuating aluminum in the beam constant, but vary how much of the attenuation material is placed upstream of the sample. The anomaly consists of two observations: The count rates drop with increasing thickness of the upstream attenuator and the time spectra show an envelope modification. We further discussed whether a change of polarization by the aluminum and ^{57}Fe-contamination of the aluminum attenuators could potentially explain the effects. However, so far as for the thickness anomaly, the physical origin of the attenuator anomaly is unknown.

6.4 The follow-up experiment

Based on the results discussed above, a new proposal p8006 [57F25] was put forward to further investigate the anomalies by more systematic studies with the to goal to identify a possible physical origin. Understanding the anomalies is also crucial for Mössbauer spectroscopy under XFEL conditions. In the long run, the observed anomalies could be used to pave the way to apply Mössbauer nuclei as spectators for the electronic environment under XFEL conditions. Which systematic studies we planned is discussed in the following.

Samples. To investigate the thickness anomaly further, more systematic studies of the samples are planned. These include first of all monolithic samples of roughly 2 μm, 4 μm, 8 μm, and 12 μm instead of the stacked samples used so far. The new set of samples also includes foils down to 1.2 μm, thus allowing to test whether samples can also appear thicker than expected. Furthermore, non-enriched samples are used because they have a different ratio of the resonant ^{57}Fe to the non-resonant ^{56}Fe and thus potentially allow an at least partial disentangling of electronic and nuclear effects.

Experimental settings. To investigate the effect of the bandwidth of the incident x-ray pulses, measurements without monochromator, with the beamline's DCM (bandwidth $\approx$ 1 eV) [Mad+21], and with a Si(840) polarization analyzer (bandwidth $\approx$ 50 meV) [Mar25] are performed. This allows

us to study the behavior for different ratios of resonant to total photon flux and decouples the effect of high intensity on the nuclei, which depends on the resonant photon flux, and the environment, for which the total photon flux is relevant.

Attenuators. In a similar fashion as in the attenuator anomaly setup (see Fig. 6.12) systematic studies of the attenuators are performed. They serve two purposes, first to study the attenuator anomaly, but second to study the thickness anomaly for different x-ray beam intensities on the sample. To exclude a material effect in the attenuator anomaly, measurements with different attenuator material, especially non-crystalline material, are conducted. Furthermore, not only different attenuator thicknesses are tested, but also a finer step size of the amount of attenuation placed upstream of the sample. This should include steps with less than half of the attenuation material placed upstream of the sample to investigate whether the attenuator anomaly is influenced by the balance of the up- and downstream thicknesses or rather governed by the amount of material upstream of the sample.

The experiment took place in March 2025, but the data evaluation is still ongoing and outside the scope of this thesis. Results of the more systematic studies performed in this experiment will be presented in [Yag_p], which is currently in preparation.

6.5 Summary and Outlook

In summary, we for the first time have reported two unexpected anomalies in nuclear resonant scattering at an XFEL. First, there is the thickness anomaly, which is that unexpectedly the measured time spectra are independent of the thickness of the samples and the fitted thickness is thinner than the physical thickness of the sample. Second, the attenuator anomaly is the count rate and time spectrum dependence on the amount of attenuating material upstream of the sample, while the total amount is constant. In the low-excitation regime, the count rate as well as the time spectra should be independent of this as long as the total amount of attenuating material in the beam does not vary.

First, we measured the time spectrum of three different foils with thicknesses of approximately $2\,\mu$m, $4\,\mu$m and $8\,\mu$m. According to standard theory, we would expect the respective time spectra to differ because the dynamical beats occur at different times. However, we found that they are all very similar. Furthermore, the time spectra can be fitted reasonably with a thinner sample thickness than the actual physical thickness. In contrast, measurements with and without monochromator of the same foil are different, although standard theory predicts no difference. The fact, that although with an unexpected thickness the data can be fitted with standard theory, suggests that there are no modifications on the nuclear time scales, which is on the nanosecond level. We further found slight differences depending on the photon number and beam intensity, as well as depending on the pulse number within a train.

Secondly, we performed measurements for a fixed foil with different amounts of aluminum attenuators in front and behind the sample. The total amount of aluminum in the beam was kept constant, such that standard linear theory would predict no differences. However, we saw a decreasing count rate for more attenuating material in front of the sample. In addition, unlike for the thickness anomaly, we saw differences in the time spectra that cannot be explained in standard nuclear forward scattering theory, especially variations on the nuclear time scale when comparing to the time spectra without aluminum attenuators. This suggests that in the setting of the attenuator anomaly, there are indeed effects with influence on the nuclear time scale.

We have further mentioned a new experiment to study the observed anomalies in a more detailed and systematic way by additional measurements. With this additional knowledge, potentially the underlying physical mechanisms can be identified.

Understanding the underlying physical mechanisms of the anomalies is crucial for further experiments at XFELs. As mentioned in the beginning, the nuclear forward scattering measurements were performed as simple calibration measurements. As long as those simple measurements are not understood, more complicated experiments are ambitious. However, there are also more complicated settings in which the samples behave as expected [Chu+18; Ger+25b]. Another aspect is that nuclear forward scattering is a standard setting in Mössbauer spectroscopy with synchrotron radiation [GBT11; Röh04; YL13]. In order to establish Mössbauer spectroscopy at XFELs one has to understand the occurring anomalies. Understanding the anomalies is not only important to interpret the data of experiments, which are standard at synchrotrons, but can also open a new dimension at XFELs. Following the lines of Mössbauer spectroscopy, the nuclei could serve as spectators for effects induced by XFEL radiation in an XFEL-pump nuclear-probe scheme.

Part II

Simulation of the de-excitation dynamics of large nuclear ensembles

Chapter 7

Numerical methods for many-body simulations

7.1 Motivation

For the simulation of the de-excitation dynamics of an ensemble of Mössbauer nuclei, a particular challenge is that the interaction between the nuclei and the incoherent loss channels operate on comparable time scales, such that neither dominates. If the coherent interaction dominates, the incoherent losses can be treated as a perturbation [AE87; Cri70; RS12]. In the case where the incoherent losses dominate, the emitters can be treated independently and the incoherent losses predominantly define the system dynamics. [GZ04; PK98]. In the case, where none of the two processes dominates, as it is the case for an ensemble of Mössbauer nuclei, those approximations are invalid and the full master equation has to be studied.

In the low-excitation limit, the resulting equations can be solved analytically (see Section 2.3.3), giving rise, e.g., to the well-known response function formalism. However, new possibilities with XFELs and the realization of an XFELO being on the horizon require a true many-body description beyond this linear case, which is still an open challenge. As already discussed in Section 2.3, the de-excitation dynamics of an ensemble of N Mössbauer nuclei can be described by a master equation with the Hamiltonian

$$H = \hbar \sum_{n,m} J_{mn} \sigma_n^+ \sigma_m^- \tag{7.1}$$

and Lindbladian

$$\mathcal{L}[\rho] = \sum_{n,m} \frac{\Gamma_{mn}}{2} \left(2\sigma_m^- \rho \sigma_n^+ - \sigma_n^+ \sigma_m^- \rho - \rho \sigma_n^+ \sigma_m^- \right) , \tag{7.2}$$

where ρ is the density matrix and the indices $n, m \in 1, \ldots, N$ label the nuclei in the ensemble. The coupling constants J_{mn} and Γ_{mn} describe the coherent and incoherent coupling between nuclei n and m, respectively, and we set $J_{ii} = 0$ by including these energy-shifts in a suitable transition frequency ω_0. The time evolution of the density matrix is then given by

$$\frac{\mathrm{d}}{\mathrm{d}t}\rho = \frac{1}{i\hbar}[H, \rho] + \mathcal{L}[\rho] , \tag{7.3}$$

and the time evolution of expectation values of operators X can be simply calculated with

$$\frac{\mathrm{d}}{\mathrm{d}t}\langle X \rangle = \mathrm{Tr}\left\{ X \frac{\mathrm{d}}{\mathrm{d}t}\rho \right\} . \tag{7.4}$$

This would be the standard quantum optical approach to simulate the de-excitation dynamics of an ensemble of N nuclei. Unfortunately, the dimension of the corresponding Hilbert space scales with 2^N, such that already for 60 nuclei the necessary computational storage exceeds that of the currently best supercomputer "El capitan" [Law] (5568 TiB system memory) according to the Top500 list [Str] and for 300 nuclei, the dimension of the Hilbert space is already larger than the number of protons in the universe [Edd31]. Therefore, solving the full master equation is only suitable for very small numbers of nuclei.

For reasonable simulations of a solid state ensemble of nuclei, a significantly higher number of nuclei needs to be simulated in order to exclude edge effects. Different approaches have been studied, e.g., analytically solving the system for some special cases [HKE16; WE23] or numerical simulations with matrix product states [Kon+25]. In this thesis, we also want to study the system mostly numerically with different methods that will be explained in this chapter.

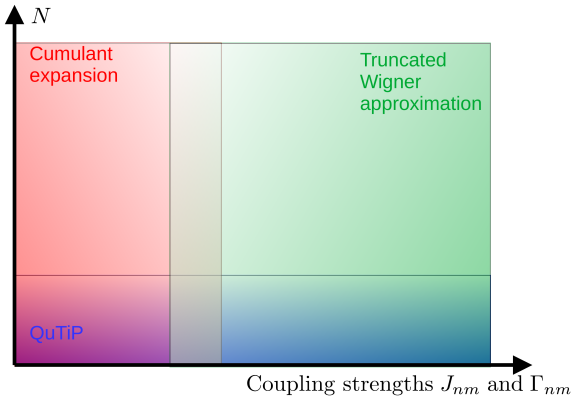

Figure 7.1: Overview over the three methods used in the many-body simulations: the python library `QuTiP`[JNN12; JNN13], the cumulant expansion [Kub62] and a specific truncated Wigner approach [MF23]. All three methods cover different regimes depending on the number of nuclei N and the coupling strengths J_{mn} and Γ_{mn}, $n \neq m$. Details on the methods are given in the main text.

7.2 Overview of established numerical methods

To simulate open many-body dynamics, a large toolbox of methods exists including packages for efficient full quantum optical calculation with few emitters [JNN12; Mer+25], using the cumulant expansion [Kub62], especially the mean-field approximation, phase-space methods [GZ04], the quantum jump approach [DCM92; MCD93], and matrix product states [Sch11; Whi92]. Here, we employ three different methods of which an overview of the operating regime is presented in the following. The methods are explained in detail in the subsequent section.

First, there is the python package `QuTiP` (Quantum Toolbox in Python) [JNN12; JNN13], in which the full quantum optical simulation, as described above, is efficiently calculated. Because it does not apply approximations it is suitable for arbitrary couplings, but due to the computational complexity it can only be used for very small numbers of nuclei.

Second, there is the cumulant expansion [Kub62], which is effectively an expansion in the coupling strength. Therefore, it is only suitable for systems in which the couplings are not too strong. However, it has a favorable scaling of the number of equations, which depends on the number of nuclei N and the order of the expansion as N^{order}. In our case, the expansion is used in first order because the free-space couplings are weak, such that 1000s of nuclei can be easily simulated. Furthermore, the choice for the first order is made because the cumulant expansion does not necessarily converge with higher order and therefore the second order is not reliable [Fow+23].

Third, a specific version of a truncated Wigner approximation developed by Mink et al. [MF23] based on the work in [HRR22; MPF22; SPR15; SW22] is used. This method works best for strong coupling. As the number of coupled differential equations is $2N$ also larger ensembles can be calculated. However, as it is a Monte-Carlo approach, the computation time depends on the number of Monte-Carlo trajectories, which depends on the observable. In general, the truncated Wigner approximation is slower than the cumulant expansion, but complements it in the coupling regime as it works the better the stronger the coupling is, which is the opposite for the cumulant expansion. We expect our system to be in the overlapping regime of both methods, such that they can be used to perform cross-checks on each other. Note that previous implementations of a truncated Wigner function have proven to be successful [HRR22; Piñ+17; SPR15], but the formulation in [MF23] is best-suited for our system.

In the following sections, the different methods are discussed in more detail.

7.3 Quantum Toolbox in Python (QuTiP)

The simplest approach to simulate an ensemble of nuclei is using `QuTiP` [JNN12; JNN13], which is a well established python package. To calculate a unitary time evolution, first the initial quantum state and a Hamiltonian is defined. For the non-unitary time evolution, the initial state is encoded in the density matrix, whose time evolution is given by Eq. (7.3). This can be either solved with an ODE solver or by diagonalization. Which one is faster depends on the number of emitters [JNN12].

Both options provide a numerical solution of the exact Hamiltonian and Lindbladian without further approximations. However, this comes with high computational costs and the number of emitters N in QuTiP simulations is severely limited to typically $N \leq 10$ on a standard computer.

Despite the crucial limitations in the number of emitters N, for small numbers QuTiP provides an important cross-check because it does not require further approximations.

7.4 Cumulant expansion

The dynamics of the nuclei can be described by the time evolution of the expectation values of population $\langle \sigma_j^{ee} \rangle$ and coherence $\langle \sigma_j^- \rangle$. They can be computed with Eq. (7.4). By inserting the specific Hamiltonian in Eq. (7.1) and Lindbladian in Eq. (7.2), the equation for the time evolution of the expectation value of an operator X can be simplified to be

$$\frac{\mathrm{d}}{\mathrm{d}t}\langle X \rangle = \frac{1}{i\hbar}\langle [X, H] \rangle + \sum_{n,m} \frac{\Gamma_{mn}}{2} \left(\langle \sigma_n^+ \left[X, \sigma_m^- \right] \rangle + \langle \left[\sigma_n^+, X \right] \sigma_m^- \rangle \right) . \tag{7.5}$$

Using this equation, for the expectation values of population and coherence of nucleus j we then find

$$\frac{\mathrm{d}}{\mathrm{d}t}\langle \sigma_l^{ee} \rangle = -\Gamma_{ll}\langle \sigma_l^{ee} \rangle - \sum_{\substack{n \\ n \neq l}} \mathcal{C}_{nl} \langle \sigma_n^+ \sigma_l^- \rangle + \mathcal{C}_{ln}^* \langle \sigma_l^+ \sigma_n^- \rangle , \tag{7.6a}$$

$$\frac{\mathrm{d}}{\mathrm{d}t}\langle \sigma_l^- \rangle = -\frac{\Gamma_{ll}}{2}\langle \sigma_l^- \rangle - \sum_{\substack{n \\ n \neq l}} \mathcal{C}_{nl}^* \left(\langle \sigma_n^- \rangle - 2\langle \sigma_l^{ee} \sigma_n^- \rangle \right) , \tag{7.6b}$$

where we introduced the complex coupling

$$\mathcal{C}_{mn} = \frac{\Gamma_{mn}}{2} + iJ_{mn} . \tag{7.7}$$

For a detailed derivation see Appendix B.2. In Eq. (7.6) not only expectation values of single operators appear, but also expectation values of products of operators. Thus, the differential equations in Eq. (7.6) do not form a closed set of equations, and the time evolution of the expectation value of the appearing products has to be included. Similarly, the equations of motion for the two-nuclei operator contain products of operators from three nuclei leading to the hierarchy problem. To truncate the hierarchy and find a closed set of equations, we can approximately represent expectation values of products of operators from k nuclei by an expression containing only products of operators from $k-1$ nuclei by using the cumulant expansion [Kub62]. This cumulant expansion is essentially an expansion in the correlations between k nuclei and therefore its applicability depends on the coupling strength between the nuclei. In first order, the expectation value of the product of two operators A_m and B_n acting on different nuclei m and n can be approximated in the cumulant expansion by [Kub62]

$$\langle A_m B_n \rangle \approx \langle A_m \rangle \langle B_n \rangle \quad (m \neq n) . \tag{7.8}$$

Similarly, for second order

$$\langle A_m B_n C_o \rangle \approx \langle A_m B_n \rangle \langle C_o \rangle + \langle A_m C_o \rangle \langle B_n \rangle + \langle A_m \rangle \langle B_n C_o \rangle - 2\langle A_m \rangle \langle B_n \rangle \langle C_o \rangle \quad (m \neq n \neq o) , \tag{7.9}$$

thus reducing the number of factors in an expectation value by one. This then leads to a closed set of equations, and the number of equations scales with the number of nuclei N and the order of the expansion as N^{order}. Unfortunately, the cumulant expansion does not converge like a perturbative approach and therefore considering higher orders does not necessarily improve the result [Fow+23].

Applying the first order cumulant expansion to the time evolution in Eq. (7.6) results in (see Appendix B.3)

$$\frac{\mathrm{d}}{\mathrm{d}t}\langle \sigma_l^{ee} \rangle = -\Gamma_{ll}\langle \sigma_l^{ee} \rangle - \sum_{\substack{n \\ n \neq l}} \mathcal{C}_{nl} \langle \sigma_n^+ \sigma_l^- \rangle + \mathcal{C}_{ln}^* \langle \sigma_l^+ \rangle \langle \sigma_n^- \rangle , \tag{7.10a}$$

$$\frac{\mathrm{d}}{\mathrm{d}t}\langle \sigma_l^- \rangle = -\frac{\Gamma_{ll}}{2}\langle \sigma_l^- \rangle - \sum_{\substack{n \\ n \neq l}} \mathcal{C}_{nl}^* \left(\langle \sigma_n^- \rangle - 2\langle \sigma_l^{ee} \rangle \langle \sigma_n^- \rangle \right) . \tag{7.10b}$$

This set of $2N$ differential equations can be efficiently solved, e.g., using the programming language `julia`. The julia package `QuantumCumulants` [PHR22] provides an implementation of the cumulant expansion for arbitrary systems. However, as in our investigations the form of Hamiltonian and Lindbladian is fixed, a custom implementation of the equations of motion is faster than the fully flexible solution provided by the package. Therefore, the package is employed only for cross-checks, while the faster custom implementation is used for the actual simulations.

7.5 Continuous-discrete truncated Wigner approximation

There exist different modifications of the truncated Wigner approximation to make it suitable for open quantum systems. Here, we focus on the continuous-discrete truncated Wigner approximation (CDTWA) developed by Mink et al. [MF23] because it can treat discrete ensembles of two-level systems properly while capturing collective effects and is thus a fitting method to simulate correlated two-level systems with dissipation. The CDTWA [MF23] will be summarized in the following.

7.5.1 General idea

The general idea of the approach is to represent operators in the Hilbert space in terms of a phase space function. To this end, so-called continuous point operators or wigner kernels $\Delta(\vec{\Omega})$ are introduced, which effectively provide an operator basis for the Hilbert space. The $\vec{\Omega}$ variables parameterize the Wigner "space". For a single particle, they are later chosen simply as $\vec{\Omega} = (\theta, \phi)$, with the straightforward generalization $\vec{\Omega} = (\theta_1, \phi_1, \theta_2, \phi_2, ...)$ to multiple particles. Then, any operator X can be written as,

$$X = \int \mathrm{d}\vec{\Omega}\, W_X(\vec{\Omega}) \cdot \Delta(\vec{\Omega})\,. \tag{7.11}$$

In this expression, the so-called Weyl symbol $W_{X(\vec{\Omega})}$ is introduced, which is the desired phase-space representation. In the case of the density operator, $X = \rho$, the Weyl symbol is called the Wigner function. The Weyl symbol can be evaluated from the operator X via

$$W_X(\vec{\Omega}) = \mathrm{Tr}\left[\Delta(\vec{\Omega})\, X\right]\,. \tag{7.12}$$

For a single spin-1/2 system, i.e., a two-level system, the point operators can be parameterized via two variables $\vec{\Omega} = (\theta, \phi)$, and the point operators are given by

$$\Delta(\theta,\phi) = \frac{1}{2}\left[\mathbb{1}_2 + \vec{s}(\theta,\phi)\,\vec{\sigma}\right] = \frac{1}{2}\begin{pmatrix} 1+\sqrt{3}\cos(\theta) & \sqrt{3}e^{-i\phi}\,\sin(\theta) \\ \sqrt{3}e^{i\phi}\,\sin(\theta) & 1-\sqrt{3}\cos(\theta)\end{pmatrix}\,. \tag{7.13}$$

Here, $\vec{\sigma}$ is the Pauli matrix vector, $\mathbb{1}_2$ the 2×2 unit operator. Further, we define a vector

$$\vec{s}(\theta,\phi) = W_{\vec{\sigma}} = \sqrt{3}\big(\sin(\theta)\cos(\phi), \sin(\theta)\sin(\phi), \cos(\theta)\big)^T\,, \tag{7.14}$$

which is the Weyl symbol of the Pauli matrix vector. The angles θ and ϕ can now be interpreted as the angles defining a point on a sphere with radius $\sqrt{3}$. To generalize this to N spin-1/2 systems, one simply replaces $\vec{s} \to \vec{s}_j$ with spin index j, and generalizes the variables to $\vec{\Omega} = \{\Omega_j\}$.

7.5.2 Initial state sampling

The initial state is stochastically sampled for the different phase space trajectories in order to capture its possible quantum nature. For this to be possible, its phase-space representation must be positive-valued to allow for a probability interpretation. To this end, Mink et al. exploit that the discrete phase-point operators give rise to positive-valued discrete "Weyl weights" in many cases. Note that these discrete operators are different from the continuous phase-point operators defined above. The four discrete phase-point operators are

$$A_{\alpha_1,\alpha_2} = \frac{1}{2}\left(\mathbb{1}_2 + \vec{r}_{\alpha_1,\alpha_2}\,\vec{\sigma}\right)\,, \tag{7.15}$$

$$\vec{r}_{\alpha_1,\alpha_2} = \left((-1)^{\alpha_2}, (-1)^{\alpha_1+\alpha_2}, (-1)^{\alpha_1}\right)^T\,, \tag{7.16}$$

with $\alpha_1, \alpha_2 \in \{0, 1\}$. Given this, the discrete initial state Weyl weights according to the variables Ω are obtained as

$$W_{\alpha_1,\alpha_2} = \frac{1}{2}\mathrm{Tr}\left[A_{\alpha_1,\alpha_2} \cdot \rho(t=0)\right] . \tag{7.17}$$

This can be translated into the continuous representation via

$$\chi_0(\theta, \phi) = \sum_{\alpha_1,\alpha_2} \delta(\theta - \theta_{\alpha_1,\alpha_2})\delta(\phi - \phi_{\alpha_1,\alpha_2})\, W_{\alpha_1,\alpha_2} , \tag{7.18}$$

where $\chi_0(\theta, \phi)$ is the Wigner function in continuous phase space, and

$$\begin{aligned} \theta_{00} = \theta_{01} &= \arccos\Big(1/\sqrt{3}\Big), \qquad & \phi_{00} &= -7\pi/4, \quad \phi_{01} = -3\pi/4, \\ \theta_{10} = \theta_{11} &= \pi - \arccos\Big(1/\sqrt{3}\Big), \qquad & \phi_{10} &= -\pi/4, \quad \phi_{11} = -5\pi/4\,. \end{aligned} \tag{7.19}$$

It can be shown that the angles above lead to the correct mapping of the continuous Wigner function in Eq. (7.13) to the discrete case in Eq. (7.15).

To give an example, for the fully excited state, the Weyl weights are given by $W_{00} = 1/2$, $W_{01} = 1/2$, and $W_{10} = W11 = 0$. Thus the initial state is sampled from $\theta = \arccos\big(1/\sqrt{3}\big)$ and $\phi \in \{-7\pi/4, -3\pi/4\}$.

7.5.3 Dynamics of variables

After sampling the initial state, we need to calculate the time evolution of the variables $\vec{\Omega}$. A general system including driving by an external field is governed by the master equation

$$\frac{\mathrm{d}}{\mathrm{d}t}\rho = -\,i\,[H, \rho] + \frac{1}{2}\sum_{mn}\Gamma_{mn}\left(2\sigma_m^-\rho\sigma_n^+ - \sigma_n^+\sigma_m^-\rho - \rho\sigma_n^+\sigma_m^-\right) , \tag{7.20}$$

with the effective Hamiltonian

$$H = -\,\frac{\Delta}{2}\sum_n \sigma_n^z - \sum_n \left(\Omega_n\sigma_n^+ + h.a.\right) + \sum_{n\neq m} J_{mn}\sigma_m^+\sigma_n^- . \tag{7.21}$$

Here Γ_{mn} describes the dissipation, Δ the detuning, Ω is the corresponding Rabi frequency, which can be time-dependent, and J_{mn} describes the coupling. In phase space, this can be mapped to a Fokker-Planck equation for the Wigner function $W_\rho(\Omega, t)$ [MF23; MPF22]. To numerically solve this equation, it is mapped to an Ito Stochastic differential equation [Gra85; MF23]

$$\begin{aligned} \mathrm{d}\theta_n = &\left[\frac{\Gamma_{nn}}{2}\cot\theta_n + \sqrt{3}\sum_{m=1}^{N}\sin\theta_m\left(J_{mn}\sin\phi_{mn} + \frac{\Gamma_{mn}}{2}\cos\phi_{mn}\right) + \mathrm{Im}\left(\Omega_n e^{i\phi_n}\right)\right]\mathrm{d}t \\ &+ \sum_{m=1}^{N} G_{nm}\left(-\cos\phi_n \mathrm{d}W_{\theta_m} + \sin\phi_n \mathrm{d}W_{\phi_m}\right) , \end{aligned} \tag{7.22a}$$

$$\begin{aligned} \mathrm{d}\phi_n = &\left[\sqrt{3}\cot\theta_n\sum_{m=1}^{N}\sin\theta_m\left(-J_{mn}\cos\phi_{mn} + \frac{\Gamma_{mn}}{2}\sin\phi_{mn}\right) + \mathrm{Re}\left(\Omega_n e^{i\phi_n}\right)\cot\theta_n - \Delta\right]\mathrm{d}t \\ &+ \sum_{m=1}^{N} G_{nm}\left(\sin\phi_n \mathrm{d}W_{\theta_m} + \cos\phi_n \mathrm{d}W_{\phi_m}\right) , \end{aligned} \tag{7.22b}$$

where $\mathrm{d}W$ are the differentials of a Wiener process, $\phi_{mn} = \phi_m - \phi_n$, and $\mathbf{G}$ a matrix such that the $\mathbf{\Gamma}$-matrix can be written as $\mathbf{\Gamma} = \mathbf{G}\mathbf{G}^T$ in the Cholesky decomposition [GV13]. This set of equations is a good approximation for large N because the expansion used for the truncated correspondence rules to receive the Fokker-Planck equation breaks down for small N [MF23].

7.5.4 Expectation values of operators

Expectation values of operators $\langle X \rangle$ can be evaluated by the mean of the corresponding Weyl symbol W_X over all trajectories, i.e., random realizations of the initial state sampling,

$$\langle X \rangle \approx \frac{1}{N_{\text{traj}}} \sum_{n=i}^{N_{\text{traj}}} W_X(\vec{\Omega}^{(n)}) \,, \tag{7.23}$$

where $\vec{\Omega} = (\theta_1, ...\theta_N, \phi_1, ..., \phi_N)$ and $\vec{\Omega}^{(n)}$ is its realization in trajectory n. This holds in every time step.

For the population $\langle \sigma_j^{ee} \rangle$ and coherence $\langle \sigma_j^{-} \rangle$ of atom j, which are the key observables in Section 7.4, the respective Weyl symbols are given by

$$W_{\sigma_j^{ee}}(\vec{\Omega}) = \frac{1}{2} \left(1 + \sqrt{3} \cos(\theta_j) \right) \,, \tag{7.24a}$$

$$W_{\sigma_j^{-}}(\vec{\Omega}) = \frac{\sqrt{3}}{2} \, e^{-i\phi_j} \sin(\theta_j) \,. \tag{7.24b}$$

The necessary number of trajectories to achieve a certain minimal uncertainty strongly depends on the observable. Depending on the observable and system parameters, typically 10,000 to 10,000,000 trajectories are needed.

7.5.5 Unphysical behavior at later times

In [MF23], Mink et al. discuss an unphysical behavior in the subradiant regime at late times when analyzing the decay of an initially fully excited system of N emitters decaying to the ground state. While in the superradiant regime $\Gamma t \lesssim 1$ the results of the truncated Wigner approximation closely match those of a second order cumulant expansion, there are strong deviations in the subradiant regime $\Gamma t \gtrsim 1$ and the total number of excitations approaches an unphysical plateau at approximately $N/10$. Furthermore, if the system is initially in the ground state, it also asymptotically approaches this plateau even in the absence of an external driving field. Thus unphysical driving of the system can occur. Mink et al. associate the effect with unphysical behavior of the subradiant modes and the distribution of eigenvalues of the incoherent $\mathbf{\Gamma}$ and coherent $\mathbf{J}$ coupling matrices, which dominate the superradiant and subradiant regimes, respectively. For the subradiant modes, it can happen that a crucial validity criterium for the derivation of Eq. (7.22) is not fulfilled, which leads to the unphysical behavior. The eigenvalues of $\mathbf{\Gamma}$ provide an estimate for the relevant time scales. As the magnitude of this effect depends on the balance between the decay and the unphysical driving, especially for a non-driven system, the results are worse the lower the initial excitation is. Note that the unphysical driving is especially severe in our situation because we want to study the de-excitation dynamics after an impulsive excitation, such that after the initial short pulse the system is not driven externally anymore.

However, we can test for physical vs. unphysical effects by using different start times of our dynamics. For physical effects, after compensation of the time shift, the dynamics should be identical. Since the origin of the unphysical effects always starts at the beginning of the simulation, a time shift would lead to different results in the case of the unphysical effects.

7.6 Summary and outlook

For a large ensemble, it is not possible to exactly solve the full master equation because of the exponential scaling of the Hilbert space with the number of nuclei. Therefore, we have discussed three different methods to calculate the de-excitation dynamics of an ensemble of nuclei, which together cover the space of number of nuclei N and coupling strength. All of the three methods have their own regime, in which they work well, but there also exist overlapping regimes available for cross-checks. For example, reducing the number of nuclei N in the cumulant expansion or the CDTWA allows for cross-checks with `QuTiP`. Furthermore, a medium coupling strength allows calculations with the cumulant expansion as well as the CDTWA.

For most parts in this thesis, we consider free-space couplings with typical ^{57}Fe parameters, where the inter-nuclear spacing is approximately three times larger than the resonant wavelength. Therefore, the couplings are typically weak and we expect the cumulant expansion to work well. Nonetheless, they are large enough to compare the results to those derived with the CDTWA. Because the

computational costs for simulations with the cumulant expansion are significantly smaller than for simulations with CDTWA, the cumulant expansion is the main method for our ensemble simulations. For selected parameters at stronger coupling, the simulations are additionally performed with the CDTWA to verify the results.

Placing the nuclei in structured environments, e.g., thin-film cavities [DLE22a], can enhance the couplings. Future investigations using enhanced couplings can also be handled by the combination of the three methods because larger couplings can be calculated with the CDTWA if the cumulant expansion is not appropriate.

Therefore, we have established a toolbox to calculate the de-excitation dynamics of an ensemble of nuclei beyond the linear regime and in different parameter regimes. This allows for many applications also beyond the scope of this thesis.

Chapter 8

Initial state preparation for CDTWA

8.1 Motivation

As we have described in the previous chapter, we want to use both the cumulant expansion as well as the CDTWA for the simulation of the nuclear dynamics because they work best in different coupling regimes and allow for cross-checks in the regime with medium coupling. As the excitation and de-excitation dynamics take place on different time scales, we usually want to disentangle those two parts of the dynamics. To study the de-excitation dynamics, we typically prepare the system already in the partially excited state

$$|\Psi\rangle = \cos\frac{\mathcal{A}}{2}|g\rangle + e^{i\phi_0}\sin\frac{\mathcal{A}}{2}|e\rangle, \tag{8.1}$$

in which it is after the excitation. Here $\mathcal{A}$ is the excitation angle on the Bloch sphere according to the area theorem and ϕ_0 a possible phase of the excited state.

However, in the CDTWA by Mink et al. [MF23] as initial states only the ground state and the fully excited state, but not a partially excited state, are discussed. In this chapter, we discuss different possibilities to prepare such a state for the CDTWA. Thereby, we investigate different schemes for the preparation. It is known that different sampling schemes can lead to different predicted dynamics [Czi+18; MPF22; PRK16]. Therefore, we demonstrate that the onset of the dynamics gives crucial insights into this problem. Finally, we evaluate the results for simulations in which the system is actually driven into the partially excited state.

8.2 Sampling the partially excited state

Using the definition in Eq. (7.17), the Weyl weights for the partially excited state are given by

$$W_{00} = \frac{1}{2}\left[\sin^2\frac{\mathcal{A}}{2} + \sin\frac{\mathcal{A}}{2}\cos\frac{\mathcal{A}}{2}\left(\cos\phi_0 - \sin\phi_0\right)\right], \tag{8.2a}$$

$$W_{01} = \frac{1}{2}\left[\sin^2\frac{\mathcal{A}}{2} - \sin\frac{\mathcal{A}}{2}\cos\frac{\mathcal{A}}{2}\left(\cos\phi_0 - \sin\phi_0\right)\right], \tag{8.2b}$$

$$W_{10} = \frac{1}{2}\left[\cos^2\frac{\mathcal{A}}{2} + \sin\frac{\mathcal{A}}{2}\cos\frac{\mathcal{A}}{2}\left(\cos\phi_0 + \sin\phi_0\right)\right], \tag{8.2c}$$

$$W_{11} = \frac{1}{2}\left[\cos^2\frac{\mathcal{A}}{2} - \sin\frac{\mathcal{A}}{2}\cos\frac{\mathcal{A}}{2}\left(\cos\phi_0 + \sin\phi_0\right)\right]. \tag{8.2d}$$

Unfortunately, non-negativity of the weights in Eq. (8.2) is only guaranteed for $\mathcal{A} = 0$ and $\mathcal{A} = \pi$, i.e., the ground state and the fully excited state. For arbitrary $\mathcal{A}$ and ϕ_0, in general, at least one weight is negative and thus the probability interpretation is not valid any more.

8.2.1 Ensuring non-negative weights

The problem with the non-negativity of the weights in Eq. (8.2) can be circumvented by an optimized set of variables $\vec{\Omega}$. A different but equivalently valid set of four points can be chosen by rotating the vector $\vec{r}_{\alpha_1,\alpha_2}$ in Eq. (7.16) by $\pi/2$ around the z-axis [Woo87]. We can generalize this with a rotation by ψ around the z-axis. This transforms the vector $\vec{r}_{\alpha_1,\alpha_2}$ into

$$\vec{r}^{\,\psi}_{\alpha_1,\alpha_2} = \begin{pmatrix}\cos(\psi) & -\sin(\psi) & 0\\ \sin(\psi) & \cos(\psi) & 0\\ 0 & 0 & 1\end{pmatrix}\cdot\begin{pmatrix}-1^{\alpha_2}\\ -1^{\alpha_1+\alpha_2}\\ -1^{\alpha_1}\end{pmatrix}, \tag{8.3}$$

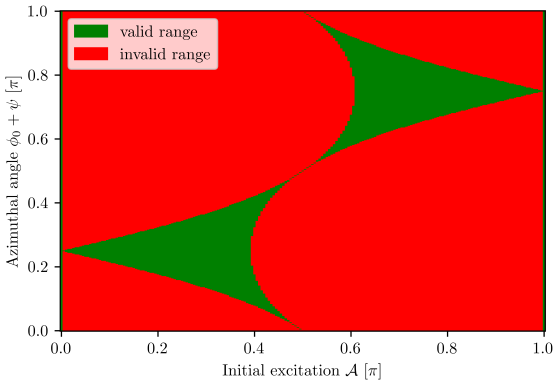

Figure 8.1: Validity range, in which all four weights in Eq. (8.5) are non-negative, as a function of the degree of initial excitation $\mathcal{A}$ and azimuthal angle $\phi_0 + \psi$. The valid regions are marked in green, the invalid ones in red.

and correspondingly $\theta^{\psi}_{\alpha_1,\alpha_2} = \theta_{\alpha_1,\alpha_2}$ and $\phi^{\psi}_{\alpha_1,\alpha_2} = \phi_{\alpha_1,\alpha_2} + \psi$, with θ_α and ϕ_α given in Eq. (7.19). Following the weight calculation procedure in Section 7.5.2 with the modified

$$A_{\alpha_1,\alpha_2}(\psi) = \frac{1}{2}\left(\mathbb{1}_2 + \vec{r}^{\,\psi}_{\alpha_1,\alpha_2} \cdot \vec{\sigma}\right) , \tag{8.4}$$

we find the following weights

$$W^{\psi}_{00} = \frac{1}{2}\left[\sin^2\frac{\mathcal{A}}{2} - \sqrt{2}\sin\frac{\mathcal{A}}{2}\cos\frac{\mathcal{A}}{2}\sin\left(\phi_0 + \psi - \frac{\pi}{4}\right)\right] , \tag{8.5a}$$

$$W^{\psi}_{01} = \frac{1}{2}\left[\sin^2\frac{\mathcal{A}}{2} + \sqrt{2}\sin\frac{\mathcal{A}}{2}\cos\frac{\mathcal{A}}{2}\sin\left(\phi_0 + \psi - \frac{\pi}{4}\right)\right] , \tag{8.5b}$$

$$W^{\psi}_{10} = \frac{1}{2}\left[\cos^2\frac{\mathcal{A}}{2} + \sqrt{2}\sin\frac{\mathcal{A}}{2}\cos\frac{\mathcal{A}}{2}\sin\left(\phi_0 + \psi + \frac{\pi}{4}\right)\right] , \tag{8.5c}$$

$$W^{\psi}_{11} = \frac{1}{2}\left[\cos\frac{\mathcal{A}}{2} - \sqrt{2}\sin\frac{\mathcal{A}}{2}\cos\frac{\mathcal{A}}{2}\sin\left(\phi_0 + \psi + \frac{\pi}{4}\right)\right] . \tag{8.5d}$$

Note that those weights are not necessarily non-negative and that an initial phase ϕ_0 can easily be taken into account by a modified ψ. Thus, we consider the combined azimuthal angle $\phi_0 + \psi$. In Fig. 8.1 for different combinations of initial excitation $\mathcal{A}$ and azimuthal angle $\phi_0 + \psi$ it is indicated whether this pair leads to all four weights being non-negative (green) or not (red). Note that because the sampling points come in pairs for a fixed value of α_1, which determines the z-component, ψ and $\psi + \pi$ lead to the same sampling points. Therefore, we evaluate ψ only from 0 to π. Although the weights are not non-negative in general, for each initial state as in Eq. (8.1) represented by $\mathcal{A}$ and ϕ_0 we can find ψ such that all four weights are non-negative. Except of states close to inversion ($\mathcal{A} = \pi/2$), for states below (above) inversion, we can choose $\phi_0 + \psi = \pi/4$ ($\phi_0 + \psi = 3\pi/4$).

The presented procedure allows us in principal to sample any initial state of the form in Eq. (8.1). The correct sampling can be demonstrated by showing that the density matrix

$$\rho = |\psi\rangle\langle\psi| = \begin{pmatrix} \sin^2\left(\frac{\mathcal{A}}{2}\right) & e^{i\phi_0}\cos\left(\frac{\mathcal{A}}{2}\right)\sin\left(\frac{\mathcal{A}}{2}\right) \\ e^{-i\phi_0}\cos\left(\frac{\mathcal{A}}{2}\right)\sin\left(\frac{\mathcal{A}}{2}\right) & \cos^2\left(\frac{\mathcal{A}}{2}\right) \end{pmatrix} , \tag{8.6}$$

where in the last step we used the matrix notation with the convention $|e\rangle = (1,0)^\intercal$ and $|g\rangle = (0,1)^\intercal$, is sampled correctly. The density matrix is sampled by [MPF22]

$$\rho = \sum_{\alpha_1,\alpha_2} W^{\psi}_{\alpha_1,\alpha_2} A^{\psi}_{\alpha_1,\alpha_2} , \tag{8.7}$$

with $W^{\psi}_{\alpha_1,\alpha_2}$ given in Eq. (8.5) and $A^{\psi}_{\alpha_1,\alpha_2}$ in Eq. (8.4). Evaluating this expression leads to the correct density matrix.

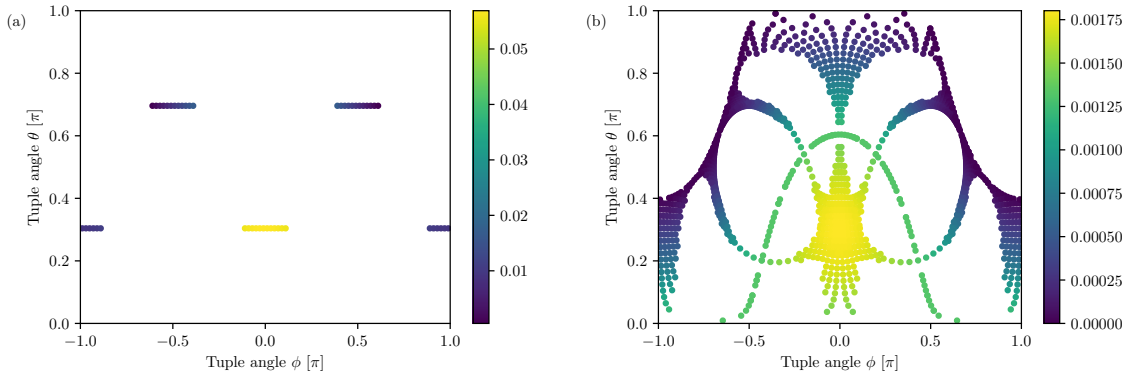

Figure 8.2: Initial state sampling tuples and corresponding weights for initial state with $\mathcal{A} = 0.7\pi$ and $\phi_0 = 0$ for (a) the rotation by ψ around the z-axis and (b) the double rotation, which consists of a rotation of ψ_z around the z-axis followed by a rotation of ψ_y around the y-axis. For each rotation, angle the resulting tuples (θ, ϕ) are calculated. If all four weights are non-negative they are displayed here with their corresponding weight indicated by the color. More details on the calculation of the tuples are given in the main text. All rotation angles are evaluated on a grid from 0 to π in steps of 0.02π.

8.2.2 Sampling schemes with more sampling points

For $\psi = 0$, the vectors $\vec{r}^{\,0}_{\alpha_1,\alpha_2}$ evaluate to $\vec{r}_{00} = (1,1,1)^\intercal$, $\vec{r}_{01} = (-1,-1,1)^\intercal$, $\vec{r}_{10} = (1,-1,-1)^\intercal$, and $\vec{r}_{11} = (-1,1,-1)^\intercal$. For a fixed z-component of the vectors, the x- and y-components are thus entangled, which can lead to wrong dynamics [Czi+18; MPF22; PRK16]. Therefore, in [MPF22] it is proposed to use a sampling scheme with arbitrary ϕ to sample the ground or excited state. This is possible because any modified set of tuples, which is generated from the default one by a unitary transformation $\mathbf{U}$, $\vec{r}' = \mathbf{U}\vec{r}$, can in principle be considered as a sampling set [Woo87; Žun15]. If all four weights are non-negative, it is a valid sampling set.

Rotation around z-axis

In Section 8.2.1, we have already discussed the generation of a modified set of tuples from the default ones in Eq. (7.19) by a rotation around the z-axis by ψ. The validity range of ψ can be read off from Fig. 8.1. For choosing $\psi = \pi/4$ in the low excitation regime ($\mathcal{A} < \pi/2$), the vectors $\vec{r}^{\,\psi}_{\alpha_1,\alpha_2}$ evaluate to $\vec{r}^{\,\psi}_{00} = (0,\sqrt{2},1)^\intercal$, $\vec{r}^{\,\psi}_{01} = (0,-\sqrt{2},1)^\intercal$, $\vec{r}^{\,\psi}_{10} = (\sqrt{2},0,-1)^\intercal$, and $\vec{r}^{\,\psi}_{11} = (-\sqrt{2},0,-1)^\intercal$, and we again see the entanglement of the x- and y-component for a fixed z-component. Similarly, we find the entanglement for the high excitation regime. However, we can resolve this entanglement by choosing two angles ψ_1 and ψ_2 in the validity range.

For the ground state and the fully excited state, it is possible to choose arbitrary ψ and it turned out that more sampling points result in more accurate dynamics [MPF22]. Therefore, also for the arbitrary state $|\Psi\rangle$ we want to sample from many points in the valid range.

Numerically this is implemented by evaluating ψ on a grid from 0 to π with steps of 0.02π. For each ψ the four weights $W^{\psi}_{\alpha_1,\alpha_2}$ and the tuples $(\theta^{\psi}_{\alpha_1,\alpha_2}, \phi^{\psi}_{\alpha_1,\alpha_2})$ are evaluated. If all four weights are non-negative, the tuples are added to the sampling list from which the initial values for θ and ϕ according to the respective weights are drawn for each trajectory. An example of the sampling tuples (θ, ϕ) and weights for the initial state with initial degree of excitation $\mathcal{A} = 0.7\pi$ and phase $\phi_0 = 0$ is displayed in Fig. 8.2(a). The weights corresponding to the tuples are represented by the colorbar. We see that we sample with different ϕ, but, unlike for the ground or excited state, not all values between 0 and π can be used. Nonetheless, for each θ we sample from more than two points, which partially resolves the x- and y-component entanglement as discussed before. As θ is not modified by the rotation, only the two values used in the original sampling scheme with four points appear.

Double rotation

We can improve the coverage of the (θ, ϕ)-space by adding a second rotation around the y-axis by ψ_y after the first rotation around the $z-$axis by ψ_z. This generalizes the vector $\vec{r}(\alpha_1, \alpha_2)$ in Eq. (7.16)

to

$$\vec{r}(\alpha_1,\alpha_2,\psi_z,\psi_y) = \begin{pmatrix} \cos(\psi_y) & 0 & -\sin(\psi_y) \\ 0 & 1 & 0 \\ \sin(\psi_y) & 0 & \cos(\psi_y) \end{pmatrix} \begin{pmatrix} \cos(\psi_z) & -\sin(\psi_z) & 0 \\ \sin(\psi_z) & \cos(\psi_z) & 0 \\ 0 & 0 & 1 \end{pmatrix} \cdot \begin{pmatrix} -1^{\alpha_2} \\ -1^{\alpha_1+\alpha_2} \\ -1^{\alpha_1} \end{pmatrix}, \tag{8.8}$$

and correspondingly

$$A(\alpha_1,\alpha_2,\psi) = \frac{1}{2}\left(\mathbb{1}_2 + \vec{r}(\alpha_1,\alpha_2,\psi_1,\psi_2)\vec{\sigma}\right). \tag{8.9}$$

Using spherical coordinates, the new vector $\vec{r}(\alpha_1,\alpha_2,\psi_1,\psi_2)$ can be represented by a modified tuple (θ',ϕ')

$$\theta' = \arccos\frac{r_z}{\sqrt{3}}, \tag{8.10}$$

$$\phi' = \text{sign}\,(r_y)\cdot\arccos\frac{r_x/\sqrt{3}}{\sin\theta'}. \tag{8.11}$$

If all four weights are non-negative, the set of tuples (θ',ϕ') is added to the set of used tuples $\vec{\Omega}$ and the corresponding weights to the distribution from which the initial variables are drawn. Note that this is possible because each set of (θ',ϕ') is a representation of the initial state on its own.

For the numerical implementation, ψ_y and ψ_z are evaluated on a grid from 0 to π in steps of 0.02π. The resulting tuples (θ',ϕ') for which all four weights are non-negative are displayed in Fig. 8.2(b), again for the initial state with initial degree of excitation $\mathcal{A} = 0.7\pi$ and phase $\phi_0 = 0$. As compared to the single rotation case in Fig. 8.2(a) this improves the coverage of the (θ,ϕ) space significantly and especially improves the number of values for θ.

The coverage of the (θ,ϕ) space can be improved further by adding a third rotation around the z-axis. However, this comes with the cost of needing more sampling trajectories, to recover the weight distribution of the initial state properly. Thus, one has to make a tradeoff of computational cost for the number of sampling trajectories and coverage of the (θ,ϕ) space to remove correlations potentially leading to wrong dynamics as we will see in Section 8.3.

Demonstrating the correct sampling of the density matrix of the initial state is difficult in the case of the double rotation because finding those rotation values ψ_z and ψ_y for which all four weights are non-negative is not straightforward. However, one can easily check the correct sampling numerically.

We note that a similar scheme to sample partially excited states from a unitary transformation of the default set of tuples is discussed in [Piñ+17].

8.2.3 Different weight function

All discussed sampling schemes so far relied on the same four base points creating the default set of tuples to sample from and unitary transformation of the default set. In [Teb+24] a slightly different approach to sample an arbitrary state represented by

$$\rho = \frac{1}{2}\left(1 + u\sigma_x + v\sigma_y + w\sigma_z\right), \tag{8.12}$$

is given. In this reference, it is proposed to sample the initial state from the Wigner function

$$W(\theta,\phi) = \frac{C}{\sin(\theta)}\delta(\theta-\theta_w)\left(1 + \frac{1}{C}\frac{u\cos(\phi)+v\sin(\phi)}{\sqrt{3-w^2}}\right)^2, \tag{8.13}$$

with $\theta_w = \arccos\left(w/\sqrt{3}\right)$ and $C = \frac{1}{2}\left(1+\sqrt{1-2\frac{u^2+v^2}{3-w^2}}\right)$. In [Teb+24], Tebbenjohanns et al. demonstrate that this always leads to non-negative weights and samples the initial state correctly.

8.3 First time step analysis

So far we have discussed several possibilities to sample the initial partially excited state. To validate the initial state sampling, we want to analyze the first time step of the z-component of the spin-operator $\langle S^z\rangle$, from which the population $\langle\sigma^{ee}\rangle$ can be easily derived by $\langle\sigma^{ee}\rangle = (\langle S^z\rangle + 1)/2$, and of the coherence $\langle\sigma^-\rangle$.

For an expectation value of a function whose parameters come from a SDE, the first time step is not just given by the differential. Instead, we need Ito's lemma [Gar+04], which is basically a generalization of the chain rule to stochastic processes. For a set of SDEs

$$\mathrm{d}\mathbf{X}_t = \mathbf{f}(t, \mathbf{X}_t)\mathrm{dt} + \mathbf{g}(t, \mathbf{X}_t)\mathrm{d}\mathbf{W}_t \,. \tag{8.14}$$

and a scalar function $Y(t, X_t)$, the time evolution of Y is given by [Gar+04]

$$\mathrm{d}Y = \left[\partial_t Y + \mathbf{f}^T \nabla Y + \frac{1}{2}\mathrm{Tr}\left(\mathbf{g}^T \mathbf{H}_Y \mathbf{g}\right)\right]\mathrm{d}t + (\nabla Y)^T \mathbf{g}\mathrm{d}\mathbf{W}_t \,, \tag{8.15}$$

with ∇Y the gradient of Y and $\mathbf{H}_Y$ the Hessian matrix of Y. Thus, the stochastic part of the SDE $\mathbf{g}$ does not only give a stochastic contribution to $\mathrm{d}Y$, but also a deterministic one. For the first time step, the stochastic noise $\mathrm{d}\mathbf{W}_t$ averages out, and the incremental first time step is given by

$$\mathrm{d}Y^{(1)} = \left[\partial_t Y + \mathbf{f}^T \nabla Y + \frac{1}{2}\mathrm{Tr}\left(\mathbf{g}^T \mathbf{H}_Y \mathbf{g}\right)\right]\mathrm{d}t \,. \tag{8.16}$$

With this, we can now evaluate the first time step evolution of

$$\langle S^z \rangle(t) = \sum_{\alpha_1, \alpha_2} W_{\alpha_1,\alpha_2} S_z(\alpha_1, \alpha_2, t) \,, \tag{8.17a}$$

$$\langle \sigma^- \rangle(t) = \sum_{\alpha_1, \alpha_2} W_{\alpha_1,\alpha_2} \sigma^-(\alpha_1, \alpha_2, t) \,, \tag{8.17b}$$

with $\alpha_1, \alpha_2 \in \{0, 1\}$, W_{α_1,α_2} the corresponding weights, and

$$S_z(\alpha_1, \alpha_2, t) = \sqrt{3}\cos\theta_{\alpha_1,\alpha_2} \,, \tag{8.18a}$$

$$\sigma^-(\alpha_1, \alpha_2, t) = \frac{\sqrt{3}}{2}\sin\theta_{\alpha_1,\alpha_2} e^{-i\phi_{\alpha_1,\alpha_2}} \,. \tag{8.18b}$$

For an observable Y the gradient is given by $\nabla Y = (\partial_\theta Y, \partial_\phi Y)^\intercal$. For the above observables $\langle S^z \rangle(t)$ and $\langle \sigma^- \rangle(t)$ the gradients are given by

$$\nabla S_z(\alpha_1, \alpha_2, t) = \begin{pmatrix} -\sqrt{3}\sin\theta_a \\ 0 \end{pmatrix} \,, \tag{8.19a}$$

$$\nabla \sigma^-(\alpha_1, \alpha_2, t) = \frac{1}{2}\begin{pmatrix} \sqrt{3} e^{-i\phi_{\alpha_1,\alpha_2}} \cos\theta_a \\ -i\sqrt{3} e^{-i\phi_{\alpha_1,\alpha_2}} \sin\theta_a \end{pmatrix} \,, \tag{8.19b}$$

and the Hessian matrices $\mathbf{H}_Y$ by

$$\mathbf{H}_{S_z} = \begin{pmatrix} -\sqrt{3}\,\cos\theta_{\alpha_1,\alpha_2} & 0 \\ 0 & 0 \end{pmatrix} \,, \tag{8.20a}$$

$$\mathbf{H}_{\sigma^-} = \frac{1}{2}\begin{pmatrix} -\sqrt{3}\,\sin\theta_{\alpha_1,\alpha_2}\, e^{-i\phi_{\alpha_1,\alpha_2}} & -i\,\sqrt{3}\,\cos\theta_{\alpha_1,\alpha_2}\, e^{-i\phi_{\alpha_1,\alpha_2}} \\ -i\,\sqrt{3}\,\cos\theta_{\alpha_1,\alpha_2}\, e^{-i\phi_{\alpha_1,\alpha_2}} & -\sqrt{3}\,\sin\theta_{\alpha_1,\alpha_2}\, e^{-i\phi_{\alpha_1,\alpha_2}} \end{pmatrix} \,. \tag{8.20b}$$

To evaluate $\mathrm{d}Y^{(1)}$, we still need g and f, which are given by the stochastic differential equation. In the following, we consider the single nucleus equations as well as the ensemble ones with uncoupled nuclei. In both cases, the analytical solution is known, and the infinitesimally small first time step is given by its first order Taylor expansion

$$\langle S_z \rangle(\Delta t) = 2 \cdot \left(\sin^2\frac{\mathcal{A}}{2} e^{-\Gamma t} - 1\right) \approx \underbrace{\left(2\sin^2\frac{\mathcal{A}}{2} - 1\right)}_{\langle S_z \rangle(t=0)} + \underbrace{\left(-2\sin^2\frac{\mathcal{A}}{2}\Gamma\Delta t\right)}_{\mathrm{d}\langle S_z \rangle(t)} \,, \tag{8.21a}$$

$$\langle \sigma^- \rangle(\Delta t) = \sin\frac{\mathcal{A}}{2}\cos\frac{\mathcal{A}}{2} e^{-\frac{\Gamma}{2}t} \approx \underbrace{\left(\sin\frac{\mathcal{A}}{2}\cos\frac{\mathcal{A}}{2}\right)}_{\langle \sigma^- \rangle(t=0)} + \underbrace{\left(-\sin\frac{\mathcal{A}}{2}\cos\frac{\mathcal{A}}{2}\frac{\Gamma}{2}\Delta t\right)}_{\mathrm{d}\langle \sigma^- \rangle(t)} \,. \tag{8.21b}$$

Single nucleus equations

At first we focus on the time evolution of a single emitter with the single rotation sampling scheme. Here, we assume an initial state

$$|\Psi\rangle = \cos\frac{\mathcal{A}}{2}|g\rangle + \sin\frac{\mathcal{A}}{2}|e\rangle\,, \tag{8.22}$$

where we have omitted a possible phase for the excited state, which is left out for simplicity and can easily be inserted into the equations. To evaluate the first step, we consider the stochastic equations of the dynamics of a single emitter [MF23]

$$\mathrm{d}\theta = \Gamma_0\left(\cot\theta + \frac{\csc\theta}{\sqrt{3}}\right)\mathrm{d}t\,, \tag{8.23a}$$

$$\mathrm{d}\phi = \sqrt{\Gamma_0\left(1 + 2\cot^2\theta + \frac{2\cot\theta\csc\theta}{\sqrt{3}}\right)}\mathrm{d}W_\phi\,, \tag{8.23b}$$

and by inserting $\theta^{\psi}_{\alpha_1,\alpha_2} = \theta_{\alpha_1,\alpha_2}$ as in Eq. (7.19) we find

$$f = \begin{cases} \begin{pmatrix}\sqrt{2}\Gamma\\ 0\end{pmatrix} & \text{for } \alpha_1,\alpha_2 = 0i \\ \begin{pmatrix}0\\ 0\end{pmatrix} & \text{for } \alpha_1,\alpha_2 = 1i \end{cases}, \tag{8.24}$$

$$\mathbf{g} = \begin{cases} \begin{pmatrix}0 & 0\\ 0 & \sqrt{3\Gamma}\end{pmatrix} & \text{for } \alpha_1,\alpha_2 = 0i \\ \begin{pmatrix}0 & 0\\ 0 & \sqrt{\Gamma}\end{pmatrix} & \text{for } \alpha_1,\alpha_2 = 1i \end{cases}. \tag{8.25}$$

Plugging those expressions together with the respective gradients given in Eq. (8.19) and Hessian matrices given in Eq. (8.20) into the first time step equation given by Eq. (8.16), we can derive the first time step of our observables of interest for different α_1, α_2

$$\mathrm{d}S_z(\alpha_1,\alpha_2)^{(1)} = \begin{cases} -2\Gamma\mathrm{d}t & \text{for } \alpha_1,\alpha_2 = 0i \\ 0 & \text{for } \alpha_1,\alpha_2 = 1i \end{cases}, \tag{8.26a}$$

$$\mathrm{d}\sigma^-(\alpha_1,\alpha_2)^{(1)} = -\frac{\Gamma}{2\sqrt{2}}e^{-i\phi_{\alpha_1,\alpha_2}}\,. \tag{8.26b}$$

Averaging over all weights as described in Eq. (8.18), we finally find

$$\mathrm{d}\langle S_z\rangle^{(1)} = -2\Gamma\sin^2\frac{\mathcal{A}}{2}\mathrm{d}t\,, \tag{8.27a}$$

$$\mathrm{d}\langle\sigma^-\rangle^{(1)} = -\frac{\Gamma}{2}\sin\frac{\mathcal{A}}{2}\cos\frac{\mathcal{A}}{2}\mathrm{d}t\,. \tag{8.27b}$$

Note that this result is independent of ψ, the rotation angle for the sampling of the Wigner function. Finally, by comparing to Eq. (8.21), we can conclude that the dynamics of the first time step are correct with the given sampling for the single emitter conclusions. This demonstrates that not only the initial state is represented accurately, but also the dynamics starts correctly.

Ensemble equations

Next, we want to perform the same analysis as for the single emitter equations for the ensemble equations in Eq. (7.22) and again use the single rotation sampling scheme. Although the ensemble equations are not exact and not a good description for low cooperativity [MF23], we can study the uncoupled case nonetheless due to its simplicity to get some insights into the dynamics. For the uncoupled case ($J_{mn} = 0$, $\Gamma_{mn} = \Gamma\delta_{mn}$) without driving ($\Omega_n = 0$) on resonance $\Delta = 0$, the ensemble equations are given by

$$\mathrm{d}\theta_n = \frac{\Gamma}{2}\left[\cot\theta_n + \sqrt{3}\sin\theta_n\right]\mathrm{d}t + \Gamma\left(-\cos\phi_n\mathrm{d}W_{\theta_n} + \sin\phi_n\mathrm{d}W_{\phi_n}\right)\,, \tag{8.28a}$$

$$\mathrm{d}\phi_n = \Gamma\left(\sin\phi_n\mathrm{d}W_{\theta_n} + \cos\phi_n\mathrm{d}W_{\phi_n}\right)\,. \tag{8.28b}$$

The equations decouple and each emitter is described by two equations. Therefore, from now on we leave out the index n for the rest of this analysis. We identify

$$f = \begin{cases} \begin{pmatrix} \frac{3}{2\sqrt{2}}\Gamma \\ 0 \end{pmatrix} & \text{for } \alpha_1 = 0 \\ \begin{pmatrix} \frac{1}{2\sqrt{2}}\Gamma \\ 0 \end{pmatrix} & \text{for } \alpha_1 = 1 \end{cases}, \tag{8.29}$$

$$\mathbf{g} = \begin{cases} \begin{pmatrix} \pm\sqrt{\Gamma}\cos\left(\frac{\pi}{4}+\psi\right) & \pm\sqrt{\Gamma}\sin\left(\frac{\pi}{4}+\psi\right) \\ \pm\frac{\sqrt{\Gamma}}{\sqrt{2}}\sin\left(\frac{\pi}{4}+\psi\right) & \pm\frac{\sqrt{\Gamma}}{\sqrt{2}}\cos\left(\frac{\pi}{4}+\psi\right) \end{pmatrix} & \text{for } \alpha_1 = 0 \\ \begin{pmatrix} \mp\sqrt{\Gamma}\sin\left(\frac{\pi}{4}+\psi\right) & \mp\sqrt{\Gamma}\sin\left(\frac{\pi}{4}-\psi\right) \\ \pm\frac{\sqrt{\Gamma}}{\sqrt{2}}\sin\left(\frac{\pi}{4}-\psi\right) & \mp\frac{\sqrt{\Gamma}}{\sqrt{2}}\sin\left(\frac{\pi}{4}+\psi\right) \end{pmatrix} & \text{for } \alpha_1 = 1 \end{cases}, \tag{8.30}$$

where the "+" ("-") depends on $\alpha_2 = 0$ ($\alpha_2 = 1$) . By plugging the expressions for f and $\mathbf{g}$ together with the respective gradients (Eq. (8.19)) and Hessian matrices (Eq. (8.20)) into the first time step equation (Eq. (8.16)) we find

$$\mathrm{d}S_z(\alpha_1,\alpha_2)^{(1)} = \begin{cases} -2\Gamma\mathrm{d}t & \text{for } \alpha_1 = 0 \\ 0 & \text{for } \alpha_1 = 1 \end{cases}, \tag{8.31}$$

$$\mathrm{d}\sigma^-(\alpha_1,\alpha_2)^{(1)} = \begin{cases} 0 & \text{for } \alpha_1 = 0 \\ \mp\frac{1+i}{2}e^{i\psi}\Gamma\mathrm{d}t & \text{for } \alpha_1 = 1 \end{cases}, \tag{8.32}$$

and finally with Eq. (8.17)

$$\mathrm{d}\langle S_z\rangle^{(1)} = -2\Gamma\sin^2\frac{\mathcal{A}}{2}\mathrm{d}t\,, \tag{8.33a}$$

$$\begin{aligned} \mathrm{d}\langle\sigma^-\rangle^{(1)} =& e^{-i\left(\frac{3\pi}{4}+\psi\right)}\sin\left(\psi+\frac{\pi}{4}\right)\frac{\Gamma}{2}\sin\frac{\mathcal{A}}{2}\cos\frac{\mathcal{A}}{2} \\ =& \begin{cases} -\Gamma\sin\frac{\mathcal{A}}{2}\cos\frac{\mathcal{A}}{2} & \text{for } \psi = \frac{\pi}{4} \\ 0 & \text{for } \psi = \frac{3\pi}{4} \end{cases}. \end{aligned} \tag{8.33b}$$

For simplicity, we only considered initial excitations $\mathcal{A}$, which can be sampled with $\psi = \pi/4$ (low excitation) or $\psi = 3\pi/4$ (high excitation), i.e., initial excitations that are not too close to $\mathcal{A} = \pi/2$. By comparing to the analytical solution in Eq. (8.21), we find that only for $\langle S_z\rangle$ the correct time evolution is retrieved. We expect $\langle\sigma^-\rangle$ to decay with $\Gamma/2$ (c.f. Eq. (8.21)), but instead find in the low excitation regime ($\psi = \pi/4$) the decay constant is Γ and thus the decay is too fast, while in the high excitation regime $\psi = 3\pi/4$ there is no decay at all in the first time step.

In Fig. 8.3, the time evolution of the population $\langle\sigma^{ee}\rangle(t) = (\langle S_z\rangle(t)+1)/2$ and the coherence $\langle\sigma^-\rangle(t)$ are shown for the 5th nucleus in a chain of 10 nuclei. For two different initial excitations $\mathcal{A}$, the solid lines show the results from the CDTWA while the dashed lines show the analytical expressions from Eq. (8.21). As demonstrated by Eq. (8.33) for the population, we find the correct dynamics at early times, but for the coherence the decay is too fast for $\mathcal{A} = 0.3\pi$ and no decay is visible for $\mathcal{A} = 0.7\pi$ at early times. In addition, the results from the sampling schemes based on two rotations as discussed in Section 8.2.2 are shown in the dark colors. The more sampling points in this scheme partially resolve the entanglement of the $x-$ and $y-$component of $\vec{r}^{\psi}_{\alpha_1,\alpha_2}$ and the deviation in the coherence reduces. However, there are still deviations between the CDTWA and the analytical results. The deviations in the population at larger times are due to the unphysical driving even in the absence of a driving field as discussed in Section 7.5.5.

Note that for the ground state or the fully excited state without external driving, the coherence is zero at all times and thus the problem with the wrong first time step in the coherence is not considered.

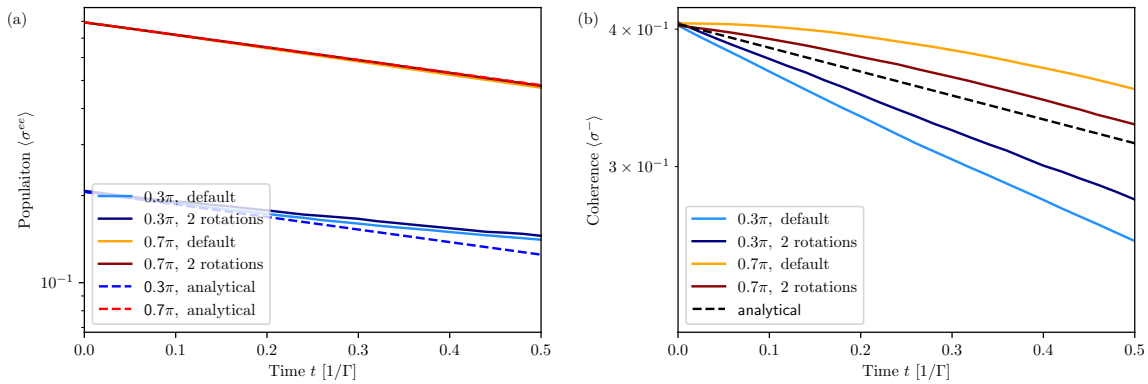

Figure 8.3: Comparison of CDTWA results (solid lines) with analytical results (dashed lines) for a chain with no couplings between the nuclei for an initial excitation of $\mathcal{A} = 0.3\pi$ (orange) and $\mathcal{A} = 0.7\pi$ (orange). In (a), the population of the 5th nucleus in a chain of 10 nuclei is displayed, in (b) the coherence. Shown are the results for two different sampling schemes, the default schemes adjusted for the partially excited state as in Section 8.2.1 (light colors) and the sampling schmes with more points based on two rotations as explained in Section 8.2.2 (dark colors). For comparison, the analytical expression in Eq. (8.21) is indicated by the dashed lines. The calculation is performed without inter-nuclear coupling ($J_{mn} = 0$, $\Gamma_{mn} = \Gamma\delta_{mn}$) and the incident light is incident perpendicular to the chain such that there are no relative phases between the nuclei.

8.3.1 Different Wigner function

Finally, we do the first time step analysis for the different Wigner function in Eq. (8.13). For simplicity, here we only consider $\langle S_z \rangle$. For the single nucleus equation in Eq. (8.23) in general we have

$$\mathbf{f} = \begin{pmatrix} \Gamma\left(\cot\theta + \frac{\csc\theta}{\sqrt{3}}\right) \\ 0 \end{pmatrix}, \tag{8.34}$$

$$\mathbf{g} = \begin{pmatrix} 0 & 0 \\ 0 & \sqrt{\Gamma\left(1 + 2\cot^2\theta + \frac{2\cot\theta\csc\theta}{\sqrt{3}}\right)} \end{pmatrix}. \tag{8.35}$$

With this result, the gradient in Eq. (8.19) and Hessian matrix Eq. (8.20), Ito's lemma for the first time step in Eq. (8.16) gives

$$\mathrm{d}S_z^{(1)}(\alpha_1, \alpha_2) = \Gamma\big(-\sqrt{3}\cos\theta_{\alpha_1,\alpha_2} - 1\big)\,\mathrm{d}t\,. \tag{8.36}$$

Finally, we need to average to find

$$\begin{aligned} \mathrm{d}\langle S_z\rangle^{(1,\mathrm{single})} &= \int \mathrm{d}\theta_{\alpha_1,\alpha_2} \int \mathrm{d}\phi_{\alpha_1,\alpha_2} W(\theta_{\alpha_1,\alpha_2}, \phi_{\alpha_1,\alpha_2}) \mathrm{d}S_z^{(1)}(\alpha_1,\alpha_2) \\ &= -\,\mathrm{d}t \int \mathrm{d}\theta_{\alpha_1,\alpha_2} \delta(\theta_{\alpha_1,\alpha_2} - \theta_w)\Gamma\big(\sqrt{3}\cos\theta_{\alpha_1,\alpha_2} + 1\big) \\ &= -\,2\Gamma\sin^2\frac{\mathcal{A}}{2}\mathrm{d}t\,, \end{aligned} \tag{8.37}$$

where for the second row we have used that $\mathrm{d}S_z^{(1)}(\alpha_1,\alpha_2)$ does not depend on ϕ_{α_1,α_2} and that $W(\theta_{\alpha_1,\alpha_2}, \phi_{\alpha_1,\alpha_2})$ is normalized. This is the correct time evolution as given in Eq. (8.21). Similarly, we find the correct result for the coherence $\langle \sigma^- \rangle$.

A similar analysis for the ensemble equations yields

$$\mathrm{d}S_z^{(1,\mathrm{ensemble})}(\theta) = \left[\frac{\Gamma}{2}\big(-\sqrt{3}\cos\theta - 3\sin^2\theta\big) + \frac{\Gamma^2}{2}\big(-\sqrt{3}\cos\theta\big)\right]\mathrm{d}t\,, \tag{8.38}$$

which does not agree with the analytical result. Furthermore, the two results from the rotated set of points in Eq. (8.33) and the different Wigner function in Eq. (8.38) differ from each other, which shows how the sampling scheme can influence the predicted dynamics.

We can conclude that also this different Wigner function, which is not based on unitary transformations of the default set of four points, samples the initial state correctly, but does not predict the dynamics properly in the presented setting.

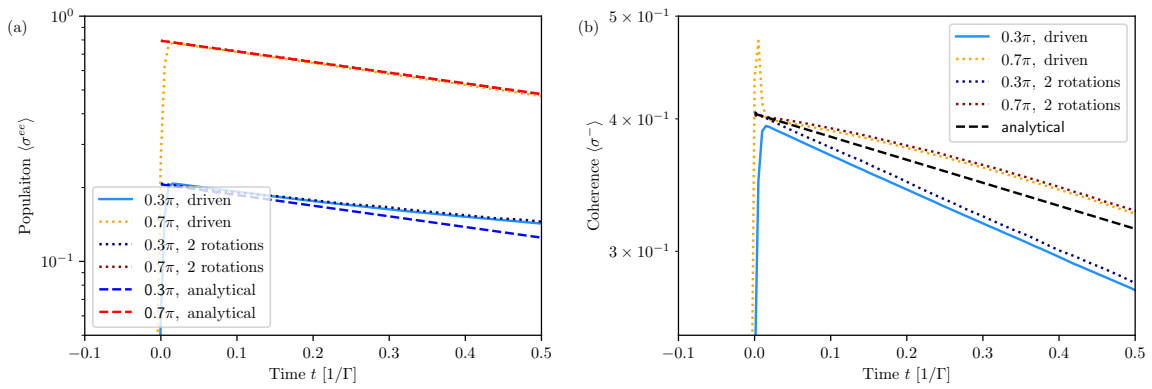

Figure 8.4: Comparison of the CDTWA results, where the system was driven into the initial state, (solid lines) with the analytical expression in Eq. (8.21) (dashed lines) for the time evolution of (a) the population $\langle\sigma^{ee}\rangle$ and (b) the coherence $\langle\sigma^{-}\rangle$. For comparison, the dashed lines show the results from Fig. 8.3, where the partially excited state is prepared directly and sampled from with the double rotation. Considered are the two different initial excitations of $\mathcal{A} = 0.3\pi$ (blue) and $\mathcal{A} = 0.7\pi$ (orange). The observables from the CDTWA are shown for the 5th nucleus in a chain of 10 nuclei without inter-nuclear coupling ($J_{mn} = 0$, $\Gamma_{mn} = \Gamma\delta_{mn}$) and the incident light is perpendicular to the chain, such that all nuclei have the same initial phase.

8.4 Driving into the initial state

In Section 8.2, we have seen different sampling schemes to prepare the system in a partially excited state as in Eq. (8.1). However, in Section 8.3 it was demonstrated that for a non-coupled and non-driven system the first time steps from the ensemble calculations and therefore potentially all following dynamics are not represented properly for the partially excited state.

Another possibility is to not prepare the system in the wanted initial state, but to prepare the system in the ground state, which can unambiguously be sampled correctly, and drive it into this state with a short Gaussian pulse

$$E(t) = e^{i\phi_0} \frac{\mathcal{A}}{\sqrt{2\pi}\sigma} \exp\left(-\frac{(t-t_0)^2}{2\sigma^2}\right) \tag{8.39}$$

at time t_0 with width σ after the start of the simulation. The simulation results are corrected for this time offset by t_0. According to the area theorem [AE87; MH67], this pulse drives the system into the desired excited state given in Eq. (8.1). As default parameters we choose $t_0 = 0.05/\Gamma$ and $\sigma = 0.005/\Gamma$ and sample the ground state with the double rotation scheme introduced in Section 8.2.2.

8.4.1 No inter-nuclear coupling

In Fig. 8.4, the time evolution of the population and of the coherence from the CDTWA initialized in the ground state and driven into the excited state is compared to the analytical expression in Eq. (8.21) for a smaller excitation of $\mathcal{A} = 0.3\pi$ (blue) and a higher excitation of $\mathcal{A} = 0.7\pi$ (orange). Here, we again consider nuclei without coupling. For the higher excitation of $\mathcal{A} = 0.7\pi$ we find good agreement with the analytical expression. However, at early times the results from the CDTWA have a slightly smaller decay rate. For the smaller excitation of $\mathcal{A} = 0.3\pi$, the agreement is slightly worse, especially for the coherence, which might be due to the unphysical effects. We also see slight deviations of the initial state values. Shorter excitation pulses should be able to improve the quality of the state preparation, but also increase the computational effort due to the necessity of finer time steps. However, the time evolution of the two observables also for the smaller excitation matches the analytical result on a similar level as in the case of sampling the wanted initial state directly, which is discussed in Fig. 8.3 and shown in Fig. 8.4 for comparison.

We can conclude that preparing the system in the ground state and driving it into the desired initial state performs as good as sampling the initial state directly with the double rotation scheme. However, driving the system into the partially excited state has the advantage, that all investigations can be performed with the same set of sampling points and effects due to different sampling points are excluded.

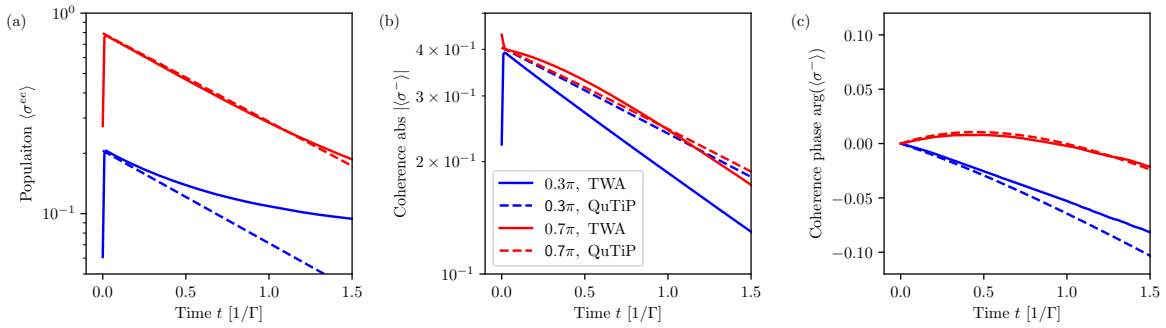

Figure 8.5: Time evolution of different observables calculated with CDTWA (solid lines) and QuTiP (dashed lines) for an initial excitation of $\mathcal{A} = 0.3\pi$ (blue) and $\mathcal{A} = 0.7\pi$ (red). Displayed are the excited state population $\langle\sigma^{ee}\rangle$, and the absolute value and phase of the coherence $\langle\sigma^{-}\rangle$ of the 5th nucleus of a linear chain with 10 nuclei. For the calculation the free-space couplings in Eq. (8.40) with the dipole moment perpendicular to the chain of nuclei ($\theta_d = 0.5\pi$) are used, and the incident light is perpendicular to the chain, such that all initial phases are the same.

8.4.2 With inter-nuclear coupling

As already mentioned, it is known for the CDTWA that the ensemble equations do not represent the single particle case, and thus also not the case of an ensemble without couplings, appropriately [MF23]. Therefore, as a final benchmark we want to cross-check the time evolution with couplings between the nuclei. In this case, no exact analytical formula is known, but we can calculate the dynamics for a small system of $N = 10$ nuclei with the python package QuTiP [JNN12; JNN13]. To this end, we use the free-space couplings in Eq. (2.33). For a linear chain along the z-direction, the free-space couplings simplify to

$$\frac{\Gamma_{mn}^{\mathrm{rad}}}{2} + iJ_{mn} = -\frac{3i\Gamma^{\mathrm{rad}}}{2}\left[\left(\frac{1}{\eta_{mn}} + \frac{i}{\eta_{mn}^2} - \frac{1}{\eta_{mn}^3}\right) - \cos^2(\theta)\left(\frac{1}{\eta_{mn}} + \frac{3i}{\eta_{mn}^2} - \frac{3}{\eta_{mn}^3}\right)\right] e^{i\eta_{mn}}, \quad (8.40)$$

with θ being the angle between the dipole moment and the chain and the normalized distance $\eta_{mn} = \eta_0|n-m|$ with $\eta = k_0 a_0 \approx 21$ being the product of wavenumber k and lattice spacing a_0. Since the CDTWA works better for higher cooperativity in the system, we neglect the internal conversion channel $\Gamma^{\mathrm{IC}} = 0$ and thus $\Gamma_{mn} = \Gamma_{mn}^{\mathrm{rad}}$.

For ^{57}Fe, the resulting time evolution is shown in Fig. 8.5 for the excited state population $\langle\sigma^{ee}\rangle$ and the absolute value and phase of the coherence $\langle\sigma^{-}\rangle$ of the 5th nuclei calculated with the CDTWA (solid lines) and QuTiP (dashed lines). The population and absolute value of the coherence in Fig. 8.5(a) and Fig. 8.5(b), respectively, agrees for the higher excitation of $\mathcal{A} = 0.7\pi$ (red line). For the smaller excitation of $\mathcal{A} = 0.3\pi$, similar to the situation without coupling in Fig. 8.4, the situation is worse. This is attributed to an unphysical driving as discussed in [MF23] and summarized in Section 7.5.5, which is the worse the lower the excitation is. Including couplings can also induce a time-dependent phase in the coherence, which is displayed in Fig. 8.5(c). We will study this in more detail in Chapter 9. Interestingly, for both initial excitations the time evolution of the coherence is not so much affected by the unphysical driving, but still the higher initial excitation matches the results from `QuTiP` better.

Finally, we can conclude that sampling the initial ground state with the double rotation sampling scheme and driving the system into the desired initial state according to the area theorem is a reasonable approach to prepare the desired initial state. This is especially the case for higher excitations, where the unphysical effects discussed in Section 7.5.5 are not as severe as for lower excitations. This is why in the remaining part of the thesis we preferably use the CDTWA above inversion $\mathcal{A} \geq 0.5\pi$.

8.5 Summary and outlook

The sampling of the initial state in the framework of the truncated Wigner approximation is a much discussed problem in the literature [MPF22; Piñ+17; PRK16]. Here we have first studied different methods to sample a partially excited initial state. Afterwards, we performed a first time step analysis to investigate whether the sampling scheme also results in the correct dynamics. This was done for

the single nucleus equations as well as for the ensemble equations without coupling. Note that the latter is a very unfavorable case for the CDTWA, which is why the results should only bring some qualitative insights, but are not assumed to be accurate. For the single nucleus equations, all sampling schemes give the correct first time step. For the ensemble equations without coupling, this is not the case. This might be due to the ensemble equations without coupling not properly representing the dynamics of the single nuclei in the ensemble [MF23]. Interestingly, we find different first time steps for different sampling schemes. This demonstrates that the choice of the sampling scheme can strongly influence the predicted dynamics. Furthermore, we investigated the situation in which the system is prepared in the ground state and driven into the desired initial state by a short pulse. Here, for the early time evolution the agreement with analytical and `QuTiP` results is on a similar level than for the results where the system was prepared directly in the partially excited state. However, if we drive the system into the partially excited state, we can prepare it in the ground state at the beginning of the simulation. This allows us to take advantage of the ground state sampling as presented in [MPF22]. In addition, the sampling is independent of the desired partially state and thus does not influence the predicted dynamics. Therefore, for the rest of the thesis, we drive the system into the partially excited state.

For future initial state preparation in the framework of the truncated Wigner approximation, we propose to not only consider whether the initial state is sampled correctly, but in addition perform a first time step analysis, as discussed here, to ensure a correct prediction of the time evolution. As an alternative to the direct preparation of the desired initial state with potentially complicated sampling schemes, we propose to prepare the system in the ground state for which the sampling is established [HRR22; MPF22], and drive the system into the desired initial state.

Chapter 9

Cumulant expansion approach to the decay dynamics of interacting Mössbauer nuclei after strong impulsive excitation

This chapter is based on the following preprint:

Cumulant expansion approach to the decay dynamics of interacting Mössbauer nuclei after strong impulsive excitation
M. Gerharz and J. Evers
arXiv:2510.00970 [quanth-ph]

Content has been reproduced verbatim, but the article was restructured to suit the format of this thesis. In particular, main text and supplementary material were merged.

9.1 Motivation

Mössbauer nuclei have already proven to be a versatile platform for quantum optics and related concepts, even though typical experiments so far have been restricted to the low-excitation limit with less than one signal photon on average due to source limitations [Fuj+21; Ger+25a; Hab+16; Hab+17; Hee+13; Hee+15a; Hee+15b; Hee+21; Hel+91; Kuz+24; Loh+25b; Naz+25; RE21; Röh+10; Röh+12; Sak+17; Sch+02; Shv+96; SVP25; Vag+14; Vel+24; VSK13; Yam+24; Zha+19]. XFELs [Ama+12; Bar+10; Dec+20; Emm+10; Ino+19; Ish+12; Liu+23; Liu+25b; Nam+21] provide access to new excitation regimes which are expected to advance the field [RE21; She12], and first experiments have already demonstrated some of the novel possibilities [Chu+18; Ger+25b; Liu+25a; Shv+23]. Towards higher excitation, more than 900 signal photons after a single x-ray excitation have been observed recently [Ger+25b], and it has been theoretically proposed that focusing the x-ray beam could significantly enhance the fraction of excited nuclei in the ensemble [LKE25b]. Further source development such as XFELOs [KSR08; Mar+23; Rau+25] could even bring full inversion of an ensemble of Mössbauer nuclei within reach [Ada+19; LKE25b].

A corresponding theoretical framework is therefore required to match the pace of experimental advances. From a theoretical point of view, the nuclear ensemble forms an interacting many-body system. As such, the problem is strongly related to other many-body systems from a theoretical point of view. A particular challenge is that in general the interaction between the nuclei and the incoherent loss channels may operate on comparable time scales, such that neither dominates. This renders some of the well-known approaches less suitable (see, e.g., the discussion in [MF23]). In the low-excitation limit, the resulting equations can analytically be solved, giving rise, e.g., to the well-known response function formalism [HT99; KAK79] and quantum optical models [HE13; KCP20; Len+20]. Towards higher excitation, different theoretical approaches have been pursued. Typical experiments excite the nuclei impulsively, fast as compared to all other time scales in the system. This allows one to separate and analytically solve the nuclear excitation [LKE25a; LKE25b]. By contrast, the subsequent decay dynamics of the interacting ensemble of nuclei is much harder to treat. It has been suggested to use a perturbative approach to characterize the nuclear dynamics in leading order beyond the linear case [WE23]. This approach allows one to derive experimental signatures for the non-linear excitation, but it fails towards higher excitation. Assuming that the dynamics is restricted to the fully symmetric superradiant subspace, the dynamics can also be evaluated [HKE16]. However, this approach fails to capture the incoherent single-particle dynamics which evolves the system out of the symmetric subspace, but is crucial in nuclei due to the non-radiative internal conversion channel [HT99; Röh04]. Recently, it has been suggested to use a matrix-product state approach [Sch11] to model the many-body dynamics [Kon+25]. This approach can handle higher excitation and allows one to analyze

photon correlations, but only a small number of nuclei can be modeled without further approximations and entanglement between the particles is only partially captured.

In the following, we pursue a different approach, which exploits that in typical bulk target materials the coupling between the nuclei is moderate. This suggests a perturbative expansion in the nuclear coupling, rather than an expansion in the degree of excitation or a truncation of the Hilbert space. One approach is the *cumulant expansion* [Kub62], which is well-known in modeling many-body dynamics in general [KK08; KK18; KR15; ROY23; RS21; SSF20] but so far has not been applied to model the dynamics of Mössbauer nuclei.

Here, we solve the nuclear many-body system using a cumulant expansion approach. We derive effective many-body equations valid for arbitrary degrees of excitation, which can efficiently be solved even for larger ensembles since their number scales linearly with that of the nuclei. Assuming further a translational invariance in an extended ensemble under homogeneous excitation conditions, we derive an effective single-particle non-linear equation of motion which captures the many-body dynamics in leading order of the cumulant expansion. It allows one to model the many-body system very efficiently, independent of the number of nuclei. Solving this equation, we show that towards higher excitation, the couplings between the nuclei imply a characteristic non-linear evolution of the nuclear dipole phase, and put forward a method to interferometrically measure it which exploits the geometry-dependence of the inter-nuclear couplings. By comparing with the case without translational invariance, we further uncover interesting finite-size effects in smaller ensembles which could also be experimentally explored.

9.2 Equations of motion

9.2.1 Decay dynamics of the nuclear many-body system

The decay dynamics can be modeled using a master equation for N nuclei [Ase+17a; FS05; HE13; Kif+10]

$$\dot{\rho} = \frac{1}{i\hbar}\,[H,\rho] + \mathcal{L}[\rho]\,, \tag{9.1}$$

$$H = -\,\hbar \sum_{n,m=1}^{N} J_{mn}\,\sigma_n^+\,\sigma_m^-\,, \tag{9.2}$$

$$\mathcal{L}[\rho] = \sum_{n,m=1}^{N} \frac{\Gamma_{mn}}{2}\left(2\sigma_m^-\rho\sigma_n^+ - \sigma_n^+\sigma_m^-\rho - \rho\sigma_n^+\sigma_m^-\right)\,, \tag{9.3}$$

where $\Gamma_{mn} = \Gamma_{mn}^{\mathrm{rad}} + \delta_{mn}\Gamma^{\mathrm{IC}}$. Here, $\mathcal{L}[\rho]$ describes the incoherent dynamics, where $\Gamma = \Gamma_{nn}$ is the total linewidth ($\Gamma = 4.7\,\mathrm{eV}$ for α-iron) comprising the radiative contribution $\Gamma_{nn}^{\mathrm{rad}}$ and the non-radiative part Γ^{IC} of the single-particle spontaneous decay. The other elements J_{nm} and $\Gamma_{nm}^{\mathrm{rad}}$ with $n \neq m$ describe the coherent and the incoherent coupling rates between two nuclei n, m which are derived by tracing out the modes of the environmental radiation field.

We proceed by deriving equations of motion for the expectation values of relevant single-particle operators σ_l^- and $\sigma_l^{ee} = \sigma_l^+\sigma_l^-$, where the former characterizes the coherence and the latter the excited-state population of atom l. Here, $\sigma_l^\pm$ are Pauli raising and lowering spin operators acting on atom l. We obtain (see Appendix B.2)

$$\frac{\mathrm{d}}{\mathrm{d}t}\langle\sigma_l^-\rangle = -\,\frac{\Gamma_{ll}}{2}\,\langle\sigma_l^-\rangle - \sum_{\substack{n=1\\n\neq l}}^{N} \mathcal{C}_{nl}^*\left(\langle\sigma_n^-\rangle - 2\,\langle\sigma_l^{ee}\sigma_n^-\rangle\right)\,, \tag{9.4}$$

$$\frac{\mathrm{d}}{\mathrm{d}t}\langle\sigma_l^{ee}\rangle = -\,\Gamma_{ll}\langle\sigma_l^{ee}\rangle - \sum_{\substack{n=1\\n\neq l}}^{N} \mathcal{C}_{nl}\,\langle\sigma_n^+\sigma_l^-\rangle + \mathcal{C}_{ln}^*\,\langle\sigma_l^+\sigma_n^-\rangle\,, \tag{9.5}$$

where $\mathcal{C}_{mn} = \frac{\Gamma_{mn}}{2} + iJ_{mn}$.

9.2.2 Cumulant expansion

The equations of motion for the single-particle expectation values Eqs. (9.4) and (9.5) depend on two-particle expectation values. This hierarchy generalizes to higher-order expectation values, rendering

an exact solution impossible. In the cumulant expansion approach, a closed set of equations is obtained by truncating this hierarchy at a given order [Kub62]. We employ the first order expansion, by approximating

$$\langle A_n\, B_m\rangle \approx \langle A_n\rangle \langle B_m\rangle \qquad (n \neq m)\,, \tag{9.6}$$

for operators acting on different atoms n and m. We obtain (see Appendix B.3)

$$\frac{\mathrm{d}}{\mathrm{d}t}\langle \bar{\sigma}_l^-\rangle = -\frac{\Gamma_{ll}}{2}\left\langle \bar{\sigma}_l^-\right\rangle - \left(1-2\left\langle \sigma_l^{ee}\right\rangle\right)\kappa_l^R\,, \tag{9.7}$$

$$\frac{\mathrm{d}}{\mathrm{d}t}\phi_l = -\left(1-2\left\langle \sigma_l^{ee}\right\rangle\right)\langle \bar{\sigma}_l^-\rangle^{-1}\kappa_l^I\,, \tag{9.8}$$

$$\frac{\mathrm{d}}{\mathrm{d}t}\langle \sigma_l^{ee}\rangle = -\Gamma_{ll}\langle \sigma_l^{ee}\rangle - 2\left\langle \bar{\sigma}_l^-\right\rangle \kappa_l^R\,, \tag{9.9}$$

$$\kappa_l = \kappa_l^R + i\kappa_l^I = \sum_{\substack{n=1\\ n\neq l}}^{N} \mathcal{C}_{nl}^{*}\langle \bar{\sigma}_n^-\rangle e^{i(\phi_n-\phi_l)}\,. \tag{9.10}$$

Here, we have further decomposed the nuclear coherences into their magnitude and their phase, $\langle \sigma_l^-\rangle = |\langle \sigma_l^-\rangle|\, e^{i\phi_l} = \langle \bar{\sigma}_l^-\rangle\, e^{i\phi_l}$. We find from Eq. (9.8) that the phase ϕ_l of the nuclear dipole moments in general has a non-linear and excitation-dependent time evolution. Below, we develop this feature as a signature for non-linear nuclear excitation.

Note that the Eqs. (9.7)-(9.9) already admit for an efficient numerical simulation, since they have a favorable linear scaling with the number of nuclei N. In contrast, the number of matrix elements of the original density operator scales exponentially with N.

9.2.3 Translationally invariant systems

We now continue the discussion by focusing on translationally invariant systems, which will allow us to reduce the computational effort further. To this end, we assume that the nuclei are arranged in an infinite translationally invariant lattice. Furthermore, we assume that the initial excitation is due to a plane wave field incident with wave vector $\vec{k}$ on all nuclei with the same magnitude. Hence, the coherences of all nuclei after the excitation differ only in their initial phases $\phi_l(0)$. In this case, Eqs. (9.7)-(9.9) become (see Appendix B.4)

$$\frac{d}{dt}\langle \bar{\sigma}^-\rangle = -\frac{\Gamma}{2}\left\langle \bar{\sigma}^-\right\rangle - \left(1-2\left\langle \sigma^{ee}\right\rangle\right)\langle \bar{\sigma}^-\rangle K^R\,, \tag{9.11}$$

$$\frac{d}{dt}\phi = -\left(1-2\left\langle \sigma^{ee}\right\rangle\right)K^I\,, \tag{9.12}$$

$$\frac{d}{dt}\langle \sigma^{ee}\rangle = -\Gamma\langle \sigma^{ee}\rangle - 2\left\langle \bar{\sigma}^-\right\rangle K^R\,, \tag{9.13}$$

$$K = K_l = \sum_{\substack{n=1\\ n\neq l}}^{N} \mathcal{C}_{nl}^{*} e^{i(\phi_n(0)-\phi_l(0))}\,. \tag{9.14}$$

Here, $\langle \bar{\sigma}^-\rangle = \langle \bar{\sigma}_l^-\rangle$, $\langle \bar{\sigma}^{ee}\rangle = \langle \bar{\sigma}_l^{ee}\rangle$ and $K = K_l$ are the same for all atoms, respectively, and K^R and K^I denote the real and imaginary part of K, respectively. Analogously, the nuclear phase evolves as $\phi_l = \phi_l(0) + \phi$ including the initial excitation phase. Finally, K is a constant which crucially determines the dynamics.

As a result we find that for typical experimental situations, the many-body dynamics can be modeled using a simple set of nonlinear equations, independent of the number of nuclei. In Section 9.4, a comparison to chains of finite length is provided, which supports the validity of our translationally invariant model.

9.3 De-excitation dynamics

9.3.1 Temporal dynamics in the low-excitation limit

Eqs. (9.11)-(9.13) immediately allow us to connect our results to known phenomena in the well-studied low-excitation limit $\langle \sigma^{ee}\rangle \approx 0$. Then, the equations of motion reduce to $\frac{\mathrm{d}}{\mathrm{d}t}\langle \bar{\sigma}^-\rangle \approx -(\Gamma/2 + K^R)\langle \bar{\sigma}^-\rangle$

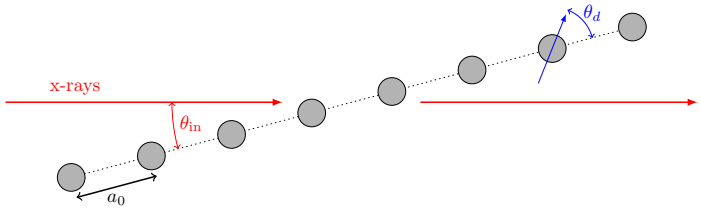

Figure 9.1: Schematic of the investigated setup. A linear chain of N nuclei (gray) placed with distance a_0 is irradiated with x-rays (red) under an incident light angle θ_{in}. The dipole moments (blue) of the nuclei are aligned with an angle θ_d with respect to the chain of nuclei.

and $\frac{\mathrm{d}}{\mathrm{d}t}\phi \approx -K^I$. From these equations we can immediately interpret the real and imaginary parts of K in terms of a superradiant broadening and an interaction-induced energy shift of the nuclear resonance, respectively [HT99; RE21; Röh+10].

9.3.2 Temporal dynamics beyond the low-excitation limit

Next we turn to the largely unexplored regime of higher excitation. We start by noting that the magnitude of the coupling parameter K generally is small as compared to Γ. The reason is that the total decay rate Γ is dominated by the non-radiative (internal conversion) parts Γ^{IC} which do not contribute to the couplings. A more detailed numerical study of K is provided below.

Therefore the phase of the nuclear dipole moment Eq. (9.11) is the most promising signature for effects of the non-linear excitation, as it is only governed by K, but not by Γ. In order to derive its time evolution, we can approximately solve for $\langle\sigma^{ee}\rangle$ by neglecting the small contribution K^R in Eq. (9.13). Inserting the solution $\langle\sigma^{ee}\rangle(t) \approx \sin^2(\mathcal{A}/2)\exp(-\Gamma t)$ into Eq. (9.11), we find

$$\phi(t) = -K^I\left[t - \frac{2}{\Gamma}\left(1 - e^{-\Gamma t}\right)\sin^2\left(\frac{\mathcal{A}}{2}\right)\right] + \phi_0\,. \tag{9.15}$$

Here, $\mathcal{A}$ is the pulse area characterizing the initial nuclear excitation via $\langle\sigma^{ee}\rangle(0) = \sin^2(\mathcal{A}/2)$ and $\langle\bar{\sigma}^{-}\rangle(0) = \sin(\mathcal{A}/2)\cos(\mathcal{A}/2)$ [AE87]. We find that the nuclear phase evolves non-linearly at intermediate times until $\langle\sigma^{ee}\rangle$ has decayed to zero, with magnitude governed by K^I.

9.3.3 Coupling parameter K

We have seen that the central quantity governing the coupled decay dynamics is the parameter K. In preparation for the following numerical study of the system, we now explore the parameter range of K^R and K^I as a function of the geometry of the nuclear ensemble. For this, we assume that the nuclear dipole moments are aligned at an angle θ_d relative to the chain axis, and that the incident plane wave x-ray pulse propagates at an angle θ_{in} with respect to the chain. A schematic of this is setup is displayed in Fig. 9.1. We model the couplings using the well-known expression for free-space dipole-dipole couplings [FS05; Kif+10]

$$J_{nm} + i\frac{\Gamma_{nm}}{2} = \frac{1}{\hbar}\,\vec{d}^{*}\cdot\chi(\vec{r}_n,\vec{r}_m)\cdot\vec{d}\,, \tag{9.16}$$

with

$$\chi_{pq}(\vec{r}_n,\vec{r}_m) = \frac{k_0^3}{4\pi\varepsilon_0}\left[\delta_{pq}\left(\frac{1}{\eta_{nm}} + \frac{i}{\eta_{nm}^2} - \frac{1}{\eta_{nm}^3}\right) - \frac{[\vec{R}_{nm}]_p\,[\vec{R}_{nm}]_q}{|\vec{R}_{nm}|^2}\left(\frac{1}{\eta_{nm}} + \frac{3i}{\eta_{nm}^2} - \frac{3}{\eta_{nm}^3}\right)\right] e^{i\eta_{nm}}\,. \tag{9.17}$$

Here it is, $\vec{R}_{nm} = \vec{r}_n - \vec{r}_m$ and $\eta_{nm} = k_0|\vec{R}_{nm}|$.

We continue the discussion for a linear chain of nuclei with a dipole moment at angle θ_d and the incident light at angle θ_{in} with respect to the chain as displayed in Fig. 9.1. For a linear chain of

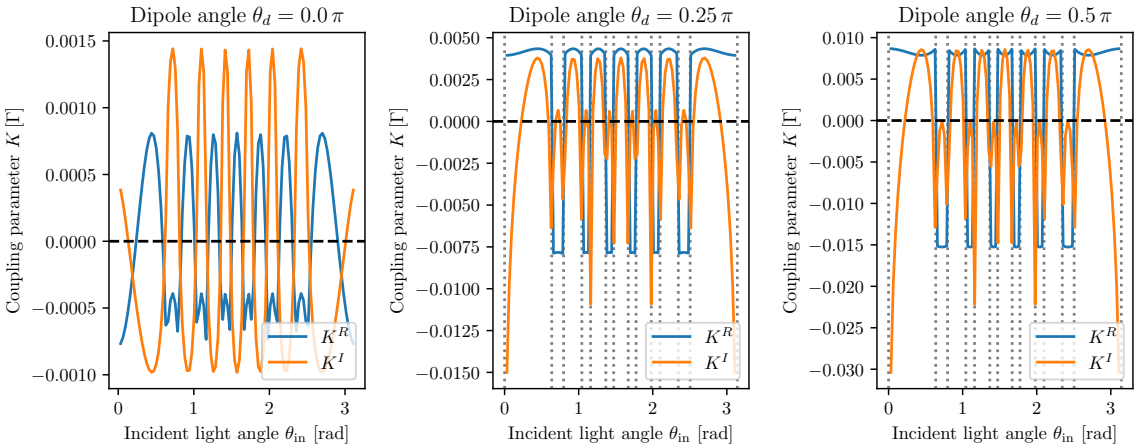

Figure 9.2: Coupling parameter K as a function of the incident angle θ_{in}. For the calculation, Eq. (9.21) is used with three different dipole angles, $\theta_d = 0$, $\theta_d = 0.25\pi$, and $\theta_d = \pi/2$, in the different panels. The dotted vertical lines indicate angles at which K formally diverges.

atoms along the z-direction, we can set $\vec{r}_n = (0, 0, n \cdot a_0)^\intercal$, where a_0 is the lattice constant. Then, $\eta_{nm} = k_0 a_0 |n - m| = \eta_0 |n - m|$, and Eq. (9.16) simplifies to

$$J_{nm} + i\frac{\Gamma_{nm}}{2} = \frac{k_0^3 |d|^2}{4\pi\hbar\varepsilon_0} \left[\left(\frac{1}{\eta_{nm}} + \frac{i}{\eta_{nm}^2} - \frac{1}{\eta_{nm}^3} \right) - \cos^2(\theta_d) \left(\frac{1}{\eta_{nm}} + \frac{3i}{\eta_{nm}^2} - \frac{3}{\eta_{nm}^3} \right) \right] e^{i\eta_{nm}}, \tag{9.18}$$

where θ_d is the orientation of the dipole moment relative to the chain as displayed in Fig. 9.1. We thus find

$$\mathcal{C}_{nm}^* = -\frac{3i\Gamma^{\text{rad}}}{2} \left[\left(\frac{1}{\eta_{nm}} + \frac{i}{\eta_{nm}^2} - \frac{1}{\eta_{nm}^3} \right) - \cos^2(\theta) \left(\frac{1}{\eta_{nm}} + \frac{3i}{\eta_{nm}^2} - \frac{3}{\eta_{nm}^3} \right) \right] e^{i\eta_{nm}}, \tag{9.19}$$

with the radiative decay rate $\Gamma^{\text{rad}} = \Gamma_{nn}^{\text{rad}}$, which is significantly smaller than the total decay rate Γ. Therefore, for an infinite chain of nuclei with free-space coupling, the coupling parameter K is given by

$$\begin{aligned} K = &- 3i\Gamma^{\text{rad}} \sum_{m=1}^{\infty} \left[\left(\frac{1}{\eta_0 m} + \frac{i}{\eta_0^2 m^2} - \frac{1}{\eta_0^3 m^3} \right) - \cos^2(\theta_d) \left(\frac{1}{\eta_0 m} + \frac{3i}{\eta_0^2 m^2} - \frac{3}{\eta_0^3 m^3} \right) \right] e^{i\,m\,\eta_0} \\ &\times \left(e^{i\,m\,\Delta\phi} + e^{-i\,m\,\Delta\phi} \right). \end{aligned} \tag{9.20}$$

This expression can be simplified using $\sum_{k=1}^{\infty} \frac{z^k}{k^s} = \text{Li}_s(z)$ if $z \neq 1$, and we find

$$\begin{aligned} K &= -\frac{3i\Gamma^{\text{rad}}}{2\eta_0} \sin^2(\theta_d)\, \mathcal{X}_1 - \frac{3\Gamma^{\text{rad}}}{4\eta_0^2} [1 + 3\cos(2\theta_d)]\, \mathcal{X}_2 - \frac{3i\Gamma^{\text{rad}}}{4\eta_0^3} [1 + 3\cos(2\theta_d)]\, \mathcal{X}_3, \\ \mathcal{X}_n &= \text{Li}_n \left(e^{i(\eta_0 + \Delta\phi)} \right) + \text{Li}_n \left(e^{i(\eta_0 - \Delta\phi)} \right), \end{aligned} \tag{9.21}$$

where $\text{Li}_n(z)$ is the polylogarithm. For the analysis, we use wavevector $k_0 = 2\pi/86\,\text{pm}$ corresponding to the resonance frequency of the Mössbauer transition in ^{57}Fe and a lattice constant $a_0 = 286\,\text{pm}$ corresponding to the nearest-neighbor spacing in α-Fe. With these parameters, the scaled distance parameter $\eta_0 = k_0 a_0 \approx 21$ reflects the weak coupling due to the comparably large separation of the nuclei, justifying the cluster expansion approach. Further, $\Delta\phi = \eta_0 \cos\theta_{\text{in}}$ characterizes the incident phase difference between two neighboring nuclei.

In Fig. 9.2, the dependence of the coupling parameter K on the incident angle θ_{in} is investigated for different dipole angles θ_d. Overall, we find that K is comparably small on the scale of the total decay rate Γ, confirming our approximation leading to Eq. (9.15). At first, we discuss the left panel in which the dipole angles is $\theta_d = 0$. This is a special situation because in this case the $1/\eta_{nm}$ term vanishes. As a result the overall coupling parameter results are small. Furthermore, it is dominated by χ_2, which is represented by a different shape of the functions as in the other panels. Especially, the singularities

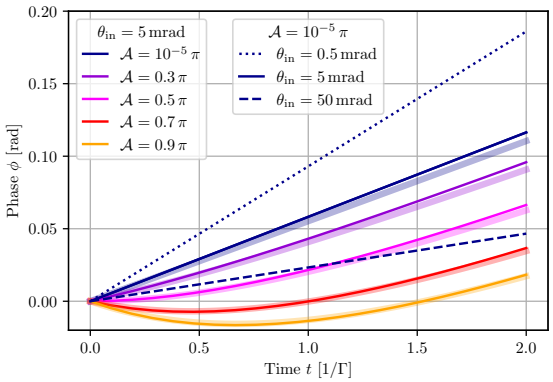

Figure 9.3: Nuclear dipole phase evolution as a function of incidence angle and degree of excitation. For a fixed incident angle $\theta_{\rm in} = 5\,{\rm mrad}$ the different colors of the solid lines indicate different degrees of initial excitation $\mathcal{A}$. The transition to a non-linear phase evolution is clearly visible. For comparison, the shaded lines show the results for the central nucleus calculated on a finite chain with $N = 3000$ nuclei. In addition, in the low-excitation regime $\mathcal{A} = 10^{-5}\pi$, the different line styles of the blue lines show the results for different incident light angles $\theta_{\rm in}$. The dipole moment is set perpendicular to the chain of nuclei ($\theta_d = \pi/2$).

do not occur in this configuration. Now, we focus on the other two panels for dipole angles $\theta_d = 0.25\pi$ and $\theta_d = 0.5\pi$, respectively. In both cases, the dependence on the incident light angle $\theta_{\rm in}$ is governed by χ_1, which is represented in the similar shape and only a different scale on the y-axis due to the $\sin^2\theta_d$ prefactor. The real part K^R essentially takes one of two values, either approximately 0.01Γ or -0.015Γ, and therefore is small as compared to Γ dominated by its non-radiative contribution. For K^I, in the center around the perpendicular incident direction, a set of characteristic minima appears. Mathematically these can be traced back to the fact that the polylogarithm ${\rm Li}_1(z) = -\ln(1-z)$ formally diverges for $z = 1$. As a result, the imaginary part of the coupling parameter K^I formally diverges for $\theta_d \neq 0$ and $\eta_0 \pm \Delta\phi = n2\pi$, for any integer n. In practice, this divergence is regularized by a finite interaction volume, e.g., limited by the photo-absorption in the target. The imaginary part can take large values. From an experimental point of view, the region of small incidence angles appears favorable, since it allows one to tune K^I over its entire range of values. The choice of a small incidence angle also ensures the possibility of a large number of nuclei in the excitation volume, as required by the assumption of translational invariance. For example, a beam of width $100\,\mu$m incident on the chain under an incident light angle of 5 mrad couples to approximately 100 million nuclei.

The formally divergence at certain incident light angles $\theta_{\rm in}$ is clearly visible and additionally indicated by the gray dotted lines. The real part of the coupling parameter K^R has an approximately constant value of $0.01\,\Gamma$ and $-0.01\,\Gamma$ with a slight asymmetry towards the negative values and jumps between those two values at the divergence angles. For the real part of the coupling parameter K^I, there are local maxima at approximately $0.01\,\Gamma$, but more interestingly close to the divergences, values with significantly larger absolute values are reached. Both the real and the imaginary part follow the behavior of $i\chi_1$ as expected. To study coupling induced effects, we are mainly interested in K^I because K^R always appears together with Γ and thus only provides a correction on the few percent level. The absolute value and thus the effect of the imaginary part of the coupling parameter K^I is strongest close to the singularities. To ensure a large number of nuclei and therefore the translational invariant approximation, we choose a grazing incidence geometry, i.e., very small incident light angles $\theta_{\rm in}$. For example a beam with a width of $100\,\mu$m hitting the chain under an incident light angle of 5 mrad excites approximately 100 million nuclei.

9.3.4 Numerical simulation of the phase evolution

We can now turn to a numerical simulation of the phase evolution governed by Eqs. (9.11)-(9.13). The result is shown in Fig. 9.3 for different degrees of initial excitations $\mathcal{A}$ and x-ray incidence angles $\theta_{\rm in}$. The blue curves correspond to the limit of linear excitation ($\mathcal{A} = 10^{-5}\pi$), with a linear time evolution as expected. From the dotted and the dashed lines we further find that the slope of the phase can be controlled via the incidence angle $\theta_{\rm in}$, as described by K^I. Next, we turn to the main results beyond the linear excitation regime. The solid lines of different color show the evolution for different initial

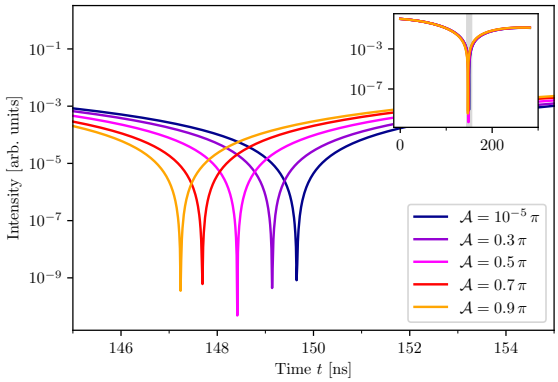

Figure 9.4: Time-dependent intensity of the x-ray scattered by two nuclear chains. The reference chain has a detuning of the nuclear resonance of $\Delta = -3\Gamma$, such that the interference between the chains leads to pronounced minima in the intensity. The non-linear phase evolution can then be observed via shifts of these minima in time. The different lines illustrate the dependence on the different degrees of excitation $\mathcal{A}$. For the sample chain the dipole moment is set perpendicular to the chain of nuclei ($\theta_d = \pi/2$) and the x-ray incidence angles for the sample [reference] chain is 5 mrad [0.22 rad]. The inset shows the signal intensity as a function of time over a larger time interval. The gray area marks the time region shown in the main panel.

degrees of excitation $\mathcal{A}$ at x-ray incidence angle $\theta_{\text{in}} = 5\,\text{mrad}$. With increasing excitation, a non-linear time evolution of the phase develops, which leads to a growing deviation from the low-excitation case. At later times, the phase evolution becomes linear again, but an excitation-dependent offset to the linear case remains.

In order to quantify the impact of the assumption of an infinite chain of atoms, the shaded colored lines display the phase evolution of the central atom in a finite chain of $N = 3000$ nuclei. The results qualitatively agree well with the infinite chain results. As discussed in Section 9.4, the small quantitative differences can be attributed to the deviation of the finite-chain coupling parameter K to that of the infinite chain, which provide a handle to experimentally explore finite-size effects in nuclear ensembles. We further compare our results to calculations based on the continuous-discrete truncated Wigner approximation (CDTWA) [MF23] in Section 9.5, an alternative approximation which is expected to work best in the case of strong nuclear correlations. We find good qualitative agreement, which supports the validity of the cluster expansion approach.

9.3.5 Experimental signatures of the non-linear phase evolution

Finally, we discuss how the non-linear phase evolution shown in Fig. 9.3 can be experimentally explored. We focus on the scattered electric field, which is commonly observed in experiments with Mössbauer nuclei. The overall electric field is obtained from a suitable summation of the contributions of each of the nuclear dipole moments $\langle \sigma_l^- \rangle$. We consider a scattering geometry in which the differences between the initial phases $\phi_l(0)$ are compensated for by the respective propagational phases from the individual nuclei to the detector, e.g., the forward scattering geometry. In this case, the residual relevant phase evolution of all nuclei is given by $\phi(t)$.

We propose to measure the time evolution of the phase $\phi(t)$ interferometrically, using two chains of nuclei. The orientation of the first chain relative to the x-ray incidence direction is varied, leading to phase evolutions as shown in Fig. 9.3. The other reference chain is fixed at an incidence angle where $K^I \approx 0$ ($\theta_{\text{in}} \approx 0.22\,\text{rad}$). In this setting, the intensity of the x-ray scattered by both chains increases together with the degree of excitation, but only the first one exhibits a non-linear phase evolution, which is ideal for interferometry with high visibility. The effect of the different phase evolutions can then most straightforwardly be measured by detuning the resonance energy of the reference sample by an energy shift Δ, e.g., via a Mössbauer drive [Gre12]. The total intensity then takes the form

$$I_{\text{comb}}(t) \propto |A_{\text{ref}}(t) e^{i\Delta \cdot t} + A_{\text{sample}} e^{i\phi_{\text{sample}}(t)}|^2, \tag{9.22}$$

where A_{ref} and A_{sample} are the amplitudes of the scattered fields of the reference chain and the sample chain, respectively. Assuming that both amplitudes approximately follow the single-particle

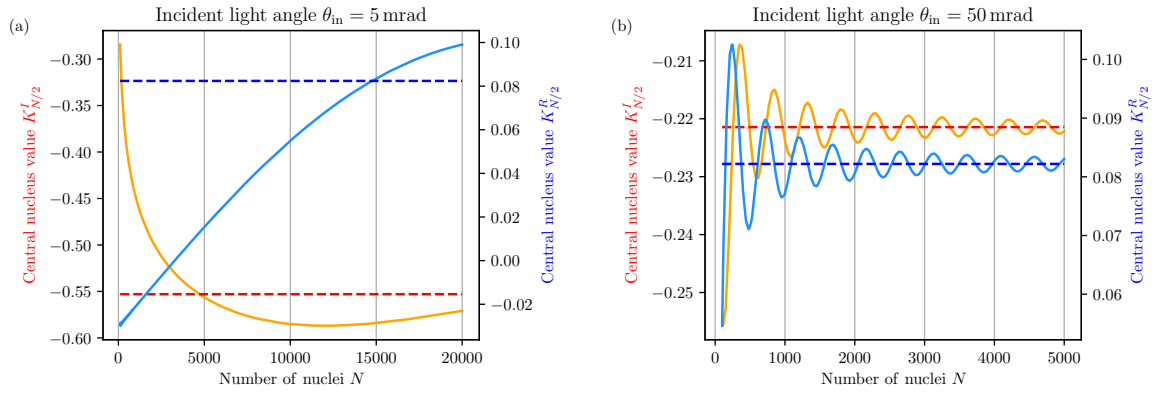

Figure 9.5: Convergence of coupling parameter K_l with increasing length of the one dimensional chain for two different incident light angles $\theta_{\text{in}} = 5\text{mrad}$ (left) and $\theta_{\text{in}} = 50\text{mrad}$ (right). The solid lines show K according to Eq. (9.14) evaluated at the central nucleus $l = N/2$. For comparison the coupling parameter K evaluated for an infinite chain of nuclei according to Eq. (9.21) is indicated by the dashed lines. The calculations are performed for dipole moment perpendicular to the chain ($\theta_d = \pi/2$).

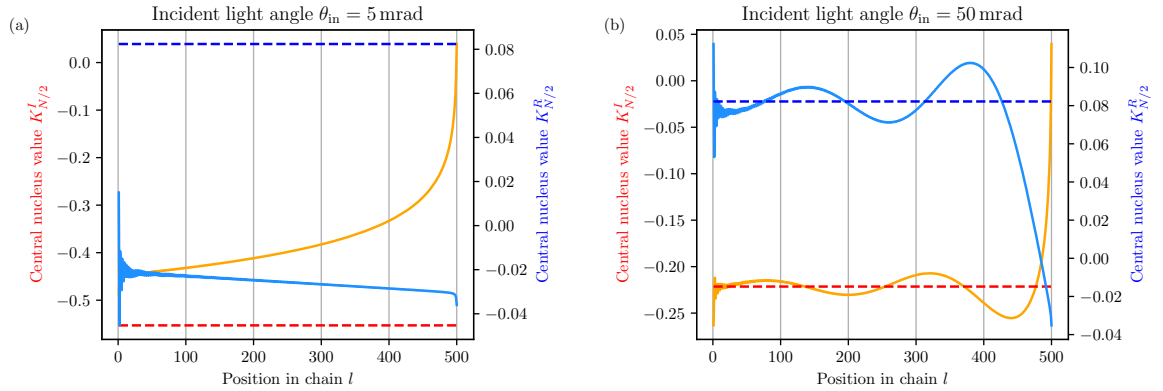

Figure 9.6: Coupling parameter K_l as a function of the position in the one-dimensional chain l for two different incident light angles $\theta_{\text{in}} = 5\text{mrad}$ (left) and $\theta_{\text{in}} = 50\text{mrad}$ (right). The solid lines show K_l according to Eq. (9.14) evaluated at nucleus l in a chain with length $N = 500$. For comparison the coupling parameter K evaluated for an infinite chain of nuclei according to Eq. (9.21) is indicated by the dashed lines. The calculations are performed for dipole moment perpendicular to the chain ($\theta_d = \pi/2$).

exponential decay $A_{\text{ref}}(t) \approx A_{\text{sample}}(t) \approx \exp(-\Gamma t/2)$, the total intensity approximately becomes

$$I_{\text{comb}} \propto e^{-\Gamma t} \sin\left[\Delta \cdot t + \phi_{\text{sample}}(t)\right] . \tag{9.23}$$

Hence, the interference between the chains leads to a modulation of the exponentially decaying intensity with frequency Δ. The non-linear phase shift of the first chain shifts this entire quantum beat pattern, facilitating its measurement.

An example for the time-dependent intensity in this detection scheme is shown in Fig. 9.4. The detuning is chosen as $\Delta = -3\,\Gamma$. The linear low-excitation case is given by the dark blue line with lowest value for $\mathcal{A}$. With increasing degree of excitation, the quantum beat minimum progressively shifts towards lower times by a few nanoseconds. Note that state-of-the-art experiments on nuclear forward scattering routinely measure the time-dependence with (sub-)nanosecond resolution.

9.4 Finite size effects

So far, we have studied the translational invariant system with the coupling parameter K being evaluated for an infinite chain. In Fig. 9.5 the coupling parameter K calculated for a finite chain with N nuclei according to Eq. (9.14) and evaluated at the central nucleus $l = N/2$ is displayed as a function of the number of nuclei in the chain. Overall, we see convergence to the asymptotic value in

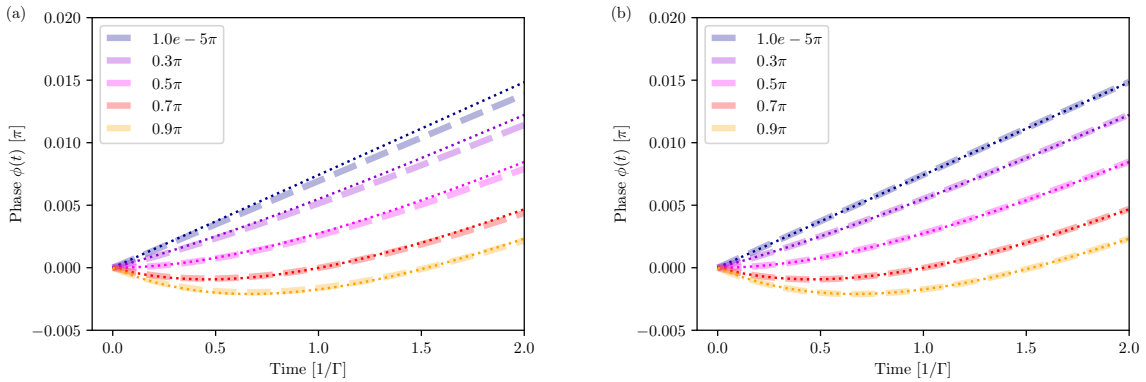

Figure 9.7: Comparison of the phase evolution computed with a finite chain evaluated at the central nucleus (dashed) and the translational invariant model (dotted). In (a) the chain has a length of $N = 362$ nuclei, which corresponds to a point of maximal deviation of K^I in Fig. 9.5(b), in (b) a length of $N = 257$ nuclei corresponding to a point of minimal deviation in K^I is chosen. The different colors indicate different initial excitations $\mathcal{A}$ according to the respective legend. The calculations are performed for dipole moment perpendicular to the chain ($\theta_d = \pi/2$) and a small incident light angle of $\theta_{\text{in}} = 50\,\text{mrad}$.

Eq. (9.21) (dashed) for increasing N. Furthermore, we see oscillations around the asymptotic value. The frequency of those is decreasing for smaller incident light angles θ_{in} as can be seen by comparing the two panels.

In Fig. 9.6, the coupling parameter for a finite chain K_l in Eq. (9.14) is evaluated as a function of the position within the chain l. Due to the asymmetry of number of nuclei left and right of a certain nucleus, this function exhibits oscillations and is asymmetric. By comparing the two different incident light angles θ_{in} in the two panels, we see that especially for K_I the variation over the chain is stronger for smaller incident light angles. The oscillations decrease with rising number of nuclei N. For smaller chains, they are however of relevance when summing the scattered electric field of all nuclei and might already in the low-excitation limit lead to modified angular patterns. For larger samples, the variations are negligible, which is why we continue with the analysis of finite size effects at the central nucleus only.

To investigate finite size effects during the time evolution in Fig. 9.7, the results for the central nucleus in a finite chain are compared to those from the translational invariant model for different initial excitations $\mathcal{A}$. For Fig. 9.7(a), the number of nuclei is $N = 362$, which corresponds to a maximal difference of the coupling parameter K^I from the asymptotic value, as can be seen from Fig. 9.5(b). Although qualitatively the overall trends of the non-linear time-evolution agree, there are noticeable quantitative differences. In Fig. 9.7(b) a smaller chain with $N = 257$ nuclei, but with minimal deviation of the coupling parameter K^I is used. Here, the quantitative agreement is significantly better than in the other case although the chain is smaller. This is already a strong indication, that the dominant finite size effect for observables on the single atom level is the convergence of the coupling parameter K.

To quantify the convergence with chain length, for each observable O we calculate the mean squared absolute difference between the result from the translational invariant model O_∞ and the finite chain of length N result O_N integrated over time $\Delta O = \frac{1}{M}\sum_{i=1}^{M} |O_\infty(t_i) - O_N(t_i)|^2$. In Fig. 9.8, the deviation ΔO is displayed for the absolute value and phase of the coherence and the population evaluated at the central nucleus in the chain $l = N/2$ as a function of the number of nuclei in the chain N. The general trend is that the deviations decrease with rising length of the chain as expected. In addition, the deviations for the absolute values of the coherence and the population are smaller because in the respective equations of motions, the relevant part of the coupling parameter K^R is dominated by the single-particle decay Γ. Besides the general convergence, there is an oscillatory structure. This structure comes from the oscillatory convergence behavior as shown in Fig. 9.5. To see this more clearly, on a second y-axis for the real and imaginary part, respectively, the squared absolute difference of the coupling parameter calculated for a finite chain K is compared to the asymptotic value given by Eq. (9.21) is displayed. The oscillatory structure of ΔO clearly follows the differences of K. Therefore, we conclude that for the central nucleus the most-dominant finite size effect is the difference in the imaginary part of the coupling parameter K^I, which in a converging but

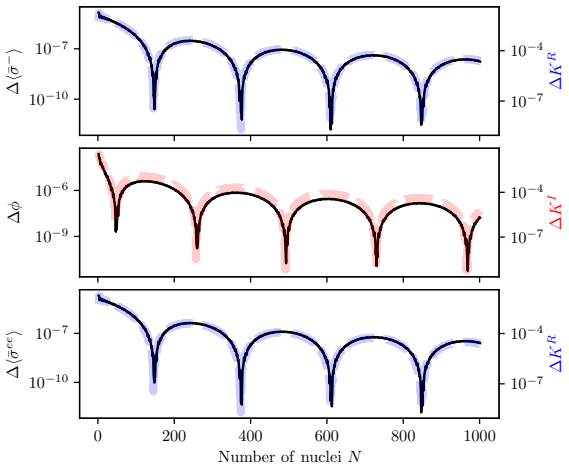

Figure 9.8: Impact of finite size effects on the nuclear dynamics. The deviation of observable O is quantified by the integrated quadratic differences over time $\Delta O = \frac{1}{M}\sum_{i=1}^{M} |O_\infty(t_i) - O_N(t_i)|^2$, where O_∞ is the result for a translationally invariant infinite chain and O_N is the result from a finite chain of length N evaluated at the central nucleus. The three panels show the deviation as a function of chain length N (black markers). The comparison is made for the absolute value of the nuclear coherence (top panel), the phase of the coherence (central panel) and the population (bottom). For comparison, on the second y-axis, the absolute difference $|K_\infty - K_N|^2$ of the dominant part (real or imaginary part) of the coupling parameter K is shown (red and blue dashed lines). The integration time is up to $t = 2/\Gamma$, the dipole is perpendicular to the chain $\theta_d = \pi/2$ and the incident light angle is $\theta_{\text{in}} = 50\,\text{mrad}$.

oscillating manner depends on the number of nuclei in the chain N.

9.5 Beyond cumulant expansion

In order to verify that the results discussed in the main text obtained from the cumulant expansion are within the validity range of the method, we compare the results with the phase evolution obtained in the framework of the CDTWA developed by Mink et al. [MF23]. This approach is known to work best for stronger couplings and higher excitations, whereas in the opposite case beyond $t = 1/\Gamma$ unphysical effects appear [MF23]. Therefore, we neglect the internal conversion for this comparison ($\Gamma^{\text{IC}} = 0$) which results in higher cooperativity and thus better validity of CDTWA, but is a less favorable parameter range for the cumulant expansion. With internal conversion, the cumulant expansion results are expected to be be more reliable. Nonetheless, the CDTWA provides a good crosscheck for the cumulant expansion results because the approximation methods are complementary to each other. In Fig. 9.9 for the central nucleus $l = N/2$ in a chain of length $N = 100$, the phase evolution calculated with the cumulant expansion and the CDTWA is compared for different initial excitations $\mathcal{A}$. For all three shown different degrees of initial excitation, the results obtained with the cumulant expansion (dashed lines) and CDTWA (solid lines) agree qualitatively well, which confirms the non-linear phase evolution.

9.6 Summary and Outlook

Motivated by recent experimental progress, we analyzed the decay dynamics of an interacting ensemble of Mössbauer nuclei after an impulsive excitation by an accelerator-based x-ray source. Unlike previous approaches, we expanded the equations of motion to leading order in the degree of interaction-induced nuclear correlations, which is justified by the comparably small coupling of nuclei in bulk material. Within this approach, we derived equations of motions for the ensemble which scale only linearly in the number of nuclei, and therefore can efficiently be simulated even for larger ensembles. Assuming further a translational invariance of the arrangement of the nuclei and the x-ray excitation, which is a good approximation for established experimental settings, we could further reduce the theoretical description to three non-linear real-valued equations which describe the dynamics of the entire ensemble. We found that the dynamics then is governed by a single coupling

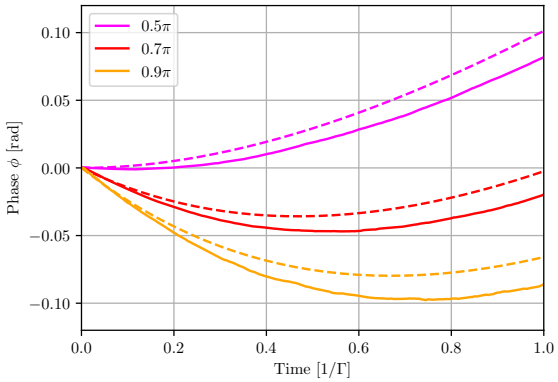

Figure 9.9: Phase evolution of the central nucleus in a chain of length $N = 100$. The figure compares results of the cumulant expansion (dashed) with corresponding results obtained from the truncated Wigner approximation (solid). The different colors indicate different initial excitations $\mathcal{A}$. The calculations are performed without internal conversion ($\Gamma^{\mathrm{IC}} = 0$) for dipole moment perpendicular to the chain ($\theta_d = \pi/2$) and a small incident light angle of $\theta_{\mathrm{in}} = 5\,\mathrm{mrad}$.

parameter K, which can be tuned in experiments.

As the main signature for higher excitation, we found that the inter-nuclear interactions lead to additional non-linear phase dynamics of the nuclear dipole moments. Based on this observation, we proposed a setup for measuring this signature, exploiting the geometry-dependence of K. This opens up an approach for the exploration of the non-linear nuclear decay dynamics.

For the future, we envision the generalization of our results to structured nuclear environments, which allow one to engineer and enhance the inter-nuclear couplings [DLE22a; DLE22b; LKE16; Loh+25b; RE21]. Such design capabilities could allow one to achieve particular control operations for the nuclear phase, or to also significantly affect the nuclear population dynamics. Furthermore, source development also brings experiments on smaller samples within reach. We identified characteristic finite-size effects which lead to both, variations in the coupling parameter K with chain length, as well as a dependence of the nuclear dynamics on their position within the chain. We envision future experiments exploring these finite-size effects, e.g., exploring the impact of the geometry on the coherence volume responsible for the collective effects observed in nuclear resonance scattering. Such studies would also form an important basis for future Mössbauer experiments with highest spatial resolution, i.e., small sample volumes.

Chapter 10

Propagation effects beyond the low-excitation regime

10.1 Motivation

Studying the nuclear forward scattering signal of a Mössbauer sample is well-established at synchrotrons [GBT11; Röh04] and we have seen in Section 2.1.4 how host material properties can be extracted from the time spectrum. Furthermore, the simple experimental setup of nuclear forward scattering makes it ideally suited for exploratory experiments at new light sources. In the low-excitation regime, the equations of motion decouple and an analytical formula can be derived, as we have seen in Section 2.3.3, and which is well-established in the theory of nuclear resonance scattering [KAK79; Röh04]. However, with recent experiments at XFELs [Chu+18; Ger+25b; Liu+25a; Shv+23] and the progress towards even more powerful x-ray light sources such as XFELOs [Mar+23; Rau+25], theoretical predictions beyond the low-excitation regime are required for two reasons. First, to extract material properties from the signal, also at potentially higher excitation, a precise understanding of the signal is required. Second, potential non-linear signatures are interesting themselves and could serve as indicators for the degree of initial excitation.

In the previous chapter, we investigated the de-excitation dynamics beyond the low-excitation regime of a very long chain, such that we can assume translational invariance and derive a simple model to describe the system [GE25]. However, in contrast to the setting discussed before, in nuclear forward scattering typically propagation effects occur, which originate from multiple scattering in extended, but finite systems [Shv+98]. Therefore, the translational invariance is not a valid assumption anymore and we have to model the full system. For the special case in which spontaneous decay is neglected, the dynamics can be described by a single differential equation [BC69], which is easily solvable numerically. Previous attempts to explore the dynamics of the system were made by numerically solving the Maxwell-Bloch equations in Eqs. (2.39) and (2.41) directly [Adi24; AGE_p], and by effective couplings and Matrix product states [Kon+25].

Here we follow a slightly different approach also by including the propagation effects via an effective coupling, but simulating the system with the cumulant expansion [Kub62] and the continuous-discrete truncated Wigner approximation (CDTWA) [MF23].

10.2 Many-body simulations

For definiteness, all calculations are made for ^{57}Fe with a lattice constant $a_0 = 286\,\mathrm{pm}$ and resonant wavelength $\lambda = 86\,\mathrm{pm}$. However, all calculations can be performed for a different Mössbauer isotope straightforwardly. Furthermore, for simplicity we consider a linear chain in z-direction.

The propagation effects are included via an effective coupling as discussed in Section 2.3.2 resulting in coupling terms

$$\tilde{J}_{mn} = \frac{\Gamma_{1\mathrm{D}}}{2} \sin\left(k_0 a_0 |n-m|\right) , \tag{10.1a}$$

$$\tilde{\Gamma}_{mn} = \Gamma \delta_{mn} - \Gamma_{1\mathrm{D}} \cos\left(k_0 a_0 |n-m|\right) , \tag{10.1b}$$

where $\Gamma_{1\mathrm{D}} = \frac{\mathrm{OD}}{2N}\Gamma$, with the optical density OD, the decay rate Γ, and the number of nuclei N. For enriched α-iron, the optical density depends on the thickness parameter b as $\mathrm{OD} \approx 4 \cdot b[\Gamma]$. This reduced coupling constant $\Gamma_{1\mathrm{D}}$ allows us to study macroscopic samples, e.g., $1\,\mu$m thick samples ($b \approx 4$) with 3500 nuclei, with smaller effective numbers of nuclei N on the order of a few hundred nuclei. Finally, the complex coupling parameter $\tilde{C}$ is given by

$$\tilde{C}_{mn} = \frac{\tilde{\Gamma}_{mn}}{2} + i\tilde{J}_{mn} = \frac{\Gamma}{2}\delta_{mn} + \frac{\Gamma_{1\mathrm{D}}}{2} \exp\left(k_0 a_0 |n-m|\right) . \tag{10.2}$$

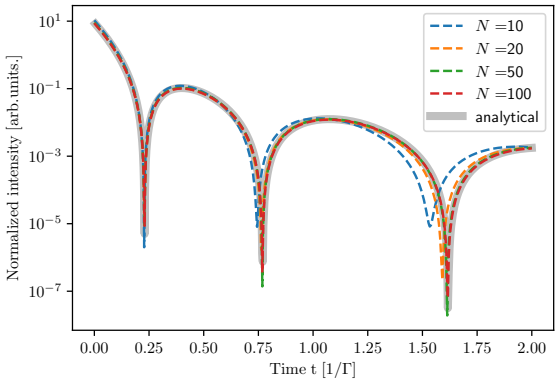

Figure 10.1: Intensity as a function of time for the analytical response function (gray solid line) and results from the cumulant expansion (colored dashed lines) in the low-excitation regime ($\mathcal{A} = 0.01\pi$). The different colors indicate the different chain lengths N. For the simulation the thickness parameter is chosen to be $b = 16\,\Gamma$. The curves are normalized such that the area under the curve equals 1.

As the main simulation tool we use the cumulant expansion, because the couplings are moderate, e.g., for $N = 100$ nuclei and $b = 4\Gamma$ it is $\Gamma_{1D} = 0.08\Gamma$. A detailed derivation of the equations of motion for the population $\langle\sigma_l^{ee}\rangle$ and coherence $\langle\sigma_l^{-}\rangle = |\langle\sigma_l^{-}\rangle|\, e^{i\phi_l} = \langle\bar{\sigma}_l^{-}\rangle\, e^{i\phi_l}$ can be found in Appendix B and results in

$$\frac{\mathrm{d}}{\mathrm{d}t}\langle\bar{\sigma}_l^{-}\rangle = -\frac{\Gamma_{ll}}{2}\langle\bar{\sigma}_l^{-}\rangle - (1 - 2\langle\sigma_l^{ee}\rangle)\,\kappa_l^R\,, \tag{10.3}$$

$$\frac{\mathrm{d}}{\mathrm{d}t}\phi_l = -(1 - 2\langle\sigma_l^{ee}\rangle)\,\langle\bar{\sigma}_l^{-}\rangle^{-1}\kappa_l^I\,, \tag{10.4}$$

$$\frac{\mathrm{d}}{\mathrm{d}t}\langle\sigma_l^{ee}\rangle = -\Gamma_{ll}\langle\sigma_l^{ee}\rangle - 2\,\langle\bar{\sigma}_l^{-}\rangle\,\kappa_l^R\,, \tag{10.5}$$

$$\kappa_l = \kappa_l^R + i\kappa_l^I = \sum_{\substack{n=1\\ n\neq l}}^{N} \tilde{\mathcal{C}}_{ln}^{*}\langle\bar{\sigma}_n^{-}\rangle e^{i(\phi_n - \phi_l)}\,, \tag{10.6}$$

with the complex coupling $\tilde{C}$ given by Eq. (10.2). Furthermore, we consider the setup in which the incident light is parallel to the chain of nuclei ($\theta_{\mathrm{in}} = 0$), such that the initial phases are given by $\phi_l = k_0 a_0 l \approx 21 \cdot l$ with wavevector $k_0 = 2\pi/\lambda$ and lattice constant a_0. The initial parameters for the population $\langle\sigma_l^{ee}\rangle(0) = \sin^2(\mathcal{A}/2)$ and absolute value of the coherence $\langle\sigma_l^{-}\rangle(0) = \sin(\mathcal{A}/2)\cos(\mathcal{A}/2)$ are determined by the initial degree of excitation $\mathcal{A}$.

The main observable to study propagation effects is the outgoing electric field after the sample, which in the forward scattering geometry is given by [MCD17]

$$E(t) = \mathcal{E}_{\mathrm{in}}(t) + i\sqrt{\frac{\Gamma_{1D}}{2}}\sum_{l=1}^{N} e^{-ik_0 a_0 l}\langle\sigma_j^{-}\rangle(t)\,. \tag{10.7}$$

In our case, the incident field is a very short pulse compared to the nuclear decay time scale and can therefore be approximated by $\mathcal{E}_{\mathrm{in}}(t) \propto \delta(t)$. The experimentally observed intensity is given by $I(t) = |E(t)|^2$.

10.3 Low-excitation regime

We start our investigations in the low-excitation regime. As we have seen in Section 2.3.3, in the low-excitation regime the outgoing electric field can be calculated analytically and the normalized electric field is given by (see Eq. (2.12))

$$E^{\mathrm{low}}(t,z) = E_{\mathrm{in}}^0\left[\delta(t) - \sqrt{\frac{b}{t}}J_1\left(2\sqrt{bt}\right)e^{-i\omega_0 t}e^{-\gamma t}\theta(t)\right]\,, \tag{10.8}$$

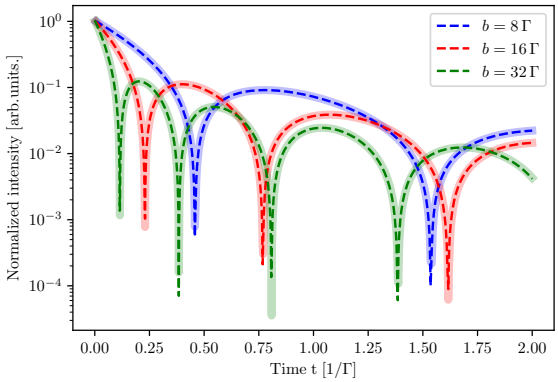

Figure 10.2: Intensity as a function of time for different thickness parameters b indicated by the different colors in the low-excitation regime ($\mathcal{A} = 0.01\pi$). Compared are the results of the analytical response function (solid lines) and the cumulant expansion (dashed lines). The length of the chain is chosen to be $N = 100$ nuclei. The curves are normalized such that the area under the curve equals 1.

where E_{in}^0 is the electric field amplitude. Therefore, in the low-excitation regime we can benchmark the results of the many-body simulation with the analytical formula. Note that here we consider the single-line case without hyperfine splitting for simplicity.

In Fig. 10.1, the scattered intensity is shown as a function of time for the analytical formula in Eq. (10.8) (gray solid line) and the many-body simulation (colored dashed lines). For the many-body simulations an initial excitation of $\mathcal{A} = 0.01\pi$ is used. We can clearly see the dips in the intensity at the roots of the Bessel function $J_1\left(2\sqrt{bt}\right)$ in all lines. For the numerical results we note that for very short chains, e.g., $N = 10$ (blue line), those dips are slightly shifted. This is because the chain is too short to appropriately represent the propagation dynamics since for $k_0 a_0 \approx 21$ from the central atoms to the edge not even a full oscillation period of the oscillating part of the couplings in Eq. (10.2) is covered. Note that $\Gamma_{1\text{D}}$ allows us to use a smaller amount of nuclei for the simulation than actually are in a chain of corresponding length. For increasing chain length, the results match the analytical result. We conclude that for the low-excitation regime we should use at least $N = 100$ nuclei. A similar shift of the minima for chains which are to short to simulate the dynamics properly is also visible in [Kon+25], but the origin is not discussed.

A comparison of the scattered intensity as a function of time between the analytical formula in Eq. (10.8) (solid lines) and the simulation results (dashed lines) for different thickness parameters b is given in Fig. 10.2. For the results with different b represented by the different colors, the minima occur at different times as expected because they are caused by the roots of the Bessel function $J_1\left(2\sqrt{bt}\right)$, whose positions depend on b. For all different thickness parameters b there is excellent agreement between the analytical and the numerical result. This demonstrates, that the cumulant expansion can accurately capture the system dynamics arising from the couplings which represent the propagation effects in the low-excitation regime.

10.4 Beyond the low-excitation regime

After we have confirmed, that the system dynamics is accurately represented in the low-excitation regime by comparing it to the analytical response function, we can now investigate the full excitation regime, for which no analytical solution exists, with the numerical simulation.

As for the low-excitation regime, we start our investigations by analyzing the convergence of the results with the number of nuclei N. To this end, Fig. 10.3 displays the intensity as a function of time for different numbers of nuclei N and two different initial excitations $\mathcal{A} = 0.5\pi$ and $\mathcal{A} = 0.9\pi$ in the two panels. For medium excitation ($\mathcal{A} = 0.5\pi$, left panel), we see that already for $N = 50$ nuclei, the results are converged like for the low-excitation case in Fig. 10.1. For the high excitation at $N = 50$ nuclei, there are still deviations especially in the position of the first minimum and in high intensity regions. Only for $N = 500$ are the results converged. Furthermore, the position of the minima for the two different initial excitations $\mathcal{A}$ in the two panels differ from each other, which is a first hint of a non-linear signature depending on the initial excitation $\mathcal{A}$.

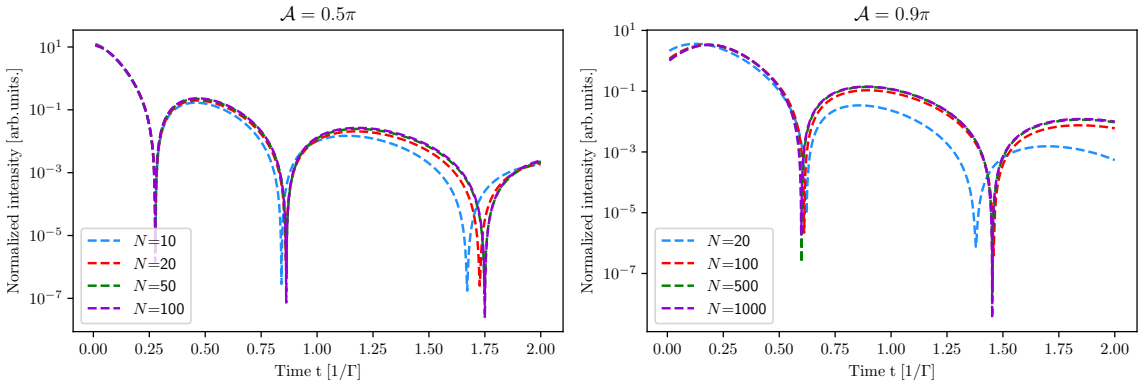

Figure 10.3: Intensity as a function of time calculated with the cumulant expansion for two different initial excitations $\mathcal{A}$. The different colors represent calculations with different chain length N. The curves are normalized such that the area under the curve equals 1 and the thickness parameter is chosen to be $b = 16\,\Gamma$.

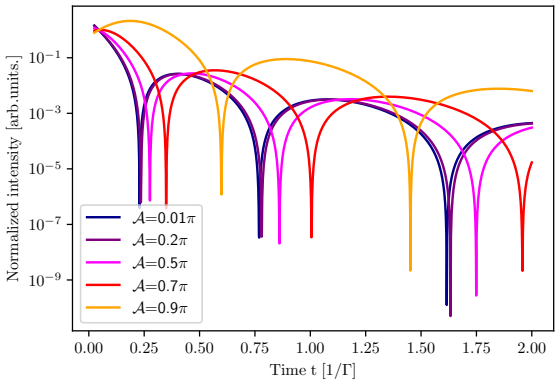

Figure 10.4: Intensity as a function of time for different initial excitations $\mathcal{A}$ represented by the different colors. For the simulation $N = 1000$ nuclei and a thickness parameter of $b = 16\,\Gamma$ is used. The curves are normalized such that the area under the curve equals 1.

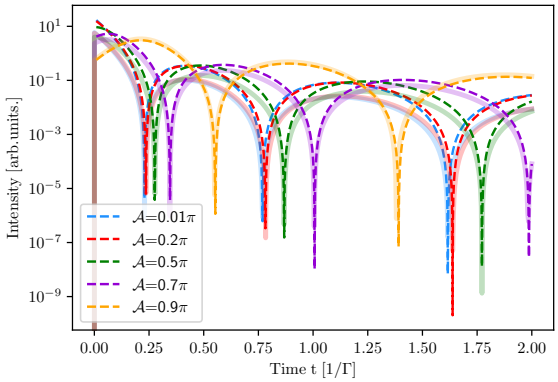

Figure 10.5: Intensity as a function of time calculated with the cumulant expansion (dashed lines) and the Burnham-Chiao ringing in Eq. (2.43) (solid lines). The different colors represent different initial excitations $\mathcal{A}$. For the cumulant model we set the decay constant in the incoherent coupling in Eq. (10.1) $\Gamma = 0$ to match the Burnham-Chiao ringing conditions. For the time scale we keep the standard Γ. The number of nuclei is set to $N = 2000$ and the thickness parameter is chosen to be $b = 16\,\Gamma$.

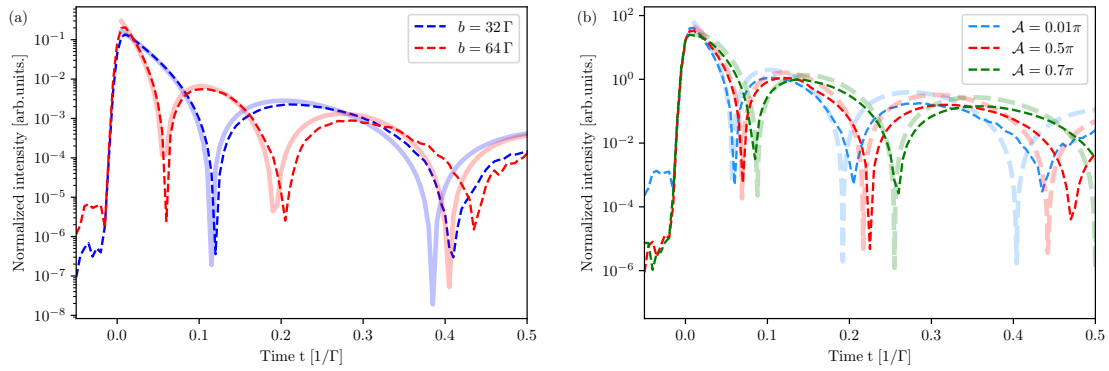

Figure 10.6: (a) Intensity as a function of time for different thickness parameters b in the low-excitation regime. Compared are the results from the CDTWA (dashed lines) and the analytical formula in Eq. (10.8) (solid lines). (b) Intensity as a function of time for different initial excitation $\mathcal{A}$ with a fixed thickness parameter $b = 64$. Compared are the results from the CDTWA (dashed lines) and the cumulant expansion (dashed lines). For the simulations $N = 100$ nuclei are used. The curves are normalized such that the area under the curve equals 1.

To study this effect in more detail, in Fig. 10.4 for a fixed number of nuclei $N = 1000$ and thickness parameter $b = 16$ the intensity is displayed as a function of time for different initial excitations $\mathcal{A}$. We see that the position of the minima shifts to later times for increasing initial excitations $\mathcal{A}$. For an initial excitation of $\mathcal{A} = 0.2\pi$, there are only tiny differences as compared to the result in the low-excitation regime ($\mathcal{A} = 0.01$). For an initial excitation of $\mathcal{A} = 0.5\pi$ the shifts of the minima are clearly visible and the amount by which the minima shift increases non-linearly with increasing initial excitation $\mathcal{A}$. A detailed study of this shifts can be found in [Adi24; AGE_p]. Further, those shifts are visible in [Kon+25], but not analyzed in detail.

To understand the shift of the dynamical beats, we can compare the result from the cumulant expansion to the results from the simple Burnham-Chiao ringing model presented in Section 2.3.2. This simple model describes the outgoing electric field by (see Eq. (2.44))

$$E(t) \propto \frac{\mathrm{d}}{\mathrm{d}t}\theta(t) = \frac{1}{\sqrt{2}}\sqrt{\frac{b}{t}}\frac{\mathrm{d}}{\mathrm{d}q}\theta(q)\,, \tag{10.9}$$

with $q = 2\sqrt{QtL}$, where $Q = b/L$ with the length of the sample L and $\frac{\mathrm{d}}{\mathrm{d}q}\theta(q)$ being governed by the following differential equation (see Eq. (2.43)):

$$\frac{\mathrm{d}^2}{\mathrm{d}q^2}\theta(q) + \frac{1}{q}\frac{\mathrm{d}}{\mathrm{d}q}\theta(q) + \sin\left(\theta(q)\right) = 0\,, \tag{10.10}$$

which is a modified Bessel differential equation with $\sin(\theta(q))$ instead of $\theta(q)$ and can be solved numerically. One crucial approximation in the derivation of this Burnham-Chiao ringing was that there is no decay during the time evolution. Therefore, to compare the results from our full simulation to Burnham-Chiao ringing, we set the decay constant to zero ($\Gamma = 0$).

In Fig. 10.5, the intensity as a function of time is calculated with the cumulant expansion (dashed lines) and the Burnham-Chiao model (solid lines) for different initial excitations $\mathcal{A}$. For all initial excitations $\mathcal{A}$ indicated by the different colors, there is excellent agreement. This indicates, that indeed the shift of the minima originates from the governing differential equation not being a Bessel differential equation for higher excitations. For higher excitations $\sin(\theta(q))$ cannot be approximated with $\theta(q)$ anymore and introduces non-linear effects.

The intuitive physical interpretation is that for higher excitation, there is more population in the excited state, such that the absorption cross section shrinks and the sample is effectively thinner [Kon+25]. This leads to the minima shifting to later times as we see in Fig. 10.2. Note however, that this is only an approximate description as the the intensity as a function of time for higher excitations cannot be represented by a Bessel function of first kind as in the low-excitation regime.

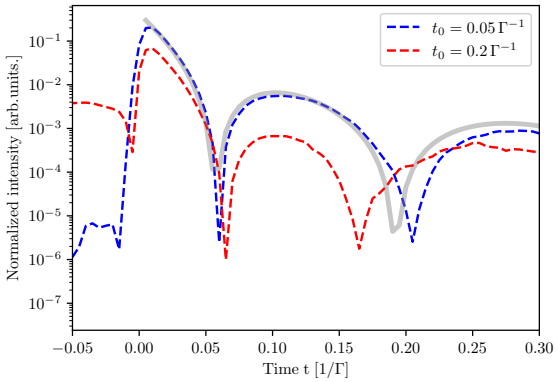

Figure 10.7: Intensity as a function of time for two different arrival times of the excitation pulse t_0. For comparison in gray, the analytical response function is displayed. For the simulation $N = 100$ nuclei and a thickness parameter of $b = 64\,\Gamma$ is used. The curves are normalized such that the area under the curve equals 1.

10.5 Validation of effect with CDTWA

Finally, as we have done in the previous chapter, we want to validate the cumulant expansion results by simulating the system with a different method, namely the CDTWA.

First, we validate the CDTWA results in the low-excitation regime by comparing them to the analytical formula (Eq. (10.8)). Fig. 10.6(a) shows the intensity as a function of time in the low-excitation regime for different thickness parameters b represented by different colors. The dashed lines show the simulation results from the CDTWA, the solid lines the result of the analytical expression for comparison. We find that also for the CDTWA the dynamical beat minima are visible. The minima positions as well as the overall curves are in good agreement with the analytical result for early times ($t < 0.4\,\Gamma^{-1}$). For later times, the agreement is worse and especially the minima are shifted. This might be due to the known unphysical effects, which can appear for a system without continuous driving (see Section 7.5.5). The unphysical driving would lead to higher populations similar to a higher initial excitation (c.f. Fig. 8.4) and the deviation increases with increasing time.

We can test for this by running the simulation for two different arrival times of the excitation pulse t_0. In Fig. 10.7, the intensity as a function of time is shown for $t_0 = 0.05\,\Gamma^{-1}$ as before (blue) and a later pulse at $t_0 = 0.2\,\Gamma^{-1}$ (red) with respect to the start of the simulation. If the deviation from the response function (gray) is physical, the deviation should not depend on t_0 after correcting the time axis for the different arrival times. However, we see that for $t_0 = 0.05\,\Gamma^{-1}$ there is reasonable agreement up to $t \approx 0.2\,\Gamma^{-1}$, while for $t_0 = 0.2\,\Gamma^{-1}$ the agreement only reached until $t \approx 0.06\,\Gamma^{-1}$. Note that the curves are normalized, such that the area under the curve equals 1, which leads to different relative heights. This indicates that the deviation indeed arises from the unphysical effects, which only depend on the start time of the simulation. Furthermore, the background level at time $t < 0$ before the excitation pulse arrival is significantly higher for the later pulse.

In the next step, we compare the results from CDTWA and cumulant expansion for different initial excitations $\mathcal{A}$. From the comparison with the analytical formula we already know that the results from CDTWA might be incorrect for later times $t > 0.4\Gamma^{-1}$. For earlier times from Fig. 10.6(b) we can see that the CDTWA results (dashed) lines agree reasonably well with the cumulant expansion results (solid lines). Especially the shift of the minima depending on the initial excitation $\mathcal{A}$ can be confirmed qualitatively but also quantitatively.

10.6 Summary and Outlook

At first, we benchmarked the cumulant expansion results with the analytical formula in the low-excitation regime. After confirming that the cumulant expansion captures the dynamics correctly, especially the dynamical beat minima, we increased the initial excitation beyond the low-excitation regime. In this analysis we noted that the position of the minima depends on the initial excitation $\mathcal{A}$, which provides a clear signature of non-liner effects beyond the low-excitation regime. Similar shifts have already been reported in other work [Adi24; AGE_p; Kon+25], however with different

simulation methods. We were able to identify the origin as non-linear effects in the simplified model of the Burnham-Chiao ringing [BC69]. Afterwards, we compared the cumulant expansion results to those obtained with the CDTWA. The results of the CDTWA are strongly influenced by the unphysical driving (see Section 7.5.5), but nonetheless we could validate the shift of the dynamical beat minima depending on the degree of excitation $\mathcal{A}$.

The shift of the dynamical beat minima provides a clear signature of appearing nonlinearities beyond the low-excitation regime. Those shifts could be used to demonstrate higher excitations with a simple experimental setting. In the distant future, an experimental demonstration of the dynamical beat shift depending on the initial excitation is expected to be realizable with an XFELO. Furthermore, the shifts could serve as diagnostics for the degree of excitation, especially if combined with a single-shot analysis [Ger+25b].

So far we have discussed the propagation effects based on the free-space dipole-dipole couplings. For the future, it would be interesting to study propagation effects beyond the linear regime in structured environments, e.g., in waveguides [Loh+25a], with the same formalism. Besides, it would be interesting to extend the formalism and include transverse couplings. As the effective couplings to model the propagation effects are the projection of the dipole-dipole couplings onto the forward mode, another interesting aspect to study in the future is whether there is a connection of the excitation-dependent phase evolution discussed in Chapter 9 and the excitation-dependent shift of the dynamical beats studied here.

Part III

Experiments performed at a synchrotron

Chapter 11

Dark-fringe interferometer with dynamic phase control for Mössbauer science

This chapter is based on the following preprint:

Dark-fringe interferometer with dynamic phase control for Mössbauer science
M. Gerharz, , D. Lentrodt, L. Bocklage, K. Schulze, C. Ott, R. Steinbrügge, O. Leupold, I. Sergeev, G. Paulus, C. H. Keitel, R. Röhlsberger, T. Pfeifer, and J. Evers
arXiv:2509.24658 [quanth-ph]

Content has been reproduced verbatim, but the article was restructured to suit the format of this thesis. While the foundations and measurement results were already discussed in [Ger21], within the scope of this thesis the interferometer was studied in detail, which is presented in this chapter, and the manuscript was prepared.

11.1 Motivation

The phenomenon of interference is ubiquitous in physics. For instance, the paradigmatic example of double-slit interference allows one to explore key concepts of quantum mechanics [FLS63]. In general, interferometers are among the most versatile and precise measurement devices. However, interferometric control and measurements become more challenging at energies of hard x-rays, due to the small x-ray wavelength. Nevertheless, interference effects also play an important role in nuclear resonance scattering, which typically operates at photon energies of order 10 keV. Already the interference between scattering involving different hyperfine transitions gives rise to the characteristic quantum beats [Röh04]. The situation becomes richer if more than one nuclear target is considered, since then also interferences between pathways involving interactions with several targets become relevant (see, e.g., [Bür+99; Hee+17; Hee+21; Pot+01]). These interferences open up a number of important applications, such as controlling the scattered γ-rays and the nuclear dynamics [Boc+21; Bür+99; Hee+13; Hee+15a; Hee+17; Hee+21; Hel+91; KKR99; Kuz+24; Lin+22; LP17; LPK12; PKE09; Pot+01; Sch+02; Shv+96; SS89; Vag+14; Vel+24; Zha+19] or in precise measurements [Boc+21; Cal+05; Goe+19; Hee+21; Loh+25b; SLT04; Stu01; Yua+25]. One example is the manipulation of the intensity of the transmitted light, e.g., motivated by the desire to remove the huge off-resonant unscattered background from the detection signal at accelerator-based x-ray sources [Che+83; Ger+85; Hee+13; Muk+15; Pot+12; Röh+00; Röh+92; SBH93; Smi+84; Smi00; SS89; Toe+11; Toe+95]. From a broader perspective, the Mössbauer interference schemes are also at the heart of the development of x-ray and nuclear quantum optics [Ada+13; Ada+19; Ada03; KK17; RES14; WK21].

The favorable properties and applications call for a further development of Mössbauer interferometry. However, traditional x-ray interferometers based on crystal optics are challenging to implement, since they require an alignment and stability of the setup on the Angstrom level [BH65; Bow96; Shv+03]. In contrast, in the multi-target Mössbauer settings the interfering pathways are not spatially separated. This has the advantage that the measurements are only susceptible to relative phase changes between the targets over the duration between the excitation and the subsequent scattering. For the archetype ^{57}Fe with a lifetime of 141 ns, this measurement cycle is fast enough to outpace many sources of mechanical noise. As a result, stabilities well below the wavelength scale have been demonstrated [Hee+21]. However, in a conventional interferometer the probed sample is placed in one of the interfering pathways, while a variable phase shift is applied to the other pathway. Neither the selective coupling to one of the paths, nor the phase variation is straightforwardly possible in the in-line configuration. Furthermore, the radiative coupling between multiple Mössbauer targets [Bür+99; Pot+01] involving x-ray scattering on more than one target spoils the analogy to traditional interfer-

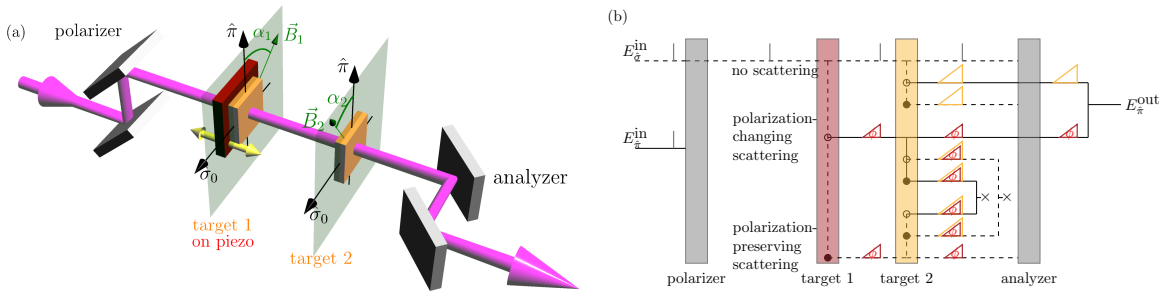

Figure 11.1: (a) Schematic setup. X-rays linearly polarized in $\hat{\sigma}$-direction enter the setup. With a polarimetry setup, the two perpendicular polarization states $E_{\hat{\sigma}}$ and $E_{\hat{\pi}}$ can be selected. Inside the polarimeter, two resonant targets are placed with their magnetization set to $\alpha_1 = \pi/4$ and $\alpha_2 = -\pi/4$, which forms the dark fringe setting, in which no light can pass the setup. The first target is mechanically moved via a piezoelectric transducer and thereby imprints a time-dependent phase onto the x-rays. This allows to dynamically control the interferometer and enables a dynamical temporal gating of the outgoing x-ray intensity. (b) Schematic representation of the different interfering paths. First, the polarizer blocks the $\hat{\pi}$-component (solid line) and lets only pass the $\hat{\sigma}$-component (dashed line) of the initial short x-ray pulse (gray vertical line) of the incoming electric field. In the first target, the light can either pass the target without scattering (top path) or is scattered into the perpendicular component (empty circle) or into the same polarization component (filled circle). Both scattering components are indicated by dark red triangles since their duration is of order of the nuclear lifetime and therefore orders of magnitude longer than the initial x-ray pulse. They have a dynamically-controllable phase ϕ relative to the initial x-ray pulse. Subsequently, similar scattering happens in the second target (orange triangle). The two double-scattering paths interfere destructively for both polarization components (crossed arrow). Finally, the analyzer blocks the $\hat{\sigma}$ components, such that the outgoing electric field behind the interferometer is given by the sum of two single-scattering paths, whose relative phase can be controlled.

ometry setups, and impedes the direct phase measurements and control [Cal+05; Goe+19; Hee+21; Smi+06].

Here, we theoretically introduce and experimentally demonstrate a dynamically-controllable x-ray interferometer for Mössbauer science which overcomes these challenges. We engineer the interference in such a way that only two co-propagating pathways contribute to the detection signal. In this setting, the radiative couplings cancel, the two pathways can individually be addressed via their different polarizations, and the transmitted intensity in the empty interferometer ideally vanishes. Thereby we combine the stability of an x-ray inline interferometer with the easy selective access to the individual interfering pathways for spatially separated pathways. Despite not being used in Mössbauer interferometers so far, due to its high sensitivity, the "dark-fringe" mode is well-established in other fields, e.g., in astrophysics [Hin+98] or gravitational-wave detection [Bon+16].

11.2 Experimental setup

The schematic setup is shown in Fig. 11.1(a). The incoming x-rays are polarized in the horizontal plane. The analyzer is aligned in crossed setting, such that the empty polarimeter ideally does not transmit any x-rays [Mar+11; Mar+21]. Each of the two targets is operated in such a way that its response also comprises scattering into the vertical polarization direction, and vice versa. Therefore, including only one of the targets into the polarimeter leads to a transmission through the analyzer. In the following, we show that a second target can be added in such a way that the transmission through the analyzer ideally vanishes again. The reason for this is that the respective contributions of the two targets to the transmission through the analyzer interfere destructively. As a result, the setting can be interpreted as an interferometer. This interpretation is further supported by the observation that in our setting, the final signal behind the analyzer only comprises the interference between the linear scattering of the first target with the linear scattering of the second target, without contribution from the radiative coupling of both targets (see Fig. 11.1(b)). Since the transmitted intensity vanishes in the idle state, the interferometer operates in the dark-fringe mode. By additionally mounting the first target on a piezo-electric transducer such that it can be mechanically displaced, the relative phase between the interfering pathways can be dynamically controlled, and thus the transmitted intensity.

11.3 Theoretical description of the interferometer

11.3.1 Polarization-dependent response of a moving target

We start with the analysis for a single target, assuming an idealized motion, which will allow us to obtain analytical expressions. For definitiveness, we consider the standard isotope ^{57}Fe with resonance frequency ω_0 and a magnetic dipole (M1) Mössbauer transition from the ground state. Following the standard approach to polarization-dependent nuclear forward scattering [Röh04; SBH99], we can relate the linear $\hat{\pi}$- and the $\hat{\sigma}$-polarized components of the outgoing electric field (E) to the incident electric field (E^{in}) by

$$\begin{pmatrix} E_{\hat{\sigma}}(\omega) \\ E_{\hat{\pi}}(\omega) \end{pmatrix} = \mathcal{E}\,\mathcal{R}(\omega,\alpha) \begin{pmatrix} E^{\mathrm{in}}_{\hat{\sigma}} \\ E^{\mathrm{in}}_{\hat{\pi}} \end{pmatrix}, \tag{11.1}$$

$$\mathcal{R}(\omega,\alpha) = g_\alpha \begin{pmatrix} R_{\mathrm{L}}(\omega) & 0 \\ 0 & R_{\mathrm{C}}(\omega) \end{pmatrix} g_\alpha^{-1}, \tag{11.2}$$

where $\mathcal{E} = \exp(ikz - \mu_e\, d/2)$ and μ_e is the electronic contribution characterizing the absorption and phase shift due to off-resonant electronic processes. g_α is a two-dimensional rotation matrix,

$$g_\alpha = \begin{pmatrix} \cos\alpha & \sin\alpha \\ -\sin\alpha & \cos\alpha \end{pmatrix}, \tag{11.3}$$

capturing the effect of the magnetic field being rotated by α from the $\hat{\pi}$ axis. For ^{57}Fe, the two response functions for transitions with linear and circular dipole moments are given by

$$R_{\mathrm{L}}(\omega) = e^{\mathcal{L}_2(\omega)+\mathcal{L}_5(\omega)}, \tag{11.4a}$$

$$R_{\mathrm{C}}(\omega) = e^{\frac{3}{4}\mathcal{L}_1(\omega)+\frac{1}{4}\mathcal{L}_3(\omega)+\frac{1}{4}\mathcal{L}_4(\omega)+\frac{3}{4}\mathcal{L}_6(\omega)}. \tag{11.4b}$$

Here, the Lorentzians $\mathcal{L}_i(\omega) = i\Gamma_c/(\omega - \omega_i - \frac{i}{2}\gamma)$ correspond to the six Zeeman transitions in magnetically-split ^{57}Fe, weighted by their respective Clebsch-Gordan coefficients, with transition frequencies ω_i, natural decay rate γ and enhanced decay rate Γ_c [SBH99].

For simplicity, we consider instantaneous phase jumps due to step-like target displacements Δz immediately after the excitation. This approximation is valid as typical rise times of the motion are of order of $1-10$ ns, which can be considered sufficiently short as compared to the nuclear lifetime of 141 ns. For temporally short incident x-ray pulses $E^{\mathrm{in}} \propto \delta(t)$, the effect of these step-like motions is characterized by the replacement [Hel+91]

$$R_{\mathrm{L/C}}(\omega) \to R_{\mathrm{L/C}}(\omega,\phi) = 1 + [R_{\mathrm{L/C}}(\omega) - 1]\, e^{i\phi}, \tag{11.5}$$

where $R_{\mathrm{L/C}}(\omega,\phi)$ denotes the response with phase jump $\phi = 2\pi\Delta z/\lambda$. The first "1" in Eq. (11.5) describes unscattered light which does not interact with the target and therefore is unaffected by the motion, whereas the resonantly scattered part proportional to $(R_{\mathrm{L/C}} - 1)$ is phase-shifted. Note that as the six hyperfine-splitted lines are well-separated, specifying the transition to linearly polarized ω_{C} or linearly polarized ω_{L}, we can approximate $R_{\mathrm{L/C}}(\omega_{\mathrm{C/L}}) \approx 1$.

11.3.2 Dynamical interference control

In order to derive the transmitted intensity behind the analyzer, we consider the archetype isotope ^{57}Fe with resonance frequency ω_0 and a magnetic dipole (M1) Mössbauer transition from the ground state. This transition has a hyperfine splitting with six lines of which two are linearly polarized along the magnetization and four are circularly polarized in the plane perpendicular to the magnetization. Each of the two identical targets has its magnetization aligned in the plane perpendicular to the x-ray propagation direction, at an angle α_i $(i = 1, 2)$ relative to the $\hat{\pi}$ direction.

From Eq. (11.1), for magnetization directions $\pm\pi/4$ the outgoing field comprises contributions in both polarization directions, even if the incident field only comprises one of the two polarization components. This is due to polarization-changing scattering contributions [SBH99]. In contrast, we combine two targets in such a way that this is not the case. After the analyzer, only the $\hat{\sigma}$ component

of the short incoming x-ray pulse impinges on target 1. The electric field after the first target then becomes

$$E^{(1)}(\omega_{\mathrm{L/C}}) = \mathcal{R}^{(1)}\left(\omega_{\mathrm{L/C}}, \phi, \alpha_1 = \frac{\pi}{4}\right)\begin{pmatrix} E^{\mathrm{in}}_{\hat{\sigma}} \\ 0 \end{pmatrix} \tag{11.6}$$

$$= \frac{\mathcal{E}}{2} E^{\mathrm{in}}_{\hat{\sigma}} \begin{pmatrix} 2 + T^{(1)}_{\mathrm{L/C}} e^{i\phi} \\ \mp T^{(1)}_{\mathrm{L/C}} e^{i\phi} \end{pmatrix}, \tag{11.7}$$

where we left out the argument $\omega_{\mathrm{L/C}}$ of the transmission functions for brevity. The signs $\mp$ are for the two different polarization contributions L/C. From the equation, we can read off the three paths after the first sample as they are illustrated in Fig. 11.1(b): the prompt unscattered contribution ("1") and the scattering components into the parallel and perpendicular polarization components ("$T^{(1)}_{\mathrm{L/C}} e^{i\phi}/2$").

Analogously, after the second target we find

$$E^{\mathrm{comb}}(\omega_{\mathrm{L/C}}) = \mathcal{E}\,\mathcal{R}^{(2)}\left(\omega_{\mathrm{L/C}}, -\frac{\pi}{4}\right)\mathcal{R}^{(1)}\left(\omega_{\mathrm{L/C}}, \phi, +\frac{\pi}{4}\right)\begin{pmatrix} E^{\mathrm{in}}_{\hat{\sigma}} \\ 0 \end{pmatrix}$$

$$= \frac{\mathcal{E}}{4} E^{\mathrm{in}}_{\hat{\sigma}} \begin{pmatrix} S^{(0)} + S^{(1)} + S^{(2)} \\ P^{(1)} + P^{(2)} \end{pmatrix}. \tag{11.8}$$

The different scattering contributions are given by

$$S^{(0)} = 4\,, \tag{11.9a}$$

$$S^{(1)} = 2\left(T^{(1)}_{\mathrm{L/C}} e^{i\phi} + T^{(2)}_{\mathrm{L/C}}\right), \tag{11.9b}$$

$$S^{(2)} = T^{(2)}_{\mathrm{L/C}} T^{(1)}_{\mathrm{L/C}} e^{i\phi} - T^{(2)}_{\mathrm{L/C}} T^{(1)}_{\mathrm{L/C}} e^{i\phi} = 0\,, \tag{11.9c}$$

$$P^{(1)} = \pm\, 2\left(T^{(2)}_{\mathrm{L/C}} - T^{(1)}_{\mathrm{L/C}} e^{i\phi}\right), \tag{11.9d}$$

$$P^{(2)} = \pm\, T^{(2)}_{\mathrm{L/C}} T^{(1)}_{\mathrm{L/C}} e^{i\phi} \mp T^{(2)}_{\mathrm{L/C}} T^{(1)}_{\mathrm{L/C}} e^{i\phi} = 0\,, \tag{11.9e}$$

and each of these nine terms corresponds to one of the interfering pathways shown in Fig. 11.1(b). Here, S/P indicates contributions to the $\hat{\sigma}$ and $\hat{\pi}$ polarization, respectively, and the superscript labels the number of targets that this pathway interacts with. Note that in both polarization components, for this particular set of chosen angles $\alpha_{1/2}$, the scattering paths involving two targets cancel each other, $S^{(2)} = 0 = P^{(2)}$. The analyzer blocks the $\hat{\sigma}$-component such that the outgoing signal behind the interferometer becomes

$$E^{\mathrm{out}}(\omega_{\mathrm{L/C}}) = \pm\frac{\mathcal{E}}{2} E^{\mathrm{in}}_{\hat{\sigma}}\left(T^{(2)}_{\mathrm{L/C}} - T^{(1)}_{\mathrm{L/C}} e^{i\phi}\right). \tag{11.10}$$

Assuming identical samples $T^{(1)}_{\mathrm{L/C}} = T^{(2)}_{\mathrm{L/C}} = T_{\mathrm{L/C}}$, the outgoing field reduces to

$$E^{\mathrm{out}}(\omega_{\mathrm{L/C}}) = \pm\frac{\mathcal{E}}{2} E^{\mathrm{in}}_{\hat{\sigma}}(1 - e^{i\phi}) T_{\mathrm{L/C}}(\omega_{\mathrm{L/C}})\,. \tag{11.11}$$

Without motion ($\phi = 0$), this outgoing field indeed vanishes in the ideal case due to destructive interference between the respective single-scattering paths, thus forming the dark-fringe setting. As a result, the interference and thus the outgoing intensity

$$\frac{I_{\perp}(\omega_{\mathrm{L/C}})}{I_{\mathrm{in}}} = |\mathcal{E}|^2 \sin^2\left(\frac{\phi}{2}\right) \left|T_{\mathrm{L/C}}(\omega)\right|^2. \tag{11.12}$$

can be dynamically controlled, e.g., by mechanical motion inducing a relative phase ϕ.

11.4 Applications of the interferometer

Although the applications were studied outside the scope of this thesis in [Ger21], we want to name them for completeness. Details can be found in [Ger+25a; Ger21]. We have seen that the interference and thus the transmitted intensity of the interferometer can be tuned by mechanical motion. We employ piezo transducers to displace one of the targets and control the output intensity on the nanosecond time scale. In the experiment, we use an event-based detection system to measure the effect of individual sudden target displacements on the interferometer transmission up to about 7.5 μs, i.e., about 50 lifetimes of the bare nuclei. This opens up two classes of applications.

On the one hand, relative displacements of the targets can precisely be measured on x-ray wavelength- and nanosecond-time scales via the transmitted intensity. This was used to measure residual relative motion between the two samples. Furthermore, the long measurement times of up to 7.5 μs allowed us to see revivals of shock waves after approximately 3 μs, that were introduced by the sudden piezo motion.

On the other hand, a deterministic displacement of the targets allows one to control the intensity of the transmitted light as a function of time. This allows for gating on nanosecond times scales and the creation of single pulses.

These two applications experimentally demonstrate the sensitivity in the dark-fringe mode in the first application, and the dynamical control of the interferometer in the second one.

11.5 Summary and outlook

In summary, we introduced and demonstrated an inline x-ray interferometer for Mössbauer science operated in the dark-fringe mode. The resulting minimum of the transmitted intensity forms an ideal starting point for a variety of applications. Mounting one of the two targets on a piezo-transducer further allows one to dynamically control the relative phase of the interfering pathways, and thus the interferometer transmission.

The dark-fringe operation is gained by operating two targets containing Mössbauer nuclei in a particular geometry, such that their individual scattering responses partially interfere. Importantly, all scattering channels involving interactions with both targets cancel each other, in stark contrast to many previous experiments involving multiple Mössbauer targets. Because of this feature, the final signal behind the analyser only comprises two interfering contributions, which are formed by individual scattering from each of the two targets. One of the two contributions then acquires an additional relative phase shift by the mechanical displacement of the corresponding sample. This particular feature allows us to directly relate the setting to a conventional interferometer with two interfering pathways.

For the future, we envision a more refined control of the mechanical displacement to generate versatile tuneable multi-peak pulses. This would allow, e.g., for the coherent control of Mössbauer nuclei [Hee+21]. If combined with seeded XFEL radiation comprising many resonant photons per shot, Ramsey-like control operations or even multi-dimensional spectroscopy could become within reach. Such control could be achieved along the lines of adaptive optics, using feedback control to determine the piezo motion which achieves the desired time-dependent x-ray pulses. On the measurement side, the polarization-dependent nature of the pathways in the dark-fringe interferometer could be harnessed to study polarization-dependent effects, such as circular dichroism, in a space- and time-resolved way. Furthermore, our approach to explore relative target motion with nanosecond time-resolution and x-ray-wavelength spatial-resolution over extended measurement times of more than 10 μs appears particularly suitable for the study of impulsively induced mechanical motion, e.g., initiated by laser pulses or x-ray scattering.

Chapter 12

Summary and outlook

In this chapter, the thesis results are summarized and an outlook is given. In particular, we focus on the broader picture of nuclear quantum optics at XFELs. More detailed conclusions are given at the end of each chapter in the main part of the thesis.

12.1 Brief summary

At the start of this thesis, Mössbauer experiments were almost exclusively performed at synchrotrons, and only a single experiment at an XFEL had been reported [Chu+18]. Over the course of this thesis, in total five experiments were carried out by the ^{57}Fe EuXFEL collaboration and the ^{45}Sc EuXFEL collaboration at the European XFEL. These experiments were not only among the first Mössbauer experiments at any XFEL, but also the first at the European XFEL and the first to employ hard x-ray self-seeding.

The first part of this thesis documents the thesis author's contributions to these first-of-their-kind experiments. Because of the novelty of the experiments, we had to develop a data-analysis pipeline, which was used in all experiments and which is expected to serve as the basis for future work. The data analysis consists of two parts: real-time analysis during data-collection and analysis of recorded data afterwards. The custom real-time routines were essential to align all experimental components and provide rapid access to key observables such as the time spectrum, which is crucial for successful operation. Unlike at synchrotrons, where standardized procedures exist, Mössbauer experiments at the European XFEL required entirely new approaches, particularly for processing resonantly scattered photons, which form the foundation of the subsequent experiment-specific analyses. We then discussed the main data analysis of the resonant x-ray excitation of the ^{45}Sc nuclear clock transition [Shv+23]. This included the processing of raw data and the extraction of the resonance curve, which was especially challenging due to the limited statistics of only 93 recorded signal photons. In addition, we designed and demonstrated a single-shot sorting method of Mössbauer time-domain data in ^{57}Fe experiments, which allows us to exploit the full dataset rather than restricting the analysis to high-photon shots [Ger+25b]. Further experiments with ^{57}Fe revealed striking and previously unreported anomalies in nuclear resonant scattering. Although the data can be fitted with standard theory, the inferred sample thicknesses disagreed with the physical values. Moreover, both the count rates and time spectra unexpectedly depended on the distribution of aluminum upstream of the sample, even though the total amount of aluminum in the beam remained constant. This behavior is entirely unexpected in the low-excitation regime.

Besides the experiments, the second part of this thesis focused on theory and simulations for future studies. We investigated the de-excitation dynamics of interacting nuclear ensembles, which forms a complicated many-body problem, including finite-size effects that may already be observable at XFELs, as well as non-linear phenomena predicted to emerge beyond the low-excitation limit, which is anticipated to be reached with an XFELO [LKE25b]. For this purpose, we established a versatile simulation toolbox combining the cumulant expansion [Kub62], the continuous-discrete truncated Wigner approximation (CDTWA) [MF23], and QuTiP [JNN12; JNN13]. We further closely investigated and extended the preparation of initial states, especially partially excited states, for the CDTWA. Using this framework, we predicted clear non-linear signatures in two settings: excitation-dependent phase evolution in one-dimensional nuclear chains [GE25], and excitation-dependent shifts of dynamical beats in nuclear forward scattering. The results of the latter one are similar to those obtained in [Adi24; AGE_p; Kon+25], but obtained with a different method. In both settings, clear signatures of non-linear behavior beyond the low-excitation approximation are visible.

Outside the XFEL context, we investigated an optimized two-foil configuration acting as an inline interferometer operated in dark-fringe mode, where the two linear polarization components serve as the interferometer arms [Ger+25a]. The optimized configuration combines the stability of an inline interferometer with the accessibility of an interferometer with separated paths.

In summary, this thesis advances the field of nuclear quantum dynamics in both experiment and theory, enabled or inspired by XFELs. Several important contributions for the first Mössbauer experiments at the European XFEL were made, thereby establishing the field at a seeded XFEL for the first time. In parallel, methods to tackle many-body and non-linear nuclear dynamics were developed, laying the groundwork for phenomena expected to emerge at present and future facilities, and first applications discussed.

12.2 Detailed summary

In Chapter 1, we motivated how the unique capabilities of XFELs can expand the scope of Mössbauer science. When this work began, Mössbauer experiments were almost exclusively performed at synchrotrons, with only a single XFEL experiment reported [Chu+18]. Over the course of the thesis, however, five experiments were carried out within our collaborations at the European XFEL. Those experiments were not only among the first Mössbauer studies at any XFEL, but also the first at the European XFEL and with hard x-ray self-seeding. The first part of this thesis presents the thesis author's contributions to these experiments. The second part is devoted to theoretical and numerical studies of nuclear ensembles, while the third part describes an additional experiment at a synchrotron.

The first part begins with the development of a dedicated analysis framework for Mössbauer experiments at the European XFEL, described in Chapter 3. Because of the novelty of these experiments, no standardized routines existed, so we designed a modular data-analysis pipeline that was essential for the success of the experiments and is expected to serve as a foundation for future work. The pipeline comprises two parts: real-time analysis during the measurements and analysis of the recorded data. The real-time routines enabled motor scans for alignment of experimental components and provided live access to key observables, such as time spectra, which is crucial for the success of the experiment. For the recorded data, we implemented standard analysis routines, such as photon arrival time extraction, which serve as the basis for subsequent experiment-specific analyses. The modular structure of the software ensures that individual steps can be refined and reused for future Mössbauer experiments at the European XFEL, but can also be adapted for data analysis at other XFELs.

Building on this framework, the first experiment presented in Chapter 4 investigated the x-ray excitation of the ^{45}Sc nuclear clock transition. The corresponding main data analysis, which lead to the resonance energy reported in [Shv+23], is presented here. A measure for the incident photon energy was established, and events with outgoing photon energies in the signal range were identified. From only 93 detected signal photons the resonance energy was then determined using three different stochastic methods – a cumulative distribution, a kernel density estimate and a histogram – all of which yielded consistent results within their uncertainties. The final value improved the precision of the resonance energy by a factor of 300 compared to previously known results [Shv+23].

Besides ^{45}Sc we also studied the archetypal Mössbauer isotope ^{57}Fe. While in the first XFEL-experiment Chumakov et al. recorded up to 68 resonant photons in a single pulse [Chu+18], at the European XFEL we were able to push this record to up to 900 signal-photons after excitation with a self-seeded pulse [Ger+25b]. This enabled us to introduce a single-shot analysis of Mössbauer time-domain data [Ger+25b]. We showed, that at XFELs there are pulses with a few hundred detected photons, such that even a single shot may already provide sufficient statistics to extract information. However, because of the stochastic nature of the photon production such pulses are rare. Most pulses result in far fewer signal photons, encoding only partial information. To address this, we developed a data-driven scheme to sort Mössbauer time-domain data on a per-shot basis. The method identifies representatives of different classes from the high-signal shots, and subsequently assigns all other shots to theses classes by comparing them to the representatives. Afterwards, the data can be evaluated separately for each class. In this way, our algorithm incorporates all recorded shots into the final analysis, making full use of the available statistics.

The last XFEL experiment, described in Chapter 6, revealed unexpected and previously unreported anomalies in nuclear forward scattering from ^{57}Fe foils, even though the nuclei are expected to remain in the low-excitation regime [LKE25b]. First, we found a thickness anomaly, i.e., the thickness extracted from the time spectra systematically deviates from the physical one, converging to about 2 μm regardless of the actual sample thickness. The fitted value differs depending on whether a monochromator is used. Remarkably, apart from this discrepancy, the time spectra can still be described well by standard theory. We further reported a second anomaly, the attenuator anomaly.

The attenuator anomaly emerged when varying the amount of attenuating aluminum upstream of the sample while keeping the total aluminum thickness constant. Contrary to expectations in the low-excitation regime, the count rate strongly depends on the placement of the aluminum, and the corresponding time spectra also differ. Since the nuclei are still assumed to be in the low-excitation regime, these anomalies are likely linked to environmental effects rather than the intrinsic nuclear dynamics. Because Mössbauer nuclei are typically employed as sensitive probes of their surroundings, the discovery of such unexpected anomalies is both intriguing and potentially transformative. Understanding them is essential for establishing Mössbauer spectroscopy at XFELs in the conventional sense, that is to probe the properties of the host material, but also to exploit potential studies of XFEL-induced effects in the host material.

In the second part of the thesis we turned from experiment to theory, addressing the de-excitation dynamics of nuclear ensembles following impulsive excitation. This setting represents a complex many-body problem, and previous approaches were insufficient to capture all relevant aspects. Our simulations go beyond the well-studied low-excitation regime and extend to arbitrary degrees of excitation, thereby accessing parameter ranges that will become increasingly relevant at current XFELs and, in particular, at future XFELOs. To enable the studies, Chapter 7 introduced a simulation toolbox combining several complementary existing methods. We mostly employ a custom implementation of the first order cumulant expansion, which due to the linear scaling with the number of nuclei is capable of efficiently simulating interacting ensembles with more than 1000 nuclei on a standard laptop. For validation and cross-checks we further employ the python package `QuTiP` [JNN12; JNN13] and a self-implemented version of the continuous-discrete truncated Wigner approximation [MF23].

Before simulations could be performed, however, in Chapter 8, we addressed the preparation of arbitrary initial states for the CDTWA, with particular focus on partially excited states. Unlike the well-studied ground and fully excited states, these had received little attention by the CDTWA so far and required modifications to the initial state sampling. We systematically examined both existing and newly developed sampling schemes and found that the predicted de-excitation dynamics are already sensitive to the choice of initial sampling in the very first time step. Finally, we decided for a strategy in which the system is initialized in the ground state and then driven into the desired state using the area theorem. This approach guarantees that all investigations rely on a consistent sampling scheme, thereby eliminating any artifacts that could arise from the choice of sampling.

The first application of the simulation toolbox in Chapter 9 are the studies of the de-excitation dynamics of a nucleus in a one-dimensional chain of coupled nuclei [GE25]. Assuming translational invariance, the system reduces to three coupled differential equations. In the low-excitation limit, the dipole-dipole couplings induce a linear phase evolution of the coherence, corresponding to a collective energy shift. At higher excitations, this phase evolution is modified, providing clear signatures beyond the low-excitation regime. The effect can, in principle, be probed via interferometric measurements. Finally, finite-size effects were investigated, revealing signatures that could potentially be observed at XFELs. The predicted effects in the phase evolution were independently confirmed using the CDTWA.

As a second application, we investigated propagation effects beyond the low-excitation regime. Here, we implemented the propagation effects by an effective coupling and primarily study the system with the cumulant expansion. We found that the dynamical beats, i.e., minima in the time spectrum in forward direction caused by propagation effects, shift depending on the initial excitation. Similar observations have been reported using other approaches [Adi24; AGE_p; Kon+25]. Furthermore, we confirmed the effect qualitatively with the CDTWA. This shift provides a clear signature of excitation beyond the low-excitation limit. Since dynamical beats are commonly used to determine the effective thickness of a sample, the excitation-dependent shifts must be accounted for when estimating thicknesses at higher excitations. Beyond this correction, the shifts also offer an unambiguous correspondence to the initial excitation level and can thus serve as a tool to categorize and sort data.

Finally, in the third part of the thesis, presented in Chapter 11, we returned to synchrotron-based studies with an experiment on an optimized interferometer configuration [Ger+25a]. In this setup, two samples are placed inside a polarimeter in such a way that they form a dark-fringe interferometer, where the two perpendicular linear polarizations serve as the interferometer arms. This design combines the stability of an inline x-ray interferometer with spatially overlapping paths and the versatility of conventional x-ray interferometers, where individual samples can be selectively coupled to one arm or the interference can be externally controlled. Operating the interferometer in the dark-fringe mode provides optimal sensitivity. Moreover, we demonstrated that all scattering paths which involve scattering in both samples cancel out, leaving only the single-scattering paths. As a

result, the interferometer can be directly mapped to a conventional two-path interferometer, with the interference between the two arms controlled by mechanically-induced phase shifts.

12.3 Outlook

In the sense of Freeman Dyson's quote "Scientific revolutions are more often driven by new tools than by new concepts.", XFELs have the potential to open a new era for Mössbauer science. The very first step was taken by Chumakov et al. [Chu+18], who in 2018 demonstrated the feasibility of using an XFEL for Mössbauer experiments, showing that pulses with more than one resonant photon could indeed be produced with a significant fraction. In recent years, enabled by advances such as hard x-ray self-seeding [Liu+23], our collaborations demonstrated how these technological advances opened the door for further new possibilities, e.g., the study of ultra-narrow transitions [Liu+25a; Shv+23] or single-shot analysis [Ger+25b].

We view the few existing experiments as the starting point of a broader success story of Mössbauer science at XFELs. The extremely narrow nuclear resonance in ^{45}Sc could enable high-precision experiments, such as measurements of gravitational red-shift over less than a millimeter, or nuclear spectroscopy at a frequency resolution surpassing that of the standard Mössbauer isotope ^{57}Fe by many orders of magnitude. The ultimate goal is to build a nuclear clock [AK15; Shv+23], which, e.g., could be used for gravitational wave detection [BC25], the search for new physics as with ^{229}Th [BC25; Fuc+25; Saf+18], or precision experiments with quantum networks [Fro+25]. The demonstrated single-shot sorting enables a new class of experiments in which different de-excitation dynamics can occur [Boc+21; KKR99; Sad+21; Sak+17; VSK13] and it is beneficial to analyze them separately. Furthermore, the time-resolved observation of the emitted photons could prepare the nuclear ensemble in a quantum state [Cab+99; Moe+07; Thi+07]. Moreover, unexpected anomalies in nuclear resonant scattering already indicate that even in the low-excitation regime differences arise compared to synchrotron experiments. Further investigation of these anomalies is crucial to understand and establish experiments with Mössbauer nuclei at XFELs. Beyond this, nuclei may serve as sensitive probes of the solid-state environment under XFEL irradiation, opening perspectives for electronic-pump–nuclear-probe schemes at XFELs. Besides following the path of the presented experiments, the improved x-ray light sources, especially the improved average flux, bring smaller sample sizes within reach, relevant for cases where only limited material is available or where finite-size effects are of interest. The availability of several resonant photons per pulse in a considerable fraction of shots provides new opportunities. It enables photon-number resolved measurements of time spectra, for which a proof-of-principle demonstration can be found in [Chu+18], but photon-number resolved measurements can also be extended to the energy spectra or other observables. Another straightforward application of the high peak flux is the study of time correlations of the observed photons with a first analysis in [Chu+18]. With upcoming improved x-ray detectors [Chu+25; Cor+24; Llo+22] not only correlations in the time domain, but also spatial correlations can be studied.

In the longer term, XFELOs are expected to excite nuclear ensembles well-beyond the low-excitation regime even reaching full excitation [LKE25b]. This would enable the implementation of additional experimental schemes, such as stimulated Raman adiabatic passage [LPK11; LPK13], nuclear Rabi oscillations [BEK06] or two-photon excitation of Mössbauer resonances [Don00]. In general, the increased average flux would push the boundaries of low-signal experiments, e.g., small samples or narrow resonances, even further. In addition, the intrinsic pulse-to-pulse coherence of an XFELO will make advanced spectroscopies, including multidimensional x-ray spectroscopy [Ada+19], feasible.

On the theoretical side, the progress with XFELs and the developments toward an XFELO have shifted the focus beyond the traditional low-excitation limit. This requieres not only refined tools, but also new concepts. Progress has been made in recent years [AGE_p; HKE16; Kon+25; LKE25b; WE23] and is accompanied by the non-linear effects studied in this thesis. Yet, most investigations so far remain specific to individual scenarios, leaving many open questions. We expect that the demand of theoretical investigations beyond the low-excitation limit will increase in the upcoming years and that the toolbox presented in this thesis can help answering current and arising questions. Questions of particular interest include the role of transverse dipole–dipole couplings in propagation effects and the behavior of temporal and spatial photon correlations in various geometries. Besides the search for effects beyond the low-excitation limit, further studies of schemes to enhance the excitation conditions, e.g., thin-film cavities [LKE25b] or tapered waveguides [Che+22], are expected to be of interest and might not only enhance the initial excitation, but also subsequent effects. In addition,

further optimization of the coupling parameters in structured environments [DLE22a; LAL25] could lead to a possible tuning of effects within the low-excitation regime as well as beyond.

Parallel to the investigations of applications of new light sources, the development of new light sources themselves continues. First proof-of-principle demonstrations of an XFELO [KSR08; Mar+23; Rau+25] have already been achieved. A more ambitious vision is the realization of a true x-ray laser based on nuclear gain — a so-called graser [BSG81]. Although earlier schemes, such as lasing without inversion [Koc92], have been ruled out due to the "graser dilemma" [BS97], research remains active. Lasing from atomic shells has been demonstrated [Roh+12], and recently a multi-photon stimulated nuclear graser scheme has been proposed [YSD24]. Further experimental progress and theoretical understanding, supported by experiments at XFELs and theory beyond the low-excitation limit, is expected to advance this field.

Looking ahead, the studies of nuclear quantum dynamics with XFELs presented here can be extended naturally along the lines developed in this thesis while many additional, so-far unexplored effects remain to be discovered and investigated. Together, these directions open up the largely unexplored landscape of Mössbauer science at XFELs and beyond.

Appendices

Appendix A

Additional information on nuclear forward scattering

In this chapter we provide additional information on nuclear forward scattering. In the first part, details on the fit routines are given, while in the second part the combined contribution of several samples, that are displaced after excitation, is discussed.

A.1 Fitting of time spectra

A.1.1 Indefiniteness of the azimuthal angle

In the fitting of the time spectra, due to the experimental setup, we only consider $\hat{\sigma} \rightarrow \hat{\pi}$ scattering, in which the azimuthal angle of the magnetic field is indefinite as we will show in the following.

Following the standard approach to polarization-dependent nuclear forward scattering [Röh04; SBH99], the linear $\hat{\sigma}$- and $\hat{\pi}$- polarized components of the outgoing electric field E can be related to the incident electric field E^{in} by

$$\begin{pmatrix} \tilde{E}_{\hat{\sigma}}(\omega) \\ \tilde{E}_{\hat{\pi}}(\omega) \end{pmatrix} = \mathcal{E}\, \mathcal{R}(\omega, \phi) \begin{pmatrix} E^{\text{in}}_{\hat{\sigma}} \\ E^{\text{in}}_{\hat{\pi}} \end{pmatrix} , \tag{A.1}$$

$$\mathcal{R}(\omega, \phi) = g_\phi \begin{pmatrix} R_{\text{L}}(\omega) & 0 \\ 0 & R_{\text{C}}(\omega) \end{pmatrix} g_\phi^{-1} , \tag{A.2}$$

where $\mathcal{E} = \exp(ikz - \mu_e\, d/2)$ and μ_e is the electronic contribution characterizing the absorption and phase shift due to off-resonant electronic processes and R_{L} and R_{C} being the two response functions for transitions with linear and circular dipole moments (see Section 2.1.2). g_ϕ is a two-dimensional rotation matrix

$$g_\phi = \begin{pmatrix} \cos\phi & \sin\phi \\ -\sin\phi & \cos\phi \end{pmatrix} , \tag{A.3}$$

capturing the effect of the magnetic field being rotated by the azimuthal angle ϕ from the $\hat{\pi}$-axis.

Assuming that the incoming light only has a polarization along the $\hat{\sigma}$-direction, according to Eq. (A.1) it is

$$\begin{pmatrix} \tilde{E}_{\hat{\sigma}}(\omega) \\ \tilde{E}_{\hat{\pi}}(\omega) \end{pmatrix} = \mathcal{E} \begin{pmatrix} R_{\text{L}} \cos^2\phi + R_{\text{C}} \sin^2\phi \\ (R_{\text{C}} - R_{\text{L}}) \cos\phi \sin\phi \end{pmatrix} . \tag{A.4}$$

Only the $\hat{\pi}$-component can pass the polarization analyzer, thus

$$I_{\text{out}}(\omega) = |\tilde{E}_{\hat{\pi}}(\omega)|^2 = \sin^2\phi \cos^2\phi \left(R_{\text{C}} - R_{\text{L}}\right)^2 , \tag{A.5}$$

and the azimuthal angle ϕ only leads to an overall scaling. However in the fits, the absolute scaling between the experimental and theoretical time spectra is not known, which is why the azimuthal angle ϕ remains indefinite in the perfectly aligned setup.

A.1.2 Fit routine

On a parameter landscape with several parameters, it is usually difficult to find the global minimum. Therefore, we follow a two-step process.

First we perform an evolutionary fitting [Coe05; Rec78]. In this case, we call a set of values for the different fit parameters the *DNA*. In the first step, a fixed number of DNA is drawn randomly with the parameters being in a user-defined interval. For each DNA the fitness, i.e., the goodness of the fit, is calculated. This step is called the first generation. For the second generation, the best DNAs from the previous one are kept. In addition, some DNAs are merged and some are newly drawn.

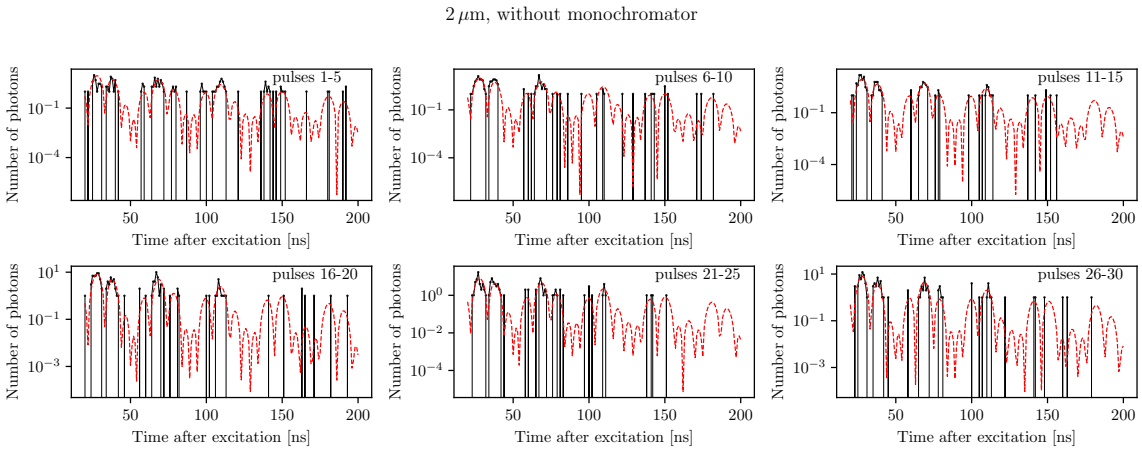

Figure A.1: Pulse resolved fit results for the 2 μm foil without monochromator. The black dots show the measured time spectra with the black line as a guide to the eye. The fits are indicated by the red dashed lines. Only the fitted time region is shown.

After repeating this procedure for several generations, the result converges and the DNA with the best fitness provides a good estimate for the global minimum.

Afterwards, a standard fit routine like "Nelder-Mead" [GH10] is used to find the local minimum close to the identified best parameters.

The theoretical calculations for the fit are performed with the python package `pynuss` [Hee19].

A.1.3 Pulse-resolved fits

In Figs. A.1 to A.6 the fits performed in Section 6.2.3 are shown. As fit parameters we fit the thickness of the sample L, the field strength of the internal magnetic field B and its orientation relative to the incident light polarization, which is described by the azimuthal ϕ and polar angle θ. Note that in the setting with a polarization analyzer in theory the azimuthal angle ϕ is undefined as we showed in Appendix A.1.1. However, in the experiment, the polarizations are not perfect, such that the azimuthal angle ϕ does have an influence on the time spectrum.

We see that the fits resemble the data reasonably well, especially for the measurements with monochromator in which the signal is stronger. Note, that in Section 6.2.3 we are mainly interested in the thickness L, which is determined by the envelop, and the internal magnetic field strength B, which leads to the additional oscillations. Both are parameters that are easy to fit even for lower signal. The magnetic field angles are mainly fitted because the alignment in the experiment was not perfect.

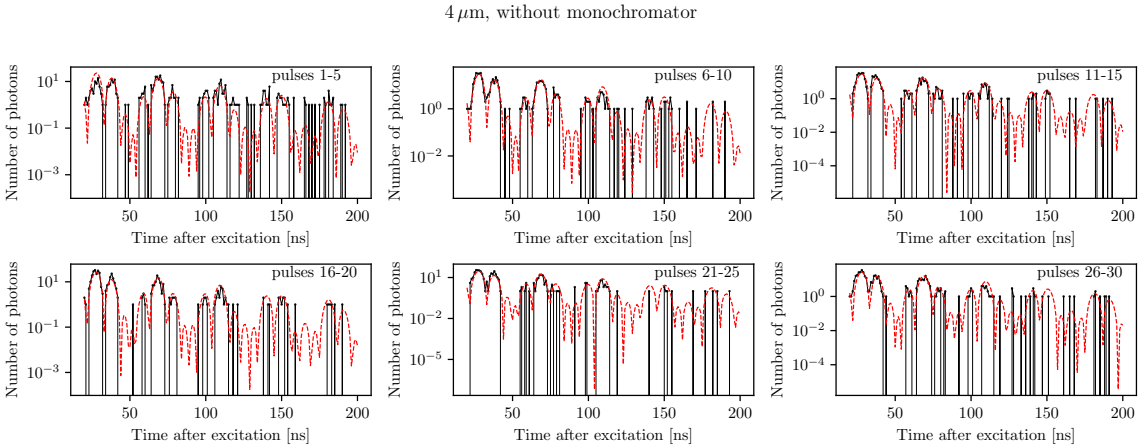

Figure A.2: Pulse resolved fit results for the 4 μm foil without monochromator. The black dots show the measured time spectra with the black line as a guide to the eye. The fits are indicated by the red dashed lines. Only the fitted time region is shown.

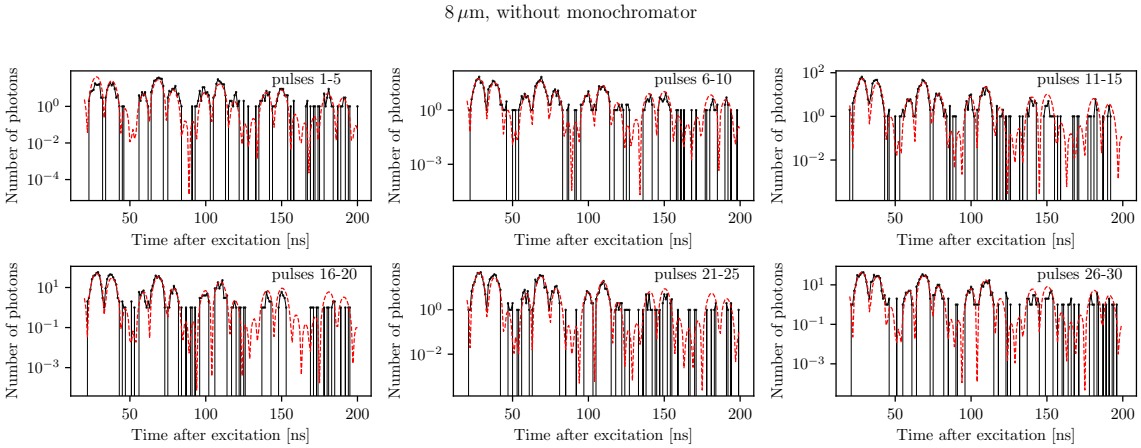

Figure A.3: Pulse resolved fit results for the 8 μm foil without monochromator. The black dots show the measured time spectra with the black line as a guide to the eye. The fits are indicated by the red dashed lines. Only the fitted time region is shown.

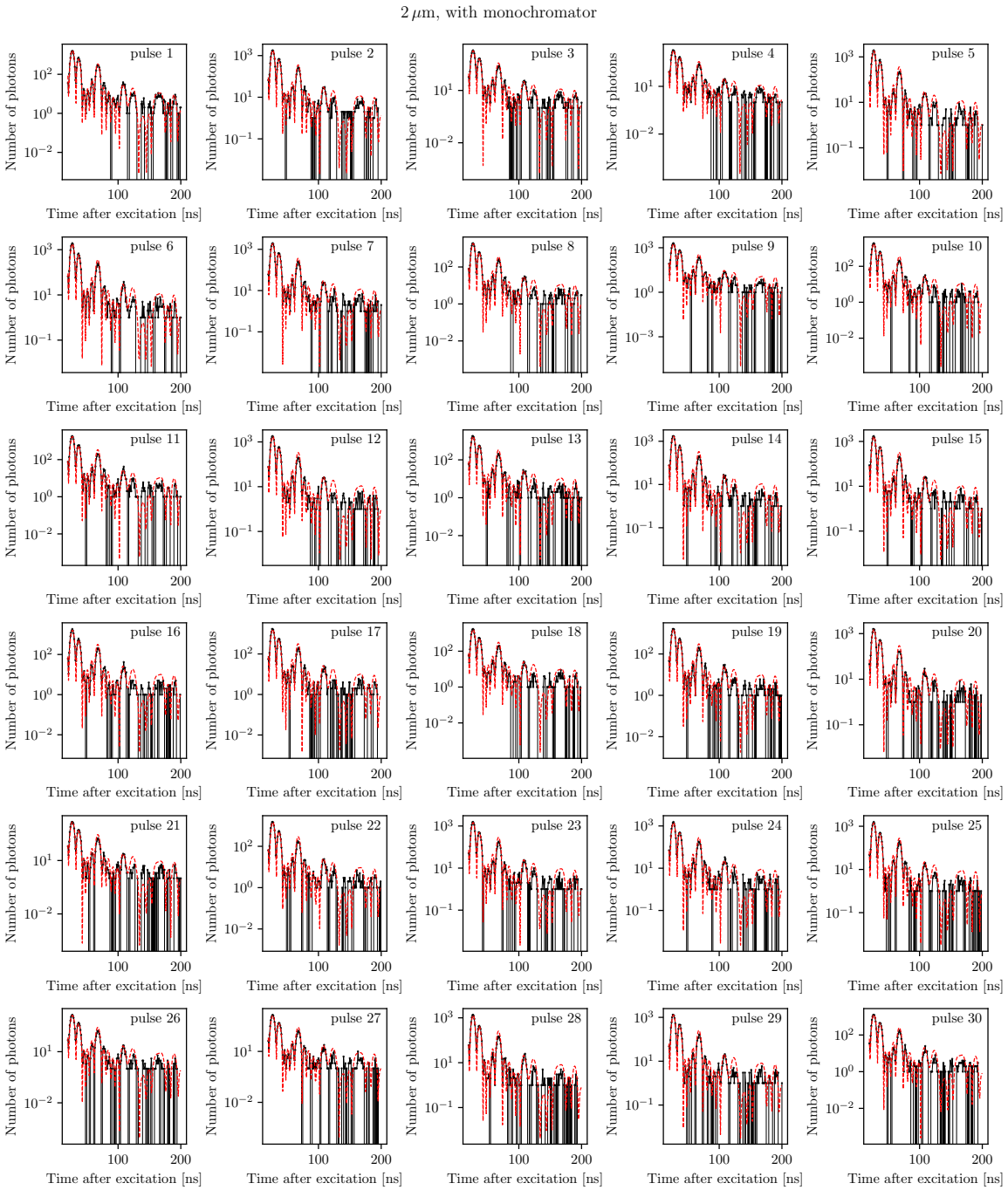

Figure A.4: Pulse resolved fit results for the 2 μm foil with monochromator. The black dots show the measured time spectra with the black line as a guide to the eye. The fits are indicated by the red dashed lines. Only the fitted time region is shown.

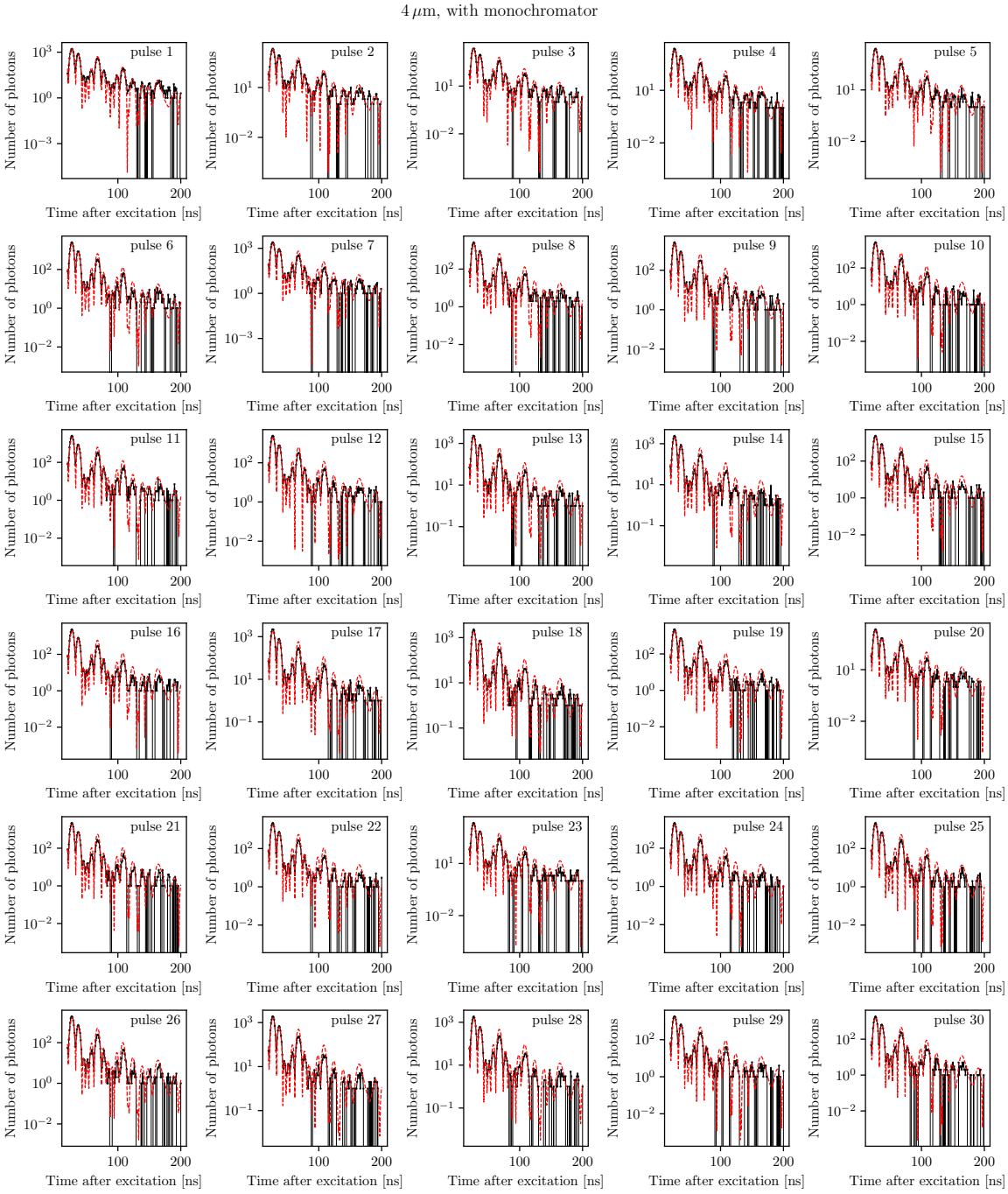

Figure A.5: Pulse resolved fit results for the 4 μm foil with monochromator. The black dots show the measured time spectra with the black line as a guide to the eye. The fits are indicated by the red dashed lines. Only the fitted time region is shown.

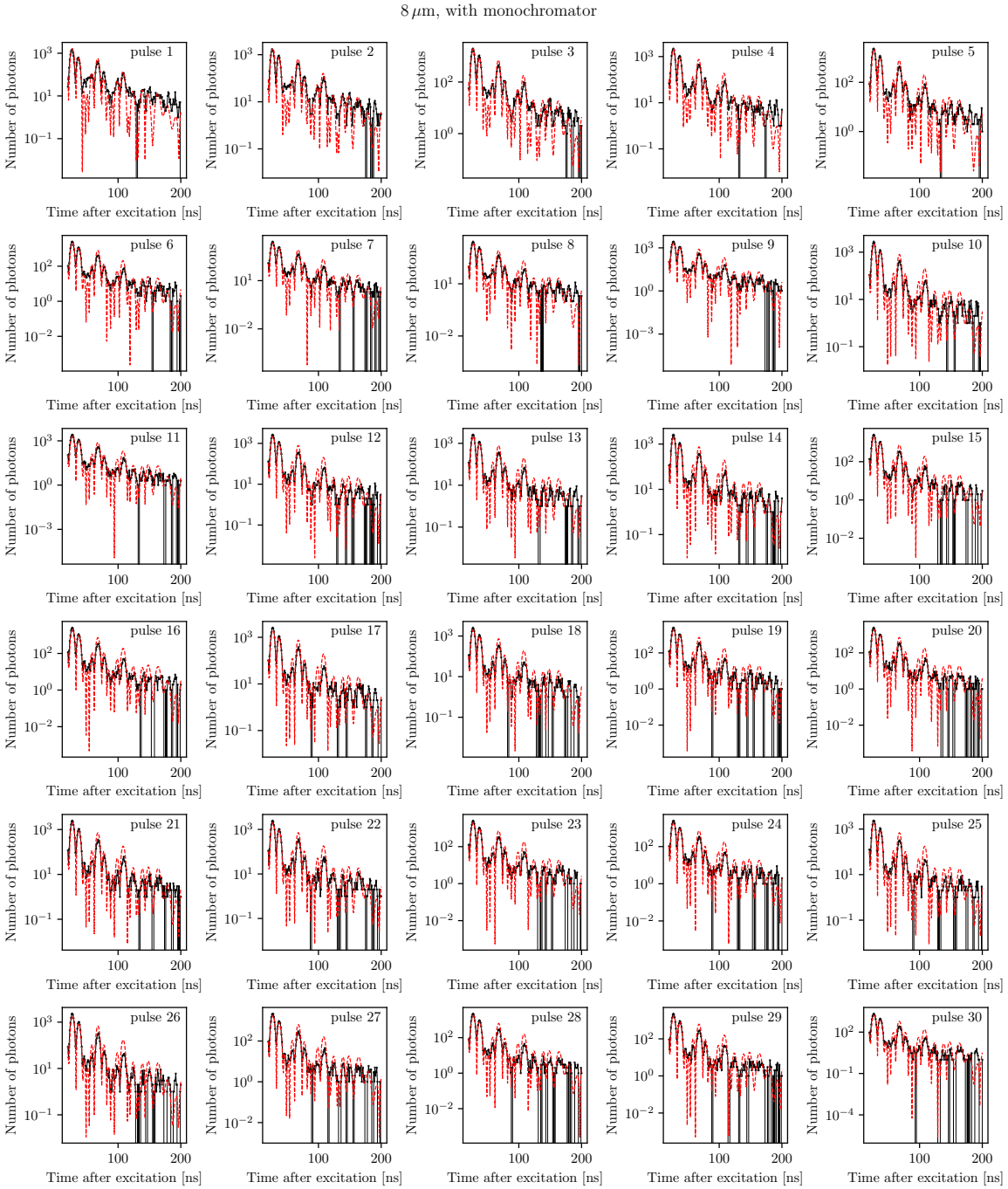

Figure A.6: Pulse resolved fit results for the 8 μm foil with monochromator. The black dots show the measured time spectra with the black line as a guide to the eye. The fits are indicated by the red dashed lines. Only the fitted time region is shown.

A.2 Combined response of moving targets

The combined response of several moving targets can be calculated following the formalism in [Hee+17; Rei14]. For a single target with phase jump to ϕ, $\phi(t) = \phi \cdot \theta(t)$ with $\theta(0) = 0$, at the time of an impulsive excitation the response function is given by [Hel+91]

$$R(\omega, \phi) = 1 + e^{i\phi}\tilde{T}(\omega)\,, \tag{A.6}$$

where $\tilde{T}(\omega)$ is the scattered contribution. Thus, the electric field behind the sample is given by (cf. Eq. (2.6))

$$\tilde{E}(\omega) = R(\omega, \phi) \cdot \tilde{E}_{\text{in}}(\omega) = E^0_{\text{in}}\, R(\omega, \phi)\,, \tag{A.7}$$

where in the last step an impulsive excitation $E(t) \propto \delta(t)$ equivalent to $\tilde{E}(\omega) = E^0_{\text{in}}$ was assumed. To include a second sample with a phase jump to ϕ_2, the electric field after the first sample is Fourier transformed into the time domain

$$\tilde{E}_1(t) = E^0_{\text{in}}\, \mathcal{F}\left[R_1(\omega, \phi_1)\right]\,, \tag{A.8}$$

and afterwards is transformed into the rest frame of the second sample with a phase jump $\phi_2(t) = \phi \cdot \theta(t)$

$$E'_1(t) = E^0_{\text{in}}\, e^{i\phi(t)} E_1(t) = E^0_{\text{in}}\, e^{i\phi_2\theta(t)} \mathcal{F}\left[\tilde{R}_1(\omega, \phi_1)\right]\,. \tag{A.9}$$

To calculate the interaction of the second sample with the above field, the field has to be transformed back into the frequency domain by the inverse Fourier transform

$$\tilde{E}'_1(\omega) = E^0_{\text{in}}\, \mathcal{F}^{-1}\left[e^{i\phi_2\theta(t)} \mathcal{F}\left[\tilde{R}_1(\omega, \phi_1)\right]\right]\,. \tag{A.10}$$

Now the electric field behind the second sample in its rest frame can be calculated to be

$$\tilde{E}'_2(\omega) = E^0_{\text{in}}\, \tilde{R}_2(\omega) \cdot \tilde{E}'_1(\omega) = E^0_{\text{in}}\, \tilde{R}_2(\omega) \cdot \mathcal{F}^{-1}\left[e^{i\phi_2\theta(t)} \mathcal{F}\left[\tilde{R}_1(\omega, \phi_1)\right]\right]\,, \tag{A.11}$$

and transformed into the time domain

$$E'_2(t) = E^0_{\text{in}}\, \mathcal{F}\left[\tilde{E}'_2(\omega)\right] = E^0_{\text{in}}\, \mathcal{F}\left[\tilde{R}_2(\omega) \cdot \mathcal{F}^{-1}\left[e^{i\phi_2\theta(t)} \mathcal{F}\left[\tilde{R}_1(\omega, \phi_1)\right]\right]\right]\,. \tag{A.12}$$

Transforming back into the lab frame gives

$$E_2(t) = E^0_{\text{in}}\, e^{-i\phi_2\theta(t)} \cdot E'_2(t) = E^0_{\text{in}}\, e^{-i\phi_2\theta(t)} \cdot \mathcal{F}\left[\tilde{R}_2(\omega) \cdot \mathcal{F}^{-1}\left[e^{i\phi_2\theta(t)} \mathcal{F}\left[\tilde{R}_1(\omega, \phi_1)\right]\right]\right]\,. \tag{A.13}$$

The expression can be further simplified by replacing $R_j(t, \phi_j) = \delta(t) + e^{i\phi_j}\tilde{T}_j(t)$, which leads to

$$\begin{aligned}
E_2(t) =& E^0_{\text{in}}\, e^{-i\phi_2\theta(t)} \cdot \mathcal{F}\left[\left(1 + \tilde{T}_2(\omega)\right) \cdot \mathcal{F}^{-1}\left[e^{i\phi_2\theta(t)}\left[\delta(t) + e^{i\phi_1}\tilde{T}_1(t)\right]\right]\right] && \text{(A.14)}\\
=& E^0_{\text{in}}\, e^{-i\phi_2\theta(t)} \cdot \left\{\left[\delta(t) + \tilde{T}_2(t)\right] * \left[e^{i\phi_2\theta(t)}\left[\delta(t) + e^{i\phi_1}\tilde{T}_1(t)\right]\right]\right\} && \text{(A.15)}\\
=& E^0_{\text{in}}\, \left(\delta(t) + e^{i\phi_1}\tilde{T}_1(t) + e^{i\phi_2}\tilde{T}_2(t) + e^{i\phi_1}\tilde{T}_1(t) * T_2(t)\right)\,, && \text{(A.16)}
\end{aligned}$$

where in the last step $\delta(x) * f(x) = f(x)$ and $\theta(t > 0) = 1$ was used. This result can be straight forwardly translated to frequency space

$$\tilde{E}_2(\omega) = E^0_{\text{in}}\, \mathcal{F}^{-1}\left[E_2(t)\right] = E^0_{\text{in}}\, \left(1 + e^{i\phi_1}\tilde{T}_1(\omega) + e^{i\phi_2}\tilde{T}_2(\omega) + e^{i\phi_1}\tilde{T}_1(\omega)\tilde{T}_2(\omega)\right)\,. \tag{A.17}$$

Analogously, for three samples, the electric field after the last sample is given by

$$\begin{aligned}
\tilde{E}_3(\omega) =& E^0_{\text{in}}\, \Big(1 + e^{i\phi_1}\tilde{T}_1(\omega) + e^{i\phi_2}\tilde{T}_2(\omega) + e^{i\phi_3}\tilde{T}_3(\omega) + e^{i\phi_1}\tilde{T}_1(\omega)\tilde{T}_2(\omega) + e^{i\phi_1}\tilde{T}_1(\omega)\tilde{T}_3(\omega)\\
&+ e^{i\phi_2}\tilde{T}_2(\omega)\tilde{T}_3(\omega) + e^{i\phi_1}\tilde{T}_1(\omega)\tilde{T}_2(\omega)\tilde{T}_3(\omega)\Big)\,. && \text{(A.18)}
\end{aligned}$$

It can be clearly seen that for the product terms describing scattering in several targets, only the phase of the first sample in which scattering occurs is relevant. The result can be generalized to N samples. The resulting electric field behind the last sample is given by

$$\tilde{E}_N(\omega) = E_{\text{in}}^0 \left[1 + \sum_{j=1}^{n} e^{i\phi_j} \cdot \tilde{T}_j(\omega) \left(\sum_{S \subseteq \{j+1,\ldots,N\}} \prod_{k \in S} \tilde{T}_k(\omega) \right) \right], \tag{A.19}$$

where the first sum over j represents the sample in which the first scattering takes place, which is why the corresponding term has a phase ϕ_j and the sum over $\mathcal{S}$ describes the samples in which the subsequent scattering takes place. The term in the large bracket can be simplified to find

$$\tilde{E}_N(\omega) = E_{\text{in}}^0 \left[1 + \sum_{j=1}^{n} e^{i\phi_j} \tilde{T}_j(\omega) \prod_{k=j+1}^{N} \left(1 + \tilde{T}_k(\omega) \right) \right] \tag{A.20}$$

$$= E_{\text{in}}^0 \left[1 + \sum_{j=1}^{n} e^{i\phi_j} \tilde{T}_j(\omega) \prod_{k=j+1}^{N} \tilde{R}_k(\omega) \right]. \tag{A.21}$$

The term in the first row allows a different view on the multiple sample response. Again the sum over j represents the sample in which the first scattering event happens. The product over k describes all different scattering combinations behind sample j by no scattering in sample k represented by "1" and scattering in sample k indicated by "$\tilde{T}_k$".

For equal samples, i.e., $\tilde{R}_k(\omega) = \tilde{R}(\omega)$ and $\tilde{T}_j(\omega) = \tilde{T}(\omega)$, the product can be further simplified to find

$$\tilde{E}_N(\omega) = E_{\text{in}}^0 \left[1 + \tilde{T}(\omega) \sum_{j=1}^{N} e^{i\phi_j} \tilde{R}(\omega)^{N-j} \right]. \tag{A.22}$$

Setting all phases $\phi_j = 0$, the expected result for N identical samples of $\tilde{E}_N(\omega) = E_0 \, \tilde{R}(\omega)^N$ is retrieved.

Appendix B

Derivation of the operator's equations of motion

In this chapter, we derive the equations of motion for the population and coherence of a nuclei, and the translational invariant model in detail.

B.1 Master equation

As we have seen in Section 2.3.1 the system is governed by the Master equation

$$\frac{\mathrm{d}}{\mathrm{d}t}\rho = \frac{1}{i\hbar}\left[H,\rho\right] + \mathcal{L}[\rho]\,, \tag{B.1}$$

which describes the time evolution of the density matrix ρ, with

$$H = \hbar \sum_{n,m} J_{mn}\, \sigma_n^+\, \sigma_m^-\,, \tag{B.2}$$

$$\begin{aligned}\mathcal{L}[\rho] &= \sum_{n,m} \frac{\Gamma_{mn}}{2}\left(2\sigma_m^-\rho\sigma_n^+ - \sigma_n^+\sigma_m^-\rho - \rho\sigma_n^+\sigma_m^-\right) + \mathcal{L}_{IC}[\rho] \\ &= \sum_{n,m} \frac{\Gamma_{mn}}{2}\left(2\sigma_m^-\rho\sigma_n^+ - \sigma_n^+\sigma_m^-\rho - \rho\sigma_n^+\sigma_m^-\right)\,,\end{aligned} \tag{B.3}$$

$$\Gamma_{mn} = \Gamma_{mn}^{\mathrm{rad}} + \delta_{mn}\Gamma^{\mathrm{IC}}\,, \tag{B.4}$$

where the coupling constants Γ_{mn} and J_{mn} depend on the photonic environment, and Γ consists of the radiative part Γ^{rad} and the internal conversion Γ^{IC} of the single-particle spontaneous decay. Note further that we assume $J_{ii} = 0$, by including these energy-shifts in a suitably defined transition frequency ω_0.

B.2 Equations of motion for operator expectation values

To derive the equations of motion, we consider an operator X that acts on the atom Hilbert space and calculate its expectation value. Note that in this first step, we take into account the possibility that X acts on multiple atoms.

$$\begin{aligned}\frac{\mathrm{d}}{\mathrm{d}t}\langle X\rangle &= \mathrm{Tr}\left\{X\frac{\mathrm{d}}{\mathrm{d}t}\rho\right\} \\ &= \frac{1}{i\hbar}\mathrm{Tr}\left\{X\left[H,\rho\right]\right\} + \mathrm{Tr}\left\{X\mathcal{L}[\rho]\right\} \\ &= \frac{1}{i\hbar}\mathrm{Tr}\left\{\left[X,H\right]\rho\right\} + \sum_{n,m}\frac{\Gamma_{mn}}{2}\mathrm{Tr}\left\{2X\sigma_m^-\rho\sigma_n^+ - X\sigma_n^+\sigma_m^-\rho - X\rho\sigma_n^+\sigma_m^-\right\} \\ &= \frac{1}{i\hbar}\left\langle\left[X,H\right]\right\rangle + \sum_{n,m}\frac{\Gamma_{mn}}{2}\mathrm{Tr}\left\{2\sigma_n^+X\sigma_m^-\rho - X\sigma_n^+\sigma_m^-\rho - \sigma_n^+\sigma_m^-X\rho\right\} \\ &= \frac{1}{i\hbar}\left\langle\left[X,H\right]\right\rangle + \sum_{n,m}\frac{\Gamma_{mn}}{2}\left(\left\langle\sigma_n^+\left[X,\sigma_m^-\right]\right\rangle + \left\langle\left[\sigma_n^+,X\right]\sigma_m^-\right\rangle\right)\,.\end{aligned} \tag{B.5}$$

In the derivation of the final form, also known as the adjoint Lindbladian, we made use of the cyclic permutation symmetry of the trace operation.

B.2.1 General single-particle operators

Next, we specialize the general equation (B.5) to single-particle operators X_l acting on atom l only. This allows us to simplify the sum and index structure considerably. We obtain

$$\begin{aligned}
\frac{\mathrm{d}}{\mathrm{d}t}\langle X_l\rangle &= i\sum_{n,m} J_{mn}\left\langle[X_l,\,\sigma_n^+\,\sigma_m^-]\right\rangle + \sum_{n,m}\frac{\Gamma_{mn}}{2}\left(\left\langle\sigma_n^+[X_l,\sigma_m^-]\right\rangle + \left\langle[\sigma_n^+,X_l]\sigma_m^-\right\rangle\right)\\
&= i\sum_{n,m} J_{mn}\left\langle[X_l,\,\sigma_n^+]\,\sigma_m^- + \sigma_n^+[X_l,\sigma_m^-]\right\rangle + \sum_n\frac{\Gamma_{nl}}{2}\left\langle\sigma_n^+[X_l,\sigma_l^-]\right\rangle + \sum_m\frac{\Gamma_{lm}}{2}\left\langle[\sigma_n^+,X_l]\sigma_m^-\right\rangle\\
&= i\sum_m J_{lm}\left\langle[X_l,\,\sigma_l^+]\,\sigma_m^-\right\rangle + i\sum_n J_{nl}\left\langle\sigma_n^+[X_l,\sigma_l^-]\right\rangle + \sum_n\frac{\Gamma_{nl}}{2}\left\langle\sigma_n^+[X_l,\sigma_l^-]\right\rangle + \sum_m\frac{\Gamma_{lm}}{2}\left\langle[\sigma_n^+,X_l]\sigma_m^-\right\rangle\\
&= \sum_n\left(\frac{\Gamma_{nl}}{2}+iJ_{nl}\right)\left\langle\sigma_n^+[X_l,\sigma_l^-]\right\rangle + \sum_m\left(\frac{\Gamma_{lm}}{2}-iJ_{lm}\right)\left\langle[\sigma_n^+,X_l]\sigma_m^-\right\rangle\,. \qquad \text{(B.6)}
\end{aligned}$$

Here, we used

$$[AB,C] = [A,C]B + A[B,C]\,, \qquad \text{(B.7)}$$
$$[A,BC] = [A,B]C + B[A,C]\,. \qquad \text{(B.8)}$$

Defining the coupling constant

$$\mathcal{C}_{mn} = \frac{\Gamma_{mn}}{2} + iJ_{mn}\,, \qquad \text{(B.9)}$$

we finally obtain

$$\frac{\mathrm{d}}{\mathrm{d}t}\langle X_l\rangle = \sum_n \mathcal{C}_{nl}\left\langle\sigma_n^+[X_l,\sigma_l^-]\right\rangle + \mathcal{C}_{ln}^*\left\langle[\sigma_l^+,X_l]\sigma_n^-\right\rangle\,. \qquad \text{(B.10)}$$

Note that the derivation of this equation did not involve any approximation going beyond the initial model - but it is only valid for single-particle operators.

B.2.2 Specific single-particle operators

We now calculate the equations of motion for two specific single-particle operators. The expectation values of interest are $\langle\sigma_l^-\rangle$ and $\langle\sigma_l^{ee}\rangle$ i.e., the coherence and the excited state population. We find

$$\begin{aligned}
\frac{\mathrm{d}}{\mathrm{d}t}\langle\sigma_l^-\rangle &= \sum_n \mathcal{C}_{nl}\left\langle\sigma_n^+[\sigma_l^-,\sigma_l^-]\right\rangle + \mathcal{C}_{ln}^*\left\langle[\sigma_l^+,\sigma_l^-]\sigma_n^-\right\rangle\\
&= \sum_n \mathcal{C}_{ln}^*\left\langle[\sigma_l^+,\sigma_l^-]\sigma_n^-\right\rangle\\
&= \sum_n \mathcal{C}_{ln}^*\left(2\left\langle\sigma_l^+\sigma_l^-\sigma_n^-\right\rangle - \left\langle\sigma_n^-\right\rangle\right)\\
&= -\frac{\Gamma_{ll}}{2}\left\langle\sigma_l^-\right\rangle - \sum_{\substack{n\\ n\neq l}}\mathcal{C}_{ln}^*\left(\left\langle\sigma_n^-\right\rangle - 2\left\langle\sigma_l^{ee}\sigma_n^-\right\rangle\right)\,, \qquad \text{(B.11)}
\end{aligned}$$

and

$$\begin{aligned}
\frac{\mathrm{d}}{\mathrm{d}t}\langle\sigma_l^{ee}\rangle &= \sum_n \mathcal{C}_{nl}\left\langle\sigma_n^+[\sigma_l^{ee},\sigma_l^-]\right\rangle + \mathcal{C}_{ln}^*\left\langle[\sigma_l^+,\sigma_l^{ee}]\sigma_n^-\right\rangle\\
&= -\sum_n \mathcal{C}_{nl}\left\langle\sigma_n^+\sigma_l^-\right\rangle + \mathcal{C}_{ln}^*\left\langle\sigma_l^+\sigma_n^-\right\rangle\\
&= -\Gamma_{ll}\langle\sigma_l^{ee}\rangle - \sum_{\substack{n\\ n\neq l}}\mathcal{C}_{nl}\left\langle\sigma_n^+\sigma_l^-\right\rangle + \mathcal{C}_{ln}^*\left\langle\sigma_l^+\sigma_n^-\right\rangle\,. \qquad \text{(B.12)}
\end{aligned}$$

For deriving those equations, we used our convention $J_{ii}=0$ and the commutators

$$[\sigma_l^+,\sigma_l^-] = \sigma_l^z = 2\sigma_l^{ee} - \mathbb{1}\,, \qquad \text{(B.13a)}$$
$$[\sigma^{ee},\sigma^-] = -\sigma^-\,, \qquad \text{(B.13b)}$$
$$[\sigma^+,\sigma^{ee}] = -\sigma^+\,. \qquad \text{(B.13c)}$$

B.3 1st order cumulant expansion

Eqs. (B.11) and (B.12) depend also on two-nuclei operators, which depend on three-nuclei operators and so on, with the last one being the equation of motion for an N-nuclei operator. However, due to computational resources we cannot take this to an arbitrary level, but need to truncate the set of equations. Because our system is only weakly coupled, we do not expect strong correlations. Therefore, here we approximate the system in the lowest order cumulant expansion, i.e., [Kub62]

$$\langle A_n B_m \rangle \approx \langle A_n \rangle \langle B_m \rangle \,, \tag{B.14}$$

for operators belonging to different atoms with indices n, m. We obtain from Eqs. (B.11, B.12):

$$\frac{\mathrm{d}}{\mathrm{d}t}\langle \sigma_l^- \rangle = -\frac{\Gamma_{ll}}{2}\left\langle \sigma_l^- \right\rangle - \left(1 - 2\left\langle \sigma_l^{ee} \right\rangle\right) \sum_{\substack{n \\ n\neq l}} \mathcal{C}_{ln}^* \left\langle \sigma_n^- \right\rangle \,, \tag{B.15}$$

$$\frac{\mathrm{d}}{\mathrm{d}t}\langle \sigma_l^{ee} \rangle = -\Gamma_{ll}\langle \sigma_l^{ee} \rangle - 2\,\mathrm{Re}\Big\{ \left\langle \sigma_l^+ \right\rangle \sum_{\substack{n \\ n\neq l}} \mathcal{C}_{ln}^* \left\langle \sigma_n^- \right\rangle \Big\} \,. \tag{B.16}$$

Note that the sum on the right hand sides of the two equations is the same, such that it only has to be evaluated once in an efficient numerical implementation:

$$\frac{\mathrm{d}}{\mathrm{d}t}\langle \sigma_l^- \rangle = -\frac{\Gamma_{ll}}{2}\left\langle \sigma_l^- \right\rangle - \left(1 - 2\left\langle \sigma_l^{ee} \right\rangle\right) \langle \mathcal{S}_l \rangle \,, \tag{B.17}$$

$$\frac{\mathrm{d}}{\mathrm{d}t}\langle \sigma_l^{ee} \rangle = -\Gamma_{ll}\langle \sigma_l^{ee} \rangle - 2\,\mathrm{Re}\Big\{ \left\langle \sigma_l^+ \right\rangle \langle \mathcal{S}_l \rangle \Big\} \,, \tag{B.18}$$

$$\mathcal{S}_l = \sum_{\substack{n \\ n\neq l}} \mathcal{C}_{ln}^* \sigma_n^- \,. \tag{B.19}$$

Further decomposing the coherence into its absolute value and phase

$$\langle \sigma_l^- \rangle = |\langle \sigma_l^- \rangle| \, e^{i\phi_l} = \langle \bar{\sigma}_l^- \rangle \, e^{i\phi_l} \,, \tag{B.20}$$

we find

$$e^{i\phi_l}\frac{\mathrm{d}}{\mathrm{d}t}\langle \bar{\sigma}_l^- \rangle + ie^{i\phi_l}\langle \bar{\sigma}_l^- \rangle \frac{\mathrm{d}}{\mathrm{d}t}\phi_l = \frac{\mathrm{d}}{\mathrm{d}t}\langle \sigma_l^- \rangle = \frac{\Gamma}{2}e^{i\phi_l}\langle \bar{\sigma}_l^- \rangle - (1 - 2\langle \sigma_l^{ee} \rangle) \sum_{\substack{n \\ n\neq l}} \mathcal{C}_{ln}^* e^{i\phi_n} \langle \bar{\sigma}_n^- \rangle \,. \tag{B.21}$$

Multiplying this equation with $\exp(-i\phi_l)$ and dividing it into its real and imaginary part, we find

$$\langle A_n \, B_n \rangle \approx \langle A_n \rangle \, \langle B_n \rangle \qquad (n \neq m) \,, \tag{B.22}$$

for operators acting on different atoms $n \neq m$. Further, we decompose the nuclear coherences into their magnitude and their phase,

$$\langle \sigma_l^- \rangle = |\langle \sigma_l^- \rangle| \, e^{i\phi_l} = \langle \bar{\sigma}_l^- \rangle \, e^{i\phi_l} \,. \tag{B.23}$$

We obtain the set of $3N$ real-valued differential equations

$$\frac{d}{dt}\langle \bar{\sigma}_l^- \rangle = -\frac{\Gamma_{ll}}{2}\left\langle \bar{\sigma}_l^- \right\rangle - \left(1 - 2\left\langle \sigma_l^{ee} \right\rangle\right) \kappa_l^R \,, \tag{B.24}$$

$$\frac{d}{dt}\phi_l = -\left(1 - 2\left\langle \sigma_l^{ee} \right\rangle\right) \langle \bar{\sigma}_l^- \rangle^{-1} \kappa_l^I \,, \tag{B.25}$$

$$\frac{d}{dt}\langle \sigma_l^{ee} \rangle = -\Gamma_{ll}\langle \sigma_l^{ee} \rangle - 2\left\langle \bar{\sigma}_l^- \right\rangle \kappa_l^R \,, \tag{B.26}$$

$$\kappa_l = \kappa_l^R + i\kappa_l^I = \sum_{\substack{n=1 \\ n\neq l}}^{N} \mathcal{C}_{ln}^* \langle \bar{\sigma}_n^- \rangle e^{i(\phi_n - \phi_l)} \,, \tag{B.27}$$

which is the set of equations used in Section 9.2.2.

B.4 Derivation of equations of motion with translational invariance in the infinite chain

Finally, we derive much simpler equations by assuming that the ensemble of atoms is infinite and translationally invariant. In practice, these conditions are reasonable fulfilled if the nuclei have equidistant spacing and finite size effects are negligible because of a large distance to the edges for most nuclei. This should be the case for many situations of interest with nuclei, given the lattice spacing of 286 pm of α-Fe. For example, a sample range of only 1 μm already has approximately 3500 lattice planes.

Under these assumptions, one might expect that each atom evolves in the same way, except for the initial phase factor that is imprinted onto it by the exciting light. In order to test this, we make an ansatz for the required expectation values as

$$\langle \sigma_l^-(t)\rangle = \langle \bar{\sigma}^-(t)\rangle\, e^{i\phi_l(t)}\,, \tag{B.28}$$

$$\langle \sigma_l^{ee}(t)\rangle = \langle \sigma^{ee}(t)\rangle\,. \tag{B.29}$$

Then, Eqs. (B.17-B.19) become

$$\begin{aligned}\frac{d}{dt}\langle\bar{\sigma}^-\rangle e^{i\phi_l(t)} &= e^{i\phi_l(t)}\frac{d}{dt}\langle\bar{\sigma}^-\rangle + i\langle\bar{\sigma}^-\rangle e^{i\phi_l(t)}\frac{d}{dt}\phi_l(t)\\ &= -\frac{\Gamma}{2}\left\langle\bar{\sigma}^-\right\rangle e^{i\phi_l(t)} - \left\langle\bar{\sigma}^-\right\rangle\left(1-2\left\langle\sigma^{ee}\right\rangle\right)\sum_{\substack{n\\ n\neq l}}\mathcal{C}_{ln}^{*}e^{i\phi_n(t)}\,.\end{aligned} \tag{B.30}$$

Thus,

$$\frac{d}{dt}\langle\bar{\sigma}^-\rangle + i\langle\bar{\sigma}^-\rangle\frac{d}{dt}\phi_l(t) = -\frac{\Gamma}{2}\left\langle\bar{\sigma}^-\right\rangle - \left\langle\bar{\sigma}^-\right\rangle\left(1-2\left\langle\sigma^{ee}\right\rangle\right)K\,, \tag{B.31}$$

$$\tag{B.32}$$

with

$$K = K_R + iK_I = \sum_{\substack{n\\ n\neq l}}\mathcal{C}_{ln}^{*}e^{i(\phi_n(t)-\phi_l(t))}\,, \tag{B.33}$$

which can be decomposed into

$$\frac{d}{dt}\langle\bar{\sigma}^-\rangle = -\frac{\Gamma}{2}\left\langle\bar{\sigma}^-\right\rangle - \left\langle\bar{\sigma}^-\right\rangle\left(1-2\left\langle\sigma^{ee}\right\rangle\right)K_R\,, \tag{B.34}$$

$$\frac{d}{dt}\phi_l(t) = -\left(1-2\left\langle\sigma^{ee}\right\rangle\right)K_I\,. \tag{B.35}$$

Regarding the populations, we find

$$\frac{d}{dt}\langle\sigma^{ee}\rangle = -\Gamma\langle\sigma^{ee}\rangle - 2\left|\left\langle\sigma^-\right\rangle\right|^2 K_R\,. \tag{B.36}$$

As a result, we find that if K is independent of l as already suggested by the omission of the subindex l to K in the above definition, i.e., it is the same for each atom, then the ansatz Eqs. (B.28, B.29) leads to a self-consistent set of equations. Thus, if the initial state satisfies the ansatz, then also the subsequent dynamics will satisfy it.

Within the limit assumed in this section, K is independent of l, which can be seen by a simple index translation of the atoms. In other words, K only depends on the relative distance and phase of two atoms l, n, and each atom l is surrounded by an equivalent set of atoms n in the case of a translationally invariant ensemble.

Note that because $\mathcal{C}_{ln}$ is constant in time and the phase difference only depends in the initial phases of nucleus l and n, the coupling parameter K is time-independent. Therefore, the system reduces to

a set of only three coupled non-linear equations, which can efficiently be solved numerically:

$$\frac{d}{dt}\langle\bar{\sigma}^{-}\rangle = -\left[\frac{\Gamma}{2} + (1 - 2\,\langle\sigma^{ee}\rangle)\; K_R\right]\left\langle\bar{\sigma}^{-}\right\rangle\,, \tag{B.37}$$

$$\frac{d}{dt}\phi_l(t) = -\,(1 - 2\,\langle\sigma^{ee}\rangle)\; K_I\,, \tag{B.38}$$

$$\frac{d}{dt}\langle\sigma^{ee}\rangle = -\Gamma\langle\sigma^{ee}\rangle - 2\,\left|\left\langle\bar{\sigma}^{-}\right\rangle\right|^2\; K_R\,, \tag{B.39}$$

$$K = K_R + iK_I = \sum_{\substack{n \\ n\neq l}} \mathcal{C}^{*}_{ln} e^{i(\phi_n(t=0) - \phi_l(t=0))}\,. \tag{B.40}$$

Bibliography

[45S22] ^{45}Sc EuXFEL collaboration. *Detection of the ultranarrow nuclear resonance of 45-Sc*. Main proposer: R. Röhlsberger, PI: Y. Shvyd'ko. 2022. DOI: 10.22003/XFEL.EU-DATA-003159-00.

[45S24] ^{45}Sc EuXFEL collaboration. *Observation of nuclear forward scattering from 45Sc: towards extreme metrology with x-rays (derived from 5296)*. Main proposer: Y. Shvyd'ko, PI: R. Röhlsberger. 2024. DOI: 10.22003/XFEL.EU-DATA-006536-00.

[57F22] ^{57}Fe EuXFEL collaboration. *Multiphoton Collective Lambshift in Nuclear Resonant Scattering*. Main proposer: R. Röhlsberger, PI: I. Uschmann. 2022. DOI: 10.22003/XFEL.EU-DATA-002778-00.

[57F23] ^{57}Fe EuXFEL collaboration. *Multiphoton Collective Lambshift in Nuclear Resonant Scattering*. Main proposer: R. Röhlsberger, PI: J. Evers. 2023. DOI: 10.22003/XFEL.EU-DATA-003334-00.

[57F25] ^{57}Fe EuXFEL collaboration. *XFEL anomalies in nuclear resonance scattering: From fundamental understanding to non-invasive precision probes*. Main proposer: J. Evers, PI: R. Röhlsberger. 2025. DOI: 10.22003/XFEL.EU-DATA-008006-00.

[AB65] F. Arecchi and R. Bonifacio. "Theory of optical maser amplifiers". In: *IEEE Journal of Quantum Electronics* 1 (1965), pages 169–178. DOI: 10.1109/JQE.1965.1072212.

[Abb+16] B. P. Abbott et al. "Observation of Gravitational Waves from a Binary Black Hole Merger". In: *Phys. Rev. Lett.* 116 (2016), page 061102. DOI: 10.1103/PhysRevLett.116.061102.

[Abe62] I. D. Abella. "Optical Double-Photon Absorption in Cesium Vapor". In: *Phys. Rev. Lett.* 9 (1962), pages 453–455. DOI: 10.1103/PhysRevLett.9.453.

[AC70] F. T. Arecchi and E. Courtens. "Cooperative Phenomena in Resonant Electromagnetic Propagation". In: *Phys. Rev. A* 2 (1970), pages 1730–1737. DOI: 10.1103/PhysRevA.2.1730.

[Ack+07] W. Ackermann et al. "Operation of a free-electron laser from the extreme ultraviolet to the water window". In: *Nature Photonics* 1 (2007), pages 336–342. DOI: 10.1038/nphoton.2007.76.

[Ada+13] B. W. Adams et al. "X-ray quantum optics". In: *Journal of Modern Optics* 60 (2013), pages 2–21. DOI: 10.1080/09500340.2012.752113.

[Ada+19] B. Adams et al. *Scientific Opportunities with an X-ray Free-Electron Laser Oscillator*. 2019. arXiv: 1903.09317 [physics.ins-det].

[Ada03] *Nonlinear Optics, Quantum Optics, and Ultrafast Phenomena with X-Rays*. Springer US. 2003. DOI: 10.1007/978-1-4615-0387-3.

[Adi24] D. Adigüzel. "Effects of non-linear excitation on the propagation of light through ensembles of nuclear two-level systems". Bachelor's Thesis. Ruprecht-Karls-Universität Heidelberg. 2024. Available online.

[AE87] L. Allen and J. Eberly. *Optical resonance and two-level atoms*. Dover books on physics and chemistry. 1987. ISBN: 0-486-65533-4.

[AGE_p] D. Adigüzel, M. Gerharz, and J. Evers. *Signatures for non-linear excitation of Mössbauer nuclei in the presence of propagation effects*. in preparation.

[AK15] B. W. Adams and K.-J. Kim. "X-ray comb generation from nuclear-resonance-stabilized x-ray free-electron laser oscillator for fundamental physics and precision metrology". In: *Phys. Rev. ST Accel. Beams* 18 (2015), page 030711. DOI: 10.1103/PhysRevSTAB.18.030711.

[Alo+20] R. Alonso-Mori et al. “Femtosecond electronic structure response to high intensity XFEL pulses probed by iron X-ray emission spectroscopy”. In: *Scientific Reports* 10 (2020). DOI: 10.1038/s41598-020-74003-1.

[Ama+12] J. Amann et al. “Demonstration of self-seeding in a hard-X-ray free-electron laser”. In: *Nature photonics* 6 (2012), pages 693–698. DOI: 10.1038/nphoton.2012.180.

[AP01] G. S. Agarwal and A. K. Patnaik. “Vacuum-induced coherences in radiatively coupled multilevel systems”. In: *Phys. Rev. A* 63 (2001), page 043805. DOI: 10.1103/PhysRevA.63.043805.

[Aqu+15] A. Aquila et al. “The linac coherent light source single particle imaging road map”. In: *Structural Dynamics* 2 (2015), page 041701. DOI: 10.1063/1.4918726. eprint: https://pubs.aip.org/aca/sdy/article-pdf/doi/10.1063/1.4918726/13755787/041701_1_online.pdf.

[Ase+17a] A. Asenjo-Garcia et al. “Atom-light interactions in quasi-one-dimensional nanostructures: A Green’s-function perspective”. In: *Phys. Rev. A* 95 (2017), page 033818. DOI: 10.1103/PhysRevA.95.033818.

[Ase+17b] A. Asenjo-Garcia et al. “Exponential Improvement in Photon Storage Fidelities Using Subradiance and “Selective Radiance” in Atomic Arrays”. In: *Phys. Rev. X* 7 (2017), page 031024. DOI: 10.1103/PhysRevX.7.031024.

[Ash03] N. Ashby. “Relativity in the Global Positioning System”. In: *Living Reviews in Relativity* 6 (2003). DOI: 10.12942/lrr-2003-1.

[Ash78] A. Ashkin. “Trapping of Atoms by Resonance Radiation Pressure”. In: *Phys. Rev. Lett.* 40 (1978), pages 729–732. DOI: 10.1103/PhysRevLett.40.729.

[Bal85] J. J. Balmer. “Notiz über die Spectrallinien des Wasserstoffs”. In: *Annalen der Physik* 261 (1885), pages 80–87. DOI: https://doi.org/10.1002/andp.18852610506.

[Bar+04] M. Bartenstein et al. “Crossover from a Molecular Bose-Einstein Condensate to a Degenerate Fermi Gas”. In: *Phys. Rev. Lett.* 92 (2004), page 120401. DOI: 10.1103/PhysRevLett.92.120401.

[Bar+10] W. Barletta et al. “Free electron lasers: Present status and future challenges”. In: *Nuclear Instruments and Methods in Physics Research Section A: Accelerators, Spectrometers, Detectors and Associated Equipment* 618 (2010), pages 69–96. DOI: https://doi.org/10.1016/j.nima.2010.02.274.

[Bar+22] T. R. M. Barends et al. “Serial femtosecond crystallography”. In: *Nature Reviews Methods Primers* 2 (2022). DOI: 10.1038/s43586-022-00141-7.

[Bar+96] A. Q. R. Baron et al. “Single-nucleus quantum beats excited by synchrotron radiation”. In: *Europhysics Letters* 34 (1996), page 331. DOI: 10.1209/epl/i1996-00460-0.

[Bar05] C. G. Barkla. “Secondary Röntgen Radiation”. In: *Nature* 71 (1905), pages 440–440. DOI: 10.1038/071440a0.

[Bar11] C. G. Barkla. “The spectra of the fluorescent Röntgen radiations”. In: *The London, Edinburgh, and Dublin Philosophical Magazine and Journal of Science* 22 (1911), pages 396–412. DOI: 10.1080/14786440908637137.

[BB13] W. H. Bragg and W. L. Bragg. “The reflection of X-rays by crystals”. In: *Proceedings of the Royal Society of London. Series A, Containing Papers of a Mathematical and Physical Character* 88 (1913), pages 428–438. DOI: 10.1098/rspa.1913.0040.

[BB86] T. Burrows and M. Bhat. “Nuclear data sheets for A = 57”. In: *Nuclear Data Sheets* 47 (1986), pages 1–134. DOI: https://doi.org/10.1016/S0090-3752(86)80047-3.

[BC25] S. Bondani and S. L. Cacciatori. *Towards detecting the temporal fluctuations from gravitational waves in asynchronous gauges*. 2025. arXiv: 2509.13321 [gr-qc].

[BC69] D. C. Burnham and R. Y. Chiao. “Coherent Resonance Fluorescence Excited by Short Light Pulses”. In: *Phys. Rev.* 188 (1969), pages 667–675. DOI: 10.1103/PhysRev.188.667.

[Bec+07] B. R. Beck et al. “Energy Splitting of the Ground-State Doublet in the Nucleus ^{229}Th”. In: *Phys. Rev. Lett.* 98 (2007), page 142501. DOI: 10.1103/PhysRevLett.98.142501.

[BEK06] T. J. Bürvenich, J. Evers, and C. H. Keitel. "Nuclear Quantum Optics with X-Ray Laser Pulses". In: *Phys. Rev. Lett.* 96 (2006), page 142501. DOI: 10.1103/PhysRevLett.96.142501.

[Bet47] H. A. Bethe. "The Electromagnetic Shift of Energy Levels". In: *Phys. Rev.* 72 (1947), pages 339–341. DOI: 10.1103/PhysRev.72.339.

[BH65] U. Bonse and M. Hart. "An x-ray interferometer". In: *Applied Physics Letters* 6 (1965), pages 155–156. DOI: 10.1063/1.1754212.

[BIH91] K.-J. Boller, A. Imamo ğlu, and S. E. Harris. "Observation of electromagnetically induced transparency". In: *Phys. Rev. Lett.* 66 (1991), pages 2593–2596. DOI: 10.1103/PhysRevLett.66.2593.

[Ble46] J. P. Blewett. "Radiation Losses in the Induction Electron Accelerator". In: *Phys. Rev.* 69 (1946), pages 87–95. DOI: 10.1103/PhysRev.69.87.

[Blo+14] B. J. Bloom et al. "An optical lattice clock with accuracy and stability at the 10–18 level". In: *Nature* 506 (2014), pages 71–75. DOI: 10.1038/nature12941.

[Blu+71] T. Blundell et al. "X-Ray Analysis and the Structure of Insulin11The Gregory Pincus Memorial Lecture." In: *Proceedings of the 1970 Laurentian Hormone Conference*. Edited by E. ASTWOOD. Volume 27. Recent Progress in Hormone Research. Boston: Academic Press, 1971, pages 1–40. DOI: https://doi.org/10.1016/B978-0-12-571127-2.50025-0.

[Boc+21] L. Bocklage et al. "Coherent control of collective nuclear quantum states via transient magnons". In: *Science Advances* 7 (2021), eabc3991. DOI: 10.1126/sciadv.abc3991.

[Boe+17] U. Boesenberg et al. "X-ray spectrometer based on a bent diamond crystal for high repetition rate free-electron laser applications". In: *Opt. Express* 25 (2017), pages 2852–2862. DOI: 10.1364/OE.25.002852.

[Boe+24] U. Boesenberg et al. "X-ray beam diagnostics at the MID instrument of the European X-ray Free-Electron Laser Facility". In: *Journal of Synchrotron Radiation* 31 (2024), pages 596–604. DOI: 10.1107/S1600577524001279.

[Boh13] N. Bohr. "I. On the constitution of atoms and molecules". In: *The London, Edinburgh, and Dublin Philosophical Magazine and Journal of Science* 26 (1913), pages 1–25.

[Bon+16] C. Bond et al. "Interferometer techniques for gravitational-wave detection". In: *Living Reviews in Relativity* 19 (2016). DOI: 10.1007/s41114-016-0002-8.

[Bon+68] T. Bonchev et al. "Possibility of Investigating Movement in a Group of Ants by the Mössbauer Effect". In: *Nature* 217 (1968), pages 96–98. DOI: 10.1038/217096a0.

[Bon60] W. L. Bond. "Precision lattice constant determination". In: *Acta Crystallographica* 13 (1960), pages 814–818. DOI: 10.1107/S0365110X60001941.

[Bos+16] C. Bostedt et al. "Linac Coherent Light Source: The first five years". In: *Rev. Mod. Phys.* 88 (2016), page 015007. DOI: 10.1103/RevModPhys.88.015007.

[Bot+22] T. Bothwell et al. "Resolving the gravitational redshift across a millimetre-scale atomic sample". In: *Nature* 602 (2022), pages 420–424. DOI: 10.1038/s41586-021-04349-7.

[Bow96] D. K. Bowen. "Applications of X-Ray Interferometry". In: *X-Ray and Neutron Dynamical Diffraction: Theory and Applications*. Edited by A. Authier, S. Lagomarsino, and B. K. Tanner. Boston, MA: Springer US, 1996, pages 381–410. DOI: 10.1007/978-1-4615-5879-8_26.

[BP07] H.-P. Breuer and F. Petruccione. *The Theory of Open Quantum Systems*. Oxford University Press. 2007. DOI: 10.1093/acprof:oso/9780199213900.001.0001.

[BS09] C. Barkla and C. Sadler. "The absorption of Röntgen rays". In: *The London, Edinburgh, and Dublin Philosophical Magazine and Journal of Science* 17 (1909), pages 739–760. DOI: 10.1080/14786440508636650.

[BS97] G. C. Baldwin and J. C. Solem. "Recoilless gamma-ray lasers". In: *Rev. Mod. Phys.* 69 (1997), pages 1085–1118. DOI: 10.1103/RevModPhys.69.1085.

[BSG81] G. C. Baldwin, J. C. Solem, and V. I. Gol'danskii. "Approaches to the development of gamma-ray lasers". In: *Rev. Mod. Phys.* 53 (1981), pages 687–744. DOI: 10.1103/RevModPhys.53.687.

[BTS98] K. Bergmann, H. Theuer, and B. W. Shore. "Coherent population transfer among quantum states of atoms and molecules". In: *Rev. Mod. Phys.* 70 (1998), pages 1003–1025. DOI: 10.1103/RevModPhys.70.1003.

[Bur+77] N. H. Burnett et al. "Harmonic generation in CO2 laser target interaction". In: *Applied Physics Letters* 31 (1977), pages 172–174. DOI: 10.1063/1.89628.

[Bür+99] U. van Bürck et al. "Pulse propagation of synchrotron radiation through a nuclear two-resonance system". In: *Phys. Rev. A* 61 (1999), page 013803. DOI: 10.1103/PhysRevA.61.013803.

[Bur19] Bureau International des Poids et Mesures. *The International System of Units (SI), 9th Edition*. BIPM, Sèvres, France. 2019. Available online.

[Bür99] U. van Bürck. "Coherent pulse propagation through resonant media". In: *Hyperfine Interactions* 123–124 (1999), pages 483–509. DOI: 10.1023/a:1017080008712.

[BW36] G. Breit and E. Wigner. "Capture of Slow Neutrons". In: *Phys. Rev.* 49 (1936), pages 519–531. DOI: 10.1103/PhysRev.49.519.

[Cab+99] C. Cabrillo et al. "Creation of entangled states of distant atoms by interference". In: *Phys. Rev. A* 59 (1999), pages 1025–1033. DOI: 10.1103/PhysRevA.59.1025.

[Cal+05] R. Callens et al. "Phase determination in nuclear resonant scattering using a velocity drive as an interferometer and phase shifter". In: *Phys. Rev. B* 72 (2005), page 081402. DOI: 10.1103/PhysRevB.72.081402.

[Cal+14] F. Calegari et al. "Ultrafast electron dynamics in phenylalanine initiated by attosecond pulses". In: *Science* 346 (2014), pages 336–339. DOI: 10.1126/science.1254061. eprint: https://www.science.org/doi/pdf/10.1126/science.1254061.

[Can+15] T. Caneva et al. "Quantum dynamics of propagating photons with strong interactions: a generalized input–output formalism". In: *New Journal of Physics* 17 (2015), page 113001. DOI: 10.1088/1367-2630/17/11/113001.

[Cav81] C. M. Caves. "Quantum-mechanical noise in an interferometer". In: *Phys. Rev. D* 23 (1981), pages 1693–1708. DOI: 10.1103/PhysRevD.23.1693.

[CCT14] H. N. Chapman, C. Caleman, and N. Timneanu. "Diffraction before destruction". In: *Philosophical Transactions of the Royal Society B: Biological Sciences* 369 (2014), page 20130313. DOI: 10.1098/rstb.2013.0313.

[Cha+06] H. N. Chapman et al. "Femtosecond diffractive imaging with a soft-X-ray free-electron laser". In: *Nature Physics* 2 (2006), pages 839–843. DOI: 10.1038/nphys461.

[Cha+11] H. N. Chapman et al. "Femtosecond X-ray protein nanocrystallography". In: *Nature* 470 (2011), pages 73–77. DOI: 10.1038/nature09750.

[Cha+18] D. E. Chang et al. "Colloquium: Quantum matter built from nanoscopic lattices of atoms and photons". In: *Rev. Mod. Phys.* 90 (2018), page 031002. DOI: 10.1103/RevModPhys.90.031002.

[Cha23] H. N. Chapman. "Fourth-generation light sources". In: *IUCrJ* 10 (2023), pages 246–247. DOI: 10.1107/s2052252523003585.

[Che+22] Y.-H. Chen et al. "Transient nuclear inversion by x-ray free electron laser in a tapered x-ray waveguide". In: *Phys. Rev. Res.* 4 (2022), page L032007. DOI: 10.1103/PhysRevResearch.4.L032007.

[Che+83] A. Chechin et al. "Coherent excitation of Moessbauer nuclei by synchrotron radiation". In: *Pis' ma v Zhurnal Ehksperimental'noj i Teoreticheskoj Fiziki* 37 (1983), pages 531–534.

[Cho+17] B. I. Cho et al. "Observation of Reverse Saturable Absorption of an X-ray Laser". In: *Phys. Rev. Lett.* 119 (2017), page 075002. DOI: 10.1103/PhysRevLett.119.075002.

[Chu+18] A. I. Chumakov et al. "Superradiance of an ensemble of nuclei excited by a free electron laser". In: *Nature physics* 14 (2018), pages 261–264. DOI: 10.1038/s41567-017-0001-z.

[Chu+25] Y. Chushkin et al. "Achieving nanosecond time resolution with a two-dimensional X-ray detector". In: *Journal of Synchrotron Radiation* 32 (2025), pages 1220–1227. DOI: 10.1107/S1600577525006599.

[CM91] O. Carnal and J. Mlynek. "Young's double-slit experiment with atoms: A simple atom interferometer". In: *Phys. Rev. Lett.* 66 (1991), pages 2689–2692. DOI: 10.1103/PhysRevLett.66.2689.

[Coe05] C. A. Coello Coello. "An Introduction to Evolutionary Algorithms and Their Applications". In: *Advanced Distributed Systems*. Edited by F. F. Ramos, V. Larios Rosillo, and H. Unger. Berlin, Heidelberg: Springer Berlin Heidelberg, 2005, pages 425–442.

[Com23] A. H. Compton. "A Quantum Theory of the Scattering of X-rays by Light Elements". In: *Phys. Rev.* 21 (1923), pages 483–502. DOI: 10.1103/PhysRev.21.483.

[Cor+24] J. Correa et al. "TEMPUS, a Timepix4-based system for the event-based detection of X-rays". In: *Journal of Synchrotron Radiation* 31 (2024), pages 1209–1216. DOI: 10.1107/S1600577524005319.

[CR98] A. Chumakov and R. Rüffer. "Nuclear inelastic scattering". In: *Hyperfine Interactions* 113 (1998), pages 59–79. DOI: 10.1023/A:1012659229533.

[Cri70] M. D. Crisp. "Propagation of Small-Area Pulses of Coherent Light through a Resonant Medium". In: *Physical Review A* 1 (1970), pages 1604–1611. DOI: 10.1103/physreva.1.1604.

[Cro+49] D. Crowfoot et al. "The X-Ray Crystallographic Investigation of the Structure of Penicillin". In: *Chemistry of Penicillin*. Edited by H. T. Clarke. Princeton: Princeton University Press, 1949, pages 310–366. DOI: doi:10.1515/9781400874910-012.

[CSW60] T. E. Cranshaw, J. P. Schiffer, and A. B. Whitehead. "Measurement of the Gravitational Red Shift Using the Mössbauer Effect in Fe^{57}". In: *Phys. Rev. Lett.* 4 (1960), pages 163–164. DOI: 10.1103/PhysRevLett.4.163.

[Czi+18] S. Czischek et al. "Quenches near criticality of the quantum Ising chain—power and limitations of the discrete truncated Wigner approximation". In: *Quantum Science and Technology* 4 (2018), page 014006. DOI: 10.1088/2058-9565/aae3f7.

[Dav+95] K. B. Davis et al. "Bose-Einstein Condensation in a Gas of Sodium Atoms". In: *Phys. Rev. Lett.* 75 (1995), pages 3969–3973. DOI: 10.1103/PhysRevLett.75.3969.

[DCM92] J. Dalibard, Y. Castin, and K. Mølmer. "Wave-function approach to dissipative processes in quantum optics". In: *Phys. Rev. Lett.* 68 (1992), pages 580–583. DOI: 10.1103/PhysRevLett.68.580.

[Dec+20] W. Decking et al. "A MHz-repetition-rate hard X-ray free-electron laser driven by a superconducting linear accelerator". In: *Nature Photonics* 14 (2020), pages 391–397. DOI: 10.1038/s41566-020-0607-z.

[Dek+05] F. M. Dekking et al. *A Modern Introduction to Probability and Statistics*. Springer London. 2005. DOI: 10.1007/1-84628-168-7.

[DES25a] D. E.-S. DESY. *Key Parameters of Undulators Operated at PETRA III*. https://photon-science.desy.de/research/technical_groups/undulators/undulators_at_petraiii/index_eng.html. Accessed: 24.09.2025. 2025.

[DES25b] D. E.-S. DESY. *Unified Data Sheet P01*. https://photon-science.desy.de/facilities/petra_iii/beamlines/p01_dynamics/unified_data_sheet_p01/index_eng.html. Accessed: 24.08.2025. 2025.

[DH00] J. Duffin and C. Hayter. "Baring the sole. The rise and fall of the shoe-fitting fluoroscope". In: *Isis* 91 (2000), pages 260–282. DOI: 10.1086/384721.

[DiD64] J. DiDomenico M. "Small-Signal Analysis of Internal (Coupling-Type) Modulation of Lasers". In: *Journal of Applied Physics* 35 (1964), pages 2870–2876. DOI: 10.1063/1.1713121. eprint: https://pubs.aip.org/aip/jap/article-pdf/35/10/2870/18333136/2870_1_online.pdf.

[Dim+24] N. Dimarcq et al. "Roadmap towards the redefinition of the second". In: *Metrologia* 61 (2024), page 012001. DOI: 10.1088/1681-7575/ad17d2.

[Dir27] P. A. M. Dirac. "The quantum theory of the emission and absorption of radiation". In: *Proceedings of the Royal Society of London. Series A, Containing Papers of a Mathematical and Physical Character* 114 (1927), pages 243–265. DOI: 10.1098/rspa.1927.0039.

[DKW02] H. T. Dung, L. Knöll, and D.-G. Welsch. "Resonant dipole-dipole interaction in the presence of dispersing and absorbing surroundings". In: *Phys. Rev. A* 66 (2002), page 063810. DOI: 10.1103/PhysRevA.66.063810.

[DLE22a] O. Diekmann, D. Lentrodt, and J. Evers. "Inverse design approach to x-ray quantum optics with Mössbauer nuclei in thin-film cavities". In: *Phys. Rev. A* 105 (2022), page 013715. DOI: 10.1103/PhysRevA.105.013715.

[DLE22b] O. Diekmann, D. Lentrodt, and J. Evers. "Inverse design in nuclear quantum optics: From artificial x-ray multilevel schemes to spectral observables". In: *Phys. Rev. A* 106 (2022), page 053701. DOI: 10.1103/PhysRevA.106.053701.

[Dol+25] S. Dold et al. "Melting, Bubblelike Expansion, and Explosion of Superheated Plasmonic Nanoparticles". In: *Physical Review Letters* 134 (2025). DOI: 10.1103/physrevlett.134.136101.

[Don00] S. Doniach. "Fourth-generation X-ray sources: some possible applications to biology". In: *Journal of Synchrotron Radiation* 7 (2000), pages 116–120. DOI: 10.1107/S0909049500004143.

[Dys49] F. J. Dyson. "The Radiation Theories of Tomonaga, Schwinger, and Feynman". In: *Phys. Rev.* 75 (1949), pages 486–502. DOI: 10.1103/PhysRev.75.486.

[Edd31] A. S. Eddington. "The End of the World: from the Standpoint of Mathematical Physics*". In: *Nature* 127 (1931), pages 447–453. DOI: 10.1038/127447a0.

[Ein05] A. Einstein. "Über einem die Erzeugung und Verwandlung des Lichtes betreffenden heuristischen Gesichtspunkt". In: *Annalen der physik* 4 (1905).

[Elw+24] R. Elwell et al. "Laser Excitation of the ^{229}Th Nuclear Isomeric Transition in a Solid-State Host". In: *Phys. Rev. Lett.* 133 (2024), page 013201. DOI: 10.1103/PhysRevLett.133.013201.

[Emm+10] P. Emma et al. "First lasing and operation of an ångstrom-wavelength free-electron laser". In: *Nature Photonics* 4 (2010), pages 641–647. DOI: 10.1038/nphoton.2010.176.

[Eura] European XFEL. *fastAdc's documentation*. https://rtd.xfel.eu/docs/fastadc/en/latest/. Accessed: 26.08.2025.

[Eurb] European XFEL. *MID Instrument Specifications*. https://www.xfel.eu/facility/instruments/mid/instrument_specifications/index_eng.html. Accessed: 24.09.2025.

[Eurc] European XFEL. *Scantool documentation*. https://rtd.xfel.eu/docs/scantool/en/latest/. Accessed: 26.08.2025.

[Eur17] European XFEL. *Scientific Data Policy of European X-Ray Free-Electron Laser Facility GmbH*. https://www.xfel.eu/sites/sites_custom/site_xfel/content/e51499/e141242/e141245/xfel_file141246/upex-scientific-data-policy%5B1%5D_eng.pdf. Accessed: 25.04.2025. 2017.

[Eur23] European XFEL. *Scientific Data Policy of European X-Ray Free-Electron Laser Facility GmbH*. https://www.xfel.eu/sites/sites_custom/site_xfel/content/e51499/e141242/e141245/xfel_file234453/ScientificDataPolicy2023_eng.pdf. Accessed: 25.04.2025. 2023.

[EuXa] EuXFEL data analysis group. *DAMNIT*. https://damnit.readthedocs.io/en/latest/. Accessed: 22.04.2025.

[EuXb] EuXFEL data analysis group. *EXtra-data*. https://extra-data.readthedocs.io/en/latest/. Accessed: 22.04.2025.

[EuXc] EuXFEL data analysis group. *EXtra-foam's documentation*. https://extra-foam.readthedocs.io/en/latest/. Accessed: 18.04.2025.

[EuXd] EuXFEL data analysis group. *metropc's documentation*. https://rtd.xfel.eu/docs/metropc/en/latest/. Accessed: 14.04.2025.

[Fan+18] H. Fangohr et al. "Data Analysis Support in Karabo at European XFEL". In: *Proc. of International Conference on Accelerator and Large Experimental Control Systems (ICALEPCS'17), Barcelona, Spain, 8-13 October 2017* (Barcelona, Spain). International Conference on Accelerator and Large Experimental Control Systems. Geneva, Switzerland: JACoW, 2018, pages 245–252. DOI: 10.18429/JACoW-ICALEPCS2017-TUCPA01.

[Fel+97] J. Feldhaus et al. “Possible application of X-ray optical elements for reducing the spectral bandwidth of an X-ray SASE FEL”. In: *Optics Communications* 140 (1997), pages 341–352. DOI: 10.1016/S0030-4018(97)00163-6.

[Fey18] R. P. Feynman. “Simulating physics with computers”. In: *Feynman and computation*. cRc Press, 2018, pages 133–153. DOI: 10.1201/9780429500459.

[Fey49] R. P. Feynman. “Space-Time Approach to Quantum Electrodynamics”. In: *Phys. Rev.* 76 (1949), pages 769–789. DOI: 10.1103/PhysRev.76.769.

[FG53] R. E. FRANKLIN and R. G. GOSLING. “Molecular Configuration in Sodium Thymonucleate”. In: *Nature* 171 (1953), pages 740–741. DOI: 10.1038/171740a0.

[FIM05] M. Fleischhauer, A. Imamoglu, and J. P. Marangos. “Electromagnetically induced transparency: Optics in coherent media”. In: *Rev. Mod. Phys.* 77 (2005), pages 633–673. DOI: 10.1103/RevModPhys.77.633.

[FKL13] W. Friedrich, P. Knipping, and M. Laue. “Interferenzerscheinungen bei Röntgenstrahlen”. In: *Annalen der Physik* 346 (1913), pages 971–988. DOI: 10.1002/andp.19133461004.

[FLS63] R. P. Feynman, R. B. Leighton, and M. Sands. Addison-Wesley, Reading, MA. 1963.

[Fow+23] P. Fowler-Wright et al. “Determining the validity of cumulant expansions for central spin models”. In: *Phys. Rev. Res.* 5 (2023), page 033148. DOI: 10.1103/PhysRevResearch.5.033148.

[Fra+61] P. A. Franken et al. “Generation of Optical Harmonics”. In: *Phys. Rev. Lett.* 7 (1961), pages 118–119. DOI: 10.1103/PhysRevLett.7.118.

[Fra17] J. Fraunhofer. “Bestimmung des Brechungs- und des Farbenzerstreungs-Vermögens verschiedener Glasarten, in Bezug auf die Vervollkommnung achromatischer Fernröhre”. In: *Annalen der Physik* 56 (1817), pages 264–313. DOI: https://doi.org/10.1002/andp.18170560706.

[Fro+25] C. Fromonteil et al. *Non-local mass superpositions and optical clock interferometry in atomic ensemble quantum networks*. 2025. arXiv: 2509.19501 [quant-ph].

[Frö+91] D. Fröhlich et al. “Coherent propagation and quantum beats of quadrupole polaritons in Cu_2O”. In: *Phys. Rev. Lett.* 67 (1991), pages 2343–2346. DOI: 10.1103/PhysRevLett.67.2343.

[FS05] Z. Ficek and S. Swain. *Quantum interference and coherence: theory and experiments*. Springer, Heidelberg. 2005.

[FT02] Z. Ficek and R. Tanaś. “Entangled states and collective nonclassical effects in two-atom systems”. In: *Physics Reports* 372 (2002), pages 369–443. DOI: https://doi.org/10.1016/S0370-1573(02)00368-X.

[Fuc+25] E. Fuchs et al. “Searching for Dark Matter with the ^{229}Th Nuclear Lineshape from Laser Spectroscopy”. In: *Phys. Rev. X* 15 (2025), page 021055. DOI: 10.1103/PhysRevX.15.021055.

[Fuj+21] K. Fujiwara et al. “Quantum Interference of Totally Reflected Mössbauer γ-Rays from a 57Fe Monolayer Embedded in a Thin Film”. In: *Journal of the Physical Society of Japan* 90 (2021), page 084705. DOI: 10.7566/JPSJ.90.084705.

[Fun+24] L. Funke et al. *Capturing Nonlinear Electron Dynamics with Fully Characterised Attosecond X-ray Pulses*. 2024. arXiv: 2408.03858 [physics.optics].

[Gar+04] C. W. Gardiner et al. *Handbook of stochastic methods*. springer Berlin. 2004.

[GBT11] P. Gütlich, E. Bill, and A. X. Trautwein. *Mössbauer Spectroscopy and Transition Metal Chemistry*. Springer Berlin Heidelberg. 2011. DOI: 10.1007/978-3-540-88428-6.

[GE25] M. Gerharz and J. Evers. *Cumulant expansion approach to the decay dynamics of interacting Mössbauer nuclei after strong impulsive excitation*. 2025. arXiv: 2510.00970 [quant-ph].

[Geh86] N. Gehrels. “Confidence limits for small numbers of events in astrophysical data”. In: *The Astrophysical Journal* 303 (1986), page 336. DOI: 10.1086/164079.

[Gel20] G. Geloni. “Self-Seeded Free-Electron Lasers”. In: *Synchrotron Light Sources and Free-Electron Lasers: Accelerator Physics, Instrumentation and Science Applications*. Edited by E. J. Jaeschke et al. Cham: Springer International Publishing, 2020, pages 191–223. DOI: 10.1007/978-3-030-23201-6_4.

[Ger+25a] M. Gerharz et al. *Dark-fringe interferometer with dynamic phase control for Mössbauer science*. 2025. arXiv: 2509.24658 [quant-ph].

[Ger+25b] M. Gerharz et al. *Single-shot sorting of Mössbauer time-domain data at X-ray free electron lasers*. 2025. arXiv: 2509.15833 [quant-ph].

[Ger+85] E. Gerdau et al. “Nuclear Bragg diffraction of synchrotron radiation in yttrium iron garnet”. In: *Phys. Rev. Lett.* 54 (1985), pages 835–838. DOI: 10.1103/PhysRevLett.54.835.

[Ger21] M. Gerharz. “Temporal phase and polarization interferometry at x-ray energies”. Master’s Thesis. Ruprecht-Karls-Universität Heidelberg. 2021. Available online.

[GG71] N. N. Greenwood and T. C. Gibb. *Mössbauer Spectroscopy*. Springer Netherlands. 1971. DOI: 10.1007/978-94-009-5697-1.

[GH10] F. Gao and L. Han. “Implementing the Nelder-Mead simplex algorithm with adaptive parameters”. In: *Computational Optimization and Applications* 51 (2010), pages 259–277. DOI: 10.1007/s10589-010-9329-3.

[GH12] F. Gao and L. Han. “Implementing the Nelder-Mead simplex algorithm with adaptive parameters”. In: *Computational Optimization and Applications* 51 (2012), pages 259–277. DOI: 10.1007/s10589-010-9329-3.

[GH82] M. Gross and S. Haroche. “Superradiance: An essay on the theory of collective spontaneous emission”. In: *Physics Reports* 93 (1982), pages 301–396. DOI: https://doi.org/10.1016/0370-1573(82)90102-8.

[Glo+12] T. E. Glover et al. “X-ray and optical wave mixing”. In: *Nature* 488 (2012), pages 603–608. DOI: 10.1038/nature11340.

[Goe+19] S. Goerttler et al. “Time-Resolved sub-Ångström Metrology by Temporal Phase Interferometry near X-Ray Resonances of Nuclei”. In: *Phys. Rev. Lett.* 123 (2019), page 153902. DOI: 10.1103/PhysRevLett.123.153902.

[Goo15] J. Goodman. *Statistical Optics*. Wiley. 2015. ISBN: 9781119009450.

[Göp31] M. Göppert-Mayer. “Über Elementarakte mit zwei Quantensprüngen”. In: *Annalen der Physik* 401 (1931), pages 273–294. DOI: 10.1002/andp.19314010303.

[Gor+18] O. Y. Gorobtsov et al. “Seeded X-ray free-electron laser generating radiation with laser statistical properties”. In: *Nature communications* 9 (2018), page 4498. DOI: 10.1038/s41467-018-06743-8.

[Gra85] R. Graham. “Covariant stochastic calculus in the sense of Itô”. In: *Physics Letters A* 109 (1985), pages 209–212. DOI: 10.1016/0375-9601(85)90304-4.

[Gre+02] M. Greiner et al. “Quantum phase transition from a superfluid to a Mott insulator in a gas of ultracold atoms”. In: *Nature* 415 (2002), pages 39–44. DOI: 10.1038/415039a.

[Gre12] N. N. Greenwood. *Mössbauer spectroscopy*. Springer Science & Business Media. 2012.

[Gru+08] J. A. Gruetzmacher et al. “Assessing the dephasing dynamics of water from linear field-resolved pulse propagation experiments and simulations in highly absorbing solutions”. In: *The Journal of Chemical Physics* 129 (2008), page 224502. DOI: 10.1063/1.2990654.

[GV13] G. H. Golub and C. F. Van Loan. *Matrix Computations*. Johns Hopkins University Press, Baltimore, MD. 2013.

[GW99] E. Gerdau and H. de Waard (Ed.) *Nuclear Resonant Scattering of Synchrotron Radiation*. Hyperfine Int. 123-125. 1999.

[GZ04] C. Gardiner and P. Zoller. *Quantum Noise: A Handbook of Markovian and Non-Markovian Quantum Stochastic Methods with Applications to Quantum Optics*. Springer. 2004. ISBN: 9783540223016.

[GZT55] J. P. Gordon, H. J. Zeiger, and C. H. Townes. "The Maser—New Type of Microwave Amplifier, Frequency Standard, and Spectrometer". In: *Phys. Rev.* 99 (1955), pages 1264–1274. DOI: 10.1103/PhysRev.99.1264.

[Hab+16] J. Haber et al. "Collective strong coupling of X-rays and nuclei in a nuclear optical lattice". In: *Nature Photonics* 10 (2016), pages 445–449. DOI: 10.1038/nphoton.2016.77.

[Hab+17] J. Haber et al. "Rabi oscillations of X-ray radiation between two nuclear ensembles". In: *Nature Photonics* 11 (2017), pages 720–725. DOI: 10.1038/s41566-017-0013-3.

[Har+13] M. Harmand et al. "Achieving few-femtosecond time-sorting at hard X-ray free-electron lasers". In: *Nature Photonics* 7 (2013), pages 215–218. DOI: 10.1038/nphoton.2013.11.

[Har+18] N. Hartmann et al. "Attosecond time–energy structure of X-ray free-electron laser pulses". In: *Nature Photonics* 12 (2018), pages 215–220. DOI: 10.1038/s41566-018-0107-6.

[Har+23] M. Harmand et al. "Single-shot X-ray absorption spectroscopy at X-ray free electron lasers". In: *Scientific Reports* 13 (2023). DOI: 10.1038/s41598-023-44196-2.

[Has+91] J. B. Hastings et al. "Mössbauer spectroscopy using synchrotron radiation". In: *Phys. Rev. Lett.* 66 (1991), pages 770–773. DOI: 10.1103/PhysRevLett.66.770.

[Hau+19] S. Hauf et al. "The Karabo distributed control system". In: *Synchrotron Radiation* 26 (2019), pages 1448–1461.

[Hay+60] H. J. Hay et al. "Measurement of the Red Shift in an Accelerated System Using the Mössbauer Effect in Fe^{57}". In: *Phys. Rev. Lett.* 4 (1960), pages 165–166. DOI: 10.1103/PhysRevLett.4.165.

[HE13] K. P. Heeg and J. Evers. "X-ray quantum optics with Mössbauer nuclei embedded in thin-film cavities". In: *Phys. Rev. A* 88 (2013), page 043828. DOI: 10.1103/PhysRevA.88.043828.

[Hed+25] L. Hedewig et al. "State-resolved femtosecond phase control in dense-gas laser–atom interaction enabled by attosecond XUV interferometry". In: *Optics Letters* 50 (2025), page 3006. DOI: 10.1364/ol.559945.

[Hee+13] K. P. Heeg et al. "Vacuum-Assisted Generation and Control of Atomic Coherences at X-Ray Energies". In: *Phys. Rev. Lett.* 111 (2013), page 073601. DOI: 10.1103/PhysRevLett.111.073601.

[Hee+15a] K. P. Heeg et al. "Interferometric phase detection at x-ray energies via Fano resonance control". In: *Phys. Rev. Lett.* 114 (2015), page 207401. DOI: 10.1103/PhysRevLett.114.207401.

[Hee+15b] K. P. Heeg et al. "Tunable Subluminal Propagation of Narrow-band X-Ray Pulses". In: *Phys. Rev. Lett.* 114 (2015), page 203601. DOI: 10.1103/PhysRevLett.114.203601.

[Hee+17] K. P. Heeg et al. "Spectral narrowing of x-ray pulses for precision spectroscopy with nuclear resonances". In: *Science* 357 (2017), pages 375–378. DOI: 10.1126/science.aan3512.

[Hee+21] K. P. Heeg et al. "Coherent X-ray–optical control of nuclear excitons". In: *Nature* 590 (2021), pages 401–404. DOI: 10.1038/s41586-021-03276-x.

[Hee14] K. P. Heeg. "X-Ray Quantum Optics With Mössbauer Nuclei In Thin-Film Cavities". PhD thesis. Ruprecht-Karls-Universität, Heidelberg. 2014. DOI: 10.11588/HEIDOK.00017869.

[Hee19] K. P. Heeg. *Software package* PYNUSS. unpublished. 2019.

[Hel+91] P. Helistö et al. "Gamma echo". In: *Phys. Rev. Lett.* 66 (1991), pages 2037–2040. DOI: 10.1103/PhysRevLett.66.2037.

[Hen12] W. F. Henning. "Nuclear Physics Applications of the Mössbauer Effect". In: *The Rudolf Mössbauer Story: His Scientific Work and Its Impact on Science and History*. Edited by M. Kalvius and P. Kienle. Berlin, Heidelberg: Springer Berlin Heidelberg, 2012, pages 145–174. DOI: 10.1007/978-3-642-17952-5_9.

[HFP64] L. Hargrove, R. L. Fork, and M. Pollack. "Locking of He–Ne laser modes induced by synchronous intracavity modulation". In: *Applied Physics Letters* 5 (1964), pages 4–5. DOI: 10.1063/1.1754025.

[Hil11] J. M. Hilbe. *Negative binomial regression*. Cambridge University Press. 2011.

[Hin+98] P. M. Hinz et al. "Imaging circumstellar environments with a nulling interferometer". In: *Nature* 395 (1998), pages 251–253. DOI: 10.1038/26172.

[HJ01] T. Hauschild and M. Jentschel. "Comparison of maximum likelihood estimation and chi-square statistics applied to counting experiments". In: *Nuclear Instruments and Methods in Physics Research Section A: Accelerators, Spectrometers, Detectors and Associated Equipment* 457 (2001), pages 384–401. DOI: https://doi.org/10.1016/S0168-9002(00)00756-7.

[HKE16] K. P. Heeg, C. H. Keitel, and J. Evers. *Inducing and detecting collective population inversions of Mössbauer nuclei*. 2016. arXiv: 1607.04116 [quant-ph].

[HL25] W. Hippler and R. Lötzsch. private communication. 2025.

[HL83] H.-J. Hartmann and A. Laubereau. "Coherent pulse propagation in the infrared on the picosecond time scale". In: *Optics Communications* 47 (1983), pages 117–122. DOI: https://doi.org/10.1016/0030-4018(83)90098-6.

[HLN64] R. E. Holland, F. J. Lynch, and K.-E. Nystén. "Lifetimes of $d_{\frac{3}{2}}$ Hole States in Scandium Isotopes". In: *Phys. Rev. Lett.* 13 (1964), pages 241–243. DOI: 10.1103/PhysRevLett.13.241.

[HR94] R. G. Helmer and C. W. Reich. "An excited state of ^{229}Th at 3.5 eV". In: *Phys. Rev. C* 49 (1994), pages 1845–1858. DOI: 10.1103/PhysRevC.49.1845.

[HRR22] J. Huber, A. M. Rey, and P. Rabl. "Realistic simulations of spin squeezing and cooperative coupling effects in large ensembles of interacting two-level systems". In: *Phys. Rev. A* 105 (2022), page 013716. DOI: 10.1103/PhysRevA.105.013716.

[HS75] T. Hänsch and A. Schawlow. "Cooling of gases by laser radiation". In: *Optics Communications* 13 (1975), pages 68–69. DOI: https://doi.org/10.1016/0030-4018(75)90159-5.

[HT99] J. Hannon and G. Trammell. "Coherent γ-ray optics". In: *Hyperfine Interactions* 123–124 (1999), pages 127–274. DOI: 10.1023/a:1017011621007.

[Hua+20] X.-C. Huang et al. "Spacing-dependent electromagnetically induced transparency with two nuclear ensembles inside an x-ray planar cavity". In: *J. Opt. Soc. Am. B* 37 (2020), pages 745–755. DOI: 10.1364/JOSAB.377328.

[Hug68] W. Huggins. "XXI. Further observations on the spectra of some the stars and nebulæ, with an attempt to determine therefrom whether these bodies are moving towards or from the earth, also observations on the spectra of the sun and of comet II., 1868". In: *Philosophical Transactions of the Royal Society of London* 158 (1868), pages 529–564. DOI: 10.1098/rstl.1868.0022.

[Ino+19] I. Inoue et al. "Generation of narrow-band X-ray free-electron laser via reflection self-seeding". In: *Nature Photonics* 13 (2019), pages 319–322. DOI: 10.1038/s41566-019-0365-y.

[IP44] D. Iwanenko and I. Pomeranchuk. "On the Maximal Energy Attainable in a Betatron". In: *Phys. Rev.* 65 (1944), pages 343–343. DOI: 10.1103/PhysRev.65.343.

[Ish+12] T. Ishikawa et al. "A compact X-ray free-electron laser emitting in the sub-ångström region". In: *Nature Photonics* 6 (2012), pages 540–544. DOI: 10.1038/nphoton.2012.141.

[JB67] B. M. Johnstone and A. J. F. Boyle. "Basilar Membrane Vibration Examined with the Mössbauer Technique". In: *Science* 158 (1967), pages 389–390. DOI: 10.1126/science.158.3799.389.

[JNN12] J. Johansson, P. Nation, and F. Nori. "QuTiP: An open-source Python framework for the dynamics of open quantum systems". In: *Computer Physics Communications* 183 (2012), pages 1760–1772. DOI: 10.1016/j.cpc.2012.02.021.

[JNN13] J. Johansson, P. Nation, and F. Nori. "QuTiP 2: A Python framework for the dynamics of open quantum systems". In: *Computer Physics Communications* 184 (2013), pages 1234–1240. DOI: 10.1016/j.cpc.2012.11.019.

[Joh67] S. C. Johnson. "Hierarchical clustering schemes". In: *Psychometrika* 32 (1967), pages 241–254. DOI: 10.1007/BF02289588.

[Jr63] J. H. W. Jr. "Hierarchical Grouping to Optimize an Objective Function". In: *Journal of the American Statistical Association* 58 (1963), pages 236–244. DOI: 10.1080/01621459.1963.10500845.

[KAK79] Y. Kagan, A. M. Afanas'ev, and V. G. Kohn. "On excitation of isomeric nuclear states in a crystal by synchrotron radiation". In: *Journal of Physics C: Solid State Physics* 12 (1979), pages 615–631. DOI: 10.1088/0022-3719/12/3/027.

[Kan+17] H.-S. Kang et al. "Hard X-ray free-electron laser with femtosecond-scale timing jitter". In: *Nature Photonics* 11 (2017), pages 708–713. DOI: 10.1038/s41566-017-0029-8.

[KB60] G. Kirchhoff and R. Bunsen. "Chemische Analyse durch Spectralbeobachtungen". In: *Annalen der Physik* 186 (1860), pages 161–189. DOI: https://doi.org/10.1002/andp.18601860602.

[KB61] G. Kirchhoff and R. Bunsen. "Chemische Analyse durch Spectralbeobachtungen". In: *Annalen der Physik* 189 (1861), pages 337–381. DOI: https://doi.org/10.1002/andp.18611890702.

[KCP20] X. Kong, D. E. Chang, and A. Pálffy. "Green's-function formalism for resonant interaction of x rays with nuclei in structured media". In: *Phys. Rev. A* 102 (2020), page 033710. DOI: 10.1103/PhysRevA.102.033710.

[Kei74] B. Keisch. "Mössbauer effect studies of fine arts". In: *Le Journal de Physique Colloques* 35 (1974), pages C6–151–C6–164. DOI: 10.1051/jphyscol:1974614.

[KEK07] M. Kiffner, J. Evers, and C. H. Keitel. "Coherent control in a decoherence-free subspace of a collective multilevel system". In: *Phys. Rev. A* 75 (2007), page 032313. DOI: 10.1103/PhysRevA.75.032313.

[KHL17] K.-J. Kim, Z. Huang, and R. Lindberg. *Synchrotron Radiation and Free-Electron Lasers: Principles of Coherent X-Ray Generation*. Cambridge University Press. 2017. DOI: 10.1017/9781316677377.

[Kie+04] R. Kienberger et al. "Atomic transient recorder". In: *Nature* 427 (2004), pages 817–821. DOI: 10.1038/nature02277.

[Kif+10] M. Kiffner et al. "Vacuum-induced processes in multi-level atoms". In: *Progress in Optics*. Volume 55. Burlington: Elsevier Science, 2010, pages 85–197. DOI: 10.1016/B978-0-444-53705-8.00003-5.

[KK08] M. Kira and S. W. Koch. "Cluster-expansion representation in quantum optics". In: *Phys. Rev. A* 78 (2008), page 022102. DOI: 10.1103/PhysRevA.78.022102.

[KK17] E. Kuznetsova and O. Kocharovskaya. "Quantum optics with X-rays". In: *Nature Photonics* 11 (2017), pages 685–686. DOI: 10.1038/s41566-017-0034-y.

[KK18] P. Kirton and J. Keeling. "Superradiant and lasing states in driven-dissipative Dicke models". In: *New Journal of Physics* 20 (2018), page 015009. DOI: 10.1088/1367-2630/aaa11d.

[KK54] J. Kenney and E. Keeping. *Mathematics of Statistics*. Van Nostrand Company. 1954.

[KK86] A. Kocharovskaya and Y. I. Khanin. "Population trapping and coherent bleaching of a three-level medium by a periodic train of ultrashort pulses". In: *Zh. Eksp. Teor. Fiz* 90 (1986), pages 1610–1618.

[KKR99] O. Kocharovskaya, R. Kolesov, and Y. Rostovtsev. "Coherent Optical Control of Mössbauer Spectra". In: *Phys. Rev. Lett.* 82 (1999), pages 3593–3596. DOI: 10.1103/PhysRevLett.82.3593.

[Kli+03] G. Klingelhöfer et al. "Athena MIMOS II Mössbauer spectrometer investigation". In: *Journal of Geophysical Research: Planets* 108 (2003). DOI: https://doi.org/10.1029/2003JE002138.

[Kli+04] G. Klingelhöfer et al. "Jarosite and Hematite at Meridiani Planum from Opportunity's Mössbauer Spectrometer". In: *Science* 306 (2004), pages 1740–1745. DOI: 10.1126/science.1104653.

[Klo+23] C. Klose et al. “Coherent correlation imaging for resolving fluctuating states of matter”. In: *Nature* 614 (2023), pages 256–261. DOI: 10.1038/s41586-022-05537-9.

[Koc92] O. Kocharovskaya. “Amplification and lasing without inversion”. In: *Physics Reports* 219 (1992), pages 175–190. DOI: https://doi.org/10.1016/0370-1573(92)90135-M.

[Kon+25] X. Kong et al. “Multiphoton emission of x-rays from cooperative resonant nuclei”. In: *Phys. Rev. Res.* 7 (2025), page 013030. DOI: 10.1103/PhysRevResearch.7.013030.

[KP16] X. Kong and A. Pálffy. “Stopping Narrow-Band X-Ray Pulses in Nuclear Media”. In: *Phys. Rev. Lett.* 116 (2016), page 197402. DOI: 10.1103/PhysRevLett.116.197402.

[KR05] L. Kaufman and P. J. Rousseeuw. *Finding groups in data: an introduction to cluster analysis*. John Wiley & Sons. 2005. DOI: 10.1002/9780470316801.

[KR15] S. Krämer and H. Ritsch. “Generalized mean-field approach to simulate the dynamics of large open spin ensembles with long range interactions”. In: *The European Physical Journal D* 69 (2015). DOI: 10.1140/epjd/e2015-60266-5.

[KR76] L. Kroger and C. Reich. “Features of the low-energy level scheme of 229Th as observed in the α-decay of 233U”. In: *Nuclear Physics A* 259 (1976), pages 29–60. DOI: https://doi.org/10.1016/0375-9474(76)90494-2.

[Kre+05] C. Krebs et al. “Rapid freeze-quench ^{57}Fe Mössbauer spectroscopy: monitoring changes of an iron-containing active site during a biochemical reaction”. In: *Inorganic chemistry* 44 (2005), pages 742–757. DOI: 10.1021/ic0485231.

[KS60] O. C. Kistner and A. W. Sunyar. “Evidence for Quadrupole Interaction of Fe^{57m}, and Influence of Chemical Binding on Nuclear Gamma-Ray Energy”. In: *Phys. Rev. Lett.* 4 (1960), pages 412–415. DOI: 10.1103/PhysRevLett.4.412.

[KSR08] K.-J. Kim, Y. Shvyd’ko, and S. Reiche. “A Proposal for an X-Ray Free-Electron Laser Oscillator with an Energy-Recovery Linac”. In: *Phys. Rev. Lett.* 100 (2008), page 244802. DOI: 10.1103/PhysRevLett.100.244802.

[Kub62] R. Kubo. “Generalized cumulant expansion method”. In: *Journal of the Physical Society of Japan* 17 (1962), pages 1100–1120. DOI: 10.1143/JPSJ.17.1100.

[Kuj+20] N. Kujala et al. “Hard x-ray single-shot spectrometer at the European X-ray Free-Electron Laser”. In: *Review of Scientific Instruments* 91 (2020), page 103101. DOI: 10.1063/5.0019935.

[Kun+97] Y. Kunimune et al. “Two-Photon Correlations in X-rays from a Synchrotron Radiation Source”. In: *Journal of Synchrotron Radiation* 4 (1997), pages 199–203. DOI: 10.1107/S0909049597006912.

[Kün63] W. Kündig. “Measurement of the Transverse Doppler Effect in an Accelerated System”. In: *Phys. Rev.* 129 (1963), pages 2371–2375. DOI: 10.1103/PhysRev.129.2371.

[Kuz+24] E. Kuznetsova et al. “Spectral Flux Enhancement of X Rays for Addressing Ultranarrow Nuclear Transitions”. In: *Phys. Rev. Lett.* 133 (2024), page 193401. DOI: 10.1103/PhysRevLett.133.193401.

[LAL25] S.-Y. Lee, S. Ahrens, and W.-T. Liao. “Gravitationally sensitive structured x-ray optics using nuclear resonances”. In: *Phys. Rev. Res.* 7 (2025), page 013158. DOI: 10.1103/PhysRevResearch.7.013158.

[Law] Lawrence Livermore National Lab. *Using El Capitan Systems: Hardware Overview*. https://hpc.llnl.gov/documentation/user-guides/using-el-capitan-systems/hardware-overview. Accessed: 06.06.2025.

[LCL] LCLS. *Projected Run 26 LCLS FEL Parameters – Update June 18, 2025*. https://lcls.slac.stanford.edu/sites/default/files/2025-06/LCLS-Parameters-Run-26.pdf. Accessed: 24.09.2025.

[LE20] D. Lentrodt and J. Evers. “Ab Initio Few-Mode Theory for Quantum Potential Scattering Problems”. In: *Phys. Rev. X* 10 (2020), page 011008. DOI: 10.1103/PhysRevX.10.011008.

[Len+20] D. Lentrodt et al. “Ab initio quantum models for thin-film x-ray cavity QED”. In: *Phys. Rev. Res.* 2 (2020), page 023396. DOI: 10.1103/PhysRevResearch.2.023396.

[Len21] D. Lentrodt. “Ab initio approaches to x-ray cavity QED - From multi-mode theory to nonlinear dynamics of Mössbauer nuclei”. PhD thesis. Ruprecht-Karls-Universität, Heidelberg. 2021. DOI: 10.11588/HEIDOK.00030671.

[Lew+94] M. Lewenstein et al. “Theory of high-harmonic generation by low-frequency laser fields”. In: *Phys. Rev. A* 49 (1994), pages 2117–2132. DOI: 10.1103/PhysRevA.49.2117.

[LI01] M. D. Lukin and A. Imamoğlu. “Controlling photons using electromagnetically induced transparency”. In: *Nature* 413 (2001), pages 273–276. DOI: 10.1038/35095000.

[Lia14] W.-T. Liao. *Coherent Control of Nuclei and X-Rays*. Springer International Publishing. 2014. DOI: 10.1007/978-3-319-02120-1.

[Lin+22] P.-H. Lin et al. “Time-Delayed Magnetic Control of X-ray Spectral Enhancement in Two-Target Nuclear Forward Scattering”. In: *Phys. Rev. Applied* 18 (2022), page L051001. DOI: 10.1103/PhysRevApplied.18.L051001.

[Liu+23] S. Liu et al. “Cascaded hard X-ray self-seeded free-electron laser at megahertz repetition rate”. In: *Nature Photonics* 17 (2023), pages 984–991. DOI: 10.1038/s41566-023-01305-x.

[Liu+25a] P. Liu et al. *Probing the Linewidth of the 12.4-keV Solid-State ^{45}Sc Isomeric Resonance*. 2025. arXiv: 2508.17538 [quant-ph].

[Liu+25b] S. Liu et al. “Updates on the Hard X-Ray Self-Seeding at the European XFEL”. In: *Synchrotron Radiation News* 38 (2025), pages 11–16. DOI: 10.1080/08940886.2025.2472607.

[LKE16] P. Longo, C. H. Keitel, and J. Evers. “Tailoring superradiance to design artificial quantum systems”. In: *Scientific Reports* 6 (2016). DOI: 10.1038/srep23628.

[LKE25a] D. Lentrodt, C. H. Keitel, and J. Evers. “Excitation of narrow x-ray transitions in thin-film cavities by focused pulses”. In: *Phys. Rev. A* 112 (2025), page 013711. DOI: 10.1103/PhysRevA.112.013711.

[LKE25b] D. Lentrodt, C. H. Keitel, and J. Evers. “Toward Nonlinear Optics with Mössbauer Nuclei Using X-Ray Cavities”. In: *Phys. Rev. Lett.* 135 (2025), page 033801. DOI: 10.1103/1lcz-r8d3.

[Llo+22] X. Llopart et al. “Timepix4, a large area pixel detector readout chip which can be tiled on 4 sides providing sub-200 ps timestamp binning”. In: *Journal of Instrumentation* 17 (2022), page C01044. DOI: 10.1088/1748-0221/17/01/C01044.

[LM28] G. Landsberg and L. Mandelstam. “Über die Lichtzerstreuung in Kristallen”. In: *Zeitschrift für Physik* 50 (1928), pages 769–780. DOI: 10.1007/bf01339412.

[LMS17] W. D. Loveland, D. J. Morrissey, and G. T. Seaborg. *Modern Nuclear Chemistry*. John Wiley & Sons, Ltd. 2017. DOI: https://doi.org/10.1002/9781119348450.

[Loh+25a] L. M. Lohse et al. “Collective Nuclear Excitation and Pulse Propagation in Single-Mode X-Ray Waveguides”. In: *Phys. Rev. Lett.* 135 (2025), page 053601. DOI: 10.1103/r2hf-9qn9.

[Loh+25b] L. M. Lohse et al. *Interferometric measurement of nuclear resonant phase shift with a nanoscale Young double waveguide*. 2025. arXiv: 2506.05823 [physics.optics].

[LP17] W.-T. Liao and A. Pálffy. “Optomechanically induced transparency of x-rays via optical control”. In: *Scientific Reports* 7 (2017), page 321. DOI: 10.1038/s41598-017-00428-w.

[LPK11] W.-T. Liao, A. Pálffy, and C. H. Keitel. “Nuclear coherent population transfer with X-ray laser pulses”. In: *Physics Letters B* 705 (2011), pages 134–138. DOI: https://doi.org/10.1016/j.physletb.2011.09.107.

[LPK12] W.-T. Liao, A. Pálffy, and C. H. Keitel. “Coherent Storage and Phase Modulation of Single Hard-X-Ray Photons Using Nuclear Excitons”. In: *Phys. Rev. Lett.* 109 (2012), page 197403. DOI: 10.1103/PhysRevLett.109.197403.

[LPK13] W.-T. Liao, A. Pálffy, and C. H. Keitel. “Three-beam setup for coherently controlling nuclear-state population”. In: *Phys. Rev. C* 87 (2013), page 054609. DOI: 10.1103/PhysRevC.87.054609.

[LR47] W. E. Lamb and R. C. Retherford. “Fine Structure of the Hydrogen Atom by a Microwave Method”. In: *Phys. Rev.* 72 (1947), pages 241–243. DOI: 10.1103/PhysRev.72.241.

[Lud+15] A. D. Ludlow et al. “Optical atomic clocks”. In: *Rev. Mod. Phys.* 87 (2015), pages 637–701. DOI: 10.1103/RevModPhys.87.637.

[Mad+21] A. Madsen et al. “Materials Imaging and Dynamics (MID) instrument at the European X-ray Free-Electron Laser Facility”. In: *Journal of Synchrotron Radiation* 28 (2021), pages 637–649. DOI: 10.1107/S1600577521001302.

[Mai60] T. H. Maiman. “Stimulated Optical Radiation in Ruby”. In: *Nature* 187 (1960), pages 493–494. DOI: 10.1038/187493a0.

[Mal+19] T. Maltezopoulos et al. “Operation of X-ray gas monitors at the European XFEL”. In: *Journal of Synchrotron Radiation* 26 (2019), pages 1045–1051. DOI: 10.1107/S1600577519003795.

[Mar+11] B. Marx et al. “Determination of high-purity polarization state of X-rays”. In: *Optics Communications* 284 (2011), pages 915–918. DOI: https://doi.org/10.1016/j.optcom.2010.10.054.

[Mar+21] B. Marx-Glowna et al. “Advanced X-ray polarimeter design for nuclear resonant scattering”. In: *Journal of Synchrotron Radiation* 28 (2021), pages 120–124. DOI: 10.1107/S1600577520015295.

[Mar+23] R. Margraf et al. “Low-loss stable storage of 1.2 Å X-ray pulses in a 14 m Bragg cavity”. In: *Nature Photonics* 17 (2023), pages 878–882. DOI: 10.1038/s41566-023-01267-0.

[Mar25] B. Marx-Glowna. private communication. 2025.

[MCD17] M. T. Manzoni, D. E. Chang, and J. S. Douglas. “Simulating quantum light propagation through atomic ensembles using matrix product states”. In: *Nature Communications* 8 (2017). DOI: 10.1038/s41467-017-01416-4.

[MCD93] K. Mølmer, Y. Castin, and J. Dalibard. “Monte Carlo wave-function method in quantum optics”. In: *J. Opt. Soc. Am. B* 10 (1993), pages 524–538. DOI: 10.1364/JOSAB.10.000524.

[Mer+24] L. Mercadier et al. “Transient absorption of warm dense matter created by an X-ray free-electron laser”. In: *Nature Physics* 20 (2024), pages 1564–1569. DOI: 10.1038/s41567-024-02587-w.

[Mer+25] A. Mercurio et al. *QuantumToolbox.jl: An efficient Julia framework for simulating open quantum systems*. 2025. arXiv: 2504.21440 [quant-ph].

[MF23] C. D. Mink and M. Fleischhauer. “Collective radiative interactions in the discrete truncated Wigner approximation”. In: *SciPost Phys.* 15 (2023), page 233. DOI: 10.21468/SciPostPhys.15.6.233.

[MH62] F. J. McClung and R. W. Hellwarth. “Giant Optical Pulsations from Ruby”. In: *Appl. Opt.* 1 (1962), pages 103–105. DOI: 10.1364/AO.1.S1.000103.

[MH67] S. L. McCall and E. L. Hahn. “Self-Induced Transparency by Pulsed Coherent Light”. In: *Phys. Rev. Lett.* 18 (1967), pages 908–911. DOI: 10.1103/PhysRevLett.18.908.

[Moe+07] D. L. Moehring et al. “Entanglement of single-atom quantum bits at a distance”. In: *Nature* 449 (2007), pages 68–71. DOI: 10.1038/nature06118.

[Mon+95] C. Monroe et al. “Demonstration of a Fundamental Quantum Logic Gate”. In: *Phys. Rev. Lett.* 75 (1995), pages 4714–4717. DOI: 10.1103/PhysRevLett.75.4714.

[Mos13] H. Moseley. “The high-frequency spectra of the elements”. In: *The London, Edinburgh, and Dublin Philosophical Magazine and Journal of Science* 26 (1913), pages 1024–1034. DOI: 10.1080/14786441308635052.

[Mös58] R. L. Mössbauer. “Kernresonanzfluoreszenz von Gammastrahlung in Ir^{191}”. In: *Zeitschrift für Physik* 151 (1958), pages 124–143. DOI: 10.1007/bf01344210.

[Moz+12] A. Mozzanica et al. “The GOTTHARD charge integrating readout detector: design and characterization”. In: *Journal of Instrumentation* 7 (2012), page C01019. DOI: 10.1088/1748-0221/7/01/C01019.

[MPF22] C. D. Mink, D. Petrosyan, and M. Fleischhauer. "Hybrid discrete-continuous truncated Wigner approximation for driven, dissipative spin systems". In: *Phys. Rev. Res.* 4 (2022), page 043136. DOI: 10.1103/PhysRevResearch.4.043136.

[MR11] G. Margaritondo and P. Rebernik Ribic. "A simplified description of X-ray free-electron lasers". In: *Journal of Synchrotron Radiation* 18 (2011), pages 101–108. DOI: 10.1107/s090904951004896x.

[Muk+15] D. Mukhopadhyay et al. "X-ray photonic microsystems for the manipulation of synchrotron light". In: *Nature Communications* 6 (2015), page 7057. DOI: 10.1038/ncomms8057.

[NA85] N. Nayak and G. S. Agarwal. "Absorption and fluorescence in frequency-modulated fields under conditions of strong modulation and saturation". In: *Phys. Rev. A* 31 (1985), pages 3175–3182. DOI: 10.1103/PhysRevA.31.3175.

[Nag+09] B. Nagler et al. "Turning solid aluminium transparent by intense soft X-ray photoionization". In: *Nature Physics* 5 (2009), pages 693–696. DOI: 10.1038/nphys1341.

[Nam+21] I. Nam et al. "High-brightness self-seeded X-ray free-electron laser covering the 3.5 keV to 14.6 keV range". In: *Nature Photonics* 15 (2021), pages 435–441. DOI: 10.1038/s41566-021-00777-z.

[Naz+25] A. Nazeeri et al. *Coupling of a nuclear transition to a Surface Acoustic Wave*. 2025. arXiv: 2509.02750 [quant-ph].

[NC10] M. A. Nielsen and I. L. Chuang. *Quantum Computation and Quantum Information: 10th Anniversary Edition*. Cambridge University Press. 2010.

[Neu+00] R. Neutze et al. "Potential for biomolecular imaging with femtosecond X-ray pulses". In: *Nature* 406 (2000), pages 752–757. DOI: 10.1038/35021099.

[Nie+05] N. C. Nielsen et al. "Phase Evolution of Solitonlike Optical Pulses during Excitonic Rabi Flopping in a Semiconductor". In: *Phys. Rev. Lett.* 94 (2005), page 057406. DOI: 10.1103/PhysRevLett.94.057406.

[Oka+19] S. Okaba et al. "Superradiance from lattice-confined atoms inside hollow core fibre". In: *Communications Physics* 2 (2019). DOI: 10.1038/s42005-019-0237-2.

[Pau+01] P. M. Paul et al. "Observation of a Train of Attosecond Pulses from High Harmonic Generation". In: *Science* 292 (2001), pages 1689–1692. DOI: 10.1126/science.1059413.

[PCC99] A. Peters, K. Y. Chung, and S. Chu. "Measurement of gravitational acceleration by dropping atoms". In: *Nature* 400 (1999), pages 849–852. DOI: 10.1038/23655.

[PHR22] D. Plankensteiner, C. Hotter, and H. Ritsch. "QuantumCumulants.jl: A Julia framework for generalized mean-field equations in open quantum systems". In: *Quantum* 6 (2022), page 617. DOI: 10.22331/q-2022-01-04-617.

[Piñ+17] A. Piñeiro Orioli et al. "Nonequilibrium dynamics of spin-boson models from phase-space methods". In: *Phys. Rev. A* 96 (2017), page 033607. DOI: 10.1103/PhysRevA.96.033607.

[PK98] M. B. Plenio and P. L. Knight. "The quantum-jump approach to dissipative dynamics in quantum optics". In: *Rev. Mod. Phys.* 70 (1998), pages 101–144. DOI: 10.1103/RevModPhys.70.101.

[PKE09] A. Pálffy, C. H. Keitel, and J. Evers. "Single-Photon Entanglement in the keV Regime via Coherent Control of Nuclear Forward Scattering". In: *Phys. Rev. Lett.* 103 (2009), page 017401. DOI: 10.1103/PhysRevLett.103.017401.

[Pla01] M. Planck. "Über das Gesetz der Energieverteilung im Normalspectrum". In: *Annalen der Physik* 309 (1901), pages 553–563. DOI: https://doi.org/10.1002/andp.19013090310.

[PM82] W. D. Phillips and H. Metcalf. "Laser Deceleration of an Atomic Beam". In: *Phys. Rev. Lett.* 48 (1982), pages 596–599. DOI: 10.1103/PhysRevLett.48.596.

[PO15] E. Peik and M. Okhapkin. "Nuclear clocks based on resonant excitation of γ-transitions". In: *Comptes Rendus. Physique* 16 (2015), pages 516–523. DOI: 10.1016/j.crhy.2015.02.007.

[Pot+01] W. Potzel et al. "Investigation of radiative coupling and of enlarged decay rates of nuclear oscillators". In: *Phys. Rev. A* 63 (2001), page 043810. DOI: 10.1103/PhysRevA.63.043810.

[Pot+12] V. Potapkin et al. "The ^{57}Fe Synchrotron Mössbauer Source at the ESRF". In: *Journal of Synchrotron Radiation* 19 (2012), pages 559–569. DOI: 10.1107/S0909049512015579.

[PR59] R. V. Pound and G. A. Rebka. "Gravitational Red-Shift in Nuclear Resonance". In: *Phys. Rev. Lett.* 3 (1959), pages 439–441. DOI: 10.1103/PhysRevLett.3.439.

[PR60] R. V. Pound and G. A. Rebka. "Apparent Weight of Photons". In: *Phys. Rev. Lett.* 4 (1960), pages 337–341. DOI: 10.1103/PhysRevLett.4.337.

[PRK16] L. Pucci, A. Roy, and M. Kastner. "Simulation of quantum spin dynamics by phase space sampling of Bogoliubov-Born-Green-Kirkwood-Yvon trajectories". In: *Phys. Rev. B* 93 (2016), page 174302. DOI: 10.1103/PhysRevB.93.174302.

[Raa+87] E. L. Raab et al. "Trapping of Neutral Sodium Atoms with Radiation Pressure". In: *Phys. Rev. Lett.* 59 (1987), pages 2631–2634. DOI: 10.1103/PhysRevLett.59.2631.

[Rac+15] D. S. Rackstraw et al. "Saturable Absorption of an X-Ray Free-Electron-Laser Heated Solid-Density Aluminum Plasma". In: *Phys. Rev. Lett.* 114 (2015), page 015003. DOI: 10.1103/PhysRevLett.114.015003.

[Rau+25] P. Rauer et al. "Lasing of a Cavity Based X-ray Source". In: (2025). Preprint available at Research Square. DOI: 10.21203/rs.3.rs-7274597/v1.

[RE21] R. Röhlsberger and J. Evers. "Quantum Optical Phenomena in Nuclear Resonant Scattering". In: *Modern Mössbauer Spectroscopy: New Challenges Based on Cutting-Edge Techniques*. Edited by Y. Yoshida and G. Langouche. Singapore: Springer Singapore, 2021, pages 105–171. DOI: 10.1007/978-981-15-9422-9_3.

[Rec78] I. Rechenberg. "Evolutionsstrategien". In: *Simulationsmethoden in der Medizin und Biologie: Workshop, Hannover, 29. Sept.–1. Okt. 1977*. Springer. 1978, pages 83–114.

[Red+13] L. Redecke et al. "Natively Inhibited Trypanosoma brucei Cathepsin B Structure Determined by Using an X-ray Laser". In: *Science* 339 (2013), pages 227–230. DOI: 10.1126/science.1229663.

[Rei14] P. Reiser. "Time domain control of x-ray quantum dynamics". Master's thesis. Ruprecht-Karls-Universität Heidelberg. 2014.

[RES14] R. Röhlsberger, J. Evers, and S. Shwartz. "Quantum and Nonlinear Optics with Hard X-Rays". In: *Synchrotron Light Sources and Free-Electron Lasers: Accelerator Physics, Instrumentation and Science Applications*. Edited by E. Jaeschke et al. Cham: Springer International Publishing, 2014, pages 1–28. DOI: 10.1007/978-3-319-04507-8_32-1.

[RK28] C. V. Raman and K. S. Krishnan. "A New Type of Secondary Radiation". In: *Nature* 121 (1928), pages 501–502. DOI: 10.1038/121501c0.

[RL24] G. B. Rybicki and A. P. Lightman. *Radiative processes in astrophysics*. John Wiley & Sons. 2024.

[RM73] E. Rowe and F. E. Mills. "Tantalus. 1. A dedicated storage ring synchrotron radiation source". In: *Part. Accel.* 4 (1973), pages 211–227.

[Röh+00] R. Röhlsberger et al. "Coherent Resonant X-Ray Scattering from a Rotating Medium". In: *Phys. Rev. Lett.* 84 (2000), pages 1007–1010. DOI: 10.1103/PhysRevLett.84.1007.

[Röh+10] R. Röhlsberger et al. "Collective Lamb Shift in Single-Photon Superradiance". In: *Science* 328 (2010), pages 1248–1251. DOI: 10.1126/science.1187770.

[Roh+12] N. Rohringer et al. "Atomic inner-shell X-ray laser at 1.46 nanometres pumped by an X-ray free-electron laser". In: *Nature* 481 (2012), pages 488–491. DOI: 10.1038/nature10721.

[Röh+12] R. Röhlsberger et al. "Electromagnetically induced transparency with resonant nuclei in a cavity". In: *Nature* 482 (2012), pages 199–203. DOI: 10.1038/nature10741.

[Röh+92] R. Röhlsberger et al. "Broad-Band Nuclear Resonant Filters for Synchrotron Radiation: a New Source for Nuclear Diffraction Experiments". In: *Europhysics Letters (EPL)* 18 (1992), pages 561–566. DOI: 10.1209/0295-5075/18/6/015.

[Röh04] R. Röhlsberger. *Coherent Elastic Nuclear Resonant Scattering*. Springer, Berlin, Heidelberg. 2004.

[Rön96] W. C. Röntgen. "On a New Kind of Rays". In: *Science* 3 (1896), pages 227–231. DOI: 10.1126/science.3.59.227.

[Ros+08] T. Rosenband et al. "Frequency Ratio of Al^+ and Hg^+ Single-Ion Optical Clocks; Metrology at the 17th Decimal Place". In: *Science* 319 (2008), pages 1808–1812. DOI: 10.1126/science.1154622.

[Rou87] P. J. Rousseeuw. "Silhouettes: A graphical aid to the interpretation and validation of cluster analysis". In: *Journal of Computational and Applied Mathematics* 20 (1987), pages 53–65. DOI: https://doi.org/10.1016/0377-0427(87)90125-7.

[ROY23] O. Rubies-Bigorda, S. Ostermann, and S. F. Yelin. "Characterizing superradiant dynamics in atomic arrays via a cumulant expansion approach". In: *Phys. Rev. Res.* 5 (2023), page 013091. DOI: 10.1103/PhysRevResearch.5.013091.

[RS12] F. Reiter and A. S. Sørensen. "Effective operator formalism for open quantum systems". In: *Phys. Rev. A* 85 (2012), page 032111. DOI: 10.1103/PhysRevA.85.032111.

[RS21] F. Robicheaux and D. A. Suresh. "Beyond lowest order mean-field theory for light interacting with atom arrays". In: *Phys. Rev. A* 104 (2021), page 023702. DOI: 10.1103/PhysRevA.104.023702.

[RSW19] J. Rossbach, J. R. Schneider, and W. Wurth. "10 years of pioneering X-ray science at the Free-Electron Laser FLASH at DESY". In: *Physics Reports* 808 (2019), pages 1–74. DOI: 10.1016/j.physrep.2019.02.002.

[Rub74] S. L. Ruby. "Mössbauer experiments without conventional sources". In: *Le Journal de Physique Colloques* 35 (1974), pages C6–209–C6–211. DOI: 10.1051/jphyscol:1974623.

[Ryd90] J. Rydberg. *Recherches sur la constitution des spectres d'émission des éléments chimiques*. Kungliga Vetenskapsakademien. 1890.

[Sad+21] S. Sadashivaiah et al. "High-Repetition Rate Optical Pump–Nuclear Resonance Probe Experiments Identify Transient Molecular Vibrations after Photoexcitation of a Spin Crossover Material". In: *The Journal of Physical Chemistry Letters* 12 (2021). PMID: 33764073, pages 3240–3245. DOI: 10.1021/acs.jpclett.0c03733.

[Saf+18] M. S. Safronova et al. "Search for new physics with atoms and molecules". In: *Rev. Mod. Phys.* 90 (2018), page 025008. DOI: 10.1103/RevModPhys.90.025008.

[Sak+17] S. Sakshath et al. "Optical pump - nuclear resonance probe experiments on spin crossover complexes". In: *Hyperfine Interactions* 238 (2017), page 89. DOI: 10.1007/s10751-017-1461-3.

[SB00] M. Shapiro and P. Brumer. "Coherent Control of Atomic, Molecular, and Electronic Processes". In: edited by B. Bederson and H. Walther. Volume 42. Advances In Atomic, Molecular, and Optical Physics. Academic Press, 2000, pages 287–345. DOI: 10.1016/S1049-250X(08)60189-5.

[SBH93] D. P. Siddons, U. Bergmann, and J. B. Hastings. "Time-dependent polarization in Mössbauer experiments with synchrotron radiation: Suppression of electronic scattering". In: *Phys. Rev. Lett.* 70 (1993), pages 359–362. DOI: 10.1103/PhysRevLett.70.359.

[SBH99] D. P. Siddons, U. Bergmann, and J. B. Hastings. "Polarization effects in resonant nuclear scattering". In: *Hyperfine Interactions* 123 (1999), pages 681–719. DOI: 10.1023/A:1017096512347.

[Sch+02] P. Schindelmann et al. "Radiative decoupling and coupling of nuclear oscillators by stepwise Doppler-energy shifts". In: *Phys. Rev. A* 65 (2002), page 023804. DOI: 10.1103/PhysRevA.65.023804.

[Sch+17] R. Schneider et al. "Quantum imaging with incoherently scattered light from a free-electron laser". In: *Nature Physics* 14 (2017), pages 126–129. DOI: 10.1038/nphys4301.

[Sch11] U. Schollwöck. "The density-matrix renormalization group in the age of matrix product states". In: *Annals of Physics* 326 (2011). January 2011 Special Issue, pages 96–192. DOI: https://doi.org/10.1016/j.aop.2010.09.012.

[Sch15] I. Schlichting. "Serial femtosecond crystallography: the first five years". In: *IUCrJ* 2 (2015), pages 246–255. DOI: 10.1107/S205225251402702X.

[Sch48] J. Schwinger. "Quantum Electrodynamics. I. A Covariant Formulation". In: *Phys. Rev.* 74 (1948), pages 1439–1461. DOI: 10.1103/PhysRev.74.1439.

[Sco15] D. W. Scott. *Multivariate density estimation: theory, practice, and visualization*. John Wiley & Sons. 2015.

[Scu+06] M. O. Scully et al. "Directed Spontaneous Emission from an Extended Ensemble of N Atoms: Timing Is Everything". In: *Phys. Rev. Lett.* 96 (2006), page 010501. DOI: 10.1103/PhysRevLett.96.010501.

[Scu09] M. O. Scully. "Collective Lamb Shift in Single Photon Dicke Superradiance". In: *Phys. Rev. Lett.* 102 (2009), page 143601. DOI: 10.1103/PhysRevLett.102.143601.

[Sei+11] M. M. Seibert et al. "Single mimivirus particles intercepted and imaged with an X-ray laser". In: *Nature* 470 (2011), pages 78–81. DOI: 10.1038/nature09748.

[Ser+06] I. Sergueev et al. "Synchrotron-radiation-based perturbed angular correlations used in the investigation of rotational dynamics in soft matter". In: *Phys. Rev. B* 73 (2006), page 024203. DOI: 10.1103/PhysRevB.73.024203.

[Set+95] M. Seto et al. "Observation of Nuclear Resonant Scattering Accompanied by Phonon Excitation Using Synchrotron Radiation". In: *Phys. Rev. Lett.* 74 (1995), pages 3828–3831. DOI: 10.1103/PhysRevLett.74.3828.

[She+04] G. Shen et al. "Phonon density of states in iron at high pressures and high temperatures". In: *Physics and Chemistry of Minerals* 31 (2004). DOI: 10.1007/s00269-004-0403-1.

[She12] G. Shenoy. "Dreams with synchrotron radiation". In: *The Rudolf Mössbauer Story: His Scientific Work and Its Impact on Science and History*. Edited by G. Kalvius and P. Kienle. Berlin, Heidelberg: Springer, 2012.

[She97] W. F. Sheppard. "On the Calculation of the most Probable Values of Frequency-Constants, for Data arranged according to Equidistant Division of a Scale". In: *Proceedings of the London Mathematical Society* s1-29 (1897), pages 353–380. DOI: https://doi.org/10.1112/plms/s1-29.1.353.

[Shv+03] Y. V. Shvyd'ko et al. "X-Ray Interferometry with Microelectronvolt Resolution". In: *Phys. Rev. Lett.* 90 (2003), page 013904. DOI: 10.1103/PhysRevLett.90.013904.

[Shv+23] Y. Shvyd'ko et al. "Resonant X-ray excitation of the nuclear clock isomer 45Sc". In: *Nature* 622 (2023), pages 471–475. DOI: 10.1038/s41586-023-06491-w.

[Shv+96] Y. V. Shvyd'ko et al. "Storage of Nuclear Excitation Energy through Magnetic Switching". In: *Phys. Rev. Lett.* 77 (1996), pages 3232–3235. DOI: 10.1103/PhysRevLett.77.3232.

[Shv+98] Y. V. Shvyd'ko et al. "Hybrid beat in nuclear forward scattering of synchrotron radiation". In: *Phys. Rev. B* 57 (1998), pages 3552–3561. DOI: 10.1103/PhysRevB.57.3552.

[Shv99] Y. V. Shvyd'ko. "Nuclear resonant forward scattering of x rays: Time and space picture". In: *Phys. Rev. B* 59 (1999), pages 9132–9143. DOI: 10.1103/PhysRevB.59.9132.

[Shw+12] S. Shwartz et al. "X-Ray Parametric Down-Conversion in the Langevin Regime". In: *Phys. Rev. Lett.* 109 (2012), page 013602. DOI: 10.1103/PhysRevLett.109.013602.

[Sie31] M. Siegbahn. *Spektroskopie der Röntgenstrahlen*. Springer Berlin Heidelberg. 1931. DOI: 10.1007/978-3-642-50783-0.

[Sik+20] T. Sikorsky et al. "Measurement of the ^{229}Th Isomer Energy with a Magnetic Microcalorimeter". In: *Phys. Rev. Lett.* 125 (2020), page 142503. DOI: 10.1103/PhysRevLett.125.142503.

[Sil86] B. W. Silverman. *Density estimation for statistics and data analysis*. Chapman & Hall/CRC, Philadelphia, PA. 1986.

[Skr+73] N. Skribanowitz et al. "Observation of Dicke Superradiance in Optically Pumped HF Gas". In: *Phys. Rev. Lett.* 30 (1973), pages 309–312. DOI: 10.1103/PhysRevLett.30.309.

[SLT04] Sturhahn, W., L'abbé, C., and Toellner, T. S. "Exo-interferometric phase determination in nuclear resonant scattering". In: *Europhys. Lett.* 66 (2004), pages 506–512. DOI: 10.1209/epl/i2003-10235-7.

[Slu+85] R. E. Slusher et al. “Observation of Squeezed States Generated by Four-Wave Mixing in an Optical Cavity”. In: *Phys. Rev. Lett.* 55 (1985), pages 2409–2412. DOI: 10.1103/PhysRevLett.55.2409.

[SM85] D. Strickland and G. Mourou. “Compression of amplified chirped optical pulses”. In: *Optics Communications* 55 (1985), pages 447–449. DOI: 10.1016/0030-4018(85)90151-8.

[Smi+06] G. V. Smirnov et al. “Nuclear γ resonance time-domain interferometry: Quantum beat and radiative coupling regimes compared in revealing quasielastic scattering”. In: *Phys. Rev. B* 73 (2006), page 184126. DOI: 10.1103/PhysRevB.73.184126.

[Smi+84] G. Smirnov et al. “Nanosecond modulation of ^{57}Fe Mössbauer radiation”. In: *Zh. Eksp. Teor. Fiz* 86 (1984), pages 1495–1504.

[Smi00] G. V. Smirnov. “Synchrotron Mössbauer source of ^{57}Fe radiation”. In: *Hyperfine Interactions* 125 (2000), pages 91–112. DOI: 10.1023/A:1012677402777.

[Smi12] G. V. Smirnov. “Coherent Nuclear Resonance Fluorescence”. In: *The Rudolf Mössbauer Story: His Scientific Work and Its Impact on Science and History*. Edited by G. Kalvius and P. Kienle. Berlin, Heidelberg: Springer, 2012.

[Smi99] G. Smirnov. “General properties of nuclear resonant scattering”. In: *Hyperfine Interactions* 123 (1999), pages 31–77. DOI: 10.1023/A:1017007520099.

[SO08] R. N. Shakhmuratov and J. Odeurs. “Off-resonance slow light”. In: *Phys. Rev. A* 78 (2008), page 063836. DOI: 10.1103/PhysRevA.78.063836.

[SPR15] J. Schachenmayer, A. Pikovski, and A. M. Rey. “Many-Body Quantum Spin Dynamics with Monte Carlo Trajectories on a Discrete Phase Space”. In: *Phys. Rev. X* 5 (2015), page 011022. DOI: 10.1103/PhysRevX.5.011022.

[SR08] G. K. Shenoy and R. Röhlsberger. “Scientific opportunities in nuclear resonance spectroscopy from source-driven revolution”. In: *Hyperfine Interactions* 182 (2008), pages 157–172. DOI: 10.1007/s10751-008-9720-y.

[SS89] Y. V. Shvyd’ko and G. V. Smirnov. “Experimental study of time and frequency properties of collective nuclear excitations in a single crystal (γ-ray resonance)”. In: *Journal of Physics: Condensed Matter* 1 (1989), pages 10563–10584. DOI: 10.1088/0953-8984/1/51/025.

[SS90] Y. Shvyd’ko and G. Smirnov. “On the direct measurement of nuclear γ-resonance parameters of long-lived ≤ 1 s) isomers”. In: *Nuclear Instruments and Methods in Physics Research Section B: Beam Interactions with Materials and Atoms* 51 (1990), pages 452–457. DOI: https://doi.org/10.1016/0168-583X(90)90567-E.

[SSF20] M. Sánchez-Barquilla, R. E. F. Silva, and J. Feist. “Cumulant expansion for the treatment of light–matter interactions in arbitrary material structures”. In: *The Journal of Chemical Physics* 152 (2020), page 034108. DOI: 10.1063/1.5138937.

[ST58] A. L. Schawlow and C. H. Townes. “Infrared and Optical Masers”. In: *Phys. Rev.* 112 (1958), pages 1940–1949. DOI: 10.1103/PhysRev.112.1940.

[Ste25] D. A. Steck. *Sodium D Line Data*. http://steck.us/alkalidata. Revision 2.3.4, 8 August 2025 (accessed 22.08.2025). 2025.

[Str] Strohmaier, Erich and Dongarra, Jack and Simon, Horst and Meuer, Martin. *TOP500 List - June 2025*. https://top500.org/lists/top500/list/2025/06/. Accessed: 28.08.2025.

[Str+22] M. Straub et al. “Differential Measurement of Electron Ejection after Two-Photon Two-Electron Excitation of Helium”. In: *Phys. Rev. Lett.* 129 (2022), page 183204. DOI: 10.1103/PhysRevLett.129.183204.

[Stu01] W. Sturhahn. “Phase problem in synchrotron Mössbauer spectroscopy”. In: *Phys. Rev. B* 63 (2001), page 094105. DOI: 10.1103/PhysRevB.63.094105.

[Stu04] W. Sturhahn. “Nuclear resonant spectroscopy”. In: *Journal of Physics: Condensed Matter* 16 (2004), S497. DOI: 10.1088/0953-8984/16/5/009.

[SVP25] A. Stejskal, V. Vrba, and V. Procházka. “Toward flexible intensity control of resonantly scattered γ-rays using multi-frequency vibrating resonant absorber”. In: *Applied Physics Letters* 126 (2025), page 084102. DOI: 10.1063/5.0249167.

[SW00] V. Schünemann and H. Winkler. “Structure and dynamics of biomolecules studied by Mössbauer spectroscopy”. In: *Reports on Progress in Physics* 63 (2000), page 263. DOI: 10.1088/0034-4885/63/3/202.

[SW22] V. P. Singh and H. Weimer. “Driven-Dissipative Criticality within the Discrete Truncated Wigner Approximation”. In: *Phys. Rev. Lett.* 128 (2022), page 200602. DOI: 10.1103/PhysRevLett.128.200602.

[SWC12] J. C. H. Spence, U. Weierstall, and H. N. Chapman. “X-ray lasers for structural and dynamic biology”. In: *Reports on Progress in Physics* 75 (2012), page 102601. DOI: 10.1088/0034-4885/75/10/102601.

[SZ97] M. O. Scully and M. S. Zubairy. *Quantum Optics*. Cambridge University Press. 1997.

[TB13] A. M. Thomas and A. K. Banerjee. *The history of radiology*. OUP Oxford. 2013.

[Teb+24] F. Tebbenjohanns et al. “Predicting correlations in superradiant emission from a cascaded quantum system”. In: *Phys. Rev. A* 110 (2024), page 043713. DOI: 10.1103/PhysRevA.110.043713.

[Thi+07] C. Thiel et al. “Generation of Symmetric Dicke States of Remote Qubits with Linear Optics”. In: *Phys. Rev. Lett.* 99 (2007), page 193602. DOI: 10.1103/PhysRevLett.99.193602.

[Tho+09] A. C. Thompson et al. *X-Ray Data Booklet*. Update: October 2009. 2009.

[Tie+24] J. Tiedau et al. “Laser Excitation of the Th-229 Nucleus”. In: *Phys. Rev. Lett.* 132 (2024), page 182501. DOI: 10.1103/PhysRevLett.132.182501.

[Toe+11] T. S. Toellner et al. “Synchrotron Mössbauer spectroscopy using high-speed shutters”. In: *Journal of Synchrotron Radiation* 18 (2011), pages 183–188. DOI: 10.1107/S090904951003863X.

[Toe+95] T. S. Toellner et al. “Polarizer/analyzer filter for nuclear resonant scattering of synchrotron radiation”. In: *Applied Physics Letters* 67 (1995), pages 1993–1995. DOI: 10.1063/1.114764.

[Tom46] S. Tomonaga. “On a Relativistically Invariant Formulation of the Quantum Theory of Wave Fields*”. In: *Progress of Theoretical Physics* 1 (1946), pages 27–42. DOI: 10.1143/ptp.1.27.

[Tom95] M. S. Tomaš. “Green function for multilayers: Light scattering in planar cavities”. In: *Phys. Rev. A* 51 (1995), pages 2545–2559. DOI: 10.1103/PhysRevA.51.2545.

[Trä12] *Springer Handbook of Lasers and Optics*. Springer Berlin Heidelberg. 2012. DOI: 10.1007/978-3-642-19409-2.

[Tro+23] F. Trost et al. “Imaging via Correlation of X-Ray Fluorescence Photons”. In: *Phys. Rev. Lett.* 130 (2023), page 173201. DOI: 10.1103/PhysRevLett.130.173201.

[UHH02] T. Udem, R. Holzwarth, and T. W. Hänsch. “Optical frequency metrology”. In: *Nature* 416 (2002), pages 233–237. DOI: 10.1038/416233a.

[URM12] J. Ullrich, A. Rudenko, and R. Moshammer. “Free-Electron Lasers: New Avenues in Molecular Physics and Photochemistry”. In: *Annual Review of Physical Chemistry* 63 (2012), pages 635–660. DOI: 10.1146/annurev-physchem-032511-143720.

[Vag+14] F. Vagizov et al. “Coherent control of the waveforms of recoilless γ-ray photons”. In: *Nature* 508 (2014), pages 80–83. DOI: 10.1038/nature13018.

[Vel+24] S. Velten et al. “Nuclear quantum memory for hard x-ray photon wave packets”. In: *Science Advances* 10 (2024), eadn9825. DOI: 10.1126/sciadv.adn9825.

[Vir+20] P. Virtanen et al. “SciPy 1.0: fundamental algorithms for scientific computing in Python”. In: *Nature Methods* 17 (2020), pages 261–272. DOI: 10.1038/s41592-019-0686-2.

[VSK13] F. G. Vagizov, E. K. Sadykov, and O. A. Kocharovskaya. “Modulation of Mössbauer radiation by pulsed laser excitation”. In: *JETP Letters* 96 (2013), pages 812–816. DOI: 10.1134/S0021364012240137.

[WC53] J. D. Watson and F. H. C. Crick. "Molecular Structure of Nucleic Acids: A Structure for Deoxyribose Nucleic Acid". In: *Nature* 171 (1953), pages 737–738. DOI: 10.1038/171737a0.

[WD75] D. Wineland and H. Dehmelt. "Proposed $10^{14}\delta\nu/\nu$ laser fluorescence spectroscopy on Tl+ mono-ion oscillator III (side band cooling)". In: *Bull. Am. Phys. Soc* 20 (1975), pages 637–637.

[WE23] L. Wolff and J. Evers. "Characterization and detection method for x-ray excitation of Mössbauer nuclei beyond the low-excitation regime". In: *Phys. Rev. A* 108 (2023), page 043714. DOI: 10.1103/PhysRevA.108.043714.

[Wen+16] L. von der Wense et al. "Direct detection of the 229Th nuclear clock transition". In: *Nature* 533 (2016), pages 47–51. DOI: 10.1038/nature17669.

[Whi92] S. R. White. "Density matrix formulation for quantum renormalization groups". In: *Phys. Rev. Lett.* 69 (1992), pages 2863–2866. DOI: 10.1103/PhysRevLett.69.2863.

[Wil+10] H.-C. Wille et al. "Nuclear resonant scattering at PETRA III : Brillant opportunities for nano – and extreme condition science". In: *Journal of Physics: Conference Series* 217 (2010), page 012008. DOI: 10.1088/1742-6596/217/1/012008.

[Wil21] P. R. Willmott. "X-Ray Sources at Large-Scale Facilities". In: *Magnetism and Accelerator-Based Light Sources*. Edited by H. Bulou et al. Cham: Springer International Publishing, 2021, pages 1–37.

[WK04] F. E. Wagner and A. Kyek. "Mössbauer Spectroscopy in Archaeology: Introduction and Experimental Considerations". In: *Hyperfine Interactions* 154 (2004), pages 5–33. DOI: 10.1023/b:hype.0000032112.94624.95.

[WK21] L. J. Wong and I. Kaminer. "Prospects in x-ray science emerging from quantum optics and nanomaterials". In: *Applied Physics Letters* 119 (2021), page 130502. DOI: 10.1063/5.0060552.

[Wol02] W. H. Wollaston. "XII. A method of examining refractive and dispersive powers, by prismatic reflection". In: *Philosophical transactions of the Royal Society of London* (1802), pages 365–380.

[Woo87] W. K. Wootters. "A Wigner-function formulation of finite-state quantum mechanics". In: *Annals of Physics* 176 (1987), pages 1–21. DOI: https://doi.org/10.1016/0003-4916(87)90176-X.

[WTA73] F. E. Wagner, K. Thoma, and M. Atoji. "Mössbauer scattering of the 166 keV gamma rays of ^{139}La". In: *Zeitschrift für Physik A Hadrons and nuclei* 262 (1973), pages 265–270. DOI: 10.1007/bf01391843.

[Yag_p] L. Yagüe Bosch. *Master's thesis*. in preparation.

[Yam+24] H. Yamashita et al. "The correlation of the gamma ray waveform with the vibration phase of the resonant absorber". In: *Interactions* 245 (2024). DOI: 10.1007/s10751-024-02214-3.

[Yar65] A. Yariv. "Internal modulation in multimode laser oscillators". In: *Journal of Applied Physics* 36 (1965), pages 388–391. DOI: 10.1063/1.1713999.

[YL13] Y. Yoshida and G. Langouche. *Mössbauer Spectroscopy: Tutorial Book*. Springer Berlin Heidelberg. 2013. DOI: 10.1007/978-3-642-32220-4.

[Yon+14] H. Yoneda et al. "Saturable absorption of intense hard X-rays in iron". In: *Nature Communications* 5 (2014). DOI: 10.1038/ncomms6080.

[You+10] L. Young et al. "Femtosecond electronic response of atoms to ultra-intense X-rays". In: *Nature* 466 (2010), pages 56–61. DOI: 10.1038/nature09177.

[YSD24] C. .-. Yang, K. M. Spohr, and D. Doria. *Multi-photon stimulated grasers assisted by laser-plasma interactions*. 2024. arXiv: 2404.10025 [physics.optics].

[Yua+25] Z. Yuan et al. "Nuclear phase retrieval spectroscopy using resonant x-ray scattering". In: *Nature Communications* 16 (2025), page 3096. DOI: 10.1038/s41467-025-58396-z.

[Zha+18] J. Zhang et al. "Towards Gotthard-II: development of a silicon microstrip detector for the European X-ray Free-Electron Laser". In: *Journal of Instrumentation* 13 (2018), P01025. DOI: 10.1088/1748-0221/13/01/P01025.

[Zha+19] X. Zhang et al. “Nuclear Quantum Memory and Time Sequencing of a Single γ Photon”. In: *Phys. Rev. Lett.* 123 (2019), page 250504. DOI: 10.1103/PhysRevLett.123.250504.

[Zha+20] Z. Zhang et al. “Statistical analysis of a self-seeded x-ray free-electron laser in the presence of the microbunching instability”. In: *Phys. Rev. Accel. Beams* 23 (2020), page 010704. DOI: 10.1103/PhysRevAccelBeams.23.010704.

[Zha+24] C. Zhang et al. “Frequency ratio of the ^{229m}Th nuclear isomeric transition and the ^{87}Sr atomic clock”. In: *Nature* 633 (2024), pages 63–70. DOI: 10.1038/s41586-024-07839-6.

[ZHO23] H. Zen, R. Hajima, and H. Ohgaki. “Full characterization of superradiant pulses generated from a free-electron laser oscillator”. In: *Scientific Reports* 13 (2023). DOI: 10.1038/s41598-023-33550-z.

[Zim+23] J. Zimmermann et al. “Finding the semantic similarity in single-particle diffraction images using self-supervised contrastive projection learning”. In: *npj Computational Materials* 9 (2023). DOI: 10.1038/s41524-023-00966-0.

[Žun15] B. Žunkovič. “Continuous phase-space methods on discrete phase spaces”. In: *EPL (Europhysics Letters)* 112 (2015), page 10003. DOI: 10.1209/0295-5075/112/10003.

Acknowledgements

First of all, I want to thank Jörg Evers for supervising this thesis, but also as a friend for many years now. You always gave me the freedom to chase the questions that fascinated me most, while at the same time making sure that I do not get stuck. I think neither of us expected the path to look the way it did in the beginning, but in the end the adventure led us to where we wanted to be regarding the covered topics. I'm also grateful to Christoph Keitel for his support as co-supervisor and director of the Theoretical Quantum Dynamics division, and to Thomas Pfeifer for the co-supervision as well as for showing me many things about XFELs and always being open to dream about the craziest experiments. For the experiments, I owe a huge thanks to Ralf Röhlsberger, not only for teaching me a lot about Mössbauer science, but also for listening to my thoughts and ideas with openness. I also really appreciated the help from Lars Bocklage, Olaf Leupold, Leon Lohse, Sakshath Sadashivaiah, Kai Schlage, Ilya Sergeev, Cornelius Strohm, Sven Velten, and Hans-Christian Wille who patiently answered all my naive "theoretician's questions" regarding Mössbauer science, and from Willi Hippler, Robert Lötzsch, Berit Marx-Glowna and Kai Schulze, who taught me about crystals and x-ray optics. And of course, none of the experiments would have been possible without the ^{57}Fe EuXFEL collaboration and the ^{45}Sc EuXFEL collaboration and the great support from DESY and EuXFEL staff, especially James Wrigley. Thanks to all of you not only for making these experiments happen, but also for the fun times we had during the beamtimes. Yes, I will bring the "Erfolgsnussecken" again to the next experiment. Back at the institute, I really enjoyed the many discussions with Christian Ott and José Crespo, and with so many others. My thanks also go to all my current and former colleagues Deniz Adigüzel, Oliver Diekmann, Robert Horn, Junhee Lee, Karoline Moll, Ze-an Peng, Luis Yagüe Bosch, and Lukas Wolff. You've been there both in physics and in everyday life, from whiteboard discussions over onion cake traditions to keeping our snack desk always filled. A very special thanks goes to Dominik Lentrodt, who has been a mentor to me in many ways over many years now. I'm also grateful to everyone who made my time at the institute such a good time — not only for the physics or science in general, but also for all the personal conversations and laughs along the way. This thanks also extends to all the contacts and friendships I made at conferences and summer schools.

The Max-Planck Institute for Nuclear Physics provided a wonderful place to do science, and I also want to acknowledge the IMPRS-QD and the HGSFP for their support.

For this thesis specifically, I want to thank Maurits Haverkort for serving as a referee and Selim Jochim and Werner Aeschbach for completing the defense committee. And thank you to Deniz Adigüzel, Rebecca Haines, Robert Horn, Annabelle Kaiser, Dominik Lentrodt, and Luis Yagüe Bosch for proofreading and for keeping me up throughout the final phase.

Der letzte und größte Dank geht an meine Familie. Ihr habt schon von klein auf immer an mich geglaubt und mich unterstützt. Während der letzten vier Jahre habt ihr mich immer wieder in schwierigen Momenten gestärkt und euch in erfolgreichen Momenten von Herzen mit mir gefreut. Vielen, vielen Dank dafür!